Advanced Quadrature Selection for Monte Carlo Variance Reduction

by

Kelly L. Rowland

A dissertation submitted in partial satisfaction of the

requirements for the degree of

Doctor of Philosophy

in

Engineering – Nuclear Engineering

and the Designated Emphasis

in

Computational and Data Science and Engineering

in the

Graduate Division

of the

University of California, Berkeley

Committee in charge:

Assistant Professor Rachel N. Slaybaugh, Chair
Associate Professor Per-Olof Persson
Professor Jasmina Vujić
Dr. Steven P. Hamilton

Spring 2018

Advanced Quadrature Selection for Monte Carlo Variance Reduction

Abstract

Advanced Quadrature Selection for Monte Carlo Variance Reduction

by

Kelly L. Rowland

Doctor of Philosophy in Engineering – Nuclear Engineering

University of California, Berkeley

Assistant Professor Rachel N. Slaybaugh, Chair

Neutral particle radiation transport simulations are critical for radiation shielding and deep penetration applications. Arriving at a solution for a given response of interest can be computationally difficult because of the magnitude of particle attenuation often seen in these shielding problems. Hybrid methods, which aim to synergize the individual favorable aspects of deterministic and stochastic solution methods for solving the steady-state neutron transport equation, are commonly used in radiation shielding applications to achieve statistically meaningful results in a reduced amount of computational time and effort. The current state of the art in hybrid calculations is the Consistent Adjoint-Driven Importance Sampling (CADIS) and Forward-Weighted CADIS (FW-CADIS) methods, which generate Monte Carlo variance reduction parameters based on deterministically-calculated scalar flux solutions. For certain types of radiation shielding problems, however, results produced using these methods suffer from unphysical oscillations in scalar flux solutions that are a product of angular discretization. These aberrations are termed "ray effects".

The Lagrange Discrete Ordinates (LDO) equations retain the formal structure of the traditional discrete ordinates formulation of the neutron transport equation and mitigate ray effects at high angular resolution. In this work, the LDO equations have been implemented in the Exnihilo parallel neutral particle radiation transport framework, with the deterministic scalar flux solutions passed to the Automated Variance Reduction Generator (ADVANTG) software and the resultant Monte Carlo variance reduction parameters' efficacy assessed based on results from MCNP5. Studies were conducted in both the CADIS and FW-CADIS contexts, with the LDO equations' variance reduction parameters seeing their best performance in the FW-CADIS method, especially for photon transport.

Contents

List of Figures

List of Tables

Acknowledgments

It takes a village to make a doctor. I cannot express how grateful I am to the colleagues, friends, family, and various community members who have supported me throughout my tenure in graduate school. Without all of your contributions, this process would have been much more difficult.

Many thanks go to my dissertation committee for their time and effort spent in improving the quality of this writing. I would like to thank the Exnihilo team at Oak Ridge National Laboratory for all of their help and guidance. Dr. Steven Hamilton, you have my sincerest gratitude for your help at all levels of this project, from working through big conceptual questions to kindly pointing out the smallest of floating point errors. This work would not have been finished in any sort of timely manner without your generosity.

My colleagues have made Berkeley an amazing place to work and grow. Drs. Phil Gorman and Katy Huff, thank you for your patience and kindness in teaching me scientific computing skills when I had none. Dr. Madicken Munk, my commiserator-in-chief, thank you for seeing me through the most trying of times and for paving a better-informed `PATH` than I would have otherwise traversed. Daniel Wooten, thank you for helping me to say no to more things. Josh Rehak, thanks for helping me keep it surreal. Ellen Edwards, thank you for continually inspiring me to challenge myself.

Berkeley Research Computing has been a great source of pride and joy for me to be a part of. Aaron Culich, I cannot thank you enough for looking at a graduate student in desperate need of help and seeing the potential for so much more. I am grateful to the Department of Nuclear Engineering for all of the free coffee that it has provided.

To my family, thank you for your endless support and encouragement. You have provided me with an incredible foundation from which I have been fortunate to pursue any and all of my dreams.

Cathy Berman, thank you for being my personal cheerleader and helping me grow into myself. Dr. Dillon Shaver, thank you for helping me pass my screening exams when I really needed it. Shola Ogunlana, thank you for leading the STRONGER family to be better versions of ourselves through each and every burpee. Mitch Crispell, thank you for bringing joy to every single person who steps into one of your dance classes. Alex Converse, thank you for the love and support that you have provided, even when it meant bearing with me through a few periods of crunch time.

Professor Rachel N. Slaybaugh, thank you for advising me in so much more than just this dissertation work. Your perspective and insights have helped me to not only bloom as a researcher, but to a grow as a person as well. I am very fortunate to have had your support in the myriad of endeavors that I have undertaken in graduate school. Thank you for caring about my well-being as an individual and broadening my horizons in ways that I never could have fathomed.

This material is based upon work supported under an Integrated University Program Graduate Fellowship as well as supported by the Department of Energy under Award Number(s) DE-NE0008661. This report was prepared as an account of work sponsored by an agency of the United States Government. Neither the United States Government nor any agency thereof, nor any of their employees, makes any warranty, express or limited, or assumes any legal liability or responsibility for the accuracy, completeness, or usefulness of any information, apparatus, product, or process disclosed, or represents that its use would not infringe privately owned rights. Reference herein to any specific commercial product, process, or service by trade name, trademark, manufacturer, or otherwise does not necessarily constitute or imply its endorsement, recommendation, or favoring by the United States Government or any agency thereof. The views and opinions of authors expressed herein do not necessarily state or reflect those of the United States Government or any agency thereof. This research used the Savio computational cluster resource provided by the Berkeley Research Computing program at the University of California, Berkeley (supported by the UC Berkeley Chancellor, Vice Chancellor for Research, and Chief Information Officer).

Chapter 1

Introduction

The work covered in this dissertation includes the implementation of the Lagrange Discrete Ordinates (LDO) equations in the Exnihilo parallel neutral particle radiation transport framework for the purpose of using the equations' solutions in Monte Carlo variance reduction parameter generation via the ADVANTG software to improve the results of simulations run with MCNP5. We start with an analysis of deterministic scalar flux results from solving the LDO equations compared against those of standard discrete ordinates quadrature set types because the LDO equations have never before been implemented in a framework such as Exnihilo. Then, we assess the performance of the Monte Carlo variance reduction parameters generated based on the forward and adjoint solutions from the various quadrature set types in the contexts of both the Consistent Adjoint-Driven Importance Sampling (CADIS) and the Forward-Weighted CADIS (FW-CADIS) methods.

1.1 Motivation

Radiation shielding is an important and interesting problem from various perspectives. Simulation of shielding scenarios is critical for health physics and nuclear security applications, but arriving at a solution for a given response of interest (e.g., neutron flux at a given location) can be computationally difficult in the context of the magnitude of particle attenuation often seen in shielding problems.

The steady-state neutron transport equation (NTE), introduced below in Section 1.3, is typically solved using either deterministic methods or stochastic (Monte Carlo) methods. We will look at each of these solution methods in further detail in Chapter 2, but briefly note here that both solution methods have individual strengths and weaknesses. So-called "hybrid" methods aim to combine the favorable aspects of deterministic and Monte Carlo methods to achieve better results. Although hybrid methods are used to significant effect in radiation shielding problems, they do not entirely mitigate the negative aspects of the combined simulation types.

One particular area of study where hybrid methods tend to fall short is in shielding

problems with highly anisotropic particle movement and particle streaming pathways. This is because the standard implementation of the CADIS and FW-CADIS methods is based on scalar particle flux rather than angular particle flux. So, solutions from deterministic calculations exclude information about how particles move toward a response of interest. For problems with strong anisotropies in the particle flux, the importance map and biased source developed using the standard space/energy treatment may not represent the real importance well enough to sufficiently improve efficiency in the Monte Carlo calculation.

This work aims to gauge the performance of Monte Carlo biasing parameters based on scalar flux solutions from solving the LDO equations. We will be employing the LDO equations' solutions in the standard CADIS and FW-CADIS methods to assess how well the LDO representation's unique treatment of scattering and asymmetry in angle incorporate angular information into the resultant scalar flux solutions and corresponding Monte Carlo biasing parameters.

1.2 Goals and Impacts

The primary goal of this work is to assess the forward and adjoint scalar flux solutions of the Lagrange Discrete Ordinates equations as input for Monte Carlo variance reduction parameter generation in the contexts of the CADIS and FW-CADIS methods. Additional research objectives in support of the primary goal for this work include:

- Implement the LDO equations in a neutral particle radiation transport framework designed to solve the traditional discrete ordinates form of the NTE.
- Choose a small variety of test cases in which to assess the various quadrature types' deterministic scalar flux solutions for efficacy in Monte Carlo variance reduction parameter generation.
- Compare forward and adjoint scalar flux solutions resultant from the LDO equations against those generated with standard discrete ordinates quadrature sets for the chosen test scenarios.
- Test the impact of biasing parameters' angular mesh refinement on Monte Carlo results across various quadrature types.

In meeting these objectives as progress towards accomplishing the primary research goal, we verify the relative accuracy of the deterministic solutions of the LDO equations and then examine how they perform as the deterministic solver for hybrid methods. The test problems used are those that challenge hybrid methods in general, and so we have generated a variety of results of interest to the community at large.

1.3 The Neutron Transport Equation

The way in which neutrons move, known as "neutron transport", is governed by the time-dependent neutron transport equation (NTE) [1]:

$$\frac{1}{v}\frac{\partial}{\partial t}\psi(\mathbf{r},E,\mathbf{\Omega},t)+\mathbf{\Omega}\cdot\nabla\psi(\mathbf{r},E,\mathbf{\Omega},t)+\Sigma_t(\mathbf{r},E)\psi(\mathbf{r},E,\mathbf{\Omega},t)= \int_0^\infty\int_{4\pi}\Sigma_s(\mathbf{r},E'\rightarrow E,\mathbf{\Omega}'\cdot\mathbf{\Omega})\psi(\mathbf{r},E',\mathbf{\Omega}',t)d\mathbf{\Omega}'dE'+Q(\mathbf{r},E,\mathbf{\Omega},t), \quad (1.1)$$

where $\mathbf{r}$ is the neutron position, E is the energy of the neutron, $\mathbf{\Omega}$ is the direction of travel of the neutron, and t is the time. The combination of $(\mathbf{r},E,\mathbf{\Omega},t)$ is generally referred to as the "phase space" of the particles. ψ denotes angular neutron flux, Σ represents the cross section of a material, and Q is any additional source (fission, a fixed source, etc.) of neutrons.

We are often interested in situations in which the particle flux is not a function of time. In these cases, we solve the time-independent (steady-state) neutron transport equation, written as

$$\mathbf{\Omega}\cdot\nabla\psi(\mathbf{r},E,\mathbf{\Omega})+\Sigma_t(\mathbf{r},E)\psi(\mathbf{r},E,\mathbf{\Omega})= \int_0^\infty\int_{4\pi}\Sigma_s(\mathbf{r},E'\rightarrow E,\mathbf{\Omega}'\cdot\mathbf{\Omega})\psi(\mathbf{r},E',\mathbf{\Omega}')d\mathbf{\Omega}'dE'+Q(\mathbf{r},E,\mathbf{\Omega}). \quad (1.2)$$

The steady-state neutron transport equation can be thought of as a balance equation in which the neutron losses represented on the left-hand side of the equation are equal to the neutron gains represented on the right-hand side of the equation [1]. The first term on the left-hand side of the steady-state NTE accounts for all neutrons lost by streaming out through the surface of the system being considered. The second term in the left-hand side of the steady-state NTE accounts for all neutrons lost to collisions; this includes neutrons lost via absorption as well as neutrons that exit the phase space of interest by scattering into a different energy and angle. The right-hand side of the equation totals system gains by summing up all neutrons that scatter into the phase space of interest from different energies and angles along with neutrons created from the source. The scattering term depends not on the individual angles $\mathbf{\Omega}$ and $\mathbf{\Omega}'$ but on their dot product.

The derivative in the first term of the steady-state NTE suggests that we must prescribe appropriate boundary conditions for the equation in order to solve the problem. The boundary conditions depend on the given problem of interest and will be discussed in more detail later. The following chapter will provide in-depth explanations of various solution methods for the time-independent NTE.

1.4 Dissertation Outline

The remainder of this dissertation is structured so as to provide a relevant theoretical background and discussion as a prelude to the eventual presentation of the results and analysis arrived at in meeting the sundry and ultimate objectives listed above in Section 1.2. Chapter 2 provides a theoretical basis of the foundation of solution methods for the NTE, followed by a discussion of pertinent work in the area of hybrid methods. Specific attention is given to developments that aimed to incorporate angular information into Monte Carlo biasing parameters; we will see in Section 2.3 that the interest in using the LDO equations' solutions for Monte Carlo variance reduction parameter generation stems from the unique way in which the LDO equations treat particle scattering.

Transitioning from theory to practice, Chapter 3 examines the traditional discrete ordinates equations and the LDO equations from the perspective of implementing both sets of equations in a neutral particle radiation transport software framework. Specific focus is given on the differences in implementing the contrasting equations; a discussion of details regarding the solution of the LDO equations in a framework designed to solve the conventional discrete ordinates equations concludes the chapter. We note that the discussion in Chapters 2 and 3 focuses on neutron transport, but the solution methods can be leveraged for photon transport as well; Chapter 4 presents the test case scenarios examined in this work with results from the various hybrid methodologies for both neutron and photon transport problems. Chapter 5 concludes the dissertation with a summary review of the results and analysis followed by a brief discussion of future work paths.

Chapter 2

Background

This chapter provides information relevant to the core parts of this research, with a particular focus on areas relevant to the novel work presented. We start by discussing the two main approaches to solving the NTE, Monte Carlo methods and deterministic methods, as the hybrid methods that are described next incorporate both types of solutions. Then, a discussion of previous work in the field of hybrid methods is given, with a specific focus on the CADIS method and variants on that method as well as significant historical work that has incorporated angular information into hybrid methods. Finally, we present a mathematical background for and derivation of the LDO equations.

2.1 Approaches to Solving the Neutron Transport Equation

2.1.1 Monte Carlo Methods

Solving the NTE using Monte Carlo methods approximates "following" the individual particles from birth to death. The purpose of particle tracking is to calculate the expectation or mean value $\bar{x}$ of some quantity of interest, often the neutron scalar flux. The estimate of this quantity takes the form of the average of N samples:

$$\hat{x} = \frac{1}{N} \sum_{n=1}^{N} x_n, \tag{2.1}$$

where x_n is the contribution from the n^{th} particle history to the quantity of interest. As the calculation proceeds, x_n is tallied from each neutron history in order to calculate the estimated or sample mean $\hat{x}$ at the end of the calculation. Errors in Monte Carlo calculations take the form of stochastic uncertainties, as the independent variables of the NTE are treated continuously. Taking this into consideration, it is useful to quantify how good of an estimate the sample value $\hat{x}$ is to the true mean value $\bar{x}$.

For some property of a Monte Carlo history x sampled from a continuous probability density function $f(x)$, the variance of that property is defined to be

$$\sigma^2(x) = \overline{x^2} - \bar{x}^2, \tag{2.2}$$

where

$$\overline{x^n} \equiv \int_{-\infty}^{\infty} x^n f(x) dx. \tag{2.3}$$

The standard deviation of the property is calculated as the square root of the variance:

$$\sigma(x) = \left(\overline{x^2} - \bar{x}^2\right)^{1/2} \tag{2.4}$$

and provides a measure of the spread of x about the mean value $\bar{x}$ [2]. With this, the variance and standard deviation of $\hat{x}$ can be expressed in terms of the variance and standard deviation of x as

$$\sigma^2(\hat{x}) = \frac{1}{N}\sigma^2(x) \tag{2.5}$$

and

$$\sigma(\hat{x}) = \frac{\sigma(x)}{\sqrt{N}}, \tag{2.6}$$

respectively. A low standard deviation indicates that the values of x are closely clustered near $\bar{x}$, while a high standard deviation indicates a large spread in the values of x. If $\hat{x}$, constructed from N values of x_n, is used to estimate $\bar{x}$, then the spread in the results of $\hat{x}$ about $\bar{x}$ is proportional to $\sigma(x)$ and falls off as the square root of the number of histories in the sample, as seen in Equation 2.6 [2]. This is to say, generally, that a greater number of histories contributing to the property of interest being calculated results in a lower standard deviation of the estimate of that property.

For a given Monte Carlo calculation, the sample variance is defined as

$$S^2 = \frac{1}{N-1}\sum_{n=1}^{N}(x_n - \hat{x})^2 \tag{2.7}$$

and is considered to be an unbiased estimator of the variance; the expectation value of the sample variance is equal to the variance, $\sigma^2(x)$ [2]. Because it is an unbiased estimator of the variance, the sample variance allows us to estimate the spread in $\hat{x}$; this is useful because $\hat{x}$ is the value that actually results from the Monte Carlo calculation. In practice, the sample variance and standard deviation are calculated as

$$S^2 = \frac{N}{N-1}\left(\widehat{x^2} - \hat{x}^2\right), \text{ where } \widehat{x^2} \equiv \frac{1}{N}\sum_{n=1}^{N} x_n^2, \tag{2.8}$$

and

$$S = \left(\frac{N}{N-1}\right)^{1/2} \left[\frac{1}{N}\sum_{n=1}^{N} x_n^2 - \hat{x}^2\right]^{1/2}, \tag{2.9}$$

respectively [2]. For large numbers of histories, $\frac{N}{N-1}$ is often set equal to one.

The simplest Monte Carlo model for particle transport problems is the "analog" model that uses the real probability that various events occur [3]. In the analog model, particles are followed from event to event, and the next event is always sampled from a number of possible events according to the real event probabilities. This is called the analog Monte Carlo model because it is directly analogous to the naturally occurring transport; it works well when a significant fraction of the particles contribute to the tally estimate and can be compared to detecting a significant fraction of the particles in the physical situation.

To quantify the efficiency of calculating a given quantity of interest, a metric known as the "figure of merit" is often used.

2.1.1.1 The Figure of Merit

The figure of merit (FOM) is defined as

$$\text{FOM} = \frac{1}{R^2 T}, \tag{2.10}$$

where R is the estimated relative error, defined as $S/\hat{x}$, and T is the computer time taken to complete the calculation [3]. This value should be approximately constant for any one Monte Carlo calculation, as R^2 is proportional to $1/N$ and T should be directly proportional to N.

As stated earlier, estimates for quantities of interest with the lowest statistical error are usually obtained for quantities to which a substantial fraction of the histories contribute. That is to say, in order to get estimates for quantities of interest that are statistically meaningful (have sufficiently low statistical error), a sizable number of the particle histories tracked should contribute to the estimate. This can be difficult to achieve in a reasonable amount of computational time for certain analog Monte Carlo calculations. That is to say, if these analog calculations were allowed to continue until convergence, they would have a very small FOM because of the sheer amount of calculation time needed for the calculation to finish. A pertinent example of this type of problem is a neutron shielding scenario, in which the neutron scalar flux varies by orders of magnitude through the shield and over the problem geometry. In these cases, "non-analog" techniques are introduced.

Non-analog Monte Carlo attempts to follow "interesting" particles more often than uninteresting ones, where an interesting particle is one that contributes much more to the quantity that needs to be estimated. Non-analog techniques are meant to increase the odds that a given particle contributes to the quantity of interest. To ensure that the average score

is the same in the non-analog model as in the analog model, the score is modified to remove the effect of biasing the natural odds.

A non-analog Monte Carlo technique will have the same expected tallies as an analog technique if the expected weight executing any given random walk is preserved. These variance reduction techniques can often decrease the relative error by sampling naturally rare events with an unnaturally high frequency and weighting the tallies appropriately. In the following subsection, several variance reduction methods are described and discussed.

2.1.1.2 Variance Reduction

Commonly used classes of variance reduction techniques are truncation methods, population control methods, and modified sampling methods [3]. Some variance reduction methods are generally applicable, while others are more specialized and carry high risk in use. Some variance reduction techniques cause an increase in computational time, but variance typically decreases faster than the increase in time, so these techniques still result in a net increase of the FOM [4].

Truncation Methods

Of the classes listed above, truncation methods are the simplest; they aim to accelerate calculations by truncating parts of phase space that do not contribute significantly to the problem solution. One example of this is geometry truncation, in which unimportant parts of the problem geometry are not modeled. Truncation methods may also be applied to other independent variables such as energy; when using energy cutoff, particles whose energy is out of the range of interest are terminated so that computation time is not spent following them.

Population Control Methods

Population control methods use particle splitting and Russian roulette to control the number of samples taken in various regions of phase space. In important regions, many samples of low weight particles are tracked, and in unimportant regions, few samples of high weight are tracked. Weight adjustments are made to the particles to ensure that the problem solution remains unbiased. Specific population control methods include geometry splitting and Russian roulette, energy splitting and roulette, weight cutoff, and weight windows [3].

Using geometry splitting with Russian roulette, particles transported from a region of higher importance to a region of lower importance undergo Russian roulette. Some of the particles will be killed a certain fraction of the time, but survivors will be counted more by increasing their weight the remaining fraction of the time. In doing this, unimportant particles are followed less often, yet the problem solution remains undistorted. If a particle is transported to a region of higher importance, it may be split into two or more particles, each with less weight and therefore counting less. In this case, important particles are followed

more often, yet the solution is again undistorted because, on average, the total weight is conserved.

In general, when a particle of weight w_0 is split into k particles, the resulting particles are each given a weight of $\frac{w_0}{k}$, conserving the expected weight. When a particle is subject to Russian rouletting, it is turned into a particle of weight $w_1 > w_0$ with probability $\frac{w_0}{w_1}$ and is killed with probability $1 - \frac{w_0}{w_1}$, again conserving the expected weight.

Geometry splitting with Russian roulette can be used to great advantage in deep penetration shielding problems. Splitting helps maintain the particle population, which diminishes rapidly in analog simulations. Conversely, geometry splitting with Russian roulette does not work well in problems that have severe angular dependence. In the most extremely anisotropic case, a particle may never enter a geometric region in which it may be split [3].

Energy splitting and Russian roulette are generally used in combination but may be employed separately. When using energy splitting, once a neutron drops below a given energy threshold, it may be split into multiple neutrons, each with an appropriately adjusted weight. This is useful when particles are more important in some energy ranges than in others. In the case of using energy rouletting, if a particle drops below a certain energy, a roulette game is played and the particle is either killed or survives with a weight increased by a factor of the reciprocal of the survival probability (to conserve overall particle population weight). These two energy-based variance reduction techniques are independent of spatial location, so a space-energy weight window (discussed below) is usually a better choice for problems with strong space-energy dependence.

When weight cutoff is employed, Russian roulette is played if a particle's weight drops below a specified cutoff value. The result of the roulette is that the particle is either killed or survives with its weight increased to a given level. Weight cutoff is most efficient when used in combination with geometry splitting (discussed above) and implicit capture (discussed below). It is important to note that, unlike in the case of the energy cutoff, the weight cutoff does not bias the solution because the particles that survive do so with increased weight.

The last population control method discussed here is the weight window, which is a phase space splitting and Russian roulette technique. The phase space may be space-energy or solely space. Each phase space cell is bounded by upper and lower weight bounds. If a particle is above the upper weight bound, it is split such that the resultant particles are all within the bounds of the weight window. If a particle is below the lower weight bound, Russian roulette is played and the particle is either terminated or permitted to survive with an increased weight within the bounds of the weight window. If a particle's weight is within the window, no action is taken. All of these scenarios are depicted in Figure 2.1, a cartoon of the weight window concept.

The weight window may be used alone to good effect, but it is particularly powerful when used in conjunction with other variance reduction techniques that introduce large variations in particle weight. Well-specified weight windows keep the Monte Carlo solution from severe perturbations resulting from high-weight particles and simultaneously keep computational resources from wasting time on low-weight particles by rouletting them.

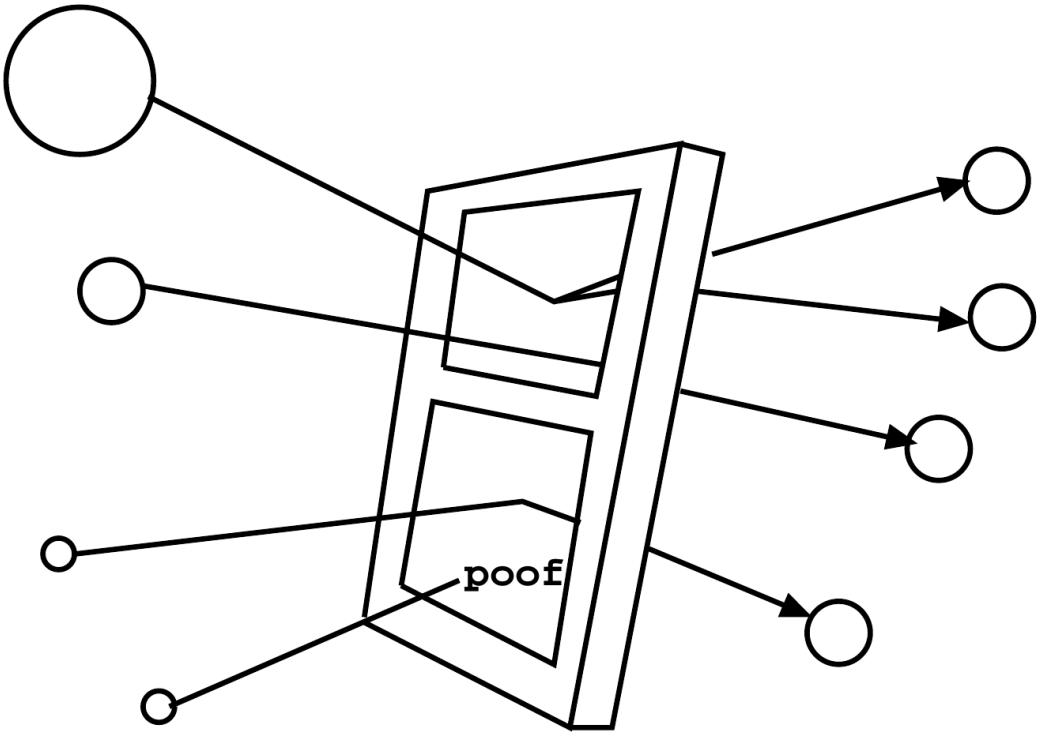

Figure 2.1: Weight window phase space splitting and Russian roulette [3].

Modified Sampling Methods

Modified sampling methods alter the statistical sampling of a problem to increase the number of tallies per particle. For a given Monte Carlo event, it is possible to sample from an arbitrary distribution rather than the physical probability as long as the particle weights are adjusted to compensate. With modified sampling methods, sampling is done from distributions that send particles in desired directions or into other desired regions of phase space such as time or energy. Modified sampling methods may also change the location or type of collisions. Categories of modified sampling methods include implicit capture, forced collisions, and source biasing.

Using implicit capture (also called implicit absorption or survival biasing), particles are never killed by absorption. Instead, a particle's weight is reduced by the absorption probability at each collision, allowing important particles to survive by not being lost to absorption. Implicit capture can be thought of as a splitting process in which a particle of weight w_0 is split into two particles: one of weight $w_0(1 - \frac{\Sigma_a}{\Sigma_t})$ that survives and is subsequently followed, and one of weight $w_0 \frac{\Sigma_a}{\Sigma_t}$ that is instantaneously killed [3].

The forced collision method increases sampling of collisions in specified spatial cells. Particles undergoing forced collisions are split into collided and uncollided parts. The collided part of the particle is forced to react within the current cell, while the uncollided part of the

particle exits the cell without collision. When the track of the uncollided particle portion is continued, it is followed with weight $w_0 e^{-\Sigma_t d}$, where w_0 is the original particle weight and d is the distance traveled between the splitting site and the cell boundary. The collided part of the particle thus reacts with weight $w_0 \left(1 - e^{-\Sigma_t d}\right)$. These resultant weights are chosen to reflect the actual physics of the problem; $e^{-\Sigma_t d}$ is the probability of exiting the cell without collision, and $1 - e^{-\Sigma_t d}$ is the probability of colliding in the cell. One of these two things must happen to the original particle of weight w_0, so we observe that the starting weight is preserved.

Finally, particle sources may be biased with respect to one or more variables. This allows for greater numbers of particles to be produced in more important ranges of each biased variable, with the particles' weights reduced accordingly. In the relevant example of the neutron shielding problem, one may start more particles at high energies and in strategic directions in order to get more particles to contribute to the desired solution. The corresponding weights of the particles are altered to correct the statistical distribution.

2.1.2 Deterministic Methods

In the case of deterministic methods, each of the six independent variables of the steady-state NTE is discretized, relevant boundary conditions are imposed, and the resulting system of linear algebraic equations is iterated over until an acceptable solution has been reached. We limit the discussion here to the discretization of the integro-differential form of the NTE and the finite-volume discrete ordinates method.

These discretizations introduce some errors into the calculations, with the discretization of some variables being more problematic than others. For example, it is functionally straightforward to discretize the energy and spatial variables, while discretizing angular space using the discrete ordinates method is more mathematically intricate and often brings deleterious errors ("ray effects") into problem solutions. Deterministic methods may converge more quickly than Monte Carlo methods, especially in the case of shielding problems, though the solutions are often plagued by the aforementioned inaccuracies.

2.1.2.1 Discretization of the Neutron Transport Equation

Energy Discretization - The Multigroup Approximation

Discretization of the energy variable is known as the "multigroup" approximation; it is relatively straightforward from a mathematical standpoint. Energy is broken up into G groups, where the g^{th} group has an upper bound of energy E_g and a lower bound of energy E_{g+1} as shown in Figure 2.2. The highest energy group has $g = 0$ and the lowest energy group has $g = G - 1$. This convention is used because neutrons are generally born at higher energies (starting in group 0 or 1) and scatter down to lower energies before undergoing an absorption reaction.

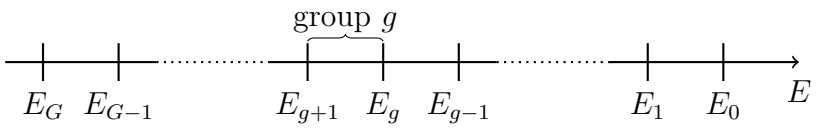

Figure 2.2: Discretized energy grid.

Discretizing the NTE with respect to energy on this grid gives the G multigroup equations

$$\mathbf{\Omega}\cdot\nabla\psi^g(\mathbf{r},\mathbf{\Omega})+\Sigma_t^g(\mathbf{r})\psi^g(\mathbf{r},\mathbf{\Omega})= \sum_{g'=0}^{G-1}\int_{4\pi}\Sigma_s^{g'\to g}(\mathbf{r},\mathbf{\Omega}'\cdot\mathbf{\Omega})\psi^{g'}(\mathbf{r},\mathbf{\Omega}')d\mathbf{\Omega}'+Q^g(\mathbf{r},\mathbf{\Omega}), \quad g=0,1,\ldots,G-1. \tag{2.11}$$

Here it is assumed that, within each energy group, the angular flux may be approximated as the product of some known function of energy $f(E)$ and the group flux $\psi^g(\mathbf{r},\mathbf{\Omega})$ as

$$\psi(\mathbf{r},E,\mathbf{\Omega})\approx f(E)\psi^g(\mathbf{r},\mathbf{\Omega}),\quad E_{g+1}<E\leq E_g\,, \tag{2.12}$$

where $f(E)$ is normalized such that $\int_{E_g+1}^{E_g} f(E)dE=1$. With this, the multigroup cross sections and the group source are similarly defined [2] as

$$\Sigma_t^g(\mathbf{r})=\int_{E_{g+1}}^{E_g}\Sigma_t(\mathbf{r},E)f(E)dE, \tag{2.13}$$

$$\Sigma_s^{g'\to g}(\mathbf{r},\mathbf{\Omega}'\cdot\mathbf{\Omega})=\int_{E_{g+1}}^{E_g}\int_{E_{g'+1}}^{E_{g'}}\Sigma_s(\mathbf{r},E'\to E,\mathbf{\Omega}'\cdot\mathbf{\Omega})f(E')dE'dE, \tag{2.14}$$

$$Q^g(\mathbf{r},\mathbf{\Omega})=\int_{E_{g+1}}^{E_g}Q(\mathbf{r},E,\mathbf{\Omega})dE. \tag{2.15}$$

Spatial Discretization

In the interest of completeness, we will briefly discuss the discretization of space. The LDO equations are inherently three-dimensional [5], so we will restrict the discussion to three-dimensional space with point positions specified by Cartesian coordinates. A general mesh cell is shown in Figure 2.3.

The mesh cell is centered at the i^{th} position along the x-axis, the j^{th} position along the y-axis, and the k^{th} position along the z-axis. Indexing is such that there are I mesh cells with $I+1$ grid points in the x-direction, J mesh cells with $J+1$ grid points in the y-direction, and K mesh cells with $K+1$ grid points in the z-direction. It is assumed that all material properties are constant within a given cell. In order to eventually solve for the scalar flux in a given system, we are interested in solving for the angular flux at the center of each mesh cell, resulting in the $G\times I\times J\times K$ equations shown in Equation 2.16.

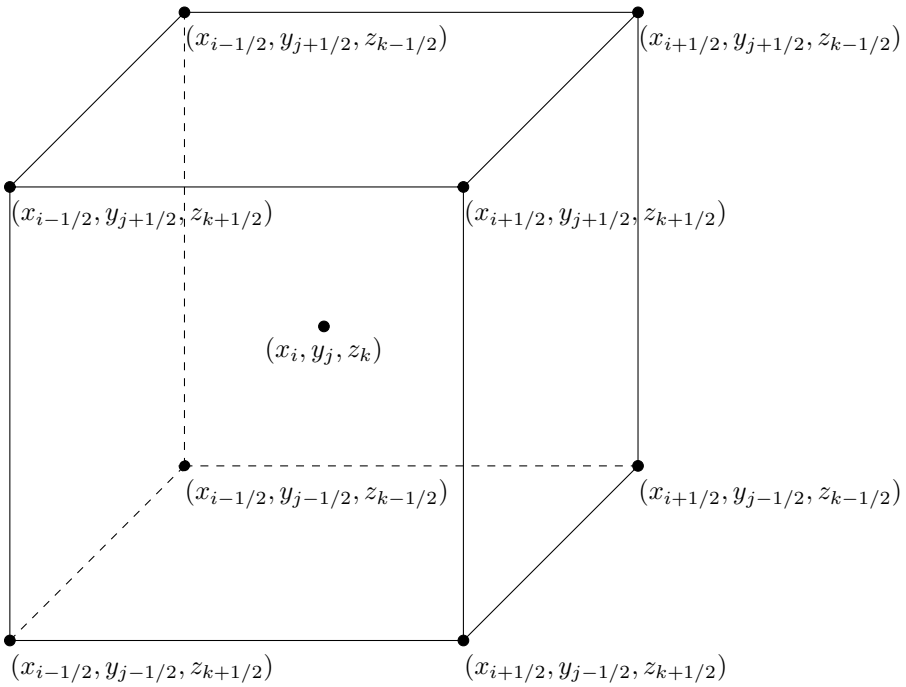

Figure 2.3: General three-dimensional mesh cell [6].

$$\begin{aligned} \boldsymbol{\Omega} \cdot \nabla \psi^g_{i,j,k}(\boldsymbol{\Omega}) + \Sigma^g_{t,i,j,k} \psi^g_{i,j,k}(\boldsymbol{\Omega}) = & \qquad g = 0, 1, \ldots, G-1, \\ \sum_{g'=0}^{G-1} \int_{4\pi} \Sigma^{g' \to g}_{s,i,j,k}(\boldsymbol{\Omega}' \cdot \boldsymbol{\Omega}) \psi^{g'}_{i,j,k}(\boldsymbol{\Omega}') d\boldsymbol{\Omega}' + Q^g_{i,j,k}(\boldsymbol{\Omega}), & \qquad \begin{aligned} i &= 1, 2, \ldots, I, \\ j &= 1, 2, \ldots, J, \\ k &= 1, 2, \ldots, K. \end{aligned} \end{aligned} \tag{2.16}$$

To solve for these cell-centered flux quantities in practice, auxiliary equations are introduced. As these are specific to the spatial discretization employed in a given solution and do not differ between the classical discrete ordinates equations and the LDO formulation, we refer the reader to Reference [7] for more detail on spatial differencing and solution methods.

Angular Discretization - Discrete Ordinates

The last part of phase space to discretize in the time-independent NTE is angle. The discrete ordinates method is the most common angular discretization method incorporated into general-purpose neutron transport codes [2]. It is a collocation method that requires the solution of the NTE to be exact at a distinct number of angles $\boldsymbol{\Omega}_n$:

$$\begin{aligned}
&\boldsymbol{\Omega}_n \cdot \nabla \psi^{g,n}_{i,j,k} + \Sigma^{g}_{t,i,j,k}\psi^{g,n}_{i,j,k} = && g = 0, 1, \ldots, G-1, \\
&\quad \sum_{g'=0}^{G-1}\sum_{\ell=0}^{P} \Sigma^{g'\to g}_{s,\ell,i,j,k}\left[Y^{e}_{\ell 0}(\boldsymbol{\Omega}_n)\phi^{g'}_{\ell 0} + \sum_{m=1}^{\ell}\left(Y^{e}_{\ell m}(\boldsymbol{\Omega}_n)\phi^{g'}_{\ell m} \right.\right. && i = 1, 2, \ldots, I, \\
&\qquad \left.\left. + Y^{o}_{\ell m}(\boldsymbol{\Omega}_n)\vartheta^{g'}_{\ell m} \right)\right] + Q^{g,n}_{i,j,k}, && j = 1, 2, \ldots, J, \\
& && k = 1, 2, \ldots, K, \\
& && n = 1, 2, \ldots, N.
\end{aligned} \tag{2.17}$$

Here, $\psi^n \equiv \psi(\boldsymbol{\Omega}_n)$ and the angles are integrated by a quadrature rule such that their corresponding weights w_n sum to 4π. Weights and ordinates ("quadrature sets") are chosen in such a way as to provide good approximations to angular integrals used to evaluate scalar flux [2, 6]. The upper limit of summation for the scattering term spherical harmonic expansion, denoted as P in Equation 2.17, is known as the "$\mathrm{P_N}$ order". The scattering cross section coefficient values $\Sigma^{g'\to g}_{s,\ell,i,j,k}$ come from data libraries based on experimental measurements.

The scattering source is expanded in terms of spherical harmonics:

$$\phi^{g}_{\ell,i,j,k} = \sum_{n=1}^{N} Y^{e}_{\ell m}(\boldsymbol{\Omega}_n) w_n \psi^{g,n}_{i,j,k} \quad \text{and} \quad \vartheta^{g}_{\ell,i,j,k} = \sum_{n=1}^{N} Y^{o}_{\ell m}(\boldsymbol{\Omega}_n) w_n \psi^{g,n}_{i,j,k}, \tag{2.18}$$

where ϕ and ϑ are referred to as the "flux moments". Here, $Y^{e}_{\ell m}(\boldsymbol{\Omega}_n)$ and $Y^{o}_{\ell m}(\boldsymbol{\Omega}_n)$ are the "even" and "odd" real components of the spherical harmonic functions, defined as [6]

$$Y^{e}_{\ell m}(\boldsymbol{\Omega}_n) = (-1)^m \sqrt{(2-\delta_{m0})\frac{2\ell+1}{4\pi}\frac{(\ell-m)!}{(\ell+m)!}} P_{\ell m}(\cos\theta)\cos(m\varphi), \tag{2.19}$$

$$Y^{o}_{\ell m}(\boldsymbol{\Omega}_n) = (-1)^m \sqrt{(2-\delta_{m0})\frac{2\ell+1}{4\pi}\frac{(\ell-m)!}{(\ell+m)!}} P_{\ell m}(\cos\theta)\sin(m\varphi). \tag{2.20}$$

In Equations 2.19 and 2.20, $P_{\ell m}(\cos\theta)$ is the associated Legendre polynomial and (θ, φ) are the components of $\boldsymbol{\Omega}$ as shown in Figure 2.4 and Equations 2.21a – 2.22. It is assumed that the double differential scattering cross section depends only on the dot product of the incoming and outgoing angles of the particle undergoing scattering.

To summarize Equations 2.17 – 2.20, we note that the double differential scattering cross section is expanded into the real components of the spherical harmonic functions, which can be represented with Legendre polynomials; these are then multiplied with the angular flux moments expanded into spherical harmonic functions.

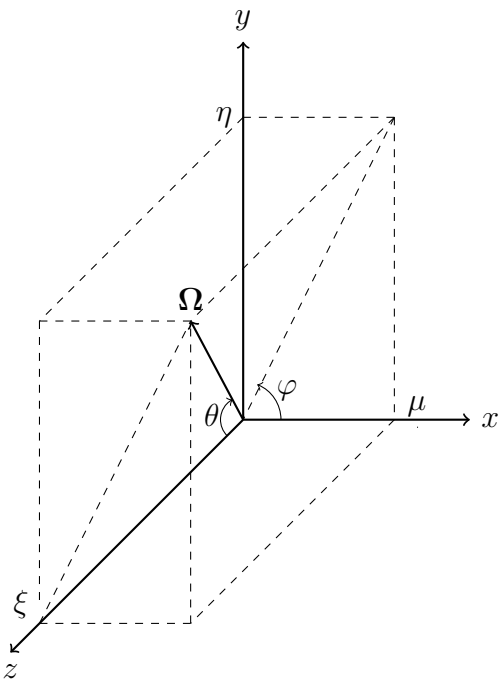

$$\xi = \cos\theta \tag{2.21a}$$

$$\mu = \sqrt{1-\xi^2}\cos\varphi \tag{2.21b}$$

$$\eta = \sqrt{1-\xi^2}\sin\varphi \tag{2.21c}$$

$$\mu^2 + \eta^2 + \xi^2 = 1 \tag{2.22}$$

Figure 2.4: Angular coordinate system [6].

Commonly-used quadrature sets include level-symmetric, Gauss- Legendre product, quadruple range (QR) product, and linear-discontinuous finite element (LDFE). The various quadrature set types have different properties with each being better for certain classes of problems. For example, relatively coarse (sixteen angles per octant) QR product quadratures are generally sufficient for generating variance reduction parameters for neutron transport problems, but more finely resolved quadrature sets are recommended for photon transport problems [8]. Level-symmetric quadrature sets are widely applied for general applications [2] but tend to exhibit far more ray effects than QR product quadratures [8]. In the following subsection, we will discuss ray effects in greater detail.

2.1.2.2 Ray Effects

Ray effects are unphysical computational anomalies in the scalar flux solution that arise from the discrete ordinates formulation. Because the NTE is only evaluated at a finite number of discrete angles, the number of directions in which particles may stream is restricted. As a consequence of this, contributions to the scalar flux from uncollided particles are limited to those from the discrete angles along which particle sources are "visible" [9]. A demonstrative example of ray effects is shown in Figure 2.5. The plot shows results from the PARTISN [10] code using a triangular $P_n - T_n$ quadrature with 48 points and a scattering ratio of $c = 0.25$ [5]. Although the point source emits neutrons isotropically, the scalar flux calculated at a given radius out from the source sees contributions only from the discrete angles along which

particles may stream. That is, the flux at a given distance from the point source is actually equal in all directions and so the figure should appear to be a sphere, but the discrete angles restrict streaming pathways to the rays shown in the image.

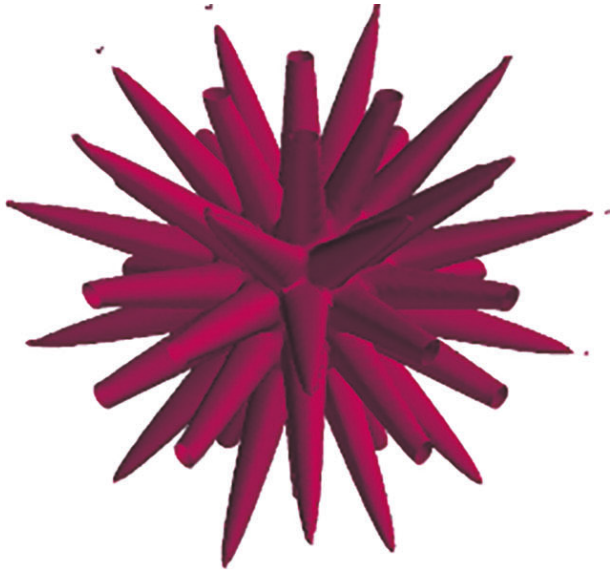

Figure 2.5: Isosurface plot of scalar flux from a point source [5].

The severity of ray effects in a given simulation depends on the properties of the sources. The largest consequences tend to occur in scenarios with localized sources and relatively minimal scattering. When using the discrete ordinates approximation in a purely absorbing medium, regardless of the accuracy of the angular flux calculations and the number of discrete angles used, it is always possible to get far enough away from a localized source such that a poor value of the scalar flux is obtained at that point [9]. In a scattering medium with localized sources, angular flux values are incorrect because they depend on integrals that are poorly approximated by the quadrature formulation. In contrast to this, neutrons exiting scattering reactions are generally less localized and consequently tend to mitigate ray effects. As we will see later in the chapter, one key point of interest in using the LDO equations as part of a hybrid method calculation is that the LDO equations mitigate ray effects when higher-order quadrature sets are used [5].

2.1.3 Hybrid Methods

Hybrid methods aim to combine the previously described Monte Carlo methods and deterministic methods in such a way as to perform calculations that result in statistically meaningful results within a tractable period of computation time. Generally, these hybrid methods are implemented such that the solution(s) from a deterministic code are used to inform a Monte Carlo code. When this is done well, the Monte Carlo code converges more quickly than without the information from the deterministic solution(s).

Specifically, an adjoint and/or forward flux solution generated by a deterministic transport solver is used to make a weight window map for a Monte Carlo run. As was noted earlier, weight windows are most effective when specified well and when used in conjunction with other variance reduction techniques. Because developing effective weight window maps can be labor-intensive and require a user to have significant *a priori* knowledge about the problem being solved, automated hybrid methods have been developed to couple deterministic solutions to Monte Carlo transport calculations.

2.2 Previous Work

Substantial effort has been placed into the development and automated execution of hybrid methods. This section will discuss previous work in this field with a particular emphasis on the present state of hybrid methods as well as hybrid methods that incorporate neutron direction of travel.

Here we begin by describing the CADIS (consistent adjoint driven importance sampling) and FW-CADIS (forward-weighted consistent adjoint driven importance sampling) methods, which are the current state of the art of Monte Carlo variance reduction parameter generation. These are introduced first because, as will be described in more detail later, this work employs solutions of the LDO equations in combination with the CADIS and FW-CADIS methods via the ADVANTG software. Following this, we present a discussion of selected work in angle-informed hybrid methods, focusing on variants of CADIS and FW-CADIS.

2.2.1 CADIS and FW-CADIS

2.2.1.1 CADIS

The CADIS method was introduced by Wagner and Haghighat in 1997 to automate Monte Carlo variance reduction parameter generation [11]. CADIS is based on the source biasing and weight window techniques described above, does not depend heavily on user experience, and was implemented as described in Reference [11] in the MCNP [3] code. Most importantly, the CADIS method produces source biasing parameters and weight window target values such that particles are born with the target weights. Since CADIS is used heavily in this work, it is pertinent to describe the theory behind the method.

The goal of most Monte Carlo neutron transport problems is to calculate some response (scalar flux, dose, etc.) at some location in phase-space. This can be posed as solving the following integral equation:

$$R = \int_P \psi(P)\sigma_d(P)dP, \tag{2.23}$$

where R is the response of interest, ψ is the neutron angular flux, and σ_d is some objective function in the phase-space $(\mathbf{r}, E, \mathbf{\Omega}) \in P$. We now introduce the adjoint identity

$$\langle \psi^\dagger, H\psi \rangle = \langle \psi, H^\dagger \psi^\dagger \rangle \tag{2.24}$$

where H is the transport operator and the dagger superscript indicates an adjoint quantity. Using Equation 2.24 and some algebraic manipulations, it can be shown that

$$R = \int_P \psi^\dagger(P) q(P) dP, \tag{2.25}$$

where $\psi^\dagger$ and q are the adjoint neutron angular flux function and the particle source density, respectively. For a given problem with a vacuum boundary condition, Equations 2.23 and 2.25 are equivalent expressions for R. The adjoint neutron angular flux function $\psi^\dagger$ has physical meaning as the expected contribution to the response R from a particle in phase-space P. In other words, the adjoint flux function is significant because it represents the importance of those source particles to the response of interest.

To calculate the response with the Monte Carlo method, the independent variables are sampled from the probability density function (PDF) $q(P)$. However, this may not be the best PDF from which to sample, so an alternative PDF $\hat{q}(P)$ can be introduced into the integral:

$$R = \int_P \left[\frac{\psi^\dagger(P) q(P)}{\hat{q}(P)} \right] \hat{q}(P) dP, \tag{2.26}$$

where $\hat{q}(P) \geq 0$ and the integral of $\hat{q}(P)$ over P is normalized to unity. Then, the alternative PDF $\hat{q}(P)$ that will minimize the variance of the response is given by

$$\hat{q}(P) = \frac{\psi^\dagger(P) q(P)}{\int_P \psi^\dagger(P) q(P) dP}. \tag{2.27}$$

Looking at Equation 2.27, we see that the numerator is the response from phase-space P and the denominator is the total response R. Thus, this definition of $\hat{q}(P)$ is a measure of the contribution from phase-space P to the response. It is useful to bias the sampling of source particles by this ratio of their contribution to the detector response.

Because the source variables are sampled from this new biased PDF, the statistical weight of the source particles must be corrected such that

$$w(P)\hat{q}(P) = w_0 q(P), \tag{2.28}$$

where w_0 is the unbiased particle starting weight and is set equal to 1. Substituting Equation 2.27 into Equation 2.28 and solving for $w(P)$ gives the following expression for the statistical weight of the particles:

$$w(P) = \frac{\int_P \psi^\dagger(P) q(P) dP}{\psi^\dagger(P)} = \frac{R}{\psi^\dagger(P)}. \tag{2.29}$$

Equation 2.29 demonstrates an inverse relationship between this adjoint (importance) function and the statistical particle weight.

Now, let us consider the transport process in this context. The integral transport equation for particle density in the phase-space P is given by

$$\psi(P) = \int K(P' \to P)\psi(P')dP' + q(P) \tag{2.30}$$

where $K(P' \to P)$ is the expected number of particles entering dP about P from an event in P'. Given the preceding discussion, we would like to transform Equation 2.30 to be in terms of the biased source distribution $\hat{q}(P)$. Defining

$$\hat{\psi}(P) = \frac{\psi(P)\psi^\dagger(P)}{\int \psi^\dagger(P)q(P)dP}, \tag{2.31}$$

we can write Equation 2.30 in terms of $\hat{q}(P)$ as

$$\hat{\psi}(P) = \frac{\psi^\dagger(P)}{\int \psi^\dagger(P)q(P)dP} \int K(P' \to P)\psi(P')dP' + \hat{q}(P). \tag{2.32}$$

Equation 2.32 can also be written as

$$\hat{\psi}(P) = \int K(P' \to P)\hat{\psi}(P') \left[\frac{\psi^\dagger(P)}{\psi^\dagger(P')}\right] dP' + \hat{q}(P)\,, \tag{2.33}$$

which allows us to define

$$\hat{K}(P' \to P) = K(P' \to P) \left[\frac{\psi^\dagger(P)}{\psi^\dagger(P')}\right] \tag{2.34}$$

and finally write

$$\hat{\psi}(P) = \int \hat{K}(P' \to P)\hat{\psi}(P')dP' + \hat{q}(P). \tag{2.35}$$

Because $K(P' \to P)$ is unknown, we simulate neutron transport in the usual unbiased way and change the number of particles emerging in P from an event in P' by the ratio of importances $\psi^\dagger(P)/\psi^\dagger(P')$. When this ratio is above one, splitting occurs, and rouletting occurs when the ratio is less than one. The statistical weights of the particles resulting from splitting and/or rouletting are then corrected such that

$$w(P)K(P' \to P) \left[\frac{\psi^\dagger(P)}{\psi^\dagger(P')}\right] = w(P')K(P' \to P) \tag{2.36}$$

or

$$w(P) = w(P') \left[\frac{\psi^\dagger(P)}{\psi^\dagger(P')}\right]. \tag{2.37}$$

With this, reduced variance can be achieved when all source and transport sampling is proportional to its importance. The source particles' energy and position are sampled from the biased source distribution

$$\hat{q}(\mathbf{r}, E) = \frac{\phi^{\dagger}(\mathbf{r}, E) q(\mathbf{r}, E)}{\int_V \int_E \phi^{\dagger}(\mathbf{r}, E) q(\mathbf{r}, E) dE \; d\mathbf{r}} = \frac{\phi^{\dagger}(\mathbf{r}, E) q(\mathbf{r}, E)}{R}. \tag{2.38}$$

Here, the physical meaning of the numerator is the detector response from space-energy element $(d\mathbf{r}, dE)$ and the denominator is the total detector response R. As in the preceding derivation, this ratio is a measure of the particles' relative contribution to the detector response.

To bias particles undergoing the transport process, the weight window technique is applied. Weight window lower bounds w_ℓ must be calculated such that the statistical weights defined in Equation 2.29 fall at the center of the weight window intervals. The width of a given interval is denoted by $c_u = w_u / w_\ell$, the ratio of upper and lower weight window values. The weight window lower bounds are then given by

$$w_\ell(\mathbf{r}, E) = \frac{w}{\left(\frac{c_u+1}{2}\right)} = \frac{R}{\phi^{\dagger}(\mathbf{r}, E)} \frac{1}{\left(\frac{c_u+1}{2}\right)}. \tag{2.39}$$

Using this definition, the weight window technique then performs particle splitting and/or rouletting consistent with the statistical weight given in Equation 2.37.

The key result of the foregoing discussion is that the statistical weights of the source particles are within the bounds of the weight windows. In other words, the source-biasing parameters and the weight window target values are consistent. This circumvents the potential of particles being immediately split or rouletted upon birth and avoids the resultant degradation in computational efficiency. We refer the reader to Reference [11] for a complete discussion of results and analysis of the initial implementation of the CADIS method.

Note that Equations 2.38 and 2.39 use the scalar adjoint flux rather than the angular flux. This is consistent with the original implementation of the CADIS method in MCNP as well as the implementation of the method in ADVANTG; the scalar adjoint neutron flux function is used in both tools [11, 8]. Historically, this was done to reduce the memory required for the deterministic calculation as well as the weight window map. Additionally, the angular adjoint flux resulting from an S_N calculation was not considered to be sufficiently accurate due to the limited number of discrete angles used for the calculation. Further, people have generally not developed weight windows that are a function of angle.

The CADIS method is very effective for automated optimization of localized detectors but falls short of efficiently optimizing distributed responses. FW-CADIS, discussed in the next section, was developed to address this issue.

2.2.1.2 FW-CADIS

FW-CADIS, introduced by Wagner, Blakeman, and Peplow in 2009, is a variation on the CADIS method to increase the efficiency of Monte Carlo calculations of distributions and

responses at multiple localized detectors [12].

For this global variance reduction method, a response with uniformly-low statistical uncertainty across all phase-space is desired. One way to target this for a given Monte Carlo simulation is to uniformly distribute the particles throughout the system. Though this is not a physical response, it is a proxy for the goal of obtaining uniform uncertainty. It also indicates the possibility of developing an adjoint importance function that represents the importance of particles to achieving the goal of uniform particle distribution.

With this new problem formulation, the problem of calculating particle density is cast into the response formulation:

$$R = \int_{4\pi} \int_{V} \int_{E} \psi(\mathbf{r}, E, \mathbf{\Omega}) f(\mathbf{r}, E, \mathbf{\Omega}) dE \; dV \; d\mathbf{\Omega}, \tag{2.40}$$

where $f(\mathbf{r}, E, \mathbf{\Omega})$ is some function that converts angular neutron flux to Monte Carlo particle density. Recall that the angular neutron flux can be defined as the product of the physical particle density n and velocity v:

$$\psi(\mathbf{r}, E, \mathbf{\Omega}) = n(\mathbf{r}, E, \mathbf{\Omega}) v(\mathbf{r}, E, \mathbf{\Omega}) \tag{2.41}$$

and the physical particle density is related to the Monte Carlo particle density m and the average particle weight $\bar{w}$ by

$$n(\mathbf{r}, E, \mathbf{\Omega}) = \bar{w}(\mathbf{r}, E, \mathbf{\Omega}) m(\mathbf{r}, E, \mathbf{\Omega}). \tag{2.42}$$

Using Equations 2.41 and 2.42, the Monte Carlo particle density can be estimated by

$$m(\mathbf{r}, E, \mathbf{\Omega}) = \frac{n(\mathbf{r}, E, \mathbf{\Omega})}{\bar{w}(\mathbf{r}, E, \mathbf{\Omega})} = \frac{\psi(\mathbf{r}, E, \mathbf{\Omega})}{\bar{w}(\mathbf{r}, E, \mathbf{\Omega}) v(\mathbf{r}, E, \mathbf{\Omega})} \tag{2.43}$$

and the total Monte Carlo density can be estimated by

$$R = \int_{4\pi} \int_{V} \int_{E} \psi(\mathbf{r}, E, \mathbf{\Omega}) \left[\frac{1}{\bar{w}(\mathbf{r}, E, \mathbf{\Omega}) v(\mathbf{r}, E, \mathbf{\Omega})} \right] dE \; dV \; d\mathbf{\Omega}. \tag{2.44}$$

If the average particle weight is set proportional to the physical particle density, then the Monte Carlo particle density should be approximately uniform in phase-space. Substituting Equation 2.41 into Equation 2.44 gives

$$R = \int_{4\pi} \int_{V} \int_{E} \psi(\mathbf{r}, E, \mathbf{\Omega}) \left[\frac{1}{\psi(\mathbf{r}, E, \mathbf{\Omega})} \right] dE \; dV \; d\mathbf{\Omega}. \tag{2.45}$$

By then defining the adjoint source as the bracketed term in the above equation,

$$q^{\dagger}(\mathbf{r}, E, \mathbf{\Omega}) = \frac{1}{\psi(\mathbf{r}, E, \mathbf{\Omega})}, \tag{2.46}$$

we can calculate an adjoint importance function that represents the importance of particles to achieving the desired objective of uniformly distributed Monte Carlo particles. This

should, in turn, correspond to approximately uniform statistical uncertainties. The method physically corresponds to weighting the adjoint source with the inverse of the forward flux; the adjoint source will be high where the forward flux is low and the adjoint source will be low where the forward flux is high. With this method, after the adjoint has been determined, the standard CADIS procedures are used to calculate consistent source biasing parameters and weight windows.

When considering implementation and use, it should be noted that, while the original CADIS method requires only one deterministic calculation, the FW-CADIS method requires two (one forward and one adjoint) deterministic calculations. Additionally, like the original CADIS method, FW-CADIS is general and could be applied to all independent variables of a problem, but the implementation has been limited to space and energy.

2.2.2 Directional CADIS

Noting the marked performance of the CADIS and FW-CADIS methods, their limited implementation in only space and energy, and the importance of particle direction, Peplow introduced directional CADIS in 2012 [13]. Two versions of directional CADIS were explored: one method that biases the source in space and energy while preserving the original angular distribution of the particles, and one method that biases the source in space, energy, and angle. Both new methods were tested against standard CADIS for seven example problems, with the Monte Carlo FOM compared among the methods for each problem.

Peplow notes that in many applications involving directionally dependent source distributions, the directional dependence is azimuthally symmetric about a given reference direction $\hat{\mathbf{d}}$. With this, the angular distribution of the particles $q_i(\mathbf{\Omega})$ can be expressed as the product of the uniform azimuthal distribution and a polar distribution about reference $\hat{\mathbf{d}}_i$. The angular particle distribution may then be written as $\frac{1}{2\pi} q_i(\mathbf{\Omega} \cdot \hat{\mathbf{d}}_i)$. Peplow also notes that the geometric size of these directional sources tends to be small enough to allow each source distribution to be expressed as the product of two separable distributions: $q_i(\mathbf{r}, E, \mathbf{\Omega}) \approx q_i(\mathbf{r}, E) q_i(\mathbf{\Omega})$.

The implementation of directional CADIS explored in this work was intended to appropriately incorporate the importance of a particle traveling in a given direction while also serving as a relatively simple modification of the standard CADIS method that is less involved than a full treatment of space, energy, and angle. It starts with the approximation that the angular component of the adjoint flux $\psi^\dagger(\mathbf{r}, E, \mathbf{\Omega})$ is separable and symmetric about the average adjoint current direction $\hat{\mathbf{n}}(\mathbf{r}, E)$ such that

$$\psi^\dagger(\mathbf{r}, E, \mathbf{\Omega}) \approx \phi^\dagger(\mathbf{r}, E) \frac{1}{2\pi} f(\mathbf{\Omega} \cdot \hat{\mathbf{n}}). \tag{2.47}$$

From this, it is proposed that weight window targets can be developed that are inversely proportional to the approximation of the adjoint angular flux:

$$\bar{w}(\mathbf{r}, E, \mathbf{\Omega}) = \frac{2\pi k}{\phi^{\dagger}(\mathbf{r}, E) f(\mathbf{\Omega} \cdot \hat{\mathbf{n}})} \tag{2.48}$$

where k is a constant of proportionality that is adjusted to make the importance map consistent with the biased source(s). The implementation of the following methods uses standard CADIS routines to compute the response per unit source R, the weight window target values $\bar{w}(\mathbf{r}, E)$, and the biased source $\hat{q}(\mathbf{r}, E)$ using only the adjoint scalar flux. The quantities are then modified to include directional information.

2.2.2.1 Without Directional Source Biasing

Peplow asserts that the biased source $\hat{q}(\mathbf{r}, E, \mathbf{\Omega})$ should be proportional to both the true particle source distribution and the space-energy component of the scalar adjoint flux:

$$\hat{q}(\mathbf{r}, E, \mathbf{\Omega}) = \frac{1}{R} \left[q(\mathbf{r}, E) \frac{1}{2\pi} q(\mathbf{\Omega} \cdot \hat{\mathbf{d}}) \right] \phi^{\dagger}(\mathbf{r}, E), \tag{2.49}$$

where the constant of proportionality R is determined by forcing $\hat{q}(\mathbf{r}, E, \mathbf{\Omega})$ to be a PDF. Since the scalar adjoint flux is used here, the directional distribution of the biased source is identical to that of the true source. Detailed in Reference [13], the constant of proportionality R is found to be equal to the response per unit source from the traditional space-energy CADIS treatment. Thus, the biased source can be expressed as

$$\hat{q}(\mathbf{r}, E, \mathbf{\Omega}) = \hat{q}(\mathbf{r}, E) \frac{1}{2\pi} q(\mathbf{\Omega} \cdot \hat{\mathbf{d}}). \tag{2.50}$$

The birth weight of a particle sampled from this distribution is independent of direction and the proportionality constant k for the target weight windows should be chosen such that the weight window targets match the birth weight of the source particles. This cannot be done generally because the particle birth weight is independent of direction, but it can be done for a single point in phase space $(\mathbf{r}_0, E_0, \mathbf{\Omega}_0)$ of the source such that

$$k = \frac{R}{2\pi} f\left(\mathbf{\Omega}_0 \cdot \hat{\mathbf{n}}(\mathbf{r}_0, E_0)\right), \tag{2.51}$$

where the average adjoint current direction $\hat{\mathbf{n}}(\mathbf{r}_0, E_0)$ is evaluated at the source location and energy and

$$\bar{w}(\mathbf{r}, E, \mathbf{\Omega}) = \bar{w}(\mathbf{r}, E) \frac{f\left(\mathbf{\Omega}_0 \cdot \hat{\mathbf{n}}(\mathbf{r}_0, E_0)\right)}{f(\mathbf{\Omega} \cdot \hat{\mathbf{n}})}. \tag{2.52}$$

Because the biased source and the weight window targets will match only at the specified direction of interest $\mathbf{\Omega}_0$ at one specific position and energy, the point $(\mathbf{r}_0, E_0, \mathbf{\Omega}_0)$ should be chosen carefully to represent the source accurately and to minimize rouletting and/or splitting of particles just after birth.

It should be noted that this approach is exact for cases where no directional biasing could be applied, e.g. monodirectional beam sources. Although the above discussion considers only one particle source, this directional CADIS method may be extended to multiple sources, as explained in detail in Reference [13].

2.2.2.2 With Directional Source Biasing

In this method, it is asserted that the biased source should be proportional to both the true particle source distribution and the approximation of the angular adjoint flux:

$$\hat{q}(\mathbf{r}, E, \mathbf{\Omega}) = \frac{1}{cR}\left[q(\mathbf{r}, E)\frac{1}{2\pi}q(\mathbf{\Omega}\cdot\hat{\mathbf{d}}_i)\right]\left[\phi^{\dagger}(\mathbf{r}, E)\frac{1}{2\pi}f(\mathbf{\Omega}\cdot\hat{\mathbf{n}}_0)\right], \tag{2.53}$$

where the constant cR is used to make $\hat{q}$ a PDF. Because the vector $\hat{\mathbf{n}}_0$ is fixed over the source, the biased source is separable into $\hat{q}(\mathbf{r}, E, \mathbf{\Omega}) = \hat{q}(\mathbf{r}, E)\hat{q}(\mathbf{\Omega})$ where $\hat{q}(\mathbf{\Omega})$ can be further separated into the product of its azimuthal and polar distributions:

$$\hat{q}(\mathbf{r}, E, \mathbf{\Omega}) = \left[\frac{1}{R}q(\mathbf{r}, E)\phi^{\dagger}(\mathbf{r}, E)\right]\left[\frac{1}{c}\frac{1}{4\pi^2}q(\mathbf{\Omega}\cdot\hat{\mathbf{d}})f(\mathbf{\Omega}\cdot\hat{n}_0)\right]. \tag{2.54}$$

Both distributions $\hat{q}(\mathbf{r}, E)$ and $\hat{q}(\mathbf{\Omega})$ are independent and each should be a PDF. For the space-energy distribution, the standard definition of R still applies. For the angular distribution, the constant c is found to be

$$c = \int \frac{1}{4\pi^2}q(\mathbf{\Omega}\cdot\hat{\mathbf{d}})f(\mathbf{\Omega}\cdot\hat{\mathbf{n}}_0)d\mathbf{\Omega}, \tag{2.55}$$

which may be evaluated using numerical integration. It should be noted that if either the original source directional distribution $q(\mathbf{\Omega})$ or the adjoint angular flux distribution at the source is isotropic, then c reduces to a value of $\frac{1}{4\pi}$.

Source particles sampled from the biased distribution are born with a starting weight of

$$\bar{w}(\mathbf{r}, E, \mathbf{\Omega}) = \frac{R}{\phi^{\dagger}(\mathbf{r}, E)}\frac{2\pi c}{f(\mathbf{\Omega}\cdot\hat{\mathbf{n}}_0)} = \bar{w}(\mathbf{r}, E)\frac{2\pi c}{f(\mathbf{\Omega}\cdot\hat{\mathbf{n}}_0)}, \tag{2.56}$$

where the constant k has been found to be equal to cR. As with the previously described method, the user selects one point $(\mathbf{r}_0, E_0, \mathbf{\Omega}_0)$ that is representative of the entire source, where the biased source will match the target weight windows. This method can also be extended to incorporate multiple sources.

2.2.2.3 Results

Sample problems of applications of interest were examined and compared between standard CADIS and directional CADIS. For most of these problems, directional CADIS outperformed standard CADIS, increasing the Monte Carlo FOM by a factor of around 2. Notable cases in which directional CADIS performed more poorly than standard CADIS are a neutron

porosity tool problem and a gamma-ray litho-density tool problem with the detector far away from the source. It should also be noted that, for a spherical boat test problem with a source far away from the boat, both standard CADIS and directional CADIS performed more poorly than an analog Monte Carlo calculation. For full details on the test results, see Reference [13]. In the conclusions of the report, Peplow notes that "it is difficult to know *a priori* which problems would benefit from the space/energy/angular treatments presented in this work more than from just using the standard space/energy CADIS."

2.2.3 CADIS-Ω

One of the most recent developments in the area of angle-informed hybrid methods is CADIS-Ω, introduced by Munk et al. in 2016 [14]. This method calculates an alternate form of the adjoint scalar flux quantity that is then used in the CADIS and FW-CADIS methods for generation of variance reduction parameters for local and global response functions, respectively.

The alternative form of the adjoint scalar flux used in CADIS-Ω is defined as

$$\phi_{\Omega}^{\dagger}(\mathbf{r}, E) = \frac{\int_{4\pi} \psi(\mathbf{r}, E, \mathbf{\Omega})\psi^{\dagger}(\mathbf{r}, E, \mathbf{\Omega})d\mathbf{\Omega}}{\int_{4\pi} \psi(\mathbf{r}, E, \mathbf{\Omega})d\mathbf{\Omega}}. \tag{2.57}$$

Here, the product $\psi(\mathbf{r}, E, \mathbf{\Omega})\psi^{\dagger}(\mathbf{r}, E, \mathbf{\Omega})$ is known as the "contributon flux"; contributons can be conceptualized as pseudo-particles that carry "response" from a particle source to a detector. The contributon flux incorporates information from both the forward particle flux as well as the adjoint particle flux. It signifies the importance of a particle born from a forward source moving towards an adjoint source. That is, when the contributon flux is used to generate an importance map, high importance will be assigned to particles that are generated at the forward source and are likely to generate a response in the detector (the adjoint source).

The CADIS-Ω method was implemented in the ADVANTG framework, with numerical experiments performed testing variance reduction for problems run in MCNP5. Several characterization problems with spatially-induced anisotropies were tested to evaluate the new method when used with CADIS and FW-CADIS. Here we will summarize the problems tested and the results; a full discussion can be found in Reference [15]. Munk identified three categories of processes that affect particle flux anisotropy: strongly directional particle sources, strong differences between material properties, and algorithmic limitations that result in ray effects.

Having grouped these processes, Munk tested a set of characterization problems, each of which have different combinations of the above anisotropy-inducing mechanisms. Munk also developed a set of metrics by which the anisotropy of the flux may be quantified over the various problems. Similar to the conclusions drawn by Peplow, Munk found that it was difficult to predict for which problems CADIS-Ω should outperform CADIS. When considering a parametric study of deterministic variables likely to affect angular flux (varying

quadrature set order and P_N order) in a characteristic problem composed of a steel beam embedded in concrete, CADIS-Ω achieved higher FOM values than standard CADIS for all quadrature and P_N orders at high energies. Similarly, for a simple labyrinth geometry of an air maze through a concrete block, CADIS-Ω achieved lower relative errors than did standard CADIS in the epithermal and fast neutron energy groups.

2.2.4 Other Notable Work

Here we will briefly summarize other notable works in the area of angle-informed hybrid methods. We first introduce AVATAR, then discuss two following methods that built off of the work.

2.2.4.1 AVATAR

AVATAR (Automatic Variance And Time of Analysis Reduction) was developed at Los Alamos National Laboratory by Van Riper et al. in the 1990s to eliminate the need for user-generated weight windows [16]. The package may be thought of as a predecessor to the various CADIS methods, as it constructs three-dimensional energy- and angle-dependent weight windows for an MCNP run from an adjoint calculation using the THREEDANT [17] deterministic code.

The scalar adjoint fluxes resulting from THREEDANT are inverted by AVATAR to get the lower weight window boundary in each mesh element of the problem. The weight windows are then normalized such that source particles are born with weights inside of the weight window. If angle-dependent weight windows are desired, the angular adjoint flux is approximated using information theory [16]; the full angular adjoint flux was deemed to require an inordinate amount of storage at the time of development.

AVATAR's weight window mesh is independent of the Monte Carlo cells, so weight windows are applied at absolute particle positions rather than when particles pass between weight window meshes. To protect against significant variance increases in particle weight (and tally) due to large sampling distance, weight windows are applied at a minimum of once per mean free path traveled by a particle.

AVATAR was tested on a model of a three-detector oil well logging tool consisting of a gamma-ray source and three gadolinium detectors. The system was intended to represent deep-penetration problems, as a small fraction of the gamma rays emitted from the source actually reach the detectors. The detector nearest the gamma-ray source has a collimator attached, adding an angular dependence to the tool modeled.

Results from AVATAR were compared against MCNP's weight window generator (WWG). For the three-detector problem described above, AVATAR's angle-dependent weight windows delivered the highest FOM for the detector nearest the source as well as the "middle" detector. The MCNP WWG delivered the highest FOM for the detector furthest from the source, but it should be noted that the MCNP geometry was hand-tuned for the WWG cases. When

considering only a single detector, the AVATAR angle-dependent weight windows outperformed the WWG for a detector near the source as well as far from the source.

2.2.4.2 Cooper and Larsen's Weight Windows

Cooper and Larsen developed a method similar to FW-CADIS that uses weight windows to distribute Monte Carlo particles uniformly throughout the system for the purpose of efficiently solving global particle transport problems [18]. Rather than using an adjoint deterministic solution for generation of weight windows, a forward solution is used. The method presented employs solution of the forward quasi-diffusion equation, a modified diffusion equation that contains multiplicative correction terms known as "Eddington factors".

The authors argue that a forward solution is more appropriate than an adjoint solution in the context of automated weight window generation for Monte Carlo variance reduction. This is supported by showing that if the center of the weight window in each cell is chosen to be proportional to the density of the physical particles in the cell, then the density of Monte Carlo particles throughout the system will be approximately constant.

Cooper and Larsen construct "isotropic" weight windows as well as angle-dependent weight windows, following the AVATAR method to formulate the latter. The authors note that a uniform particle distribution in angle is not always optimal with respect to computational efficiency, especially when considering problems with significant streaming. It is the case that the angle-dependent weight windows developed in this work actually have the potential to reduce the FOM due to excessive Monte Carlo particle splitting in nonstreaming regions. To mitigate this by decreasing the amount of splitting incurred, the weight window experienced by particles traveling in directions opposite to the preferred direction is raised. This preserves the scalar flux, but not the current [18].

Results are presented for two two-dimensional problems. In both problems, weight windows were updated twice – once after one-third of the histories had completed and again after two-thirds of the particle histories had finished. The weight window parameters were chosen to ensure a stable quasi-diffusion solution. The two problems were chosen to rigorously test the global Monte Carlo method; the problems are optically thick with scattering ratios sufficiently low such that the scalar flux decreases by several orders of magnitude far away from the particle source. To observe the performance of the method on problems with significant angular effects, the first problem includes a duct and the second problem includes a barrier.

For the problem including a duct, the Monte Carlo FOM values calculated in the individual spatial cells are vastly improved by the use of both weight window types developed in this work. In particular, the solution estimates for the scalar flux are very noisy far from the solution when only survival biasing is used. Additionally, the angle-dependent weight window generates a slightly higher FOM in the duct region than the isotropic weight window. Similarly, for the problem including a barrier, the use of either type of weight window developed here results in a drastically more uniform particle distribution. Again, the angular weight window outperformed the isotropic weight window. Thus, from this work, we observe that

incorporating angular information into weight window generation can significantly improve Monte Carlo FOM for problems with strong geometric anisotropies.

2.2.4.3 LIFT

LIFT, the local importance function transform, was introduced by Turner and Larsen in 1997 [19, 20] as a new automatic Monte Carlo variance reduction method that closely approximates a zero-variance method through the use of biasing parameters. The LIFT method is partially based on the exponential transform, which adjusts the distance to collision such that particles traveling toward the region of interest undergo fewer collisions than particles traveling away from the region of interest. Particle weights are adjusted accordingly to keep the simulation unbiased. On top of the conventional exponential transform, the LIFT method adds in energy and angular biasing in each cell of the system.

LIFT uses scalar flux information from a deterministic adjoint solution to bias the source distribution, distance to collision, scattering angle, and energy. The adjoint scalar flux is also used to formulate weight windows. In the implementation presented, the weight windows are not angle-dependent. The authors note that, in the LIFT implementation, the angle-dependent weight windows require the use of an analytic expression for the angular flux at every boundary and collision site and that this extra computational effort does not generally yield increased efficiency for the Monte Carlo calculation that then employs the angle-dependent weight windows.

The LIFT strategy can be summarized in two steps. First, an analytic function is derived that is piecewise continuous in space and angle and approximates the adjoint solution within each energy group and spatial cell of the Monte Carlo system. Then, this approximate representation of the adjoint solution is used to transform the original forward problem into a new problem that can be solved by a Monte Carlo simulation with reduced variance. Increased accuracy in the approximation of the adjoint solution results in greater reduction of the variance, approaching zero variance in the solution when using an exact representation. The authors note that this limit is unachievable and that the algebraic cost of obtaining and using more accurate adjoint solutions must be balanced against the desired FOM.

The authors compare LIFT against AVATAR, considered to be one of the most efficient automated variance reduction techniques used in a major production code at the time of publication. The overall result stated in Reference [19] is that LIFT outperforms AVATAR in most problems. The reasons given for this are that LIFT particles have significantly shorter histories than AVATAR particles and that LIFT particles have smaller weight fluctuations than AVATAR particles and thus require less splitting and Russian roulette. It is noted, however, that the two methods perform comparably for problems where biasing is difficult (AVATAR does not use any biasing techniques other than survival biasing, which LIFT also employs in addition to its other biasing).

It is seen that the LIFT method loses its advantage over survival biasing as the scattering ratio of a given problem approaches unity. While FOM values from LIFT increase, the acceleration of the method compared to survival biasing becomes negligible [19]. In Reference

[20], numerical results and comparisons against AVATAR are presented. We will briefly summarize the results and conclusions here, focusing on results from the most complex scenario tested, as the work presented in this dissertation is concerned with three-dimensional multigroup problems.

Cooper and Larsen tested the LIFT method in combination with results from various types of deterministic solutions as well as in combination with weight windows generated from AVATAR. The most complex scenario tested was multigroup in energy and featured a concrete cube with a duct running through it. The duct was also concrete but with a lower density than the bulk material; it had the source at one end, the detector at the other end, and three bends along its path. In general, it was found that incorporating angular information into the AVATAR and LIFT solutions improved the FOM for the Monte Carlo calculation when using either code [20]. Taking this result into consideration as well as other conclusions drawn in work discussed earlier in this chapter, we move forward onto discussing the LDO equations, which will be developed and then used to incorporate angular information into Monte Carlo variance reduction parameter generation.

2.3 The Lagrange Discrete Ordinates (LDO) Equations

The Lagrange Discrete Ordinates (LDO) equations, shown in Equation 2.79, are formally the same as the classical discrete ordinates equations. The LDO equations differ from the discrete ordinates equations in how the scattering source is calculated and in the representation of the angular flux. In this section, we give a mathematical background for and a derivation of the LDO equations.

2.3.1 Mathematical Background

Prior to deriving the LDO equations, it is useful to summarize relevant material from approximation theory for functions defined on $\mathbb{S}^2$, the unit sphere in $\mathbb{R}^3$. We start by denoting the space of square integrable functions on $\mathbb{S}^2$ as $L^2(\mathbb{S}^2)$, where an orthonormal basis for $L^2(\mathbb{S}^2)$ is given by the spherical harmonic functions

$$Y_\ell^m(\theta,\varphi) = (-1)^\ell \sqrt{\frac{2\ell+1}{4\pi}\frac{(\ell-m)!}{(\ell+m)!}} P_\ell^m(\cos\theta) e^{im\varphi}. \tag{2.58}$$

Here, $\ell \geq 0$, $|m| \leq \ell$, P_ℓ^m is the associated Legendre function, and θ and φ are the polar and azimuthal components of $\mathbf{\Omega}$, respectively. For a given positive integer $L > 0$, we define the rotationally invariant subspace of the spherical harmonics, $\mathcal{H}_L$, as

$$\mathcal{H}_L = \text{span}\{Y_\ell^m : |m| \leq \ell, 0 \leq \ell \leq L\}, \tag{2.59}$$

with dimension $d_L = \dim \mathcal{H}_L = (L+1)^2$. Said differently, $\mathcal{H}_L$ is the vector space that is the intersection of all subspaces containing Y_ℓ^m; it is the set of all linear combinations of Y_ℓ^m. The space $\mathcal{H}_L$ admits a "reproducing kernel" given by

$$K(\mathbf{\Omega} \cdot \mathbf{\Omega}') = \sum_{\ell=0}^{L} \frac{2\ell+1}{4\pi} P_\ell(\mathbf{\Omega} \cdot \mathbf{\Omega}') \,, \tag{2.60}$$

where P_ℓ is the ℓ^{th} degree Legendre polynomial and K satisfies

$$f(\mathbf{\Omega}) = \int_{\mathbb{S}^2} K(\mathbf{\Omega} \cdot \mathbf{\Omega}') f(\mathbf{\Omega}') d\mathbf{\Omega}' \tag{2.61}$$

for all $f \in \mathcal{H}_L$.

Let $S = \{\mathbf{\Omega}_i\}_{i=1}^M$ be a given set of points (discrete directions) in $\mathbb{S}^2$ and assume that $M = d_L$. That is, the number of directions is equal to the dimension of the subspace $\mathcal{H}_L$. Then, the set S is said to be a fundamental system of points for $\mathcal{H}_L$ if the evaluation functionals

$$f \mapsto f(\mathbf{\Omega}_i), \quad i = 1, 2, \ldots, M, \quad f \in \mathcal{H}_L \tag{2.62}$$

are linearly independent. Using a spherical harmonics basis for $\mathcal{H}_L$, this is equivalent to requiring that the interpolation matrix $\mathbf{Y}$, shown in Equation 2.63, be nonsingular.

$$\mathbf{Y} = \begin{pmatrix} Y_0^0(\mathbf{\Omega}_1) & Y_0^0(\mathbf{\Omega}_2) & Y_0^0(\mathbf{\Omega}_3) & \ldots & Y_0^0(\mathbf{\Omega}_M) \\ Y_1^{-1}(\mathbf{\Omega}_1) & Y_1^{-1}(\mathbf{\Omega}_2) & & & \\ Y_0^1(\mathbf{\Omega}_1) & & \ddots & & \vdots \\ \vdots & & & & \\ Y_L^L(\mathbf{\Omega}_1) & \ldots & & & Y_L^L(\mathbf{\Omega}_M) \end{pmatrix} \tag{2.63}$$

Fundamental systems of points can be constructed geometrically or through optimization techniques. Here, we employ fundamental systems designed using numerical techniques to maximize the logarithm of the determinant of the Gram matrix, where the Gram matrix is constructed as $\mathbf{G} = \mathbf{Y}^\dagger \mathbf{Y}$ and $\mathbf{Y}^\dagger$ is the conjugate transpose (Hermitian adjoint) of $\mathbf{Y}$. This requirement leads to well-conditioned interpolation matrices. With the fundamental system of points $\{\mathbf{\Omega}_i\}_{i=1}^{d_L}$, Lagrange functions on the sphere can be defined such that

$$L_i(\mathbf{\Omega}_j) = \delta_{i,j}, \quad i, j = 1, 2, \ldots, d_L. \tag{2.64}$$

These functions $\{L_i\}_{i=1}^{d_L}$ then form a basis for $\mathcal{H}_L$. Next, we define another set of functions

$$K_i(\mathbf{\Omega}) \equiv K(\mathbf{\Omega} \cdot \mathbf{\Omega}_i), \quad i = 1, 2, \ldots, d_L. \tag{2.65}$$

Using Equations 2.62 and 2.65, the Lagrange functions and the reproducing kernel functions are related by

$$\int_{\mathbb{S}^2} L_i(\mathbf{\Omega}) K(\mathbf{\Omega}_j \cdot \mathbf{\Omega}) d\mathbf{\Omega} = \langle L_i, K_j \rangle = L_i(\mathbf{\Omega}_j) = \delta_{i,j}, \quad i,j = 1,2,\ldots,d_L. \tag{2.66}$$

This indicates that $\{K_i\}_{i=1}^{d_L}$ and $\{L_i\}_{i=1}^{d_L}$ form bi-orthogonal bases for the subspace $\mathcal{H}_L$ and so one basis can be written in terms of the other:

$$L_i(\mathbf{\Omega}) = \sum_{j=1}^{d_L} \langle L_i, L_j \rangle K_j(\mathbf{\Omega}), \tag{2.67}$$

$$K_j(\mathbf{\Omega}) = \sum_{i=1}^{d_L} \langle K_i, K_j \rangle L_i(\mathbf{\Omega}). \tag{2.68}$$

Now, define the $d_L \times d_L$ matrix $\mathbf{L}$ with elements $(\mathbf{L})_{i,j} = \langle L_i, L_j \rangle$. Using the addition theorem, the Gram matrix $\mathbf{G} = \mathbf{Y}^\dagger \mathbf{Y}$ then has the elements $(\mathbf{G})_{i,j} = K(\mathbf{\Omega}_i \cdot \mathbf{\Omega}_j) = \langle K_i, K_j \rangle$. Equations 2.67 and 2.68 imply that $\mathbf{LG} = \mathbf{I}$, where $\mathbf{I}$ is the $d_L \times d_L$ identity matrix. As mentioned previously, by the construction of the extremal point systems, the Gram matrix is well-conditioned and so the matrix elements $\langle L_i, L_j \rangle = (\mathbf{G}^{-1})_{i,j}$ can be computed accurately. Additionally, the reproducing kernel can be easily calculated using the three-term recursion relation for Legendre polynomials, so Equation 2.67 gives a convenient way to calculate the necessary Lagrange functions.

Using this framework, for any $f \in \mathcal{H}_L$,

$$f(\mathbf{\Omega}) = \sum_{i=1}^{d_L} f(\mathbf{\Omega}_i) L_i(\mathbf{\Omega}) \tag{2.69}$$

and so we can define a quadrature on $\mathcal{H}_L$ by

$$\begin{aligned} \int_{\mathbb{S}^2} f(\mathbf{\Omega}) d\mathbf{\Omega} &= \sum_{i=1}^{d_L} \int_{\mathbb{S}^2} f(\mathbf{\Omega}_i) L_i(\mathbf{\Omega}) d\mathbf{\Omega} \\ &= \sum_{i=1}^{d_L} w_i f(\mathbf{\Omega}_i), \end{aligned} \tag{2.70}$$

where

$$w_i = \int_{\mathbb{S}^2} L_i(\mathbf{\Omega}) d\mathbf{\Omega} = \sum_{j=1}^{d_L} \langle L_i, L_j \rangle. \tag{2.71}$$

In summary, the $\mathcal{H}_L$ subspace has three different basis sets: the spherical harmonics, the reproducing kernel functions, and the Lagrange functions. For the reproducing kernel

functions and the Lagrange functions to be a basis, it is required that the number of directions be equal to the dimension of the subspace. That is to say, for a Lagrange or reproducing kernel basis to exist, the number of quadrature points must be $(L+1)^2$. This is what precludes many commonly-used quadrature sets from generating a Lagrange basis and is why extremal point systems and corresponding positive weight quadratures are used here. Next, we will continue with the derivation of the LDO equations.

2.3.2 Derivation of the LDO Equations

With the appropriate mathematical background in place, we will now derive the LDO equations, keeping in mind that the end results is a set of equations that are formally the same as the discrete ordinates equations. First, we define

$$\psi_L(\mathbf{r}, E, \mathbf{\Omega}) = \sum_{n=1}^{N} \psi^n(\mathbf{r}, E) L_n(\mathbf{\Omega}), \tag{2.72}$$

where, again, $L_n(\mathbf{\Omega})$ is the n^{th} Lagrange element and N is the dimension of the rotationally invariant subspace of the spherical harmonics as defined in Equation 2.59. The coefficients $\psi^n(\mathbf{r}, E)$ will be determined through collocation. Equation 2.72 is then substituted into the NTE:

$$\mathbf{\Omega} \cdot \nabla \psi_L(\mathbf{r}, E, \mathbf{\Omega}) + \Sigma_t(\mathbf{r}, E)\psi_L(\mathbf{r}, E, \mathbf{\Omega}) = \int_0^\infty \int_{\mathbb{S}^2} \Sigma_s(\mathbf{r}, E' \to E, \mathbf{\Omega}' \cdot \mathbf{\Omega})\psi_L(\mathbf{r}, E', \mathbf{\Omega}')d\mathbf{\Omega}'dE' + Q(\mathbf{r}, E, \mathbf{\Omega}). \tag{2.73}$$

Next, we define the residual

$$r_L(\mathbf{r}, E, \mathbf{\Omega}) \equiv \mathbf{\Omega} \cdot \nabla \psi_L(\mathbf{r}, E, \mathbf{\Omega}) + \Sigma_t(\mathbf{r}, E)\psi_L(\mathbf{r}, E, \mathbf{\Omega}) - \int_0^\infty \int_{\mathbb{S}^2} \Sigma_s(\mathbf{r}, E' \to E, \mathbf{\Omega}' \cdot \mathbf{\Omega})\psi_L(\mathbf{r}, E', \mathbf{\Omega}')d\mathbf{\Omega}'dE' - Q(\mathbf{r}, E, \mathbf{\Omega}). \tag{2.74}$$

The energy variable is discretized with a standard multigroup approach as is done in the discrete ordinates equations:

$$r_L^g(\mathbf{r}, \mathbf{\Omega}) = \mathbf{\Omega} \cdot \nabla \psi_L^g(\mathbf{r}, \mathbf{\Omega}) + \Sigma_t^g(\mathbf{r})\psi_L^g(\mathbf{r}, \mathbf{\Omega}) - \sum_{g'=0}^{G-1} \int_{\mathbb{S}^2} \Sigma_s^{g' \to g}(\mathbf{r}, \mathbf{\Omega}' \cdot \mathbf{\Omega})\psi_L^{g'}(\mathbf{r}, \mathbf{\Omega}')d\mathbf{\Omega}' - Q^g(\mathbf{r}, \mathbf{\Omega}), \quad g = 0, 1, \ldots, G-1. \tag{2.75}$$

Next, the scattering integral is evaluated analytically. In this evaluation, we suppress energy dependence for brevity.

$$\begin{aligned}
\int_{\mathbb{S}^2} \Sigma_s(\mathbf{r}, \boldsymbol{\Omega}' \cdot \boldsymbol{\Omega}) \psi_L(\mathbf{r}, \boldsymbol{\Omega}') d\boldsymbol{\Omega}' &= \int_{\mathbb{S}^2} \Sigma_s(\mathbf{r}, \boldsymbol{\Omega}' \cdot \boldsymbol{\Omega}) \sum_{n=1}^{N} \psi^n(\mathbf{r}) L_n(\boldsymbol{\Omega}') d\boldsymbol{\Omega}' \\
&= \sum_{n=1}^{N} \psi^n(\mathbf{r}) \int_{\mathbb{S}^2} \Sigma_s(\mathbf{r}, \boldsymbol{\Omega}' \cdot \boldsymbol{\Omega}) L_n(\boldsymbol{\Omega}') d\boldsymbol{\Omega}' \\
&= \sum_{n=1}^{N} \psi^n(\mathbf{r}) \int_{\mathbb{S}^2} \Sigma_s(\mathbf{r}, \boldsymbol{\Omega}' \cdot \boldsymbol{\Omega}) \sum_{m=1}^{N} \langle L_n, L_m \rangle K_m(\boldsymbol{\Omega}') d\boldsymbol{\Omega}' \\
&= \sum_{n=1}^{N} \psi^n(\mathbf{r}) \sum_{m=1}^{N} \langle L_n, L_m \rangle \int_{\mathbb{S}^2} \Sigma_s(\mathbf{r}, \boldsymbol{\Omega}' \cdot \boldsymbol{\Omega}) K_m(\boldsymbol{\Omega}') d\boldsymbol{\Omega}' \\
&= \sum_{n=1}^{N} \psi^n(\mathbf{r}) \sum_{m=1}^{N} \langle L_n, L_m \rangle \Sigma_{s,L}(\mathbf{r}, \boldsymbol{\Omega}_m \cdot \boldsymbol{\Omega}).
\end{aligned} \tag{2.76}$$

Here, the reproducing property of the function K was used and $\Sigma_{s,L}(\mathbf{r}, \boldsymbol{\Omega}_m \cdot \boldsymbol{\Omega})$ denotes the scattering cross section restricted to maximum degree L [21]. It is assumed that total and absorption group cross sections are independent of angle. Equations 2.72 and 2.76 are then substituted into the residual expression:

$$\begin{aligned}
r_L^g(\mathbf{r}, \boldsymbol{\Omega}) = \\
&\boldsymbol{\Omega} \cdot \sum_{n=1}^{N} \left[\nabla \psi^{g,n}(\mathbf{r})\right] L_n(\boldsymbol{\Omega}) + \Sigma_t^g(\mathbf{r}) \sum_{n=1}^{N} \psi^{g,n}(\mathbf{r}) L_n(\boldsymbol{\Omega}) \\
&- \sum_{g'=0}^{G-1} \sum_{n'=1}^{N} \sum_{m=1}^{N} \langle L_{n'}, L_m \rangle \Sigma_{s,L}^{g' \to g}(\mathbf{r}, \boldsymbol{\Omega}_m \cdot \boldsymbol{\Omega}) \psi^{g',n'}(\mathbf{r}) \\
&\qquad - Q^g(\mathbf{r}, \boldsymbol{\Omega}).
\end{aligned} \qquad g = 0, 1, \ldots, G-1. \tag{2.77}$$

Next, the collocation procedure requires the residual to be zero at the points $\{\boldsymbol{\Omega}_n\}_{n=1}^N$. This leads to the $G \times N$ equations

$$\begin{aligned}
&\boldsymbol{\Omega}_n \cdot \nabla \psi^{g,n}(\mathbf{r}) + \Sigma_t^g(\mathbf{r}) \psi^{g,n}(\mathbf{r}) = \\
&\sum_{g'=0}^{G-1} \sum_{m=1}^{N} \sum_{n'=1}^{N} \langle L_{n'}, L_m \rangle \Sigma_{s,L}^{g' \to g}(\mathbf{r}, \boldsymbol{\Omega}_m \cdot \boldsymbol{\Omega}_n) \psi^{g',n'}(\mathbf{r}) + Q^{g,n}(\mathbf{r}),
\end{aligned} \qquad \begin{array}{l} g = 0, 1, \ldots, G-1, \\ n = 1, 2, \ldots, N. \end{array} \tag{2.78}$$

In the collocation procedure, we have made use of the interpolation property of the Lagrange functions, i.e. $L_a(\boldsymbol{\Omega}_b) = \delta_{a,b}$.

Finally, we discretize the spatial variable in the same way as was done for the discrete ordinates equations, giving the $G \times I \times J \times K \times N$ multigroup LDO equations:

$$\begin{aligned} \boldsymbol{\Omega}_n \cdot \nabla \psi^{g,n}_{i,j,k} + \Sigma^{g}_{t,i,j,k} \psi^{g,n}_{i,j,k} = & \\ \sum_{g'=0}^{G-1} \sum_{m=1}^{N} \sum_{n'=1}^{N} \langle L_{n'}, L_m \rangle \Sigma^{g' \to g}_{s,L,i,j,k} (\boldsymbol{\Omega}_m \cdot \boldsymbol{\Omega}_n) \psi^{g',n'}_{i,j,k} + Q^{g,n}_{i,j,k}, & \end{aligned} \quad \begin{aligned} & g = 0, 1, \ldots, G-1, \\ & i = 1, 2, \ldots, I, \\ & j = 1, 2, \ldots, J, \\ & k = 1, 2, \ldots, K, \\ & n = 1, 2, \ldots, N. \end{aligned} \tag{2.79}$$

Here, N is the number of discrete angles used in the formulation and is a property of the maximum degree of integration of the quadrature set on which the equations are based, L_n is the n^{th} Lagrange function, and $\Sigma_{s,L}$ is the scattering cross section restricted to maximum degree L.

The difference in how the scattering source is calculated between Equations 2.17 and 2.79 has important implications, which we will explore in Chapter 3. The most apparent difference is that the LDO equations do not require the calculation of spherical harmonic moments of the angular flux. It is also important to note that the extremal point systems on which the LDO equations are based do not possess symmetries like those of the commonly-used quadrature sets discussed earlier.

The LDO formulation has never before been implemented in a full-scale radiation transport framework, nor has it been studied in the context of Monte Carlo variance reduction parameter generation. The following chapter will discuss the implementation of the LDO equations in the Exnihilo software package as well as the methodology employed for using the equations' solutions in automated Monte Carlo variance reduction parameter generation.

Chapter 3

Method Description and Implementation

This chapter discusses the implementation and solution of the LDO equations in Denovo, the parallel discrete ordinates radiation transport code package in the Exnihilo code suite [22]. First, a comparison of the traditional formulation of the discrete ordinates equations with the LDO equations is presented to demonstrate the difference in implementing the two separate sets of equations. Then, a brief discussion of scattering is given to highlight the specific differences between the two sets of equations with respect to how scattering is handled from the perspective of implementation. Following that is an overview of the quadrature sets used in solving the LDO equations in Denovo. Finally, we list and discuss the restrictions of using the LDO equations in combination with Exnihilo and ADVANTG for the purpose of Monte Carlo variance reduction parameter generation.

3.1 Operator Form

3.1.1 Traditional Discrete Ordinates Formulation

When considering deterministic methods, it is often instructive to think about the NTE in operator form. In accordance with the discretization in Section 2.1.2.1, the operator form of the traditional discrete ordinates equations [6] is

$$\mathbf{L}\Psi = \mathbf{MS}\Phi + Q, \tag{3.1}$$

$$\Phi = \mathbf{D}\Psi \text{ where } \mathbf{D} = \mathbf{M}^{\top}\mathbf{W}, \tag{3.2}$$

$$\left(\mathbf{I} - \mathbf{DL}^{-1}\mathbf{MS}\right)\Phi = \mathbf{DL}^{-1}Q. \tag{3.3}$$

The operators will be defined below, with the exception of $\mathbf{L}$, the transport operator. When solving Equation 3.3, the operation $\mathbf{L}^{-1}$ is referred to as a "sweep"; $\mathbf{L}$ is implicitly formed as a lower-left triangular matrix and is inverted by "sweeping" through the spatial mesh in the

direction of particle flow [6]. With this formulation, at each spatial unknown, with energy groups defined over the range $g \in [0, G-1]$ as described previously, we can write

$$\mathbf{L}\begin{pmatrix}\Psi_0\\ \Psi_1\\ \vdots\\ \Psi_{G-1}\end{pmatrix} = \begin{pmatrix}[\mathbf{M}] & 0 & 0 & 0\\ 0 & [\mathbf{M}] & 0 & 0\\ 0 & 0 & \ddots & \vdots\\ 0 & 0 & \cdots & [\mathbf{M}]\end{pmatrix}\begin{pmatrix}[\mathbf{S}]_{0\to 0} & [\mathbf{S}]_{1\to 0} & \cdots & [\mathbf{S}]_{G-1\to 0}\\ [\mathbf{S}]_{0\to 1} & [\mathbf{S}]_{1\to 1} & \cdots & [\mathbf{S}]_{G-1\to 1}\\ \vdots & \vdots & \ddots & \vdots\\ [\mathbf{S}]_{0\to G-1} & [\mathbf{S}]_{1\to G-1} & \cdots & [\mathbf{S}]_{G-1\to G-1}\end{pmatrix}\begin{pmatrix}\Phi_0\\ \Phi_1\\ \vdots\\ \Phi_{G-1}\end{pmatrix} + \begin{pmatrix}Q_0\\ Q_1\\ \vdots\\ Q_{G-1}\end{pmatrix}, \tag{3.4}$$

where the notation $[\cdot]_g$ indicates a block matrix over all unknowns for a single group.

Here, the angular flux vector for group g over angles $1, \ldots, N$ is defined as

$$\Psi_g = \begin{pmatrix}\psi_1^g & \psi_2^g & \psi_3^g & \cdots \psi_N^g\end{pmatrix}^\top, \tag{3.5}$$

with the external source vector Q_g defined similarly. The operator $\mathbf{M}$ is the "moment-to-discrete" matrix and is used to project harmonic moments onto discrete angle space. It is defined as

$$[\mathbf{M}] = \begin{pmatrix}Y_{00}^e(\mathbf{\Omega}_1) & Y_{10}^e(\mathbf{\Omega}_1) & Y_{11}^o(\mathbf{\Omega}_1) & Y_{11}^e(\mathbf{\Omega}_1) & \cdots & Y_{PP}^o(\mathbf{\Omega}_1) & Y_{PP}^e(\mathbf{\Omega}_1)\\ Y_{00}^e(\mathbf{\Omega}_2) & Y_{10}^e(\mathbf{\Omega}_2) & Y_{11}^o(\mathbf{\Omega}_2) & Y_{11}^e(\mathbf{\Omega}_2) & \cdots & Y_{PP}^o(\mathbf{\Omega}_2) & Y_{PP}^e(\mathbf{\Omega}_2)\\ Y_{00}^e(\mathbf{\Omega}_3) & Y_{10}^e(\mathbf{\Omega}_3) & Y_{11}^o(\mathbf{\Omega}_3) & Y_{11}^e(\mathbf{\Omega}_3) & \cdots & Y_{PP}^o(\mathbf{\Omega}_3) & Y_{PP}^e(\mathbf{\Omega}_3)\\ \vdots & \vdots & \vdots & \vdots & \ddots & \vdots & \vdots\\ Y_{00}^e(\mathbf{\Omega}_N) & Y_{10}^e(\mathbf{\Omega}_N) & Y_{11}^o(\mathbf{\Omega}_N) & Y_{11}^e(\mathbf{\Omega}_N) & \cdots & Y_{PP}^o(\mathbf{\Omega}_N) & Y_{PP}^e(\mathbf{\Omega}_N)\end{pmatrix}. \tag{3.6}$$

Note that $[\mathbf{M}]$ is dependent only on angle and is therefore the same for each energy group. The operator $\mathbf{D}$ is the "discrete-to-moment" matrix; it is used to calculate the moments of the angular flux from discrete angular flux values. $\mathbf{D}$ is calculated as $\mathbf{M}^\top\mathbf{W}$, where $\mathbf{W}$ is a diagonal matrix of quadrature weights [6], and it is written as

$$[\mathbf{D}] = \begin{pmatrix} w_1 Y_{00}^e(\mathbf{\Omega}_1) & w_2 Y_{00}^e(\mathbf{\Omega}_2) & w_3 Y_{00}^e(\mathbf{\Omega}_3) & \cdots & w_N Y_{00}^e(\mathbf{\Omega}_N) \\ w_1 Y_{10}^e(\mathbf{\Omega}_1) & w_2 Y_{10}^e(\mathbf{\Omega}_2) & w_3 Y_{10}^e(\mathbf{\Omega}_3) & \cdots & w_N Y_{10}^e(\mathbf{\Omega}_N) \\ w_1 Y_{11}^o(\mathbf{\Omega}_1) & w_2 Y_{11}^o(\mathbf{\Omega}_2) & w_3 Y_{11}^o(\mathbf{\Omega}_3) & \cdots & w_N Y_{11}^o(\mathbf{\Omega}_N) \\ w_1 Y_{11}^e(\mathbf{\Omega}_1) & w_2 Y_{11}^e(\mathbf{\Omega}_2) & w_3 Y_{11}^e(\mathbf{\Omega}_3) & \cdots & w_N Y_{11}^e(\mathbf{\Omega}_N) \\ \vdots & \vdots & \vdots & \ddots & \vdots \\ w_1 Y_{PP}^o(\mathbf{\Omega}_1) & w_2 Y_{PP}^o(\mathbf{\Omega}_2) & w_3 Y_{PP}^o(\mathbf{\Omega}_3) & \cdots & w_N Y_{PP}^o(\mathbf{\Omega}_N) \\ w_1 Y_{PP}^e(\mathbf{\Omega}_1) & w_2 Y_{PP}^e(\mathbf{\Omega}_2) & w_3 Y_{PP}^e(\mathbf{\Omega}_3) & \cdots & w_N Y_{PP}^e(\mathbf{\Omega}_N) \end{pmatrix}. \tag{3.7}$$

Like [**M**], [**D**] is dependent only on angle and is the same for each energy group. The scattering cross section matrices are defined as

$$[\mathbf{S}]_{g' \to g} = \begin{pmatrix} \Sigma_{\mathrm{s},0}^{g' \to g} & 0 & 0 & 0 & 0 & 0 & 0 \\ 0 & \Sigma_{\mathrm{s},1}^{g' \to g} & 0 & 0 & 0 & 0 & 0 \\ 0 & 0 & \Sigma_{\mathrm{s},1}^{g' \to g} & 0 & 0 & 0 & 0 \\ 0 & 0 & 0 & \Sigma_{\mathrm{s},1}^{g' \to g} & 0 & 0 & 0 \\ 0 & 0 & 0 & 0 & \ddots & 0 & 0 \\ 0 & 0 & 0 & 0 & 0 & \Sigma_{\mathrm{s},P}^{g' \to g} & 0 \\ 0 & 0 & 0 & 0 & 0 & 0 & \Sigma_{\mathrm{s},P}^{g' \to g} \end{pmatrix}, \tag{3.8}$$

where these scattering cross section coefficient values come from data libraries based on experimental measurements. Finally, the flux moment vectors are defined as

$$\Phi_g = \begin{pmatrix} \phi_{00}^g & \phi_{10}^g & \vartheta_{11}^g & \phi_{11}^g & \phi_{20}^g & \cdots & \vartheta_{PP}^g & \phi_{PP}^g \end{pmatrix}^\top, \tag{3.9}$$

where the flux moments are evaluated as listed in Equation 2.18. As we will describe below in Section 3.1.4, the goal of solving the discrete ordinates equations is to solve for these flux moments and then use the flux moments to calculate the scalar flux. In summary, the traditional discrete ordinates discretizations are captured in the preceding matrices; they can be used to analyze behavior and performance and can be compared against other discretizations.

3.1.2 LDO Formulation

As discussed in Chapter 2, although the LDO equations are formally the same as the traditional discrete ordinates equations, there are several key differences between the sets of equations. Here we present and discuss the operator form of the LDO equations as a comparison to the operator form of the discrete ordinates equations shown above. The operator form of the LDO equations is

$$\mathbf{L}\Psi = \tilde{\mathbf{S}}\mathbf{J}\Psi + Q, \tag{3.10}$$

$$\left(\mathbf{I} - \mathbf{L^{-1}}\tilde{\mathbf{S}}\mathbf{J}\right)\Psi = \mathbf{L^{-1}}Q. \tag{3.11}$$

Letting $\mathbf{D} \equiv \mathbf{I}$ with $\mathbf{L^{-1}} = \mathbf{IL^{-1}} = \mathbf{DL^{-1}}$, we then have

$$\left(\mathbf{I} - \mathbf{DL^{-1}}\tilde{\mathbf{S}}\mathbf{J}\right)\Psi = \mathbf{DL^{-1}}Q. \tag{3.12}$$

Equation 3.12 is in the same form as Equation 3.3, so we can apply the same solution techniques to both sets of equations.

In contrast to Equation 3.3, however, Equation 3.12 contains the Lagrange interpolation matrix $\mathbf{J}$ rather than the moment-to-discrete operator $\mathbf{M}$, and $\tilde{\mathbf{S}}$ contains the new formulation of scattering cross sections specific to the LDO equations. Additionally, when solving the LDO equations, we are solving for the angular flux coefficients rather than flux moments. Now, at each spatial unknown, with energy groups again defined over the range $g \in [0, G-1]$, we have

$$\begin{aligned}\mathbf{L}\begin{pmatrix}\Psi_0\\ \Psi_1\\ \vdots\\ \Psi_{G-1}\end{pmatrix} = &\\ &\begin{pmatrix}[\tilde{\mathbf{S}}]_{0\to0} & [\tilde{\mathbf{S}}]_{1\to0} & \cdots & [\tilde{\mathbf{S}}]_{G-1\to0}\\ [\tilde{\mathbf{S}}]_{0\to1} & [\tilde{\mathbf{S}}]_{1\to1} & \cdots & [\tilde{\mathbf{S}}]_{G-1\to1}\\ \vdots & \vdots & \ddots & \vdots\\ [\tilde{\mathbf{S}}]_{0\to G-1} & [\tilde{\mathbf{S}}]_{1\to G-1} & \cdots & [\tilde{\mathbf{S}}]_{G-1\to G-1}\end{pmatrix}\begin{pmatrix}[\mathbf{J}] & 0 & 0 & 0\\ 0 & [\mathbf{J}] & 0 & 0\\ 0 & 0 & \ddots & \vdots\\ 0 & 0 & \cdots & [\mathbf{J}]\end{pmatrix}\begin{pmatrix}\Psi_0\\ \Psi_1\\ \vdots\\ \Psi_{G-1}\end{pmatrix}\\ &+\begin{pmatrix}Q_0\\ Q_1\\ \vdots\\ Q_{G-1}\end{pmatrix},\end{aligned} \tag{3.13}$$

where the block matrix notation still holds. The angular flux coefficient vector and external source vector are formed as listed in Equation 3.5. The operator $[\mathbf{J}]$ performs the Lagrange interpolation. It is constructed as the inverse of the Gram matrix, $\mathbf{G}$, which is calculated as

$$\mathbf{G} = \begin{pmatrix}\sum_{\ell=0}^{L}\frac{2\ell+1}{4\pi}P_\ell(\mathbf{\Omega}_1\cdot\mathbf{\Omega}_1) & \sum_{\ell=0}^{L}\frac{2\ell+1}{4\pi}P_\ell(\mathbf{\Omega}_1\cdot\mathbf{\Omega}_2) & \cdots & \sum_{\ell=0}^{L}\frac{2\ell+1}{4\pi}P_\ell(\mathbf{\Omega}_1\cdot\mathbf{\Omega}_N)\\ \sum_{\ell=0}^{L}\frac{2\ell+1}{4\pi}P_\ell(\mathbf{\Omega}_2\cdot\mathbf{\Omega}_1) & \sum_{\ell=0}^{L}\frac{2\ell+1}{4\pi}P_\ell(\mathbf{\Omega}_2\cdot\mathbf{\Omega}_2) & \cdots & \sum_{\ell=0}^{L}\frac{2\ell+1}{4\pi}P_\ell(\mathbf{\Omega}_2\cdot\mathbf{\Omega}_N)\\ \vdots & \vdots & \ddots & \vdots\\ \sum_{\ell=0}^{L}\frac{2\ell+1}{4\pi}P_\ell(\mathbf{\Omega}_N\cdot\mathbf{\Omega}_1) & \sum_{\ell=0}^{L}\frac{2\ell+1}{4\pi}P_\ell(\mathbf{\Omega}_N\cdot\mathbf{\Omega}_2) & \cdots & \sum_{\ell=0}^{L}\frac{2\ell+1}{4\pi}P_\ell(\mathbf{\Omega}_N\cdot\mathbf{\Omega}_N)\end{pmatrix}. \tag{3.14}$$

Like [**M**] and [**D**] in the traditional discrete ordinates formulation, [**J**] depends only on angle and is the same for all energy groups. Finally, the new scattering cross section matrix is:

$$[\tilde{\mathbf{S}}]_{g'\to g} = \begin{pmatrix} \Sigma_{\mathrm{s,L}}^{g'\to g}(\mathbf{\Omega}_1\cdot\mathbf{\Omega}_1) & \Sigma_{\mathrm{s,L}}^{g'\to g}(\mathbf{\Omega}_1\cdot\mathbf{\Omega}_2) & \cdots & \Sigma_{\mathrm{s,L}}^{g'\to g}(\mathbf{\Omega}_1\cdot\mathbf{\Omega}_N) \\ \Sigma_{\mathrm{s,L}}^{g'\to g}(\mathbf{\Omega}_2\cdot\mathbf{\Omega}_1) & \Sigma_{\mathrm{s,L}}^{g'\to g}(\mathbf{\Omega}_2\cdot\mathbf{\Omega}_2) & \cdots & \Sigma_{\mathrm{s,L}}^{g'\to g}(\mathbf{\Omega}_2\cdot\mathbf{\Omega}_N) \\ \vdots & \vdots & \ddots & \vdots \\ \Sigma_{\mathrm{s,L}}^{g'\to g}(\mathbf{\Omega}_N\cdot\mathbf{\Omega}_1) & \Sigma_{\mathrm{s,L}}^{g'\to g}(\mathbf{\Omega}_N\cdot\mathbf{\Omega}_2) & \cdots & \Sigma_{\mathrm{s,L}}^{g'\to g}(\mathbf{\Omega}_N\cdot\mathbf{\Omega}_N) \end{pmatrix}, \tag{3.15}$$

where each element of $[\tilde{\mathbf{S}}]_{g'\to g}$ is calculated as

$$\Sigma_{\mathrm{s,L}}^{g'\to g}(\mathbf{\Omega}_n\cdot\mathbf{\Omega}_m) = \sum_{\ell=0}^{L}\frac{2\ell+1}{4\pi}\Sigma_{\mathrm{s},\ell}^{g'\to g}P_\ell(\mathbf{\Omega}_n\cdot\mathbf{\Omega}_m). \tag{3.16}$$

In Equation 3.16, $\Sigma_{\mathrm{s},\ell}^{g'\to g}$ are the same cross section coefficients that are stored in the traditional scattering matrix given in Equation 3.8. We again note that the operator **D** is replaced by the identity matrix in the LDO formulation; incorporation of the quadrature set weights in the LDO equations is discussed in Section 3.1.4. In the LDO formulation Equations 3.14 – 3.16, L, the order at which the scattering expansion is truncated, is arbitrary. However, values of $\Sigma_{\mathrm{s},\ell}^{g'\to g}$ must exist for all values of $\ell \in [0, L]$, so we typically set L equal to the same scattering expansion $\mathrm{P_N}$ order P in Equations 3.6 – 3.8. A more detailed comparison of scattering between the discrete ordinates formulation and the LDO formulation is given below in Section 3.2.1.

To recap, space and energy are handled in the same way between the two different formulations, while angular discretization and scattering are handled differently. The traditional discrete ordinates formulation uses the **M** and **D** operators to project harmonic moments onto discrete angle space and to calculate moments of the angular flux from discrete angular flux values, respectively. In contrast, the LDO formulation employs the interpolation matrix **J** and the scattering matrix $\tilde{\mathbf{S}}$ to capture angular information in the problem. We will look at the operator sizing for the two formulations in the next section to verify that these differences are compatible with respect to implementing the LDO equations in a software framework that was written to solve the discrete ordinates equations.

3.1.3 Operator Sizes

To evaluate the feasibility of constructing and solving the LDO equations in Denovo, it is pertinent to look at the dimensions of the operator forms of each equation. By doing this, we verify that the data structures for the discrete ordinates form can be leveraged to solve the LDO equations.

The sizes used for the discrete ordinates equations are

$$\begin{aligned}
G &= \text{number of energy groups,}\\
N &= \text{number of discrete angles,}\\
P &= \text{scattering expansion } P_N \text{ order,}\\
T &= (P+1)^2 = \text{number of flux moments,}\\
C &= \text{number of spatial cells,}\\
E &= \text{number of unknowns per spatial cell.}
\end{aligned}$$

Now, we define

$$a = G \times N \times C \times E \quad \text{and} \quad b = G \times T \times C \times E. \tag{3.17}$$

The operator sizes of the original formulation are then

$$\begin{aligned}
\mathbf{I} &= (a \times a);\\
\mathbf{D} &= (b \times a), \quad [\mathbf{D}] = (TCE \times NCE);\\
\mathbf{L} = \mathbf{L^{-1}} &= (a \times a);\\
\mathbf{M} &= (a \times b), \quad [\mathbf{M}] = (NCE \times TCE);\\
\mathbf{S} &= (b \times b), \quad [\mathbf{S}] = (TCE \times TCE);\\
\Phi &= (b \times 1), \quad \Phi_g = (TCE \times 1);\\
\Psi &= (a \times 1), \quad \Psi_g = (NCE \times 1);\\
Q &= (a \times 1), \quad Q_g = (NCE \times 1).
\end{aligned}$$

The sizes used in the LDO formulation are

$$\begin{aligned}
G &= \text{number of energy groups,}\\
H &= \text{degree of spherical harmonics subspace to integrate,}\\
N &= (H+1)^2 = \text{number of discrete angles,}\\
P &= \text{scattering expansion } P_N \text{ order,}\\
T &= (H+1)^2 = \text{number of angular flux coefficients,}\\
C &= \text{number of spatial cells,}\\
E &= \text{number of unknowns per spatial cell.}
\end{aligned}$$

Again, we define a and b as calculated in Equation 3.17. The operator sizes of the LDO formulation are then

$$\begin{aligned}
\mathbf{I} = \mathbf{D} &= (a \times a); \\
\mathbf{L} = \mathbf{L^{-1}} &= (a \times a); \\
\tilde{\mathbf{S}} &= (a \times a),\ [\tilde{\mathbf{S}}] = (NCE \times NCE); \\
\mathbf{J} &= (a \times a),\ [\mathbf{J}] = (NCE \times NCE); \\
\Psi &= (a \times 1),\ \Psi_g = (NCE \times 1); \\
Q &= (a \times 1),\ Q_g = (NCE \times 1).
\end{aligned}$$

In the LDO formulation, since the number of flux coefficients is tied to the degree of the subspace of spherical harmonics being integrated, $T = N$ and thus $a = b$. With this in mind, we observe that the operator dimensions in the two different formulations are compatible, which facilitates the use of the Exnihilo framework to solve the LDO equations. However, as noted throughout the chapter, the LDO formulation requires particular treatment in several ways when forming and solving the equations.

3.1.4 Scalar Flux

In the traditional formulation of the discrete ordinates equations, the scalar flux is defined as the zeroth moment in the expansion of the angular flux into spherical harmonic functions [6]. In Denovo, it is calculated for a given spatial cell and energy group as

$$\phi = \int_{4\pi} \psi d\mathbf{\Omega} = \sqrt{4\pi} \int_{4\pi} Y_{00}^{e} \psi d\mathbf{\Omega} = \sqrt{4\pi} \phi_{00}^{g}. \tag{3.18}$$

Thus, based on Equation 3.18, Denovo only retrieves the first entry of the angular flux moment storage vector when called upon to calculate the scalar flux.

When solving the LDO equations, the scalar flux is calculated as a weighted sum of the angular flux moments:

$$\phi = \int_{4\pi} \psi d\mathbf{\Omega} = \sum_{n=1}^{N} w_n \psi_n, \tag{3.19}$$

where the weights are those associated with the particular quadrature set and the angular flux coefficients are those values stored in the Denovo flux moment vector. In order to keep the Denovo scalar flux output functionality consistent between LDO quadratures and other quadrature sets, the scalar flux value calculated in Equation 3.19 is multiplied by $\frac{1}{4\pi}$ and written into the first entry of the flux moment storage vector after the calculation has finished.

3.2 Scattering

3.2.1 Matrix Formulation

As mentioned in Chapter 2, the most apparent difference between the standard discrete ordinates equations and the LDO equations is the discrepancy between the two sets of equations' scattering terms. Although the same scattering cross section coefficients are used in both methods when running Denovo, the coefficients are used to construct the scattering terms differently. Recall the operator forms discussed above and consider the following demonstrative example.

Suppose we are considering one spatial cell of a system with two energy groups and a P_1 scattering expansion. It is assumed that particles may scatter between the two energy groups as well as within each energy group. For the traditional discrete ordinates equations, the scattering matrices are

$$[\mathbf{S}]_{0\to0} = \begin{pmatrix} \Sigma_{s0}^{0\to0} & 0 & 0 & 0 \\ 0 & \Sigma_{s1}^{0\to0} & 0 & 0 \\ 0 & 0 & \Sigma_{s1}^{0\to0} & 0 \\ 0 & 0 & 0 & \Sigma_{s1}^{0\to0} \end{pmatrix}, \; [\mathbf{S}]_{1\to0} = \begin{pmatrix} \Sigma_{s0}^{1\to0} & 0 & 0 & 0 \\ 0 & \Sigma_{s1}^{1\to0} & 0 & 0 \\ 0 & 0 & \Sigma_{s1}^{1\to0} & 0 \\ 0 & 0 & 0 & \Sigma_{s1}^{1\to0} \end{pmatrix},$$
$$[\mathbf{S}]_{0\to1} = \begin{pmatrix} \Sigma_{s0}^{0\to1} & 0 & 0 & 0 \\ 0 & \Sigma_{s1}^{0\to1} & 0 & 0 \\ 0 & 0 & \Sigma_{s1}^{0\to1} & 0 \\ 0 & 0 & 0 & \Sigma_{s1}^{0\to1} \end{pmatrix}, \; [\mathbf{S}]_{1\to1} = \begin{pmatrix} \Sigma_{s0}^{1\to1} & 0 & 0 & 0 \\ 0 & \Sigma_{s1}^{1\to1} & 0 & 0 \\ 0 & 0 & \Sigma_{s1}^{1\to1} & 0 \\ 0 & 0 & 0 & \Sigma_{s1}^{1\to1} \end{pmatrix}. \tag{3.20}$$

In contrast, the LDO scattering matrix for within-group scattering in the lower group is

$$[\tilde{\mathbf{S}}]_{0\to0} = \begin{pmatrix} \Sigma_{\mathrm{s},1}^{0\to0}(\boldsymbol{\Omega}_1\cdot\boldsymbol{\Omega}_1) & \Sigma_{\mathrm{s},1}^{0\to0}(\boldsymbol{\Omega}_1\cdot\boldsymbol{\Omega}_2) & \cdots & \Sigma_{\mathrm{s},1}^{0\to0}(\boldsymbol{\Omega}_1\cdot\boldsymbol{\Omega}_N) \\ \Sigma_{\mathrm{s},1}^{0\to0}(\boldsymbol{\Omega}_2\cdot\boldsymbol{\Omega}_1) & \Sigma_{\mathrm{s},1}^{0\to0}(\boldsymbol{\Omega}_2\cdot\boldsymbol{\Omega}_2) & \cdots & \Sigma_{\mathrm{s},1}^{0\to0}(\boldsymbol{\Omega}_2\cdot\boldsymbol{\Omega}_N) \\ \Sigma_{\mathrm{s},1}^{0\to0}(\boldsymbol{\Omega}_3\cdot\boldsymbol{\Omega}_1) & \Sigma_{\mathrm{s},1}^{0\to0}(\boldsymbol{\Omega}_3\cdot\boldsymbol{\Omega}_2) & \cdots & \Sigma_{\mathrm{s},1}^{0\to0}(\boldsymbol{\Omega}_3\cdot\boldsymbol{\Omega}_N) \\ \vdots & \vdots & \ddots & \vdots \\ \Sigma_{\mathrm{s},1}^{0\to0}(\boldsymbol{\Omega}_N\cdot\boldsymbol{\Omega}_1) & \Sigma_{\mathrm{s},1}^{0\to0}(\boldsymbol{\Omega}_N\cdot\boldsymbol{\Omega}_2) & \cdots & \Sigma_{\mathrm{s},1}^{0\to0}(\boldsymbol{\Omega}_N\cdot\boldsymbol{\Omega}_N) \end{pmatrix}. \tag{3.21}$$

The LDO scattering matrices for particle movement between the two energy groups as well as within the higher energy group have been omitted for brevity; these matrices are constructed in the same fashion as Equation 3.21. In this example LDO scattering matrix, a given entry is calculated as

$$\begin{aligned}\Sigma_{\mathrm{s},1}^{0\to0}(\mathbf{\Omega}_n\cdot\mathbf{\Omega}_m) &= \sum_{\ell=0}^{L=1}\frac{2\ell+1}{4\pi}\Sigma_{\mathrm{s},\ell}^{0\to0}P_\ell(\mathbf{\Omega}_n\cdot\mathbf{\Omega}_m)\\ &= \frac{2(0)+1}{4\pi}\Sigma_{\mathrm{s},0}^{0\to0}P_0(\mathbf{\Omega}_n\cdot\mathbf{\Omega}_m)+\frac{2(1)+1}{4\pi}\Sigma_{\mathrm{s},1}^{0\to0}P_1(\mathbf{\Omega}_n\cdot\mathbf{\Omega}_m)\\ &= \frac{1}{4\pi}\Sigma_{\mathrm{s},0}^{0\to0}+\frac{3}{4\pi}(\mathbf{\Omega}_n\cdot\mathbf{\Omega}_m)\Sigma_{\mathrm{s},1}^{0\to0}.\end{aligned} \tag{3.22}$$

Equations 3.20 and 3.21 show several important and distinct differences between the two formulations. In the traditional discrete ordinates formulation, the scattering matrices themselves do not incorporate angular information; they merely hold the constant scattering cross section coefficients. Angular information is incorporated into the system solution via the **M** and **D** matrices. In contrast, in the LDO formulation, the scattering cross section expansion is contained within the scattering matrix itself. Despite the structural differences, Equations 3.20 and 3.21 employ the same cross section coefficients, as seen in the expansion listed in Equation 3.22.

3.2.2 Cross Section Reconstruction

To demonstrate the formal equivalence of how scattering is handled between the traditional discrete ordinates formulation and the LDO formulation,we present a brief example of scattering cross section reconstruction as a function of angle.

For this example, we will look at the scattering cross section of water at 300 K as a function of $\mathbf{\Omega}\cdot\mathbf{\Omega}'$, the cosine of the outgoing and incoming angles. Here we plot the scattering cross sections for the highest energy group (group 0) of a coarse (8 energy groups) test cross section library distributed with the SCALE software package [23]. A P_3 scattering expansion is used.

In Figure 3.1, we see that the group-to-group cross section with the greatest variation in angle is the downscattering from group 0 to group 1. In the interest of demonstrating how well particular quadrature types reconstruct scattering cross section as a function of angle, we will restrict the following reconstructions to this particular group-to-group cross section. Figure 3.2 shows this cross section reconstructed with the coarsest quadruple range (QR) and LDO quadrature sets available in Exnihilo. The QR quadrature set has one angle per octant and the LDO quadrature set is the "md003.00016" set of ordinates and weights listed in Table 3.1.

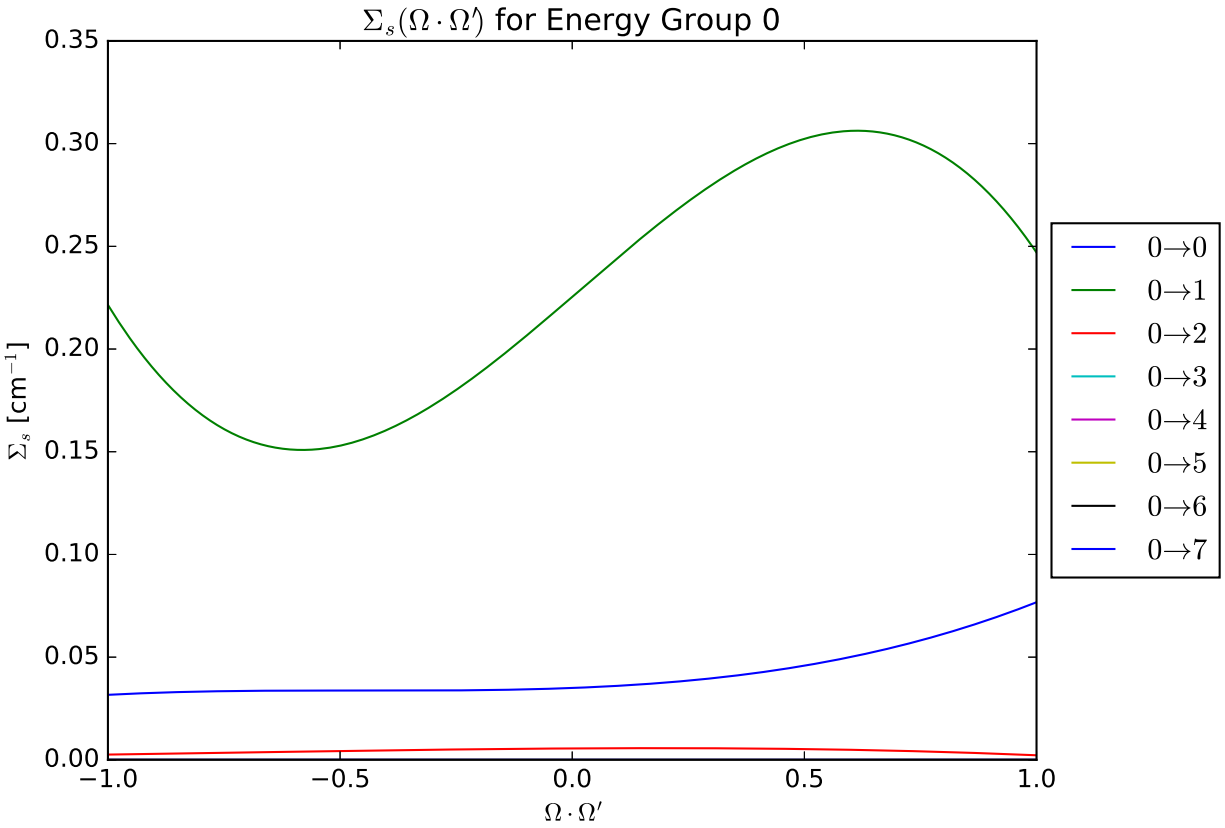

Figure 3.1: Water scattering cross section as a function of angle in the highest energy group.

In Figure 3.2 we see that the coarse QR and LDO quadrature sets both capture the forward-peakedness of this cross section. The QR quadrature set contains fewer unique values of $\mathbf{\Omega} \cdot \mathbf{\Omega}'$ than does the LDO quadrature set, however, and the LDO quadrature set produces values of Σ_s that are closer to the extremal values of the reference cross section curve. The potential impact of this is the possibility of being able to use relatively coarse LDO quadrature sets in solving a problem while incorporating the problem's angular dependence better than a standard quadrature set of a similar coarseness would.

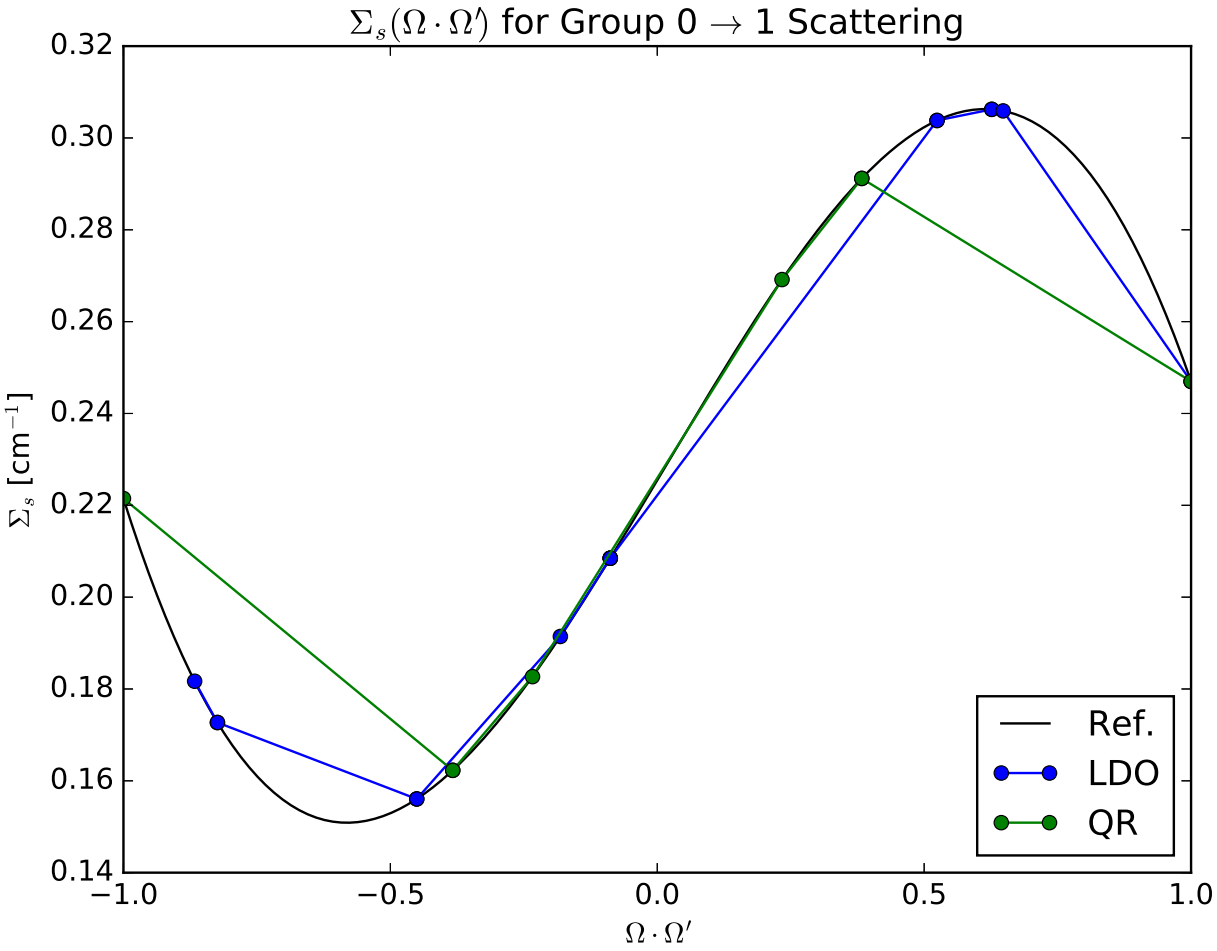

Figure 3.2: Group 0 → 1 scattering cross section reconstructed with coarse angular meshes.

Finer angular meshes of both quadrature set types are shown in Figure 3.3; in this plot the QR quadrature set has 128 angles and the LDO quadrature set has 144 angles. It is seen that both quadrature set types match the reference cross section curve quite well when the angular mesh is refined. This is unsurprising for the QR quadrature set and serves as a confirmation that the LDO formulation is formally the same as the traditional discrete ordinates equations.

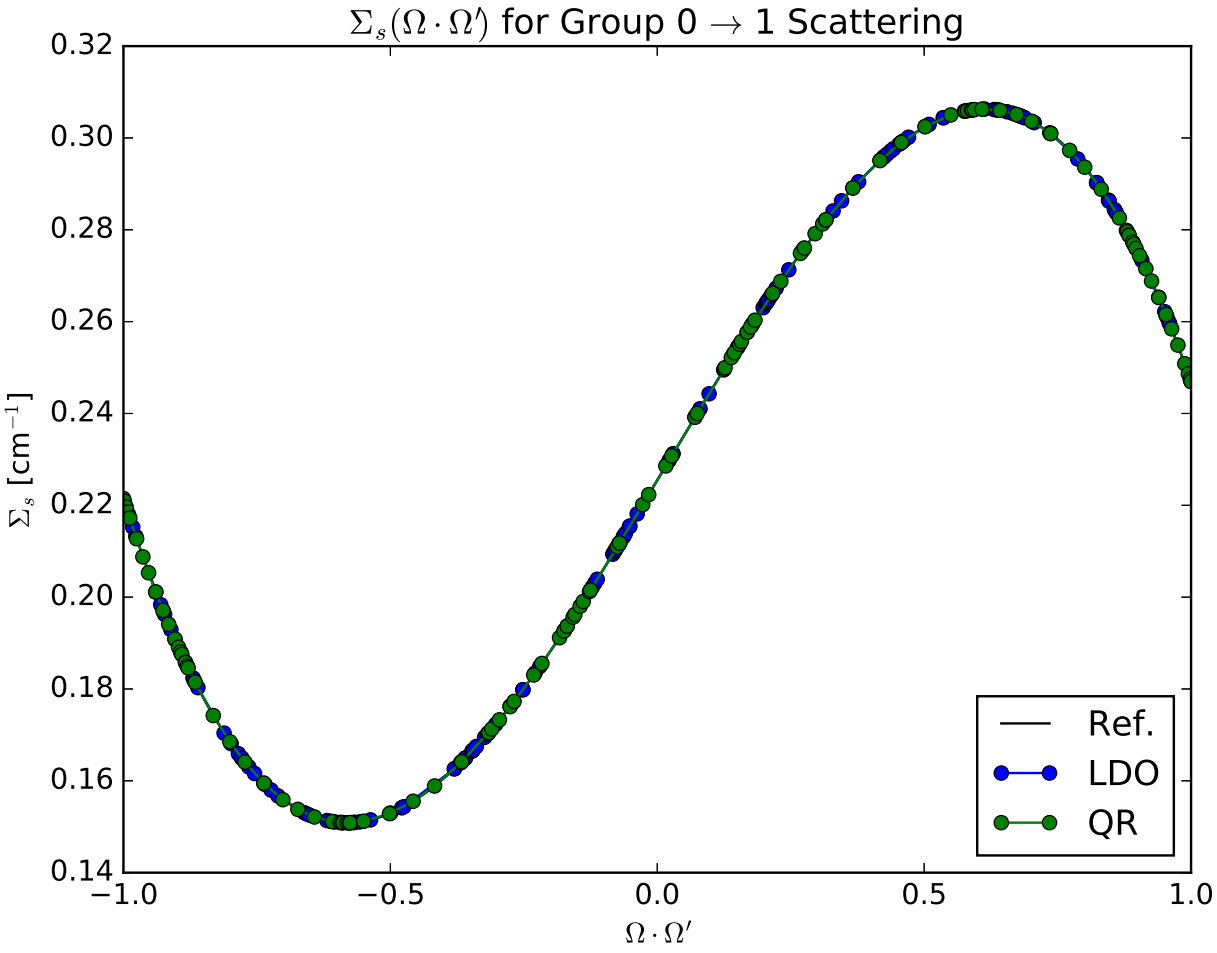

Figure 3.3: Group 0 → 1 scattering cross section reconstructed with fine angular meshes.

3.2.3 Scattering in Denovo

In Denovo and most other discrete ordinates codes, the operation $\mathbf{L}^{-1}$ in Equation 3.3 represents a sweep through the system mesh in the directions of particle travel [7]. We can rewrite Equation 3.3 to reframe it as solving for the total source Q:

$$Q = \mathbf{D}\mathbf{L}^{-1}\left(\mathbf{M}Q_m + Q_d\right). \tag{3.23}$$

Here, the operators are the same as those in Equation 3.3, Q_m is the sum of the "moment-based" sources, and Q_d is the sum of the "discrete" sources [24] as shown in Equation 3.24. Recalling Equation 3.23, moment-based sources are those to which the moment-to-discrete operator $\mathbf{M}$ is applied in the traditional discrete ordinates formulation. Discrete sources are not operated on by $\mathbf{M}$ and may be restricted to a subset of the discrete angles used in a given problem.

$$Q_m = \sum_{s=1}^{S_m} Q_{m,s} \quad \text{and} \quad Q_d = \sum_{s=1}^{S_d} Q_{d,s}, \tag{3.24}$$

where $Q_{m,s}$ is a particular moment-based sweep source, $Q_{d,s}$ is a particular discrete-based sweep source, S_m is the total number of moment-based sources in the system, and S_d is the total number of discrete sources [24]. Figure 3.4 shows the sweep source hierarchy implemented in Denovo, where the goal of the infrastructure is to calculate the total source listed in Equation 3.23 by performing a transport sweep over the combined particle sources.

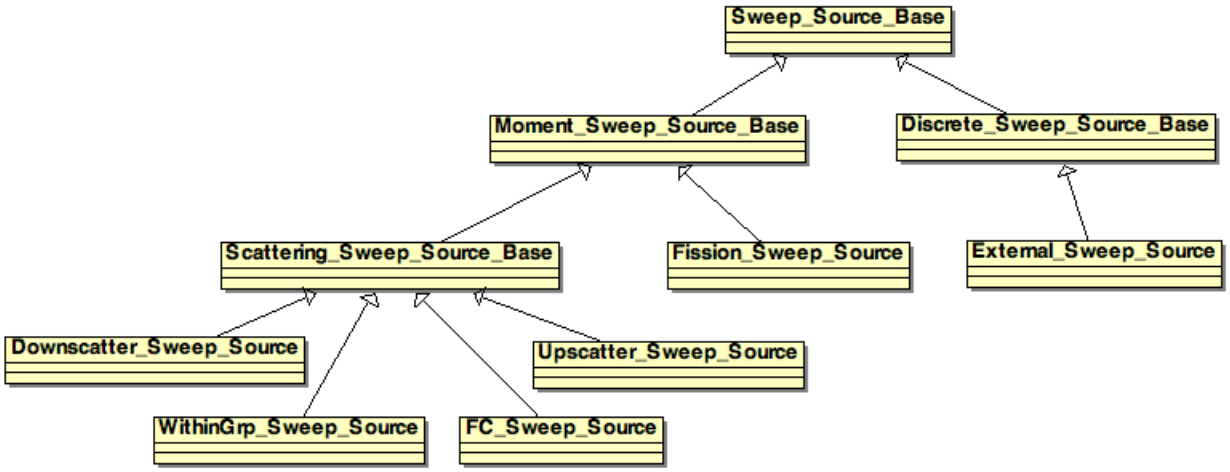

Figure 3.4: Sweep source hierarchy in Denovo [24].

From this diagram, it is apparent that all scattering derives from a common base class, the scattering sweep source base, and that this base class derives from the moment-based sweep source class. The types of scattering supported include downscattering, within-group scattering, upscattering, and first-collision scattering. The scattering classes share a great deal of functionality, hence the implementation of the common base class. Because the scattering sweep source is a type of moment-based sweep source, we note the particular difference in the operator forms of the discrete ordinates and LDO formulations and how that translates into implementing scattering calculations in Denovo.

In the LDO formulation, the interpolation matrix $\mathbf{J}$ is applied to the moment-based sources. Looking at Equations 3.3 and 3.12, it is apparent that the operator order is different between the traditional discrete ordinates formulation and the LDO formulation, Namely, the product of the scattering matrix and the moment-to-discrete or interpolation matrix is reversed between the two sets of equations. To handle this difference, a "scattering calculator" was implemented in the scattering sweep source base class such that the scattering sweep source is calculated in accordance with the formulation of the equation set being solved.

3.3 Selection of Quadrature Sets

As mentioned in Section 2.3.1, the LDO equations are developed with and must be evaluated at a fundamental system of points for the subspace of spherical harmonics. Ahrens provides references for examples of construction methods of these point systems [5]. Like Ahrens, we have chosen to use the extremal point sets developed and distributed by Womersley [25].

Womersley's extremal systems are generated such that the associated Gram matrix is positive definite [25]; these matrices are of interest to work with from an implementation standpoint because of their low condition numbers. In Table 3.1 we give an example of a point set generated by Womersley. The point set is of degree 3 and thus contains 16 points.

Table 3.1: The "md003.00016" quadrature set developed by Womersley [25].

μ	η	ξ	w
0.00000000000000000	0.0000000000000000	1.0000000000000000	0.73999377643692810
0.89273429807179527	0.0000000000000000	-0.45058348066286125	0.73999377643692787
-0.14301510478336188	0.98579910306911467	-0.088015954189755163	0.73999377643692688
-0.73214276086495222	0.51082433836573149	-0.45058348066286003	0.73999377643692854
0.65748213697787805	-0.7831172071742225	-0.088015954189756496	0.73999377643692765
-0.70626478165373330	0.4595590936077425	0.52407635945553088	0.92161132427900849
-0.60670408850507063	-0.4914548265981833	0.62661538904237324	0.73999377643692887
-0.29492456926406690	-0.9812320737717869	-0.18150577463199227	0.92161132427900960
0.21767572867043725	-0.7831172071742269	0.62661538904237279	0.73999377643692787
-0.51446703219451573	-0.23748738235169115	-0.82396809162048790	0.73999377643692743
0.85155965361038066	-0.013788611344369470	0.52407635945553044	0.92161132427900860
0.28603020956672459	-0.48914548265981850	-0.82396809162048790	0.73999377643692776
0.14962969730741976	0.47595590936077353	-0.86664694427906974	0.92161132427900883
-0.96739492195887000	-0.23748738235169184	-0.088015954189756274	0.73999377643692821
0.68136471239214502	0.72663286501151070	-0.088015954189756274	0.73999377643692898
0.22843682262779150	0.72663286501151014	0.64793618324097579	0.73999377643692754

We note that all of Womersley's extremal systems are generated such that the first point in each set is situated along the z-axis. These systems are rotationally invariant with respect to the maximization of the logarithm of the determinant of the associated Gram matrix, so the point sets may be rotated in space if this vector placement is undesirable for a given scenario. The work presented and discussed in Chapter 4 uses the point sets posted by Womersley; exploration of using rotated extremal point sets is a potential area of future work.

3.4 Restrictions

Several restrictions exist for solving the LDO equations in the Exnihilo framework as well as employing the solutions in the ADVANTG software. Some of these restrictions are a result

of implementing the LDO equations in a framework designed to solve the traditional discrete ordinates equations, while other restrictions are merely current limitations of the software pieces used in this work.

3.4.1 Boundary Conditions

Although it is mathematically possible to use reflective boundary conditions for the LDO equations (given their interpolatory nature), the current implementations of the various codes used in this work restrict the solutions to vacuum (black) boundary conditions at the time of this writing. The primary reason for this is that the ADVANTG software does not support the use of reflective boundary conditions, and the LDO equations were implemented into the Exnihilo framework for the purpose of using the solutions in ADVANTG for Monte Carlo variance reduction parameter generation. To a lesser extent, the Exnihilo framework was built with symmetric quadrature sets in mind, and so the use of reflective boundary conditions with the LDO equations was considered to be an effort beyond the scope of this work.

3.4.2 Uncollided Flux

The use of an "analytic" approximation of the uncollided flux source, a method employed to reduce ray effects from point sources or other small sources [22], is not available when solving the LDO equations through Exnihilo. This approximation is obtained in Denovo by solving the following equations for the group uncollided flux moments for every mesh cell in the calculation domain:

$$\mathbf{\Omega} \cdot \nabla \psi^g(\mathbf{\Omega}) + \Sigma_t^g \psi^g(\mathbf{\Omega}) = \frac{Q_p^g}{4\pi} \delta(r - r_p), \tag{3.25}$$

where $|r - r_p|$ is the geometric distance between the flux source and some particular point and the analytic solution of the above equations is

$$\psi^g(\mathbf{\Omega}) = \delta(\mathbf{\Omega} - \mathbf{\Omega}_{p \to r}) \frac{Q_p^g}{4\pi |r - r_p|^2} e^{-\tau(r, r_p)}. \tag{3.26}$$

In Equation 3.26, the term $\delta(\mathbf{\Omega} - \mathbf{\Omega}_{p \to r})$ indicates that the angular flux at a given point is only nonzero for the the angle that passes directly from the source through the particular point of interest. The "optical path length" $\tau(r, r_p)$ is the integral of the total cross section from the source location to the point of interest and is calculated via ray tracing.

Because the Exnihilo framework was written to solve the traditional form of the discrete ordinates equations, these flux moment solutions in Equation 3.26 are based on the expansion listed in Equation 2.18. That is to say, when using the analytic uncollided flux approximation, the flux moments are calculated using the components of the spherical harmonic functions listed in Equations 2.19 and 2.20. So, the solutions do not apply to the LDO equations and this treatment cannot be used. All tests in the following chapter were run with the

uncollided flux treatment turned off; implementing this approximation for use with the LDO equations in Denovo remains an area of future work.

3.4.3 Particle Sources

When considering neutron transport problems of interest, a small variety of particle source types appear frequently. One typical source type is an isotropic source, in which particles are emitted uniformly in all directions. Specifically, isotropic point sources, in which the physical size of the source itself is negligible, are routinely used in both experimental work and simulations.

Point sources must be approximated as small volumetric sources when solving the LDO equations in Denovo. When a point source is used in a system, Denovo calculates the uncollided flux from that point source using the analytic solution to the NTE. As mentioned previously, this is done to alleviate ray effects. However, as discussed above in Section 3.4.2, these analytic solutions are not applicable when solving the LDO equations. Thus, when a point source is specified in combination with the LDO equations, it is treated as a small volume source instead. In this case, an equal contribution of the source strength is added to every angular flux coefficient in the cell in which the particle source resides. This is notably different from the traditional discrete ordinates formulation in Denovo, in which the source strength is added only to the zeroth flux moment for reasons described in Section 3.1.4.

Finally in this section, we note that this work is limited to isotropic particle sources. At the time of this writing, ADVANTG does not support directional sources [15]; Monte Carlo particle importance maps generated with ADVANTG and Denovo automatically use an isotropic source distribution regardless of the particle source input. Since the ultimate goal of implementing the LDO equations in the Exnihilo framework is to use the results for Monte Carlo variance reduction parameter generation via ADVANTG, implementation of the use of directional sources when solving the LDO equations in Denovo was not pursued in this work.

3.4.4 Fixed Source vs. Criticality Calculations

All scenarios tested in this work are fixed-source problems, though the LDO equations are applicable to k-eigenvalue (criticality) problems in principle. Ray effects, which we are interested in using solutions of the LDO equations to mitigate, largely come from localized sources, as discussed in Section 2.1.2.2. Due to the distributed nature of fission sites in a typical light water reactor, the particle flux in a given criticality calculation will be relatively isotropic and unlikely to incur ray effects within the reactor core. Furthermore, at the time of this writing, ADVANTG only supports generation of Denovo input for fixed-source problems.

Chapter 4

Test Cases and Results

In this chapter we present the test case scenarios simulated in this work as well as the results of the various simulations performed. First, a description of the scenarios is given to detail the geometry and cross section configurations used. Next, a comparison of deterministic results for the test scenarios is given, with discussion and emphasis placed on the difference in the results between different types of quadrature sets. Then, we present results and analysis of the performance of the quadrature sets' associated Monte Carlo variance reduction parameters in the context of both CADIS and FW-CADIS simulations. Finally, a summary of the results is given to conclude the chapter.

4.1 Test Case Scenarios

4.1.1 Steel Plate in Water

The first test case we describe is an idealized geometry of a steel plate embedded in water; it is modeled after the scenario presented in Reference [26]. A diagram of the problem geometry is shown in Figure 4.1 and a list of material properties used in the problem is given in Table 4.1. In Figure 4.1, the orange region contains the source material, the black region is composed of steel, the blue regions indicate water, and the white region is composed of air.

The problem measurements are $53 \times 50 \times 140$ cm. The scenario is uniform in the y-direction and materials vary mainly in the z-direction. The source region extends from 0 to 15 cm, the steel shield extends between 15 and 30 cm, the water and steel plate extend from 30 to 130 cm, and the air extends from 130 to 140 cm. The steel plate is 3 cm wide and is centered at $x = 26.5$ cm. Vacuum boundary conditions were used at the problem boundaries.

A non-uniform Cartesian mesh was used for the spatial discretization in the deterministic calculations. In the x-direction, voxel width is 5 cm between $x = 0$ cm and $x = 25$ cm, 0.5 cm between $x = 25$ cm and $x = 28$ cm, and 5 cm between $x = 28$ cm and $x = 53$ cm. A

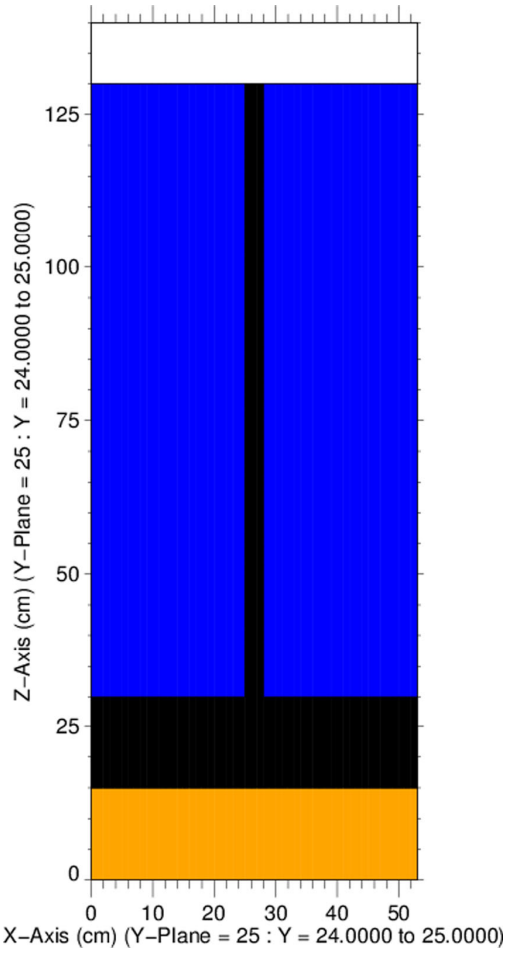

Figure 4.1: Steel plate in water geometry ($x - z$ slice through $y = 25$ cm) [26].

uniform spacing of voxel width 1 cm was used in the y-direction. In the z-direction, the spatial cell width is 3 cm between $z = 0$ cm and $z = 30$ cm and 2 cm between $z = 30$ cm and $z = 140$ cm.

The composition of the neutron source block is a homogenization of water, zirconium, and uranium and was calculated based on the geometry and composition of the Rowlands UO_2 pin cell benchmark specification [27]. The source is a U-235 fission spectrum that is uniformly distributed throughout the homogenized material. The compositions of air, carbon steel, and water were taken from the Compendium of Material Composition Data for Radiation Transport Modeling [28]. For this scenario, we are interested in the forward flux solutions at the end of the steel plate.

Table 4.1: Materials and compositions in the steel plate in water scenario.

Material	**Isotopes (Atomic %)**	
Source	U-235	(0.000247)
	U-238	(0.009287)
	Zr-nat.	(0.004009)
	H-1	(0.037394)
	O-16	(0.034927)
Air	N-14	(0.784431)
	O-16	(0.210748)
	Ar-nat.	(0.004671)
	C-nat.	(0.000150)
Carbon Steel	C-nat.	(0.022831)
	Fe-nat.	(0.977169)
Water	H-1	(2)
	O-16	(1)

4.1.2 Dog-Legged Void Neutron (DLVN)

The next problem modeled is the dog-legged void neutron (DLVN) experimental benchmark, which was designed to measure neutron streaming in iron with air voids. The model used in the following calculations was constructed from References [29, 30, 31]. The two materials used in the problem are elemental iron and polyethylene. The polyethylene composition used was C_2H_4. This is listed as "polyethylene, non-borated" and is material 248 in Reference [28].

The problem measurements are $40 \times 54 \times 48$ inches. A uniform spatial mesh was imposed over the entire problem, with voxels measuring 1 inch per side. The neutron source in this problem is a Cf-252 point source located at the center of the $x-$ and $y-$directions and at $z = 9$ inches. For reasons noted in Section 3.4.3, this point source was approximated as a small volumetric source in the tests in this work. We are interested in the forward flux solutions at the various detector locations shown in Figure 4.2.

The experimental configuration is symmetric about the $y - z$ plane at $x = 0$ and so is usually simulated with a reflecting boundary at $x = 0$ and vacuum boundaries on all other sides of the configuration. For the tests in this work, the use of reflecting boundary conditions was not available (see Section 3.4.1), so the model used was constructed to represent the entire experimental geometry configuration. Vacuum boundary conditions were applied to the outside of the entire problem.

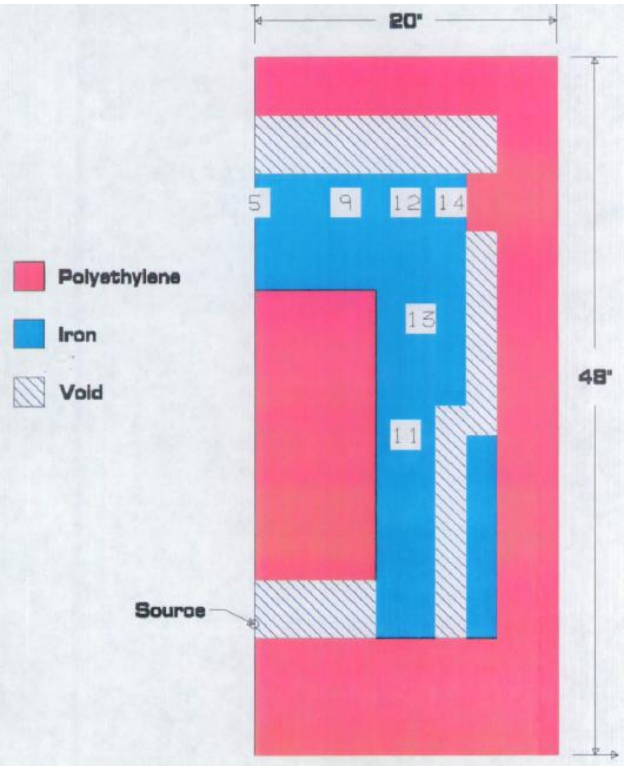

Figure 4.2: Centerline cutaway of DLVN setup [29].

4.1.3 Ispra Sodium Benchmark

The Ispra sodium benchmark experiment was constructed as part of experiments to study neutron deep penetration in homogeneous materials commonly used in advanced nuclear reactors. It is included in the Shielding Integral Benchmark Archive and Database (SINBAD) data library [32]. We will give a brief overview of the material and geometry configuration here and refer the reader to Reference [32] for a complete description of the experiment.

The neutron source consists of fission neutrons originating from an enriched U disc that was subjected to a neutron flux leaving the thermal column of a TRIGA MARK II reactor. An irradiation tunnel assembly composed of steel containers filled with Na was constructed in front of the neutron source converter. The total length of the irradiation tunnel was 400 cm. A diagram of the experimental geometry is shown in Figure 4.3; we are interested in the forward flux solutions in the detector array located along the midline of the assembly.

In the simulation of this benchmark configuration, the boundaries are -300 cm and 500 cm in the $x-$direction and -400 and 400 cm in both the $y-$ and $z-$directions. The spatial mesh in this problem is uniform in the $y-$ and $z-$directions with a voxel width of 5 cm per side in these dimensions. The $x-$direction mesh was created such that voxels are 10 cm wide between x = -300 and -100 cm, 5 cm wide between x = -100 and 400 cm, and 10 cm wide between x = 400 and 500 cm. The problem has vacuum boundary conditions.

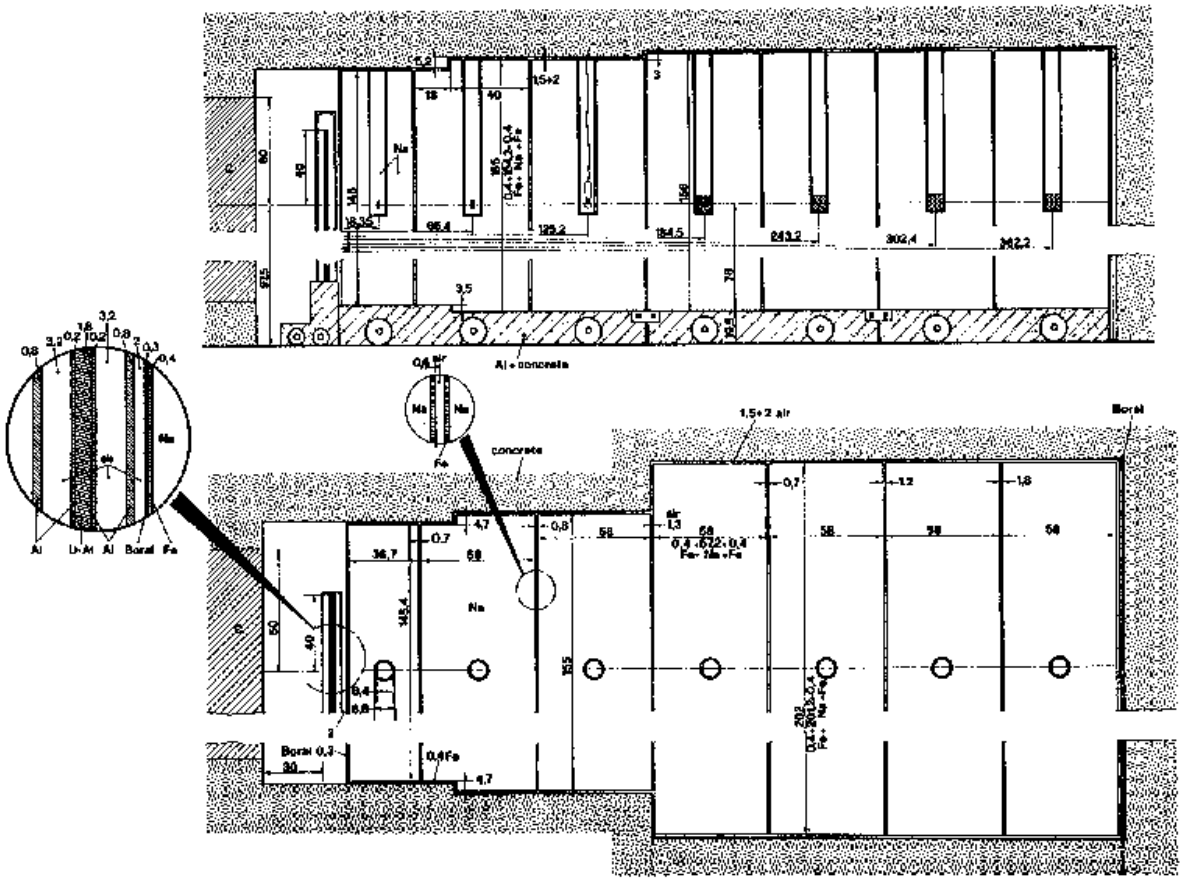

Fig. 2: **Vertical and horizontal cross section of sodium assembly at Euracos II facility**

Figure 4.3: Cross sectional views of the sodium benchmark assembly.

4.1.4 Simplified Portal Monitor

The final problem described here is a simplified portal monitor scenario. Portal monitors are large detector panels used to screen cargo for illicit radioactive materials. The problem models a cargo container holding a Ba-133 photon point source and large blocks of homogenized iron and polyethylene. The geometry and material configuration used in this test is the same as the example problem listed in Section 7.2 of the ADVANTG technical report [8]; slight modifications were made to the given MCNP input deck such that the problem could be studied with both CADIS and FW-CADIS calculations. Diagrams of the simplified portal monitor problem are shown in Figure 4.4.

In Figure 4.4, the different colors represent different materials. The NaI detectors are red and the gray material is concrete. The two types of material blocks are iron, shown in green, and polyethylene, shown in white. The steel cargo container surrounds the particle source

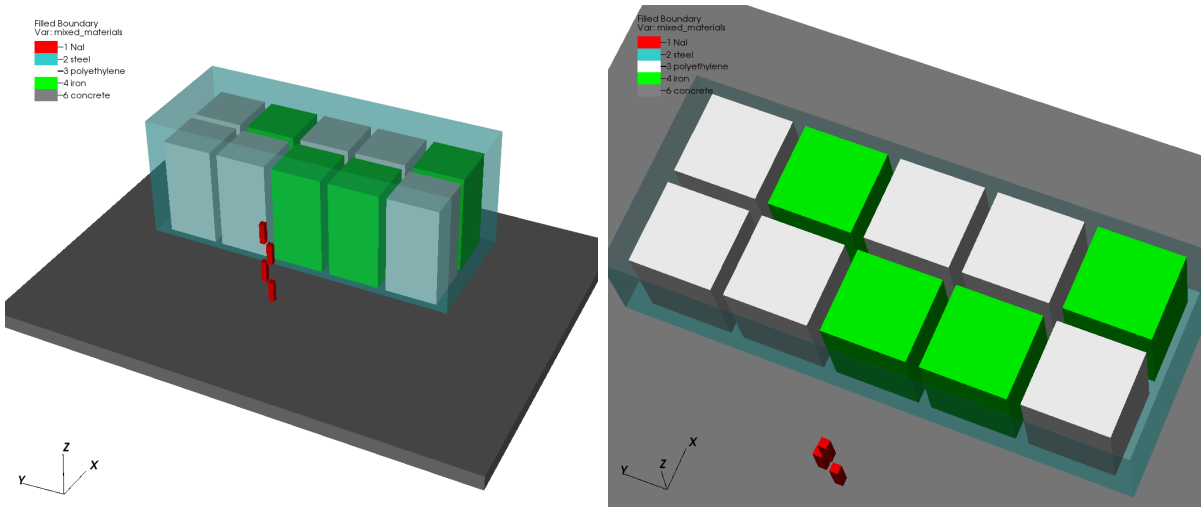

Figure 4.4: Top and side views of simplified portal problem [8].

and material blocks and is a semitransparent blue. Here we are interested in the forward flux solutions at the four detector locations.

A non-uniform Cartesian mesh that captures all of the problem's material boundaries was constructed for this simulation. The voxels are nominally 10 cm thick within the cargo container. Additional mesh planes parallel to the $x-$axis were added to the gaps between the homogenized iron and polyethylene blocks [8]. Vacuum boundary conditions are present at all problem edges.

4.1.5 Calculation Parameters

4.1.5.1 Deterministic

All of the deterministic calculations used 32 processes on a 2.8GHz AMD Opteron™ 6320 Processor [33], two for each logical CPU unit. With this in mind, all deterministic calculations were set to use the same Denovo computational block structure of 8 blocks in the $x-$dimension, 4 blocks in the $y-$dimension, and 1 block in the $z-$dimension; thus the total number of computational blocks equals the number of processes. Denovo uses the Koch-Baker-Alcouffe (KBA) parallel sweep algorithm for high parallel efficiency in calculating transport sweeps [7]; the aforementioned block structure was chosen to achieve the same parallel decomposition among all test case deterministic simulations.

All but one of the test cases use the same coarse energy group structure specified in the "27n19g" library; the groups in this library are listed in Table A-1 of Appendix A of the ADVANTG technical report [8]. The exception to this is the simplified portal problem. The highest energy emission line of Ba-133 is 383.8 keV, so weight window bounds above this energy would not be used in the Monte Carlo simulation. Thus, the highest energy group of the deterministic calculations was set to group number 41, which has an upper energy of

400 keV [8]. Because energy discretization is treated the same way between the traditional discrete ordinates formulation and the LDO equations, it was assumed that energy group structure would not greatly impact the comparative results.

The step characteristics (SC) spatial discretization was used in all of the deterministic calculations based on the recommendation listed in Section 9.1.3 of the Exnihilo user manual [22]. In the DLVN and portal monitor scenarios, the point sources are approximated as small spherical volumetric sources (see Section 3.4.3 for detail).

Except for the Galerkin quadratures, all runs used a P_5 scattering expansion. At the time of this writing, Galerkin quadrature sets are implemented in the Exnihilo framework with the restriction that the P_N order be one greater than the S_N order. That is, for the Galerkin quadrature set of S_N order 2, the corresponding P_N order is set equal to 3, and for the Galerkin quadrature set of S_N order 4, the P_N order is 5.

4.1.5.2 Monte Carlo

The Monte Carlo calculations in this work were run on one Dell PowerEdge C6220 server blade node with two Intel Xeon 10-core Ivy Bridge processors (a total of 20 cores) [34]. All calculations were specified to use 21 MPI tasks; MCNP reserves one "master" process for communication and transports particles with the remaining available tasks [3]. So, for the purpose of parallel efficiency, one transport process per hardware core was used here.

All of the Monte Carlo calculations were run with a fixed number of particle histories to simulate. For the steel plate in water, Ispra sodium benchmark, and simplified portal monitor cases, all calculations used 1×10^9 particle histories in both the CADIS and FW-CADIS contexts. The DLVN experimental benchmark case was simulated with 1×10^{10} neutron histories as it was modeled after calculations in Reference [29]. All Monte Carlo tally results and following calculations are reported with the one standard deviation confidence interval $\bar{x}(1 \pm R)$ where the relative error $R \equiv S_{\bar{x}}/\bar{x}$ [3].

4.2 Deterministic Forward Flux Calculations

Before investigating deterministic flux solutions resultant from solving the LDO equations as input for Monte Carlo variance parameter generation, it behooves us to compare the LDO deterministic results against those of standard quadrature set types. We start here by presenting results and analysis for forward scalar flux solutions using different quadrature types for the four test cases. We assume extensibility of these results to adjoint scalar flux solutions since the changes to the Exnihilo code suite made in this work did not impact the transport solvers in the Denovo package.

For all of the quadrature set types and sizes discussed above, a forward simulation of each test case was run via the Exnihilo framework. The following results show a representative quadrature set chosen for each type. With the exception of the Galerkin quadrature set featured, the angular refinement of the representative quadrature sets was chosen such that

the quadrature sets have approximately the same total number of angles. The QR quadrature set is of order 4 and has 128 angles, the LDFE set is order 1 with 128 angles, and the LDO set is of order 11 with 144 angles. The Galerkin quadrature set chosen as the representative example here is of order 4 and has 24 angles. This set was chosen because its corresponding P_N order is 5 and so the scattering data used matches that of the other quadrature types.

Because more results were generated than are presented here, a fuller set of figures is hosted at `http://dx.doi.org/10.6084/m9.figshare.6063053`.

4.2.1 Quadrature Sets

In these preliminary deterministic calculations, forward solutions for the test cases were generated using quadruple range (QR), Galerkin, linear-discontinuous finite element (LDFE), and LDO quadrature sets. All test cases were run with the same quadrature sets; increasing sizes of quadrature sets were used to ascertain the angular mesh refinement necessary for a given quadrature type to converge to a solution.

QR quadrature sets were chosen to generate the reference results against which the LDO results are compared. QR was selected because they are commonly used in hybrid methods for Monte Carlo variance reduction parameter generation and therefore provide a relevant baseline. The Exnihilo framework allows the user to select the number of polar and azimuthal angles in each octant when using a QR quadrature set; for these studies, the number of polar and azimuthal angles per octant were each set to the same value, with the values ranging from one per octant (for a total of eight angles) to nine per octant (for a total of 648 angles).

LDFE and Galerkin quadrature sets were also chosen because of their interesting mathematical properties. Compared to QR quadrature sets, LDFE quadrature sets have been shown to exhibit more accurate solutions for the scalar flux in both simple and more complex geometry and material configurations [35]; they approximate the angular flux using direction cosines and are determined by requiring that the integration of the related interpolation basis functions is equal to the surface area of a unit sphere. For LDFE quadrature sets, if N is the order of the quadrature, there are $4^{(N+1)}$ angles per octant [22]. In this work, the LDFE quadrature orders used were one (128 total angles) and two (8192 total angles).

Galerkin quadrature sets offer several advantages relative to the standard S_N method for problems with highly anisotropic scattering [36]. Similar to the LDO equations, the "hybrid collocation-Galerkin-S_N" method developed by Morel has the same algebraic structure as the traditional discrete ordinates equations but employs a nonstandard scattering treatment. For reasons discussed below in Section 4.1.5.1, the Galerkin quadrature orders used were 2 and 4. For an S_N order N, a given Galerkin quadrature set (as implemented in Exnihilo) has a total of $N(N+2)$ angles; the Galerkin quadrature sets used in this work have 8 and 24 total angles, respectively.

The degrees and sizes of the LDO quadrature sets used are listed in Table 4.2.

Table 4.2: Properties of LDO quadrature sets used in preliminary scaling studies.

Quadrature Order (N)	Number of Points
3	16
5	36
8	81
9	100
11	144
12	169
13	196
14	225

4.2.2 Steel Plate in Water

Figure 4.5 shows a representative forward scalar flux slice plot for each quadrature type. Each of the flux slices is at the midplane of the $y-$dimension such that $y = 25$ cm. The geometry/material borders are outlined on each plot as well. All plots show the same expected result – the scalar flux is highest in the source region and drops off by orders of magnitude along the $z-$axis.

To more thoroughly evaluate the LDO quadrature set in this test case, we will look more closely at the differences between the representative LDO flux and the three other quadrature types. Figure 4.6 shows three plots of relative flux differences; each plot compares the representative LDO quadrature set against one of the standard quadrature set types. The relative flux difference is calculated as

$$\phi_{\text{diff}} = \frac{|\phi_{\text{LDO}} - \phi_{\text{ref}}|}{\phi_{\text{ref}}} \tag{4.1}$$

where ϕ_{ref} is the scalar flux calculated using the standard quadrature set and is taken to be the reference value. For all three of the standard quadrature sets, the area of greatest agreement with the LDO scalar flux is towards the bottom of the problem geometry, with discrepancies growing along the $z-$axis. The greatest difference can be seen between the LDO and Galerkin quadrature sets, while the LDO and QR quadrature sets agree best. The area of greatest discrepancy between the QR and LDO flux solutions is in the region of air just beyond the steel beam. We will look more in depth as to why this is in Section 4.3.1 and briefly note here that this particular deviation is most likely due to issues in processing iron cross section data inherent to deterministic calculations.

Table 4.3 lists the minimum, maximum, and average differences between various quadrature types for the flux slices plotted in Figure 4.6. We compare the representative LDO flux solution to the solutions from the three standard representative quadrature types and also compare the Galerkin and LDFE results against the QR result. On average, the LDO forward flux solution matches the QR flux solution more closely than it matches either the

Galerkin or LDFE flux solutions. Additionally, the LDO flux solution matches the QR flux solution more closely than do either of the Galerkin and LDFE flux solutions.

Table 4.3: Steel plate forward scalar flux extremal and average relative differences.

Comparison	**Min. Diff.**	**Max. Diff.**	**Avg. Diff.**
LDO/QR	6×10^{-6}	1.09×10^{-1}	2.21×10^{-2}
LDO/Galerkin	2×10^{-5}	4.51×10^{0}	9.30×10^{-1}
LDO/LDFE	5×10^{-7}	2.79×10^{-1}	9.42×10^{-2}
Galerkin/QR	3×10^{-5}	8.24×10^{-1}	2.90×10^{-1}
LDFE/QR	2×10^{-7}	2.48×10^{-1}	9.63×10^{-2}

Looking at Figures 4.5 and 4.6 we note that the forward scalar flux solutions from the LDO equations capture the same physical trends as the standard quadrature type solutions and also that the LDO flux solution most closely matches that using the QR quadrature set. Additionally, Table 4.3 shows an average difference of 2.2% between the plotted flux solutions from the representative LDO and QR quadrature sets, which is the lowest average difference seen in the comparisons here. As QR quadratures are commonly used for Monte Carlo variance reduction parameter generation, the relative agreement of the LDO scalar flux with the QR scalar flux motivates the exploration of the use of LDO scalar flux solutions for Monte Carlo variance reduction parameter generation.

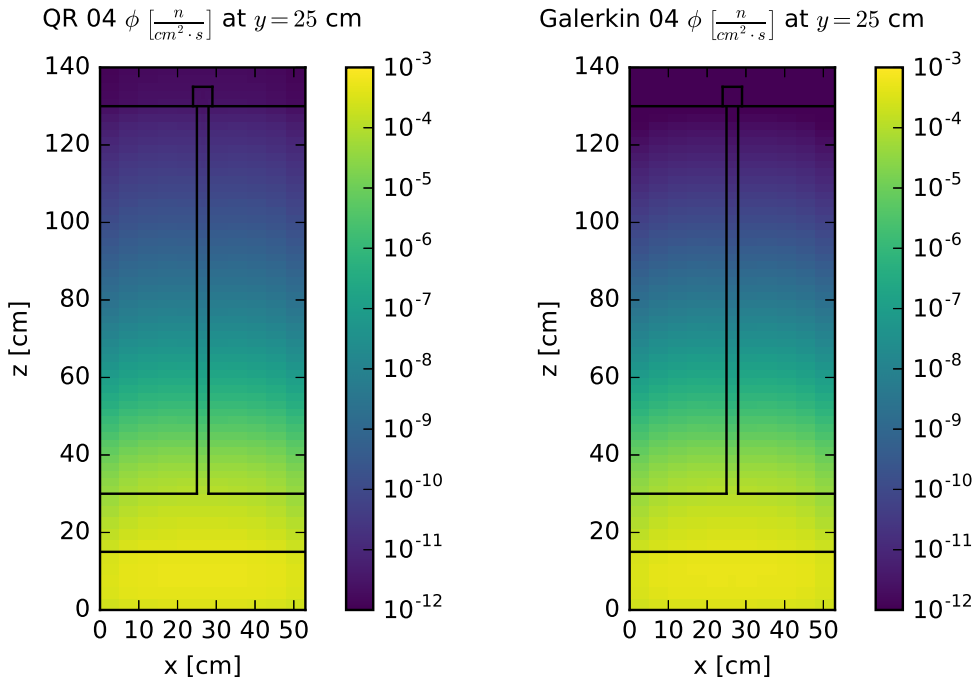

(a) QR forward flux slice.

(b) Galerkin forward flux slice.

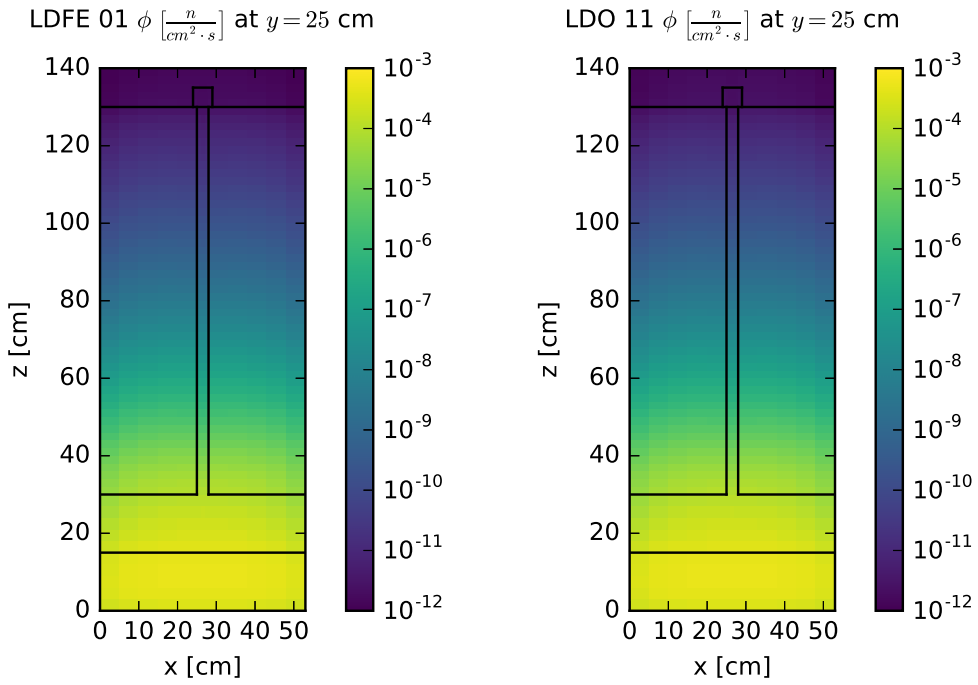

(c) LDFE forward flux slice.

(d) LDO forward flux slice.

Figure 4.5: Steel plate forward scalar flux slices.

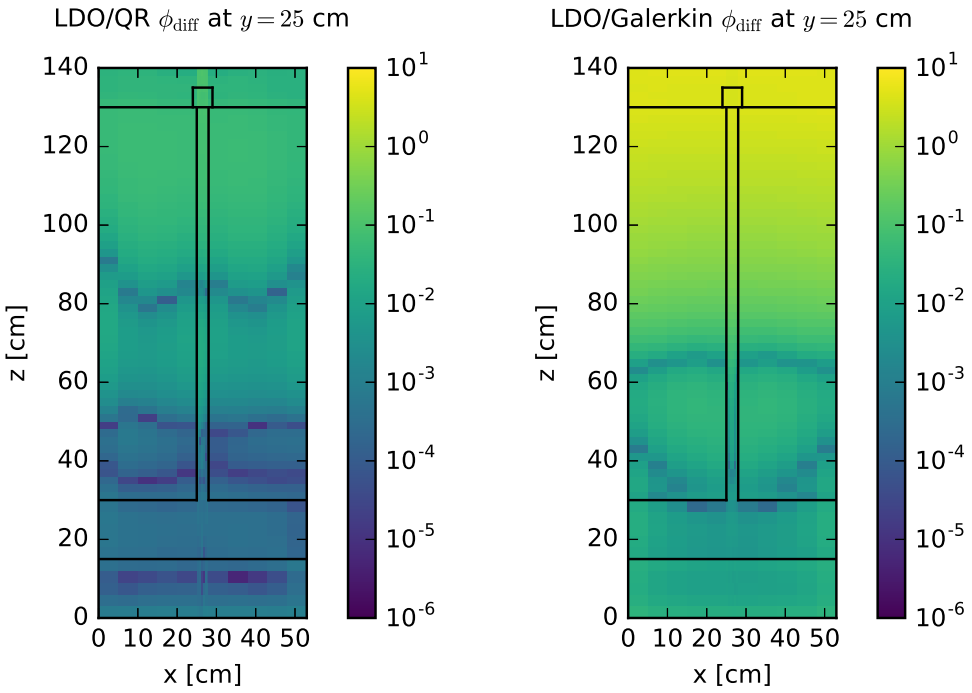

(a) LDO/QR flux rel. diff.

(b) LDO/Galerkin flux rel. diff.

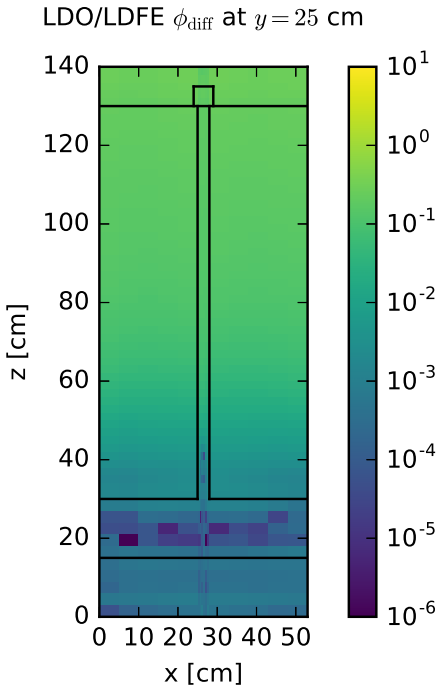

(c) LDO/LDFE flux rel. diff.

Figure 4.6: Steel plate forward scalar flux relative difference slices.

4.2.3 DLVN

For the DLVN test case, we present flux slice plots for the same representative quadrature sets listed in Section 4.2.2. Although the entire DLVN experimental geometry was simulated, here we plot only half of the configuration; this is the typical view of the benchmark seen in the literature.

Figure 4.7 shows the forward scalar flux for each of the representative quadrature sets at the midplane of $y = 27$ inches (68.58 cm). Each of the plots has outlines of the material boundaries with the detector locations delineated as well. As expected, the flux is highest at the neutron source and decreases as particles move through the experimental configuration. With this, we again look at the differences between the representative LDO flux and the three other quadrature types.

As with the previous test case, the flux differences are calculated with Equation 4.1. In the DLVN scenario, the differences stem from the source location. This is not surprising; the particle source here is approximately a point source and so these differences are appearing in the form of ray effects, where the discrete angles in the LDO quadrature set do not overlap with the angles in a given standard quadrature set. Similar to the steel plate in water test case, the LDO scalar flux best matches the QR scalar flux and the largest differences are seen between the LDO and Galerkin scalar flux plots. Looking at Figure 4.8b, the areas of greatest discrepancy appear as ray effects; the relative coarseness of the representative Galerkin quadrature set angular mesh is likely the cause of this. This is visibly pronounced in the DLVN case because of the geometrically small particle source; it is also likely the source of the LDO/Galerkin discrepancy seen above for the steel plate embedded in water, but ray effects are lessened in that scenario by the larger volumetric source.

Lastly, it is instructive to compare the results of the forward deterministic scalar flux solutions with the experimentally measured flux values at the detector locations. Table 4.4 lists the experimentally measured [31] and deterministically calculated scalar flux values at the detector locations noted in Figure 4.2. Table 4.5 lists the percent differences between the deterministically calculated flux values and experimentally determined flux values with the lowest difference for each detector location emphasized.

Table 4.4: DLVN benchmark experimental and simulated scalar flux values [n/cm^2/s].

	Det. #5	Det. #9	Det. #11	Det. #12	Det. #13	Det. #14
Exp. Flux	6.97×10^{-8}	1.57×10^{-7}	8.81×10^{-6}	2.60×10^{-7}	1.42×10^{-6}	2.74×10^{-7}
QR	4.98×10^{-8}	1.68×10^{-7}	8.65×10^{-5}	4.92×10^{-7}	2.71×10^{-6}	1.45×10^{-6}
Galerkin	3.24×10^{-8}	1.47×10^{-7}	8.19×10^{-5}	4.43×10^{-7}	2.95×10^{-6}	9.55×10^{-7}
LDFE	5.12×10^{-8}	1.76×10^{-7}	9.17×10^{-5}	5.14×10^{-7}	2.93×10^{-6}	1.47×10^{-6}
LDO	4.56×10^{-8}	1.39×10^{-7}	7.88×10^{-5}	4.28×10^{-7}	2.37×10^{-6}	1.28×10^{-6}

Looking at Table 4.5 we see that all of the calculated values fall outside of the experimental uncertainty of five percent [31]. The results from the LDO quadrature set most closely

Table 4.5: Percent differences between DLVN experimental and simulated scalar flux values.

	Det. #5	Det. #9	Det. #11	Det. #12	Det. #13	Det. #14
QR	**25.58**	6.89	881.94	89.09	90.63	428.81
Galerkin	53.48	**6.37**	829.72	70.56	107.7	**248.42**
LDFE	26.61	12.3	940.41	97.75	106.4	435.01
LDO	34.61	11.2	**794.75**	**64.46**	**66.77**	368.24

match the experimental results for half of the detector locations. This begs the question of how the LDO equations would perform in the context of the FW-CADIS method for the DLVN problem since the adjoint source can be set to multiple detector locations. Table 4.6 lists the extreme and average values of the forward flux relative difference slices shown in Figure 4.8 with Galerkin/QR and LDFE/QR comparisons included for reference. We see that, on average, the LDO forward flux solution matches the QR forward flux solution better than it matches those of the other quadrature types. However, in this case, the LDFE flux solution matches the QR flux solution on average better than any other quadrature type, including the LDO flux solution (5% difference versus 8.4% difference).

Table 4.6: DLVN benchmark forward scalar flux extremal and average relative differences.

Comparison	**Min. Diff.**	**Max. Diff.**	**Avg. Diff.**
LDO/QR	2×10^{-4}	8.40×10^{-1}	8.44×10^{-2}
LDO/Galerkin	1×10^{-6}	2.14×10^{0}	2.42×10^{-1}
LDO/LDFE	3×10^{-5}	8.71×10^{-1}	1.17×10^{-1}
Galerkin/QR	3×10^{-4}	6.37×10^{-1}	1.92×10^{-1}
LDFE/QR	3×10^{-5}	2.67×10^{-1}	5.05×10^{-2}

Noting the potential performance of the LDO quadrature sets in the FW-CADIS context and having observed fairly good agreement between the LDO forward flux result and the QR forward flux result, we will further pursue solutions of the LDO equations as input for Monte Carlo variance reduction parameter generation for the DLVN problem.

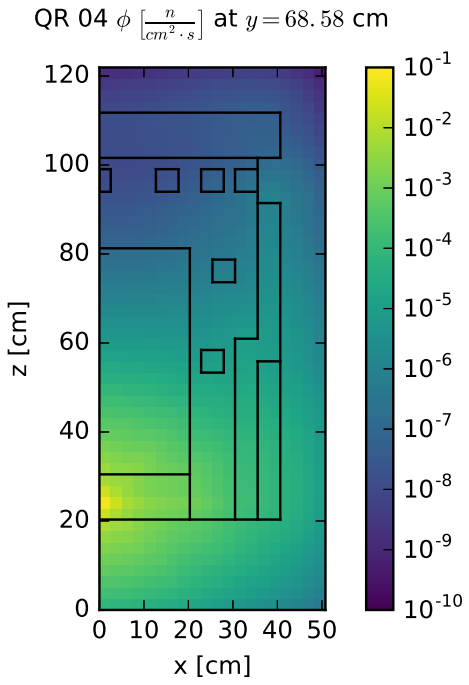

(a) QR forward flux slice.

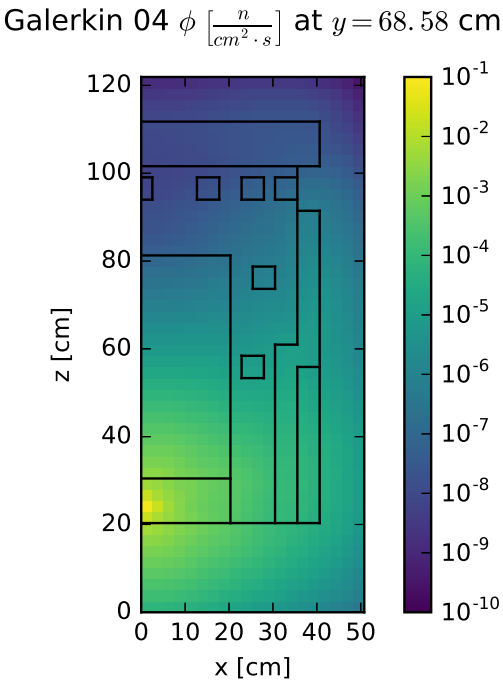

(b) Galerkin forward flux slice.

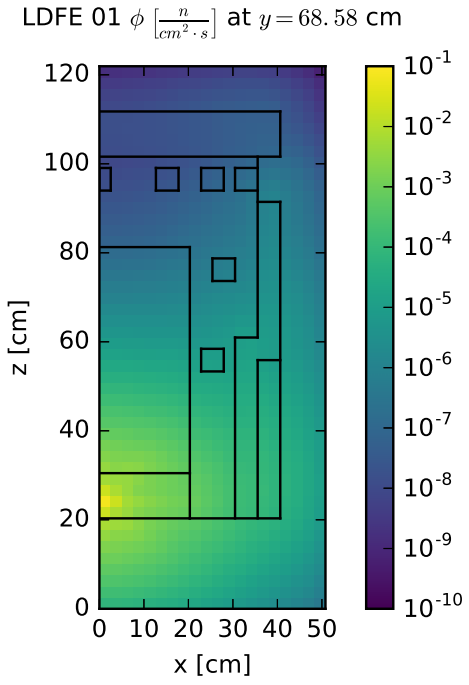

(c) LDFE forward flux slice.

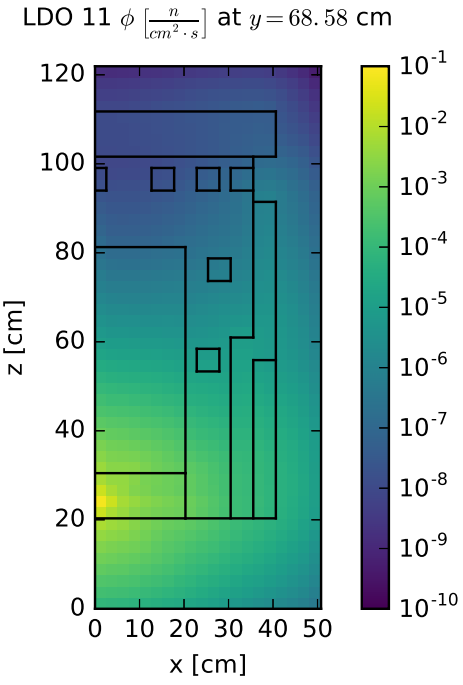

(d) LDO forward flux slice.

Figure 4.7: DLVN benchmark forward scalar flux slices.

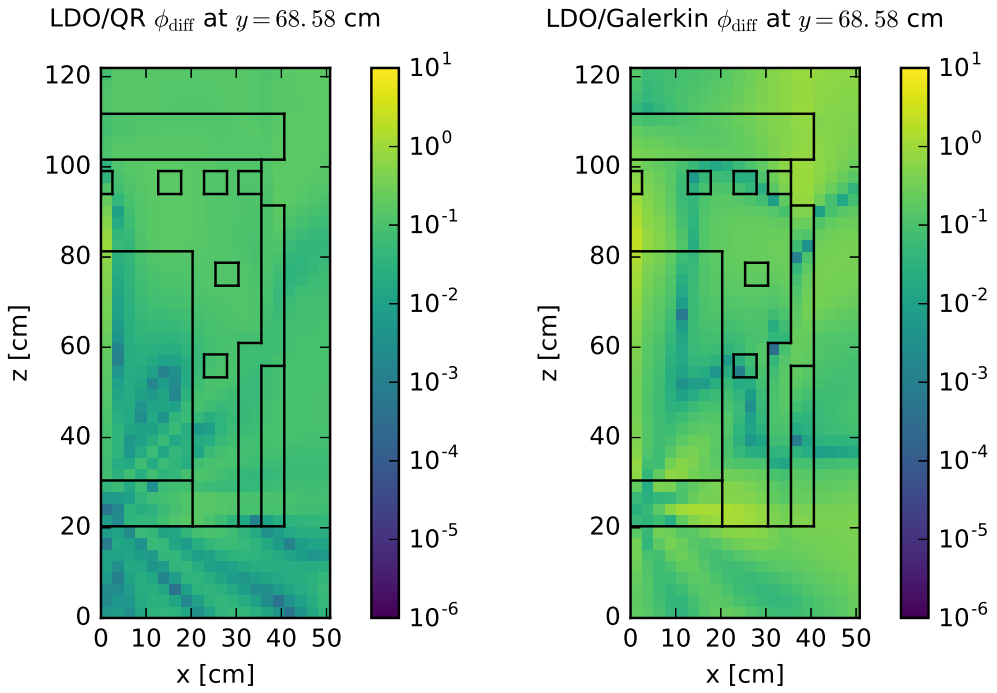

(a) LDO/QR flux rel. diff.

(b) LDO/Galerkin flux rel. diff.

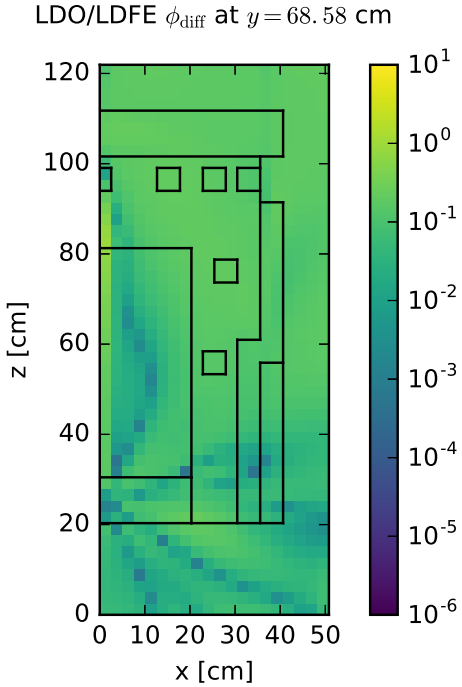

(c) LDO/LDFE flux rel. diff.

Figure 4.8: DLVN benchmark forward scalar flux relative difference slices.

4.2.4 Ispra Sodium Benchmark

For this test case, the representative LDO quadrature set is of order 9 and has 100 total angles (as opposed to the LDO set of order 11 used for the other cases). Of the LDO quadrature orders listed in Table 4.2, only the smallest four quadrature sets (orders 3, 5, 8, and 9) were available for use with the given test case and computational hardware configuration. Recalling the discussion in Chapter 3, we will point out that, when solving the LDO equations, the angular flux coefficient solution vector scales as the number of discrete angles used in the simulation. This solution vector exists for every energy group in every spatial cell and this particular test case used over 3 million spatial cells. So, the use of the larger LDO quadrature sets was not possible given the parameters listed above in Section 4.1.5.1 because the memory requirement exceeded what was available.

Figure 4.9 shows flux slice plots for each representative quadrature set with outlines of the neutron source, the sodium apparatus boundaries, and the detector locations in the experimental configuration. All plots are at the problem midplane of $y = 0$ cm. Ray effects are particularly apparent in all of the flux slices. Although the particle source is a volume rather than a point, the geometry of the source volume creates the anisotropies observed in the solutions. Additionally, the volume of the source is comparatively small relative to the overall scenario geometry, so we see ray effects on this larger scale.

Let us again look at the differences between the representative LDO flux and the three other quadrature types. As with the previous test cases, the flux difference is calculated using Equation 4.1. Like the DLVN test case, Figure 4.10 shows numerous ray effects. The ray effects are likely exacerbated by the use of a coarser LDO quadrature set, but the primary cause is most likely the anisotropic disk source. Like the preceding two test cases, the worst match is between the LDO and Galerkin results. Here, the comparisons of the LDO flux solution with the QR and LDFE flux solutions look fairly similar, with the areas of best agreement located in the sodium container and the regions of greatest discrepancy located along rays far from the neutron source disk.

As this test case scenario is an actual experimental benchmark, it is pertinent to compare the results of the simulations performed in this work against the experimental data listed in the benchmark. Keeping in mind that this work aims to compare the calculations using LDO quadrature sets with calculations using standard quadrature sets, we present a simplified analysis and comparison here to gauge the representative LDO quadrature set among the representative standard quadrature sets. For each detector location in the sodium block, the absolute saturation activity of the ^{32}S(n,p)^{32}P reaction was measured experimentally using sulfur detectors. The listed activity values are normalized for varying detector mass such that the activities are listed in becquerels per gram [37].

To compare the scalar flux output resultant from the Exnihilo calculations with the absolute saturation activity values listed in the experimental benchmark, we use the flux values to calculate a reaction rate density [1] comparable with the listed activity values:

$$A = N\sigma\phi, \tag{4.2}$$

where A is the specific activity in becquerels per gram, N is the number density of the sulfur detectors in atoms per gram, σ is the cross section of the ^{32}S(n,p)^{32}P reaction in cm^2, and ϕ is the scalar flux at the detector location in neutrons per cm^2 per second. For these calculations, we have used the values of $N = 0.0188\times10^{24}$ atoms per gram of sulfur [32] and an average cross section value of $\sigma = 6.5\times10^{-26}$ cm^2 [38]. Additionally, since the neutron source strength is normalized to unity in Exnihilo, the flux values were multiplied by a factor of 1.948×10^{11}, the calculated number of source neutrons per second exiting the source disk in the direction of the detectors [32]. The ^{32}S(n,p)^{32}P reaction has a threshold of 2.7 MeV [37], so the scalar flux values used in these calculations are those corresponding to the two highest energy groups in the 27n19g library. Results are listed in Table 4.7 with detector #1 located closest to the neutron source and detector #7 located farthest from the source.

Table 4.7: Ispra sodium benchmark experimental and simulated detector activities [Bq/g].

	Det. #1	Det. #2	Det. #3	Det. #4	Det. #5	Det. #6	Det. #7
Exp. Act.	3.237×10^{4}	1.971×10^{3}	1.036×10^{2}	6.270×10^{0}	4.200×10^{-1}	3.030×10^{-2}	1.990×10^{-3}
Exp. Err.	5.7%	5.7%	5.7%	6.0%	6.0%	6.0%	15.0%
QR	2.472×10^{4}	7.474×10^{2}	6.507×10^{1}	3.142×10^{0}	8.114×10^{-2}	4.152×10^{-3}	2.446×10^{-4}
Galerkin	2.435×10^{4}	6.702×10^{2}	4.460×10^{1}	1.870×10^{0}	3.969×10^{-2}	1.665×10^{-3}	7.228×10^{-5}
LDFE	2.463×10^{4}	7.071×10^{2}	6.031×10^{1}	2.787×10^{0}	6.862×10^{-2}	3.395×10^{-3}	1.953×10^{-4}
LDO	2.471×10^{4}	7.446×10^{2}	6.512×10^{1}	3.087×10^{0}	7.796×10^{-2}	3.926×10^{-3}	2.255×10^{-4}

It is apparent that the activities calculated using the scalar flux values from Exnihilo do not match those determined experimentally; this is likely due to the simplifications made in the activity calculations using the simulations' scalar flux output. That is, using a finer energy group structure and more sophisticated cross section values would produce detector activities closer to those determined experimentally. However, the values arrived at here are still instructive in analyzing overall physical trends and useful for comparing the LDO quadrature set against the standard quadrature sets.

Table 4.8 lists the ratios of the deterministic activity calculations to the experimental values to explore the behavior of the different quadrature types. For each detector location, the ratio closest to unity is emphasized. It is immediately apparent that the QR scalar flux values are the most closely matching for all detector locations except Detector #3, where the LDO scalar flux value is the closest. Even so, for all detector locations, the LDO ratio value is closer to the QR ratio value than are either the LDFE or Galerkin ratios.

Table 4.8: Ispra sodium benchmark experimental and simulated detector activity ratios.

	Det. #1	Det. #2	Det. #3	Det. #4	Det. #5	Det. #6	Det. #7
QR	**0.764**	**0.379**	0.628	**0.501**	**0.193**	**0.137**	**0.123**
Galerkin	0.752	0.340	0.431	0.298	0.095	0.055	0.036
LDFE	0.761	0.359	0.582	0.445	0.163	0.112	0.098
LDO	0.763	0.378	**0.629**	0.492	0.186	0.130	0.113

Like the experimental activities, the activities calculated with the deterministic scalar flux values decrease logarithmically as the distance from the source increases. For all of the quadrature types, the calculated activities decrease more quickly than the experimental results. Detectors 2, 3, 5, 6, and 7 all see the deterministically calculated activities at one order of magnitude lower than the respective experimental activities (except for the case of the Galerkin quadrature result at detector 7 which is two orders of magnitude below the experimental activity). One possible reason for these discrepancies is the presence of iron in the structure of the benchmark assembly. As we will discuss more in depth in Section 4.3.1, it is not unexpected that deterministically calculated results in the presence of iron are lower than those seen experimentally.

Table 4.9 lists the extreme and average values of the forward flux solution relative differences shown in Figure 4.10 as well as comparisons of the QR flux solution against those of the Galerkin and LDFE flux solutions. On average, all of the flux solutions show poor agreement, with the best match being a 26% difference between the LDO and LDFE forward flux solutions.

Table 4.9: Ispra sodium benchmark forward flux extremal and average relative differences.

Comparison	**Min. Diff.**	**Max. Diff.**	**Avg. Diff.**
LDO/QR	2×10^{-6}	2.78×10^{1}	5.00×10^{-1}
LDO/Galerkin	8×10^{-6}	2.38×10^{4}	6.57×10^{1}
LDO/LDFE	1×10^{-6}	7.75×10^{0}	2.61×10^{-1}
Galerkin/QR	3×10^{-6}	1.16×10^{0}	4.24×10^{-1}
LDFE/QR	7×10^{-6}	2.29×10^{1}	7.59×10^{-1}

For all of the detector locations, we see in Table 4.7 that the activity calculated with the representative LDO quadrature set demonstrates good agreement with the QR quadrature set. The LDO results in this table match the QR results more closely than do the Galerkin and LDFE results and, of the standard quadrature set results, the LDO results are closest to QR results. We find the LDO results' proximity to the QR results sufficient justification to pursue the exploration of Monte Carlo variance reduction parameter generation using the LDO equations for this test case.

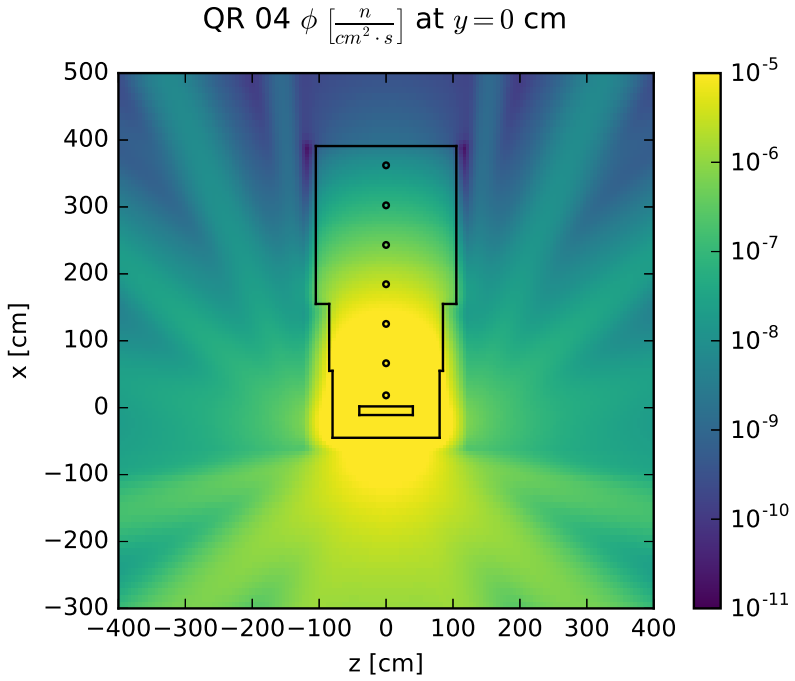

(a) QR forward flux slice.

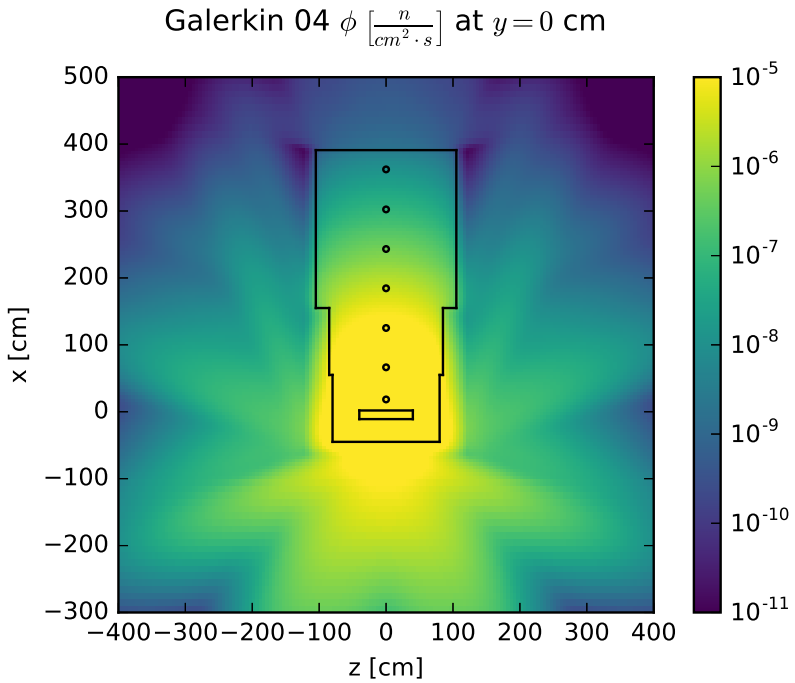

(b) Galerkin forward flux slice.

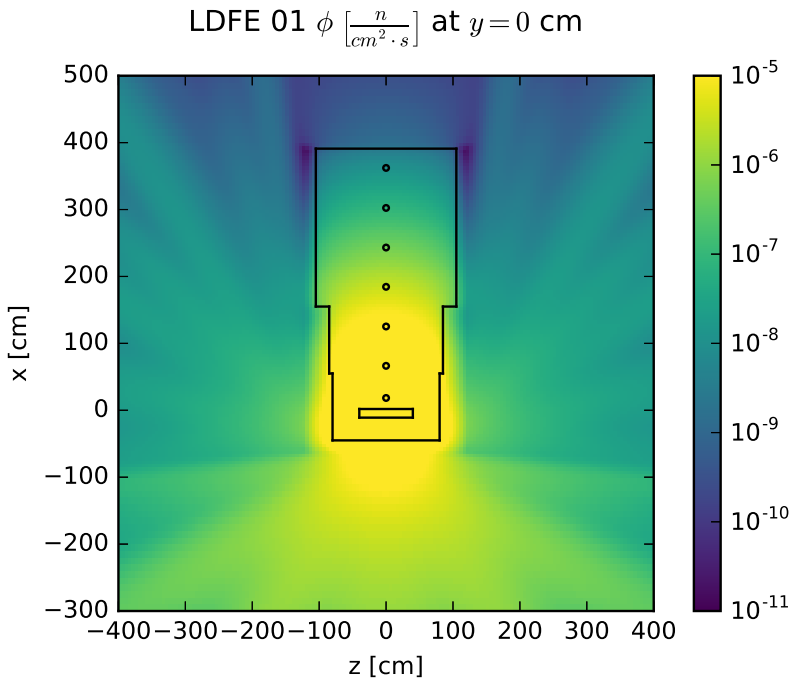

(c) LDFE forward flux slice.

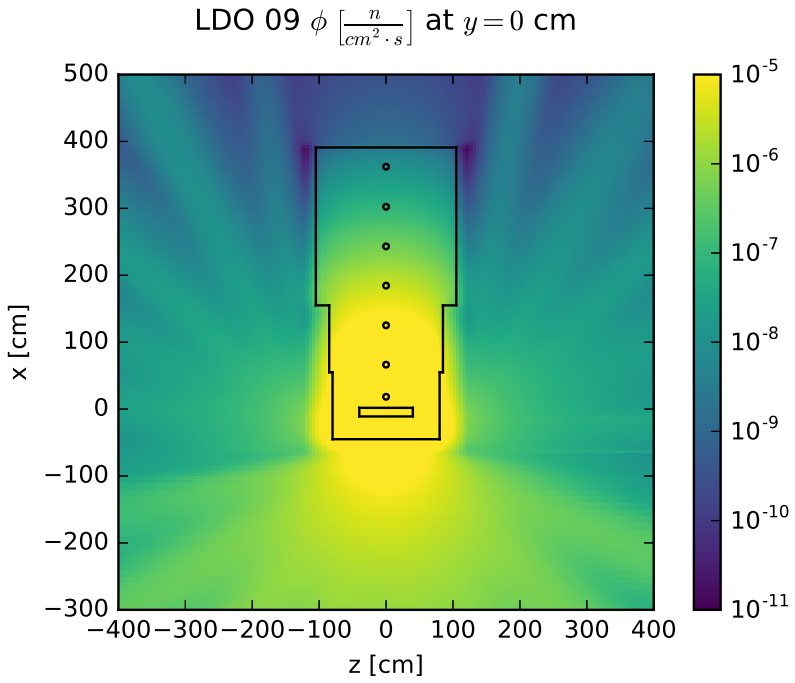

(d) LDO forward flux slice.

Figure 4.9: Ispra sodium benchmark forward scalar flux slices.

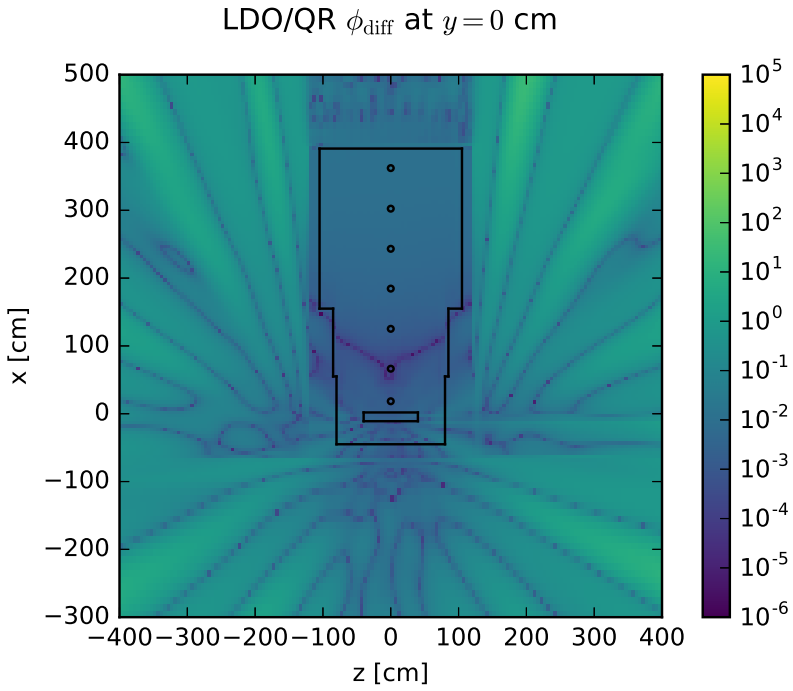

(a) LDO/QR flux relative difference.

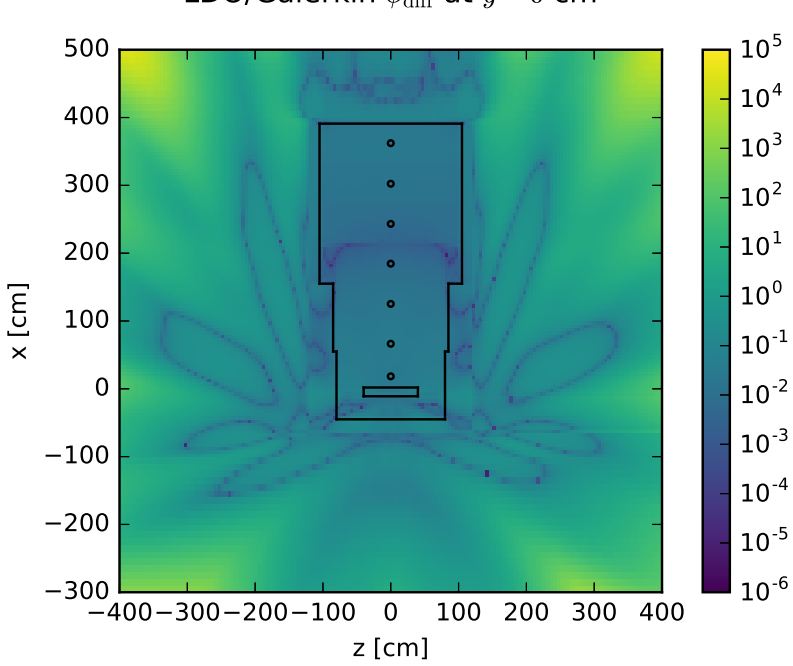

(b) LDO/Galerkin flux relative difference.

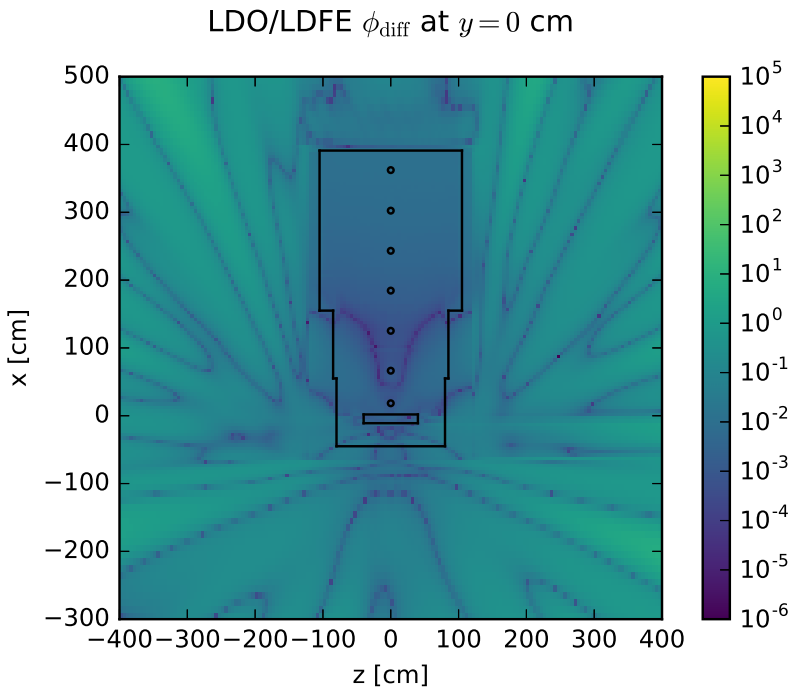

(c) LDO/LDFE flux relative difference.

Figure 4.10: Ispra sodium benchmark forward scalar flux relative difference slices.

4.2.5 Simplified Portal Monitor

Lastly, we look at the simplified portal monitor problem with the small photon source. Of the test cases presented here, the forward solutions differ most greatly for this problem. Figure 4.11 shows forward scalar flux solutions for the representative quadrature sets with the material pallets, detector array, and shipping container outlines overlaid on the plots. Flux slices are plotted at the midplane of $z = 243.84$ cm (96 inches). All of the flux solutions display ray effects as a result of the streaming paths created by the material variation of the pallets inside of the shipping container.

As with the previous test cases, we look at the differences between the representative LDO flux and the three other quadrature types. Figure 4.12 shows flux differences similar to the difference plots for the Ispra sodium benchmark problem; that is, the differences largely appear as ray effects. This is unsurprising given the combination of the small volume of the photon source in the problem and the inherent difficulty of accurately simulating particle streaming in deterministic calculations. Again we see that the LDO scalar flux solution exhibits strong disagreement with the Galerkin scalar flux solution. The LDO/QR and LDO/LDFE comparison plots show discrepancies of similar orders of magnitude and all of

the relative difference plots exhibit the greatest difference along the $y-z$ plane streaming pathway located in the center of the shipping container.

Table 4.10 lists the minimum, maximum, and average values of the relative differences in the forward scalar flux solutions, shown in Figure 4.12. As with all of the previous cases, comparisons between the QR flux solution and the Galerkin and LDFE flux solutions are included for reference. None of the flux solutions in this case show particularly good agreement on average; the closest solutions are the LDFE and QR flux solutions which have an average difference of about 24%. Of the three standard quadrature types, the LDO forward flux solution matches the QR forward flux solution most closely.

Table 4.10: Portal monitor forward scalar flux extremal and average relative differences.

Comparison	**Min. Diff.**	**Max. Diff.**	**Avg. Diff.**
LDO/QR	1×10^{-6}	1.43×10^{2}	3.07×10^{-1}
LDO/Galerkin	7×10^{-5}	1.22×10^{2}	1.96×10^{0}
LDO/LDFE	6×10^{-5}	1.53×10^{2}	3.33×10^{-1}
Galerkin/QR	4×10^{-5}	2.47×10^{0}	3.93×10^{-1}
LDFE/QR	2×10^{-5}	2.09×10^{0}	2.38×10^{-1}

Given the localized small volumetric particle source used in the problem in combination with the streaming pathways created by the scenario's material and geometry configuration, it is unsurprising that the forward flux solutions generated with the various representative quadrature sets show only fair agreement. Still, in the interest of exploring the LDO quadratures' solutions for Monte Carlo variance reduction parameter generation for this problem transporting photons, we will compare the results of the different quadrature sets in the CADIS and FW-CADIS contexts.

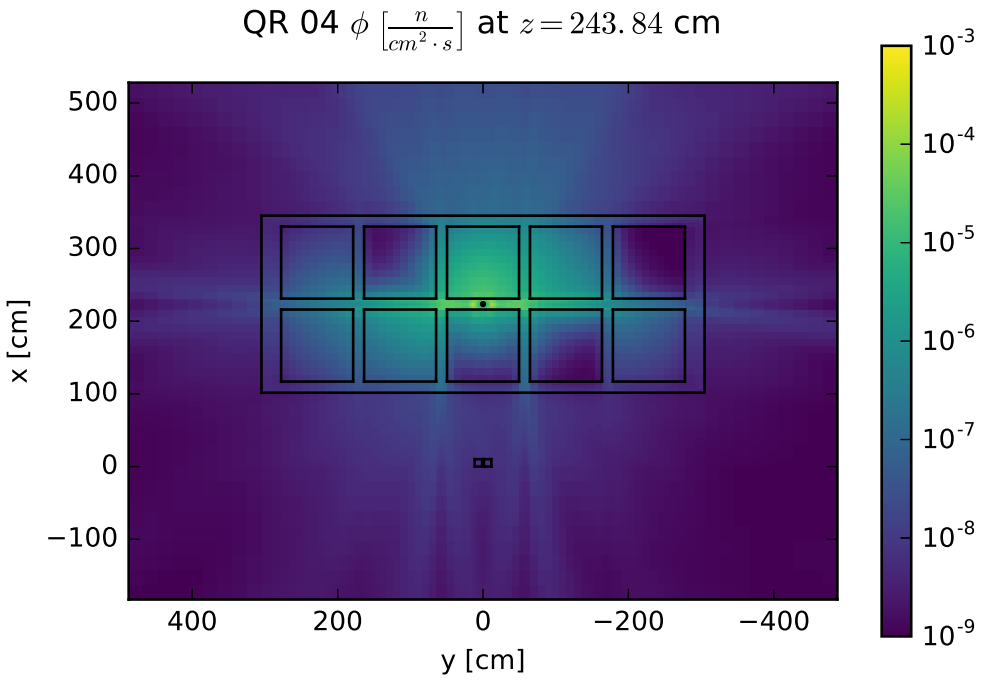

(a) QR forward flux slice.

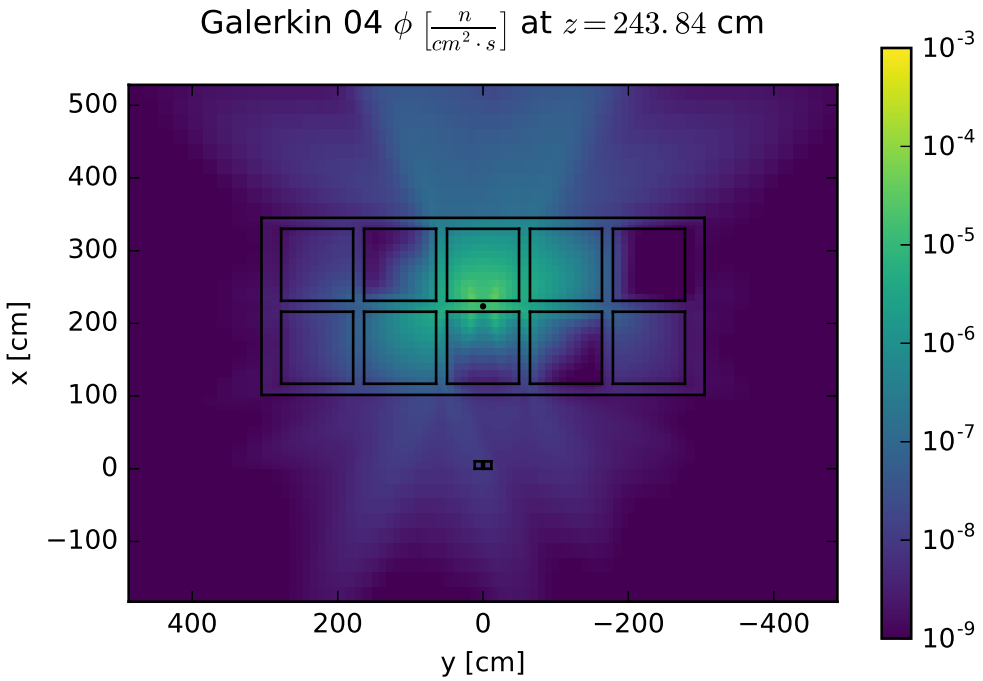

(b) Galerkin forward flux slice.

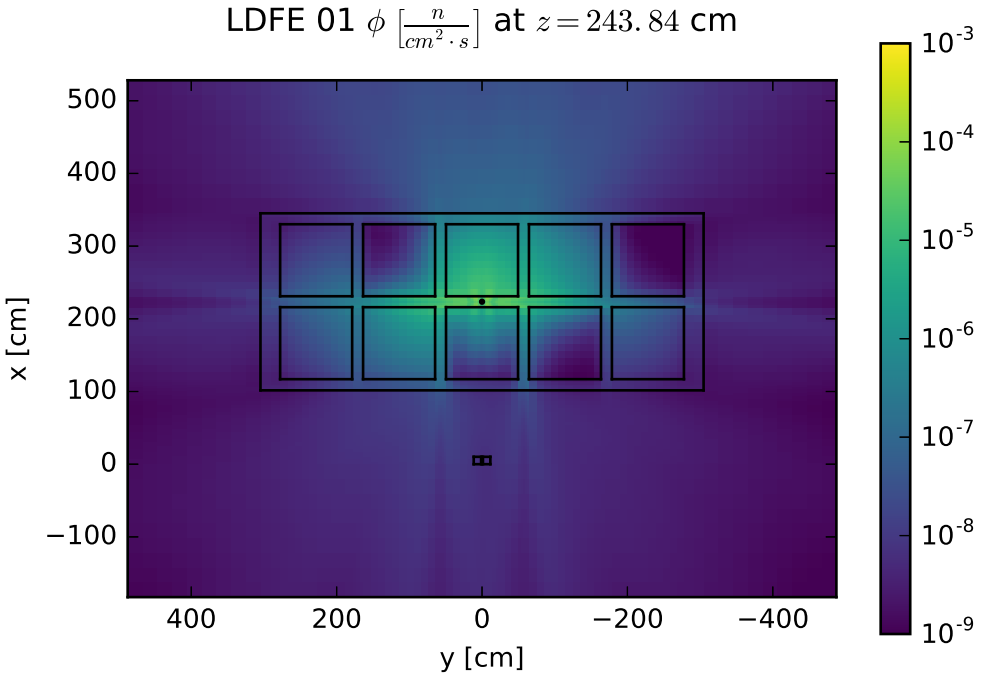

(c) LDFE forward flux slice.

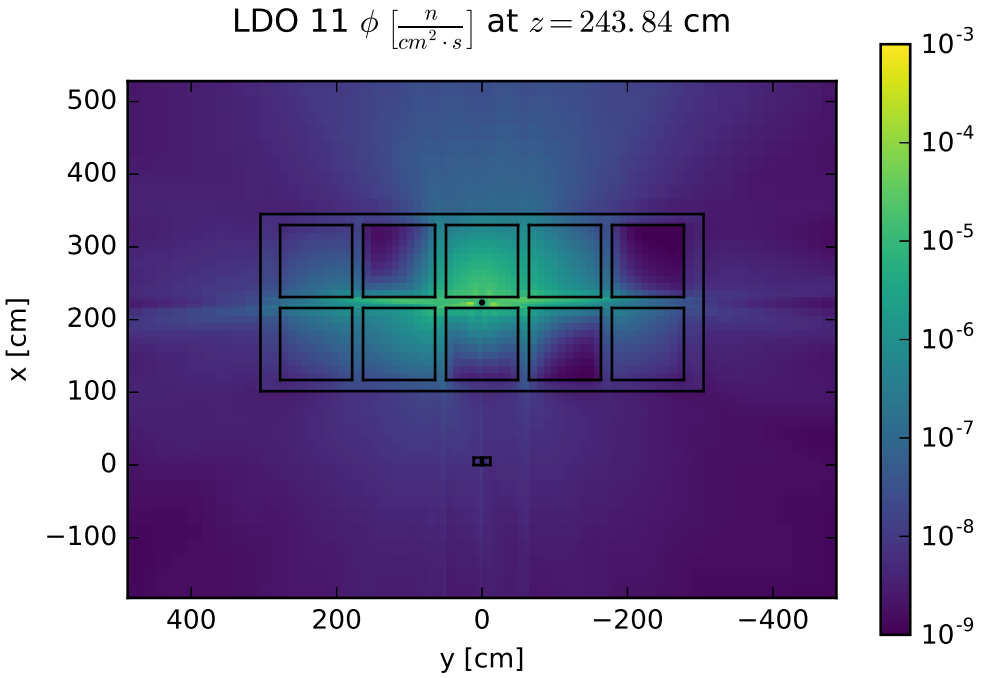

(d) LDO forward flux slice.

Figure 4.11: Simplified portal monitor scenario forward scalar flux slices.

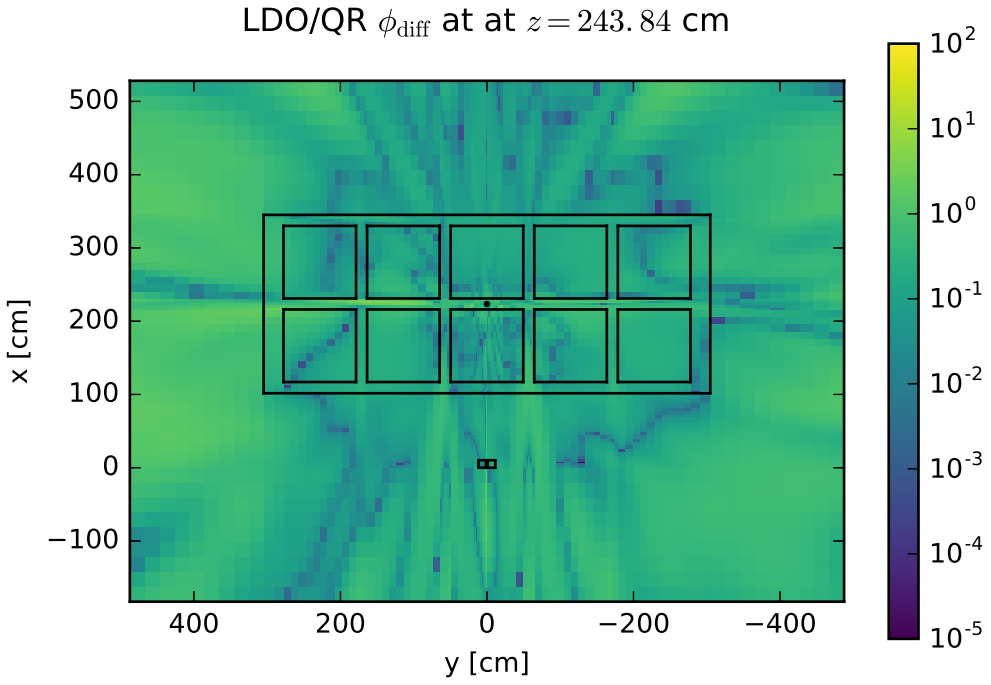

(a) LDO/QR flux relative difference.

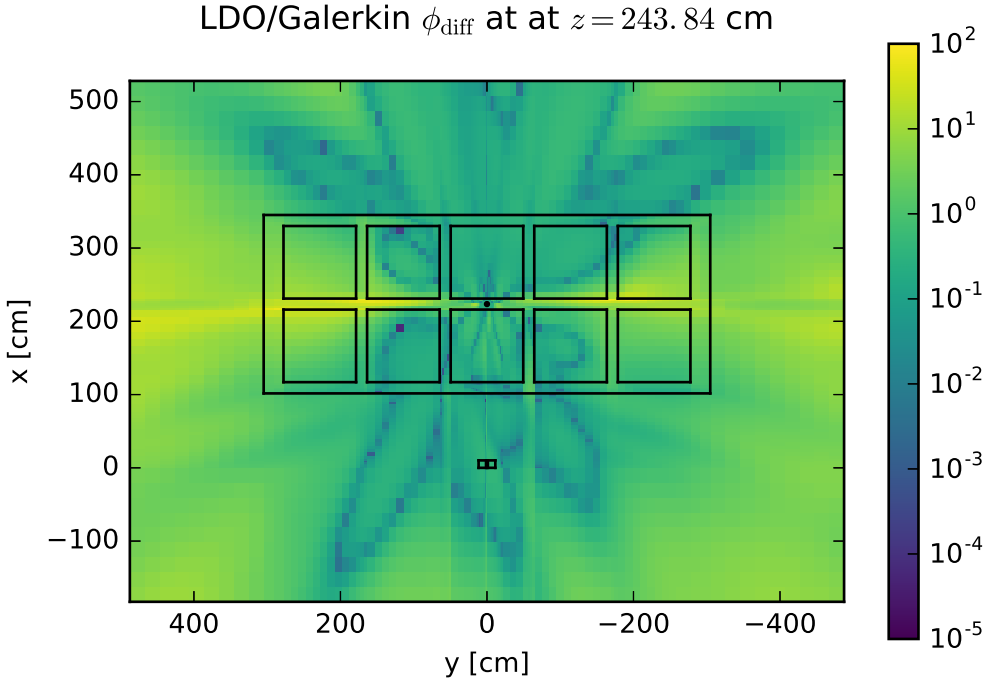

(b) LDO/Galerkin flux relative difference.

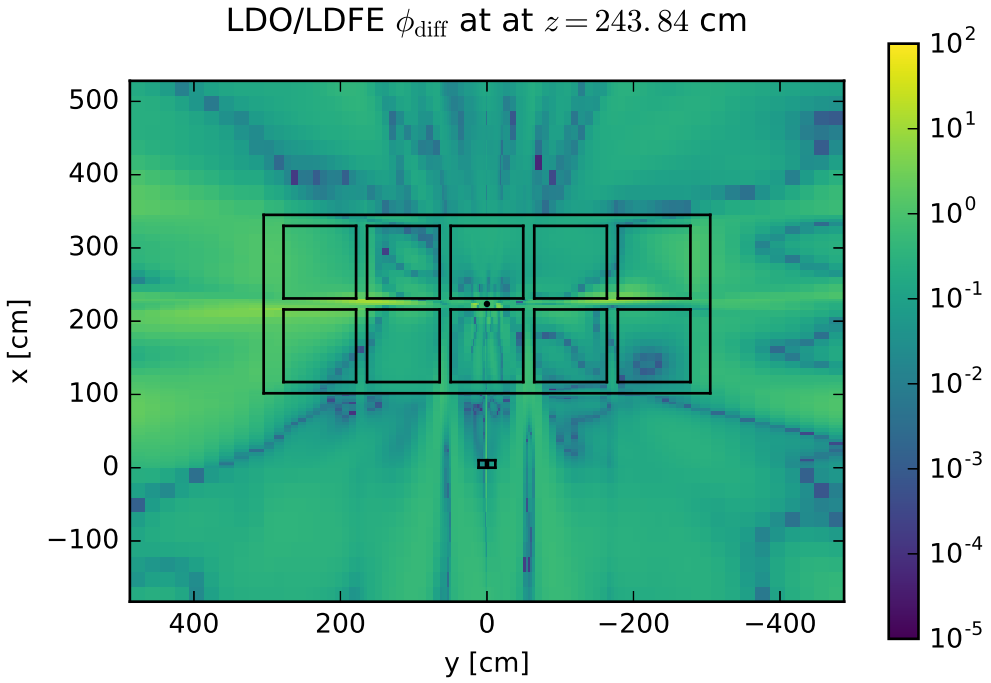

(c) LDO/LDFE flux relative difference.

Figure 4.12: Simplified portal monitor scenario forward scalar flux relative difference slices.

4.2.6 Summary

For the test cases here, we have compared the forward scalar flux solutions resultant from solving the LDO equations against those arising from solving the traditional discrete ordinates equations with a small variety of standard quadrature set types. Particular attention was paid to the comparison of the LDO results with the QR results, as QR quadrature sets are commonly used in Monte Carlo variance reduction parameter generation and the larger goal of this work is to assess the efficacy of the LDO equations' solutions in Monte Carlo variance reduction parameter generation. In each test case, the results from solving the LDO equations best matched those from using the QR quadrature set in the traditional discrete ordinates formulation. Additionally, for the two benchmark test cases, the LDO equations produced results that were commensurate to those of all standard quadrature sets when the deterministic results were compared against experimental values.

4.3 CADIS Calculations

Having found that the LDO equations' forward scalar flux solutions are comparable to those of standard quadrature sets, we move on to test the various quadrature sets' performance for

Monte Carlo variance reduction parameter generation. We begin by looking at the test case scenarios in the context of the CADIS method, described in Section 2.2.1.1. Since the CADIS method uses the deterministic adjoint scalar flux solution to generate Monte Carlo variance reduction parameters, it is pertinent to first examine the deterministic adjoint scalar flux solutions for each of the representative quadrature sets for each test case. Then, we move on to the Monte Carlo results to examine the different quadrature types' efficacy in Monte Carlo variance reduction.

4.3.1 Steel Plate in Water

For the CADIS calculations for the steel plate embedded in water, the adjoint source was set to be the detector tally. Figure 4.13 shows the deterministically calculated adjoint scalar flux solutions for the representative quadrature sets. As expected, the flux is highest at the detector location and decreases logarithmically moving backwards along the $z-$axis. From there, we also examine the relative differences between the LDO solution and those from the standard quadrature sets. Results are shown in Figure 4.14 with extremal and average values listed in Table 4.11. As seen previously, the LDO solution matches the QR solution better than it matches the Galerkin or LDFE solutions. In this case, the LDFE solution has a lower maximum relative difference compared to the QR solution than does the LDO solution, but we see that the LDO solution matches the QR solution more closely than does the LDFE solution on average (4.1% difference versus 12.5% difference).

Table 4.11: Steel plate CADIS adjoint scalar flux extremal and average relative differences.

Comparison	**Min. Diff.**	**Max. Diff.**	**Avg. Diff.**
LDO/QR	3×10^{-5}	4.54×10^{-1}	4.13×10^{-2}
LDO/Galerkin	1×10^{-3}	3.50×10^{1}	3.27×10^{0}
LDO/LDFE	5×10^{-5}	6.96×10^{-1}	1.14×10^{-1}
Galerkin/QR	4×10^{-4}	9.71×10^{-1}	4.60×10^{-1}
LDFE/QR	7×10^{-5}	4.26×10^{-1}	1.25×10^{-1}

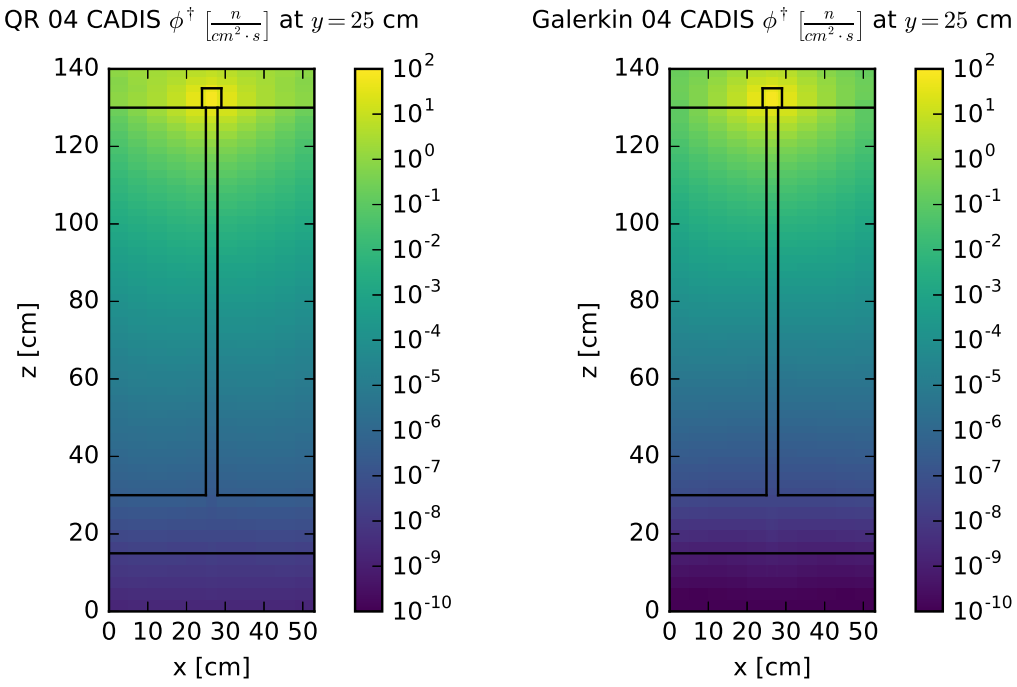

(a) QR adjoint flux slice.

(b) Galerkin adjoint flux slice.

(c) LDFE adjoint flux slice.

(d) LDO adjoint flux slice.

Figure 4.13: Steel plate adjoint scalar flux slices for the CADIS method.

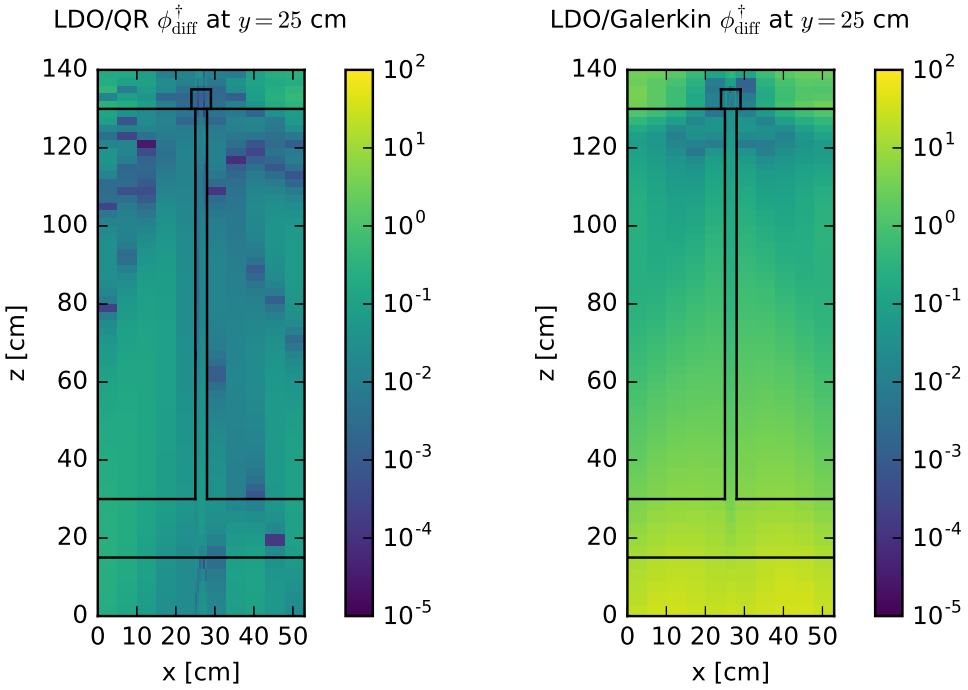

(a) LDO/QR flux rel. diff.

(b) LDO/Galerkin flux rel. diff.

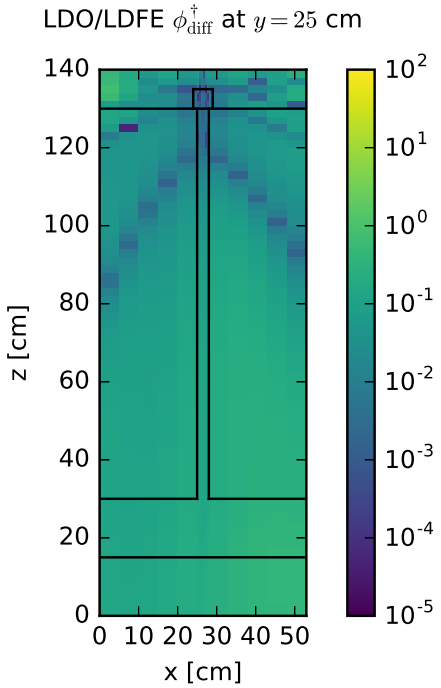

(c) LDO/LDFE flux rel. diff.

Figure 4.14: Steel plate adjoint scalar flux relative difference slices for the CADIS method.

Following this, we examine the Monte Carlo results; recall that 1×10^9 neutron histories were used in these calculations. Figure 4.15 shows the MCNP-reported flux tally for the detector at the end of the steel plate for each angular mesh refinement for each quadrature type. We note that the Monte Carlo runs with biasing parameters from the Galerkin quadrature set of order 2 and the LDO quadrature set of order 5 were not able to finish in a timely manner for the hardware configuration used in this work, so Monte Carlo results for those two data points are not included here. The flux tally results are plotted as a function of angular mesh refinement to observe the impact of angular mesh refinement on flux tally solution for the different quadrature types. Figure 4.15 also includes the flux tally value for an unbiased Monte Carlo calculation as a reference point of comparison; it is shown as a horizontal black line with dashed lines on either side indicating the one standard deviation confidence interval.

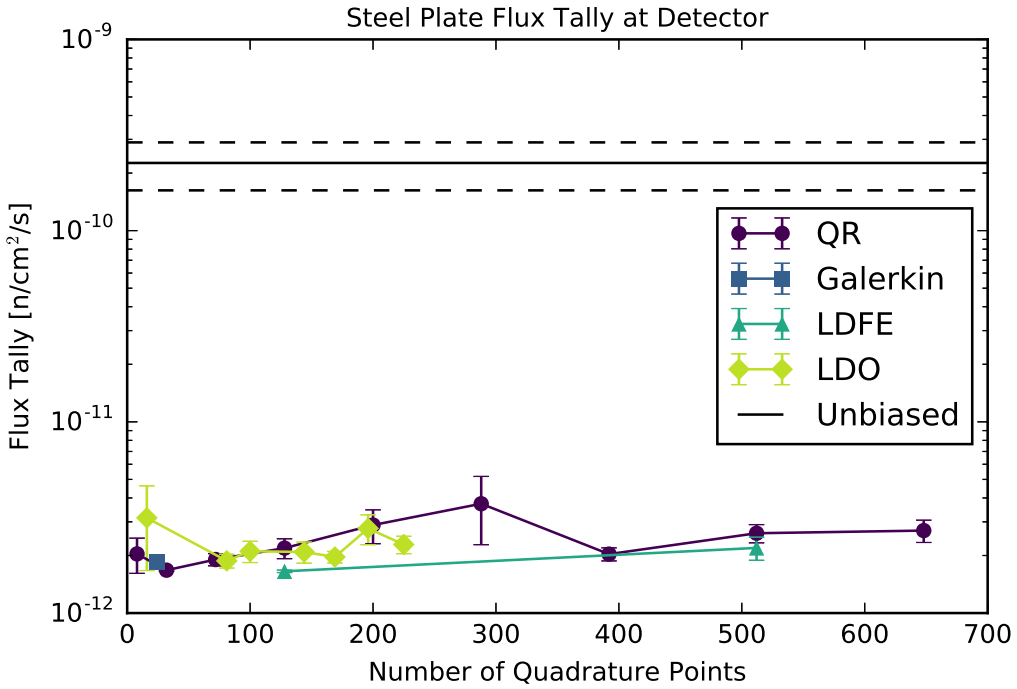

Figure 4.15: MCNP-reported flux tally values at the end of the steel plate.

All of the biased results tend towards a tally calculation on the order of 10^{-12}, while the unbiased tally calculation is on the order of 10^{-10}. We will pause here to explore one reason behind this discrepancy. Figure 4.16 shows the MCNP-reported flux tally broken down into energy bins with boundaries set to those of the 27n19g library. In this plot, only tallies corresponding to calculations using biasing parameters from the four representative quadrature sets are included. We see an extreme difference in the results from the biased calculations versus the results from the unbiased calculation between neutron energies of 1 keV and 1 MeV.

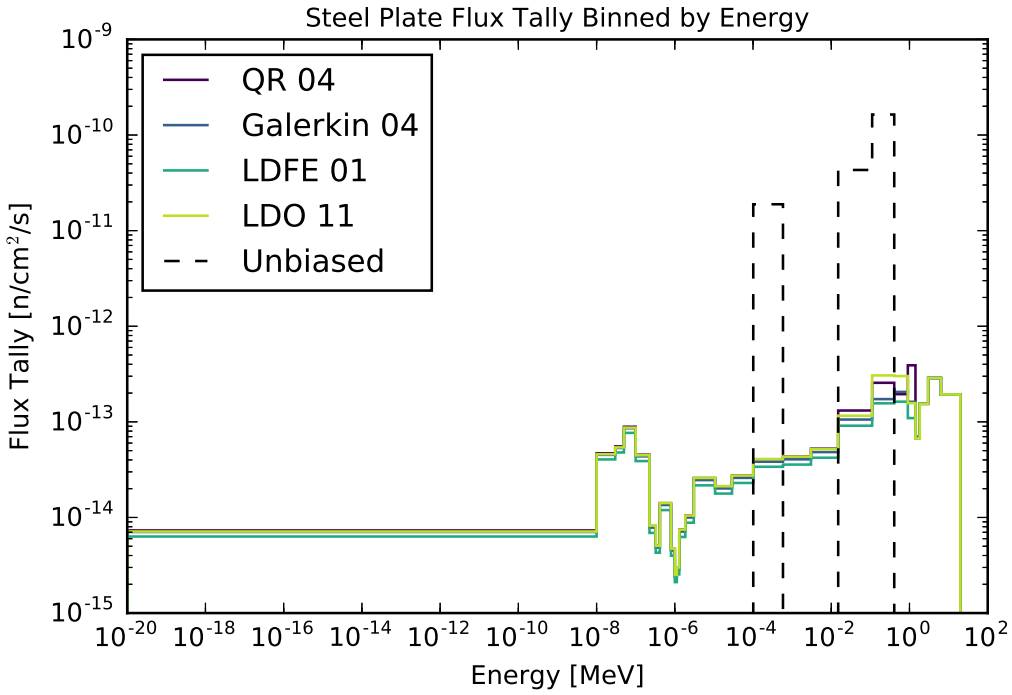

Figure 4.16: Steel plate detector tally broken down by energy bin.

This phenomenon has been previously documented [26] and can be largely attributed to the resonances in the iron cross section, shown in Figure 4.17 with the 27n19g library energy group boundaries overlaid. The unresolved resonance region in the iron cross section spans multiple energy groups, leading to inaccuracies in the discretized multigroup cross section values used in deterministic calculations. To put this directly in the context of the test case scenario at hand, Figure 4.18 shows the detector tally broken down by energy bin overlaid on the iron total cross section. Unsurprisingly, the energy regions of large discrepancy are those in which the iron cross section resonances lie.

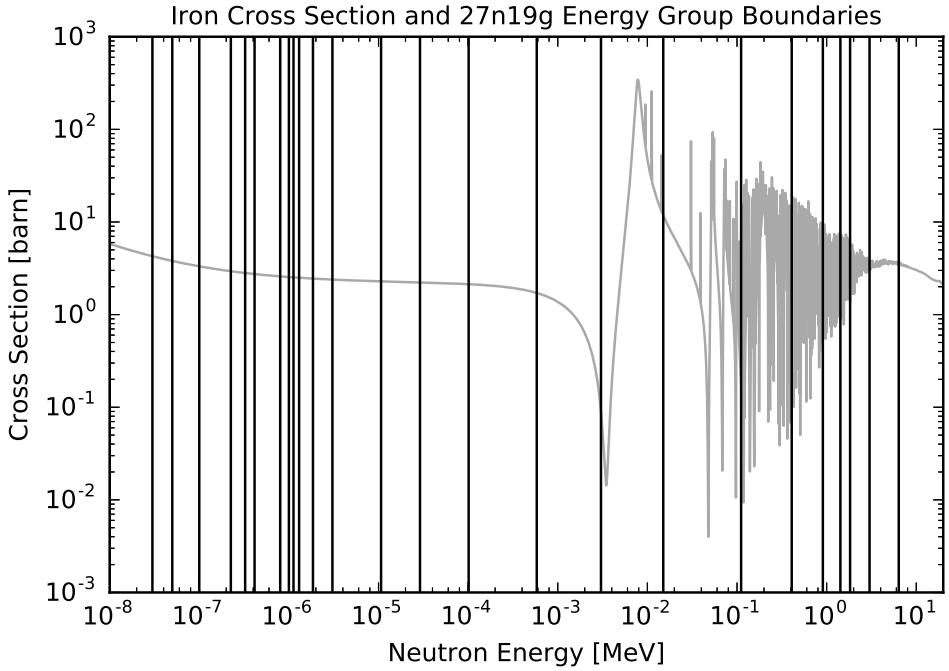

Figure 4.17: ENDF iron total reaction cross section with 27n19g energy group limits [39, 8].

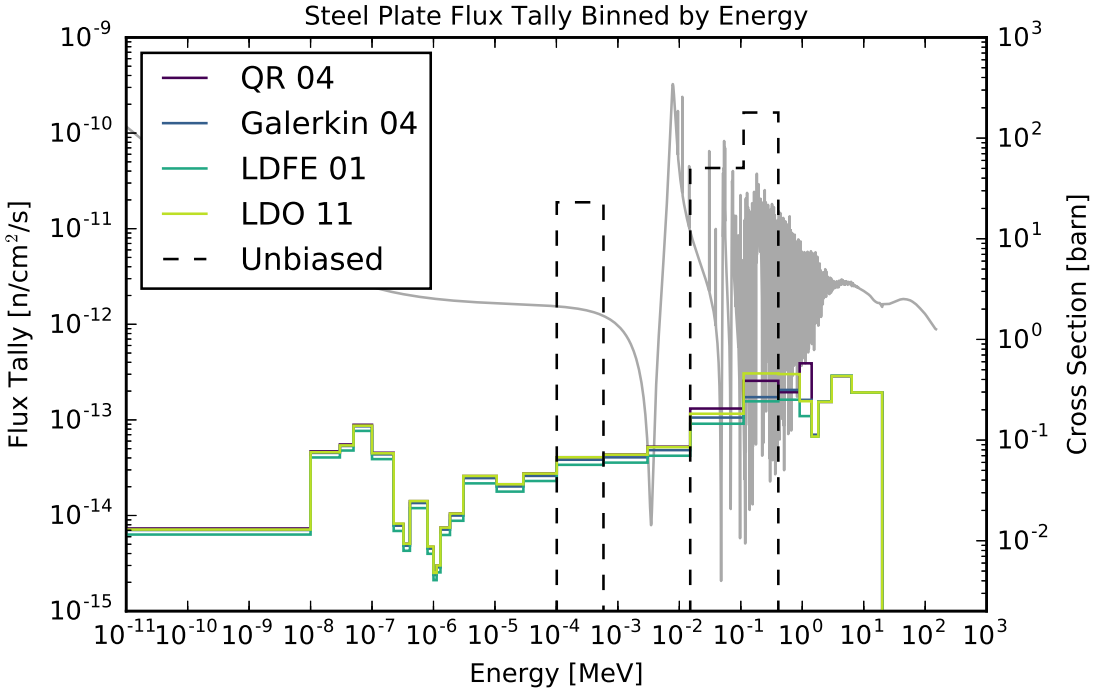

Figure 4.18: Steel plate detector tally broken down by energy bin with iron cross section.

Having explored the discrepancy between the biased and unbiased tally results, we move on to looking at the Figures of Merit for the various Monte Carlo run results. Figure 4.19 shows the reported FOM value for the detector tally for the various quadrature sets and orders. We again plot the results as a function of angular mesh refinement with a black horizontal line denoting the FOM for the unbiased Monte Carlo calculation. The biasing parameters corresponding to the LDFE quadrature set of order 1 result in the highest FOM value while those of the QR set of order 1 result in the lowest FOM value. For all LDO quadrature sets of order 8 and above, the Figures of Merit are one order of magnitude greater than that of the unbiased calculation.

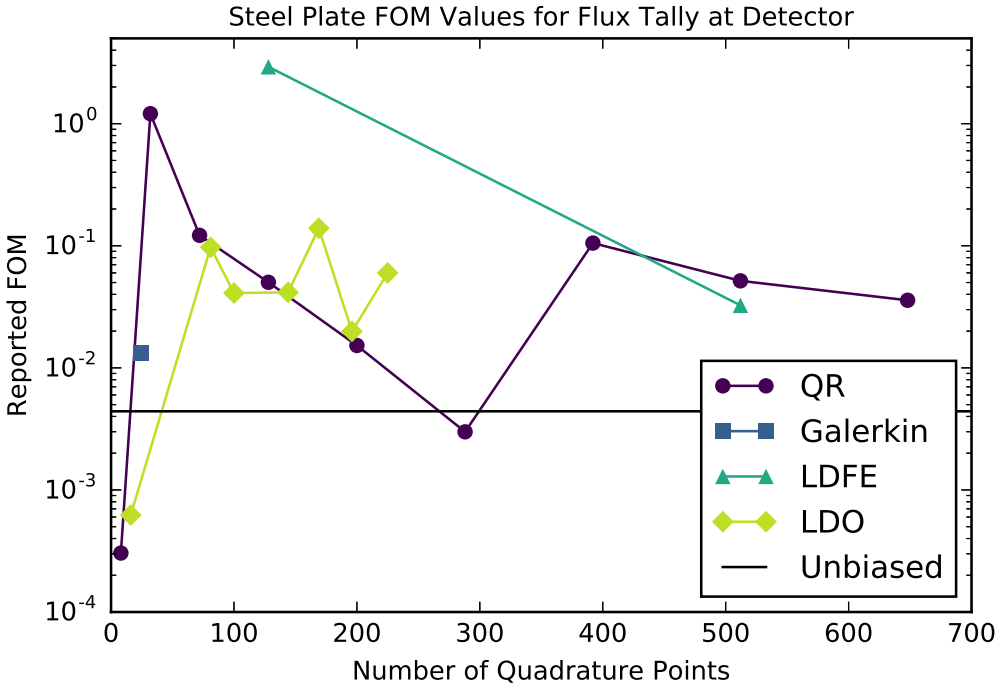

Figure 4.19: FOM values for MCNP flux tally at the end of the steel plate.

To conclude this section, we consider the overall trends in angular mesh refinement in Figures 4.15 and 4.19. It appears that the angular mesh refinement does not have a great impact on the flux tally value in this scenario, as all of the biased tally results fall within the same order of magnitude and do not exhibit any trends as a function of the number of discrete angles used. The Figures of Merit vary somewhat more greatly. Specifically, the LDO biasing parameters appear to gather around FOM values of 0.005 even as the number of discrete angles used is increased. So, for the steel plate in water detector tally in the context of the CADIS method, one could use a relatively low-order (i.e., order 8) LDO quadrature set to generate Monte Carlo biasing parameters that result in a Figure of Merit comparable to (and better than most of, as seen here) those produced by finer angular meshes.

4.3.2 DLVN

To study the DLVN problem in the context of the CADIS method, the adjoint source was set to be the tally located at detector #14 in the original experiment. All of the adjoint scalar flux solutions shown in Figure 4.20 reflect this; the adjoint flux is highest at the specified detector location. The differences in the adjoint scalar flux solutions shown in Figure 4.21 appear as ray effects from the relatively localized source at the detector location as well as in the streaming pathway in the dog-legged void section. Table 4.12 lists the extremal and average values of the relative differences between the LDO and standard quadrature results. Comparisons between the Galerkin and LDFE quadrature sets versus the QR set are also given for reference. On average, the LDO adjoint flux solution agrees best with the QR adjoint flux solution with a difference of approximately 3.8%.

Table 4.12: DLVN CADIS adjoint scalar flux extremal and average relative differences.

Comparison	**Min. Diff.**	**Max. Diff.**	**Avg. Diff.**
LDO/QR	1×10^{-5}	1.24×10^{0}	3.78×10^{-2}
LDO/Galerkin	3×10^{-4}	5.01×10^{0}	3.56×10^{-1}
LDO/LDFE	2×10^{-5}	9.67×10^{-1}	6.04×10^{-2}
Galerkin/QR	6×10^{-1}	7.62×10^{-1}	2.00×10^{-1}
LDFE/QR	2×10^{-5}	3.07×10^{-1}	5.31×10^{-2}

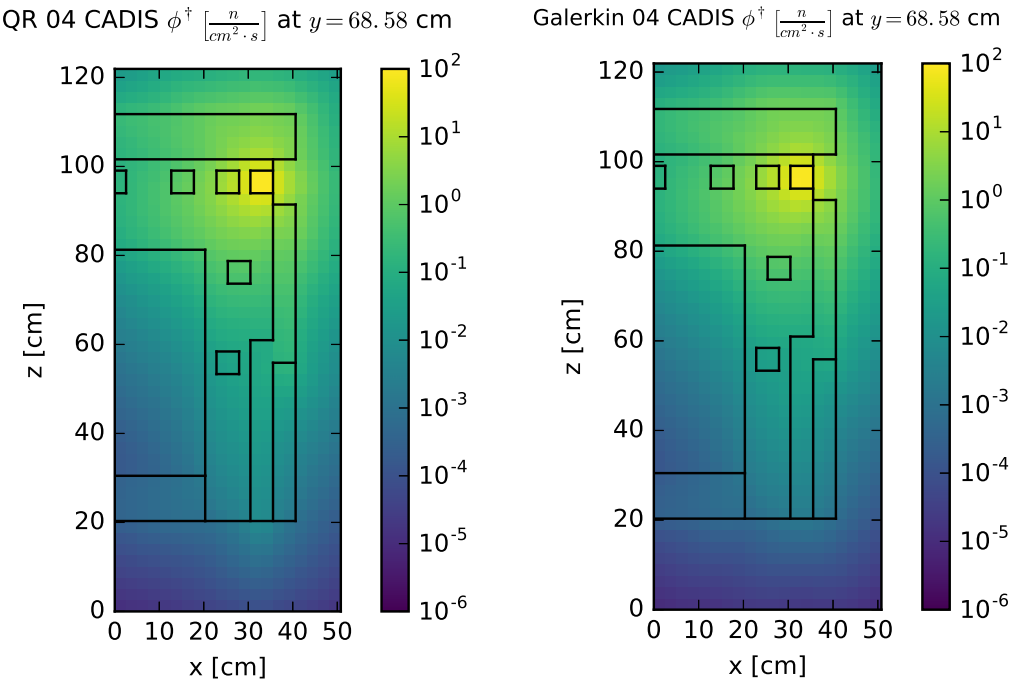

(a) QR adjoint flux slice.

(b) Galerkin adjoint flux slice.

(c) LDFE adjoint flux slice.

(d) LDO adjoint flux slice.

Figure 4.20: DLVN adjoint scalar flux slices for the CADIS method.

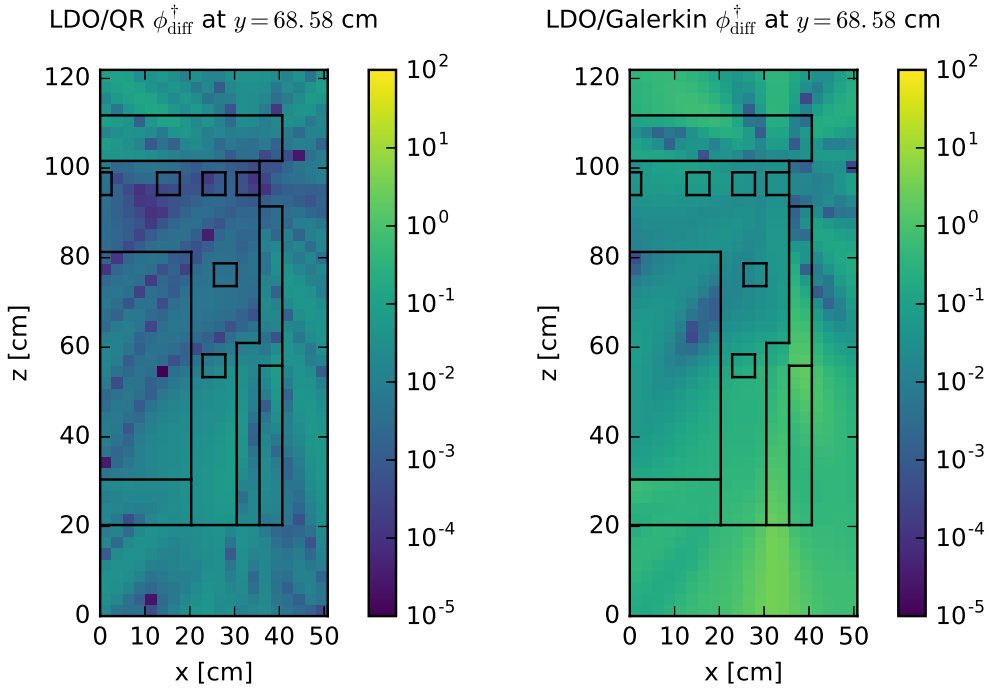

(a) LDO/QR flux rel. diff.

(b) LDO/Galerkin flux rel. diff.

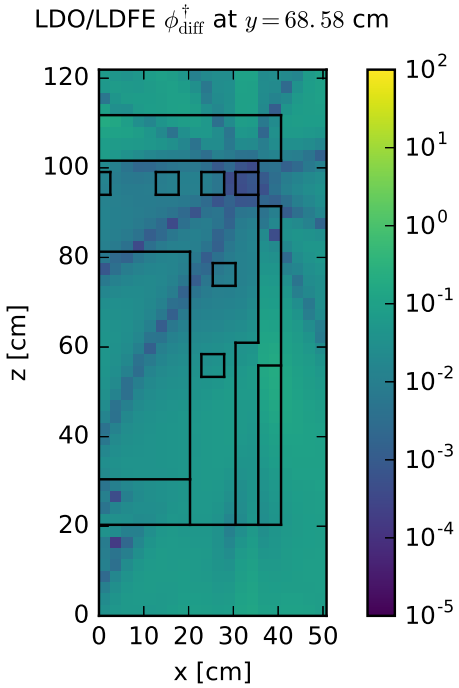

(c) LDO/LDFE flux rel. diff.

Figure 4.21: DLVN adjoint scalar flux relative difference slices for the CADIS method.

Moving forward, we look at the Monte Carlo results. For the DLVN case, $1{\times}10^{10}$ neutron histories were simulated. Since the CADIS method is for one local adjoint source, which we have set to detector #14 here, the discussion in this section will focus on the results for this specific detector location. Figure 4.22 shows the MCNP-reported tally for the forward scalar flux at the location of detector #14. Here we see that all of the biased calculation values fall within the error of the unbiased result. However, all of these tally calculations (biased and unbiased) do not match the experimentally calculated flux value of $2.74{\times}10^{-7}$ ± 5% n/cm^2/s at detector #14.

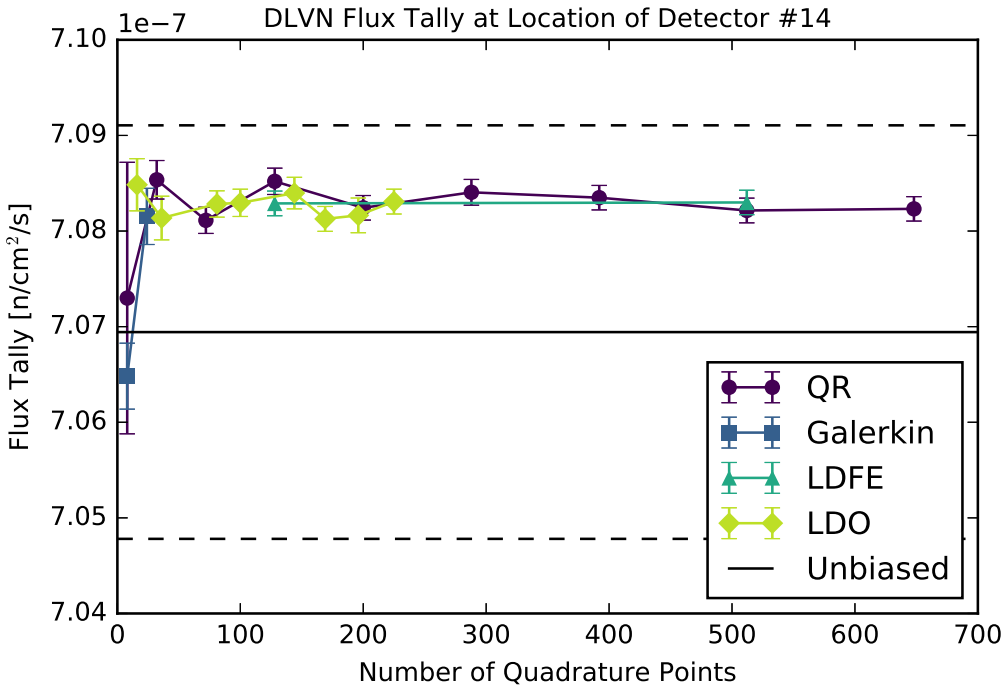

Figure 4.22: Flux tally at detector #14 in the DLVN problem with the CADIS method.

Figures 4.22 and 4.23 show similar convergence behavior with respect to angular mesh refinement for the biased tally calculations and Figure of Merit values. Beyond the lowest-order angular mesh refinement for each quadrature type studied here, the tally result for this detector location using the CADIS method is not impacted by further refining the angular mesh. The Figures of Merit for the tally calculations reach a similar upper bound, but this happens more slowly with respect to angular mesh refinement for the LDO quadrature sets. Like the tally in the steel plate case above, the LDO quadrature set of order 8 is the optimal choice with respect to flux tally result and FOM value for detector #14 in the DLVN experimental benchmark problem in the CADIS context.

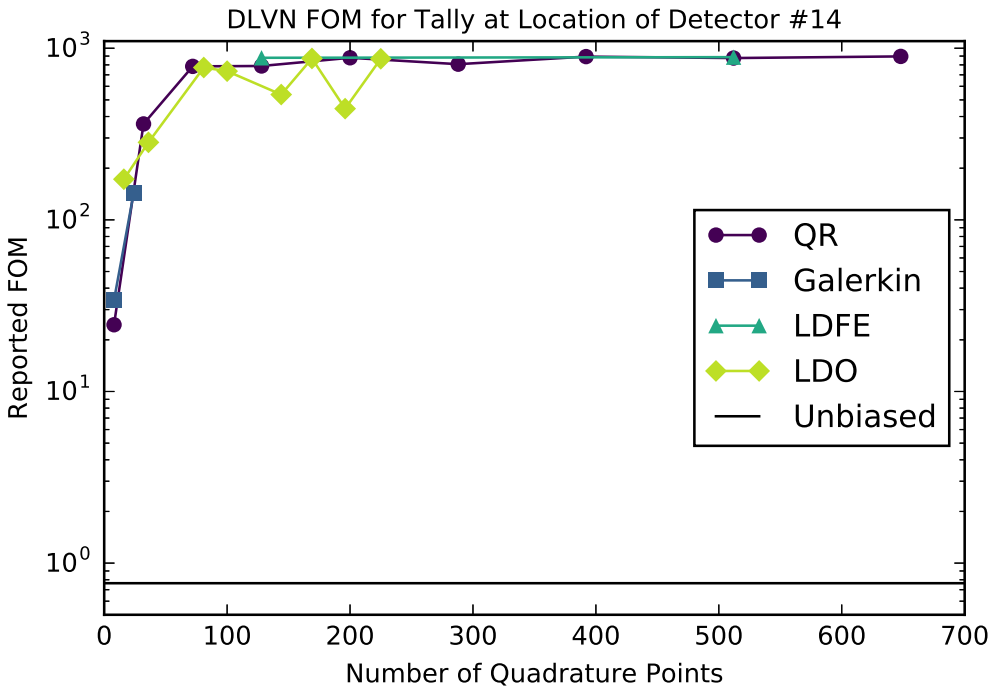

Figure 4.23: FOM values for the DLVN problem detector #14 tally with the CADIS method.

4.3.3 Ispra Sodium Benchmark

For these CADIS calculations, the adjoint source was set to be the detector location farthest from the experimental neutron source. As with the previous cases, we will first examine the adjoint scalar flux solutions and then move on to the Monte Carlo results. The representative LDO quadrature set used in the deterministic calculations here is of order 9 with only 100 total angles and is coarser than the other representative quadrature sets.

The adjoint scalar flux solutions are shown in Figure 4.24 with relative differences plotted in Figure 4.25 and listed in Table 4.13. Since this source is relatively localized in the overall problem scale, ray effects are seen in the adjoint flux solutions as well as in the relative difference plots. For this case, the Galerkin adjoint scalar flux matches most closely with the QR adjoint scalar flux; a finer LDO angular mesh would likely show better agreement.

Table 4.13: Ispra sodium test CADIS adjoint flux extremal and average relative differences.

Comparison	**Min. Diff.**	**Max. Diff.**	**Avg. Diff.**
LDO/QR	1×10^{-8}	1.46×10^{2}	9.71×10^{-1}
LDO/Galerkin	2×10^{-5}	2.52×10^{5}	5.74×10^{2}
LDO/LDFE	1×10^{-6}	3.32×10^{2}	1.28×10^{0}
Galerkin/QR	5×10^{-6}	1.00×10^{0}	4.62×10^{-1}
LDFE/QR	6×10^{-7}	8.10×10^{1}	1.19×10^{0}

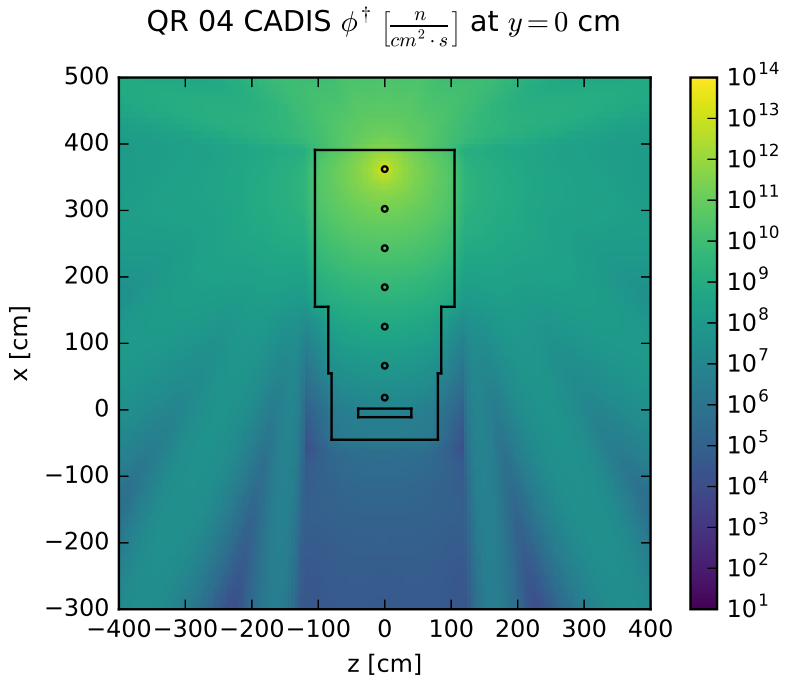

(a) QR adjoint flux slice.

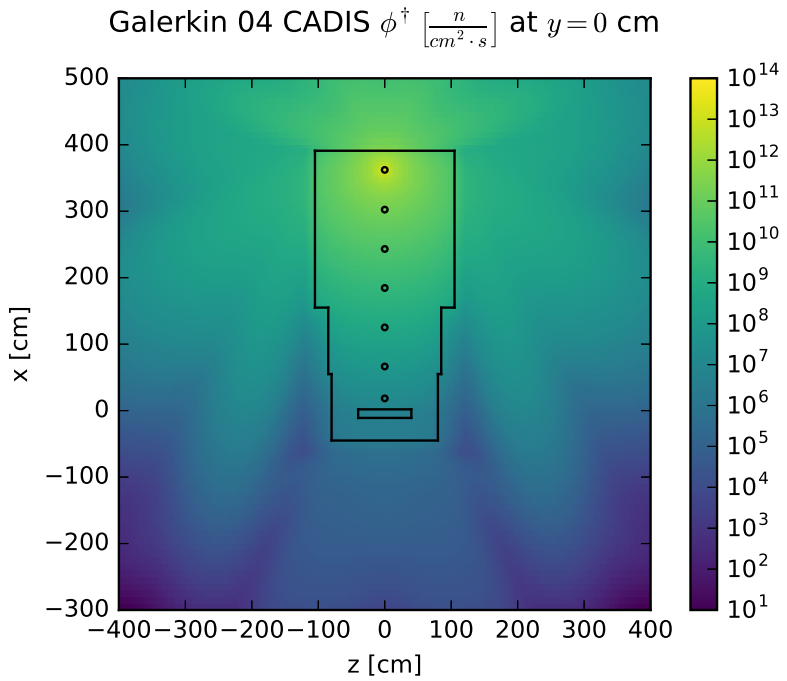

(b) Galerkin adjoint flux slice.

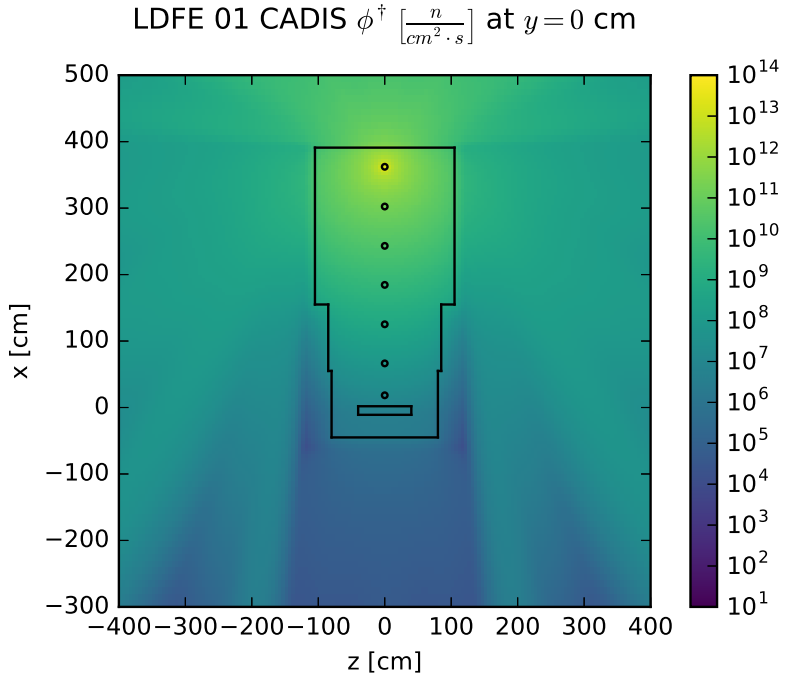

(c) LDFE adjoint flux slice.

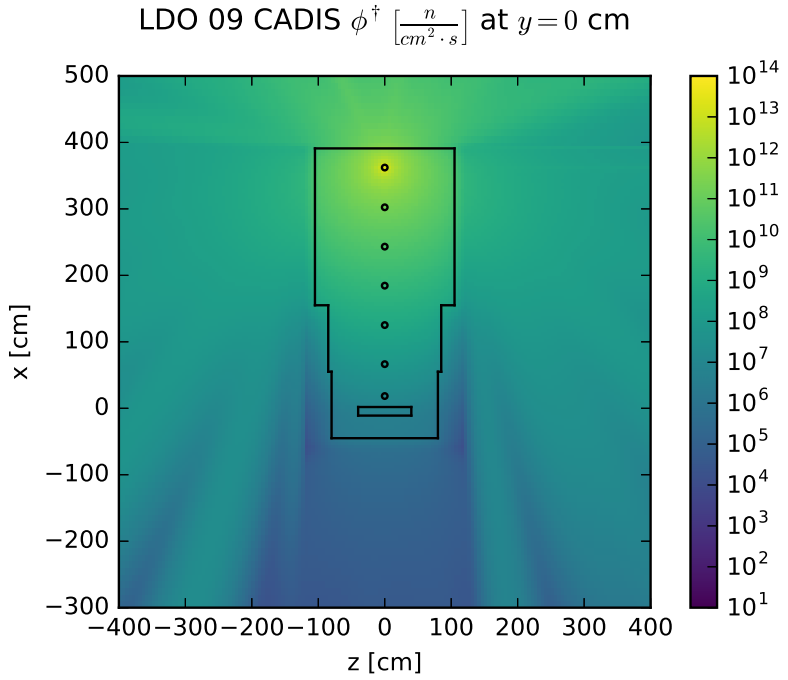

(d) LDO adjoint flux slice.

Figure 4.24: Ispra sodium adjoint scalar flux slices for the CADIS method.

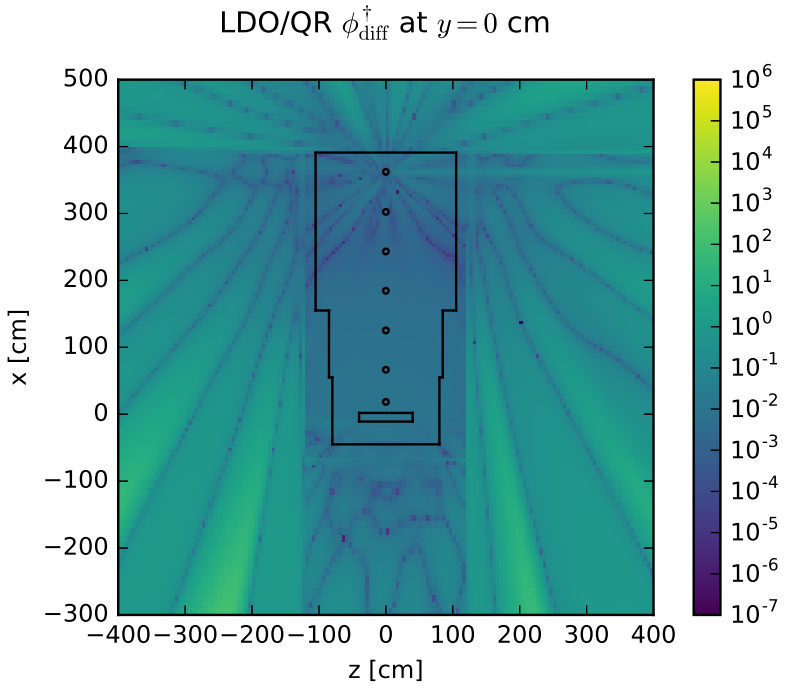

(a) LDO/QR flux relative difference.

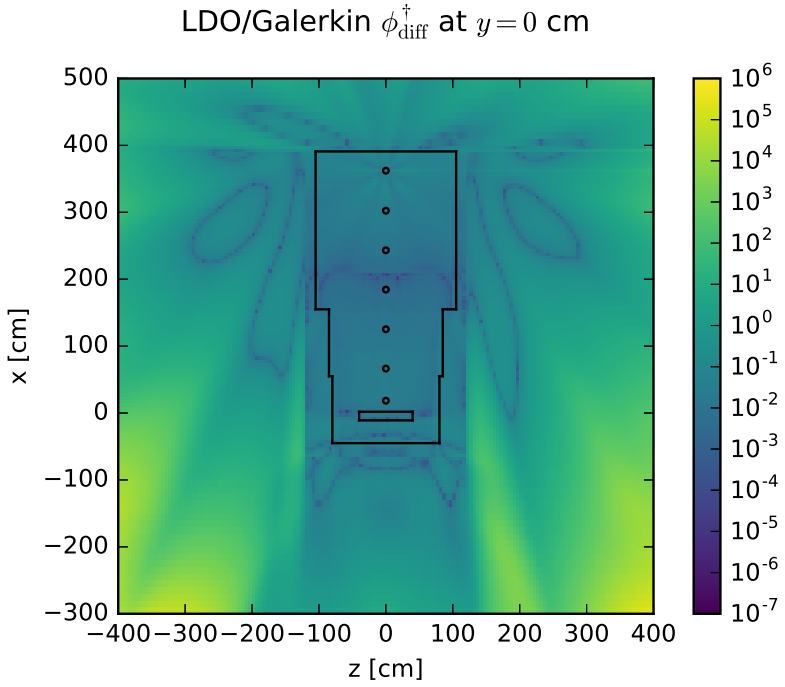

(b) LDO/Galerkin flux relative difference.

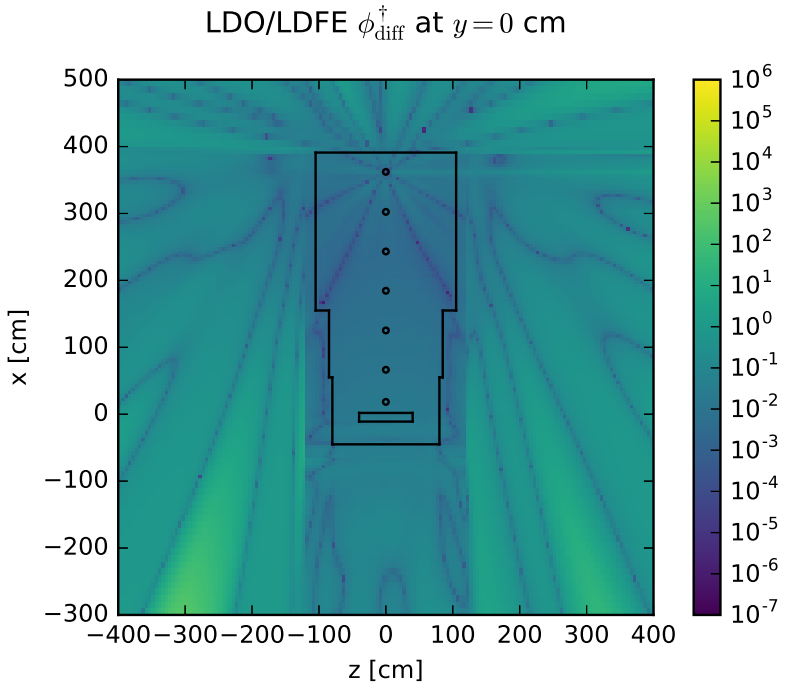

(c) LDO/LDFE flux relative difference.

Figure 4.25: Ispra sodium adjoint scalar flux relative difference slices for the CADIS method.

Again, we will focus the analysis here on the Monte Carlo results for the detector location set to be the adjoint source in the CADIS context. Here, 1×10^{9} neutron histories were simulated. Figure 4.26 shows the calculated activity values for the far detector location as a function of angular mesh refinement. All activity values were calculated using the forward scalar flux reported by MCNP in combination with Equation 4.2 and the data listed in Section 4.2.4. All of the biased results fall well within the statistical error of the unbiased calculation, but the calculations are all four orders of magnitude greater than the experimentally calculated activity of 0.00199 Bq/g listed in Table 4.7. One likely reason for this is that the MCNP flux tallies used in these calculations include neutrons of all incident energies and not only those above the threshold for the ^{32}S(n,p)^{32}P reaction measured experimentally.

Figure 4.26 exhibits no trend for the calculated activity with respect to angular mesh refinement; the coarsest angular mesh of each quadrature type studied here is sufficient to achieve the same forward flux tally and calculated activity value. The FOM values plotted in Figure 4.27 show differing trends for the different quadrature types. The QR biasing parameters tend toward a Figure of Merit of approximately 1000, with the exception of those from the quadrature set of order 4. Of the LDO quadrature sets tested here, the best performance comes from the coarsest angular mesh, with the finest angular mesh not far behind. So, for the Ispra sodium benchmark case in the CADIS method context, the LDO quadrature set of order 3 would be the best one to use (of the LDO quadrature sets).

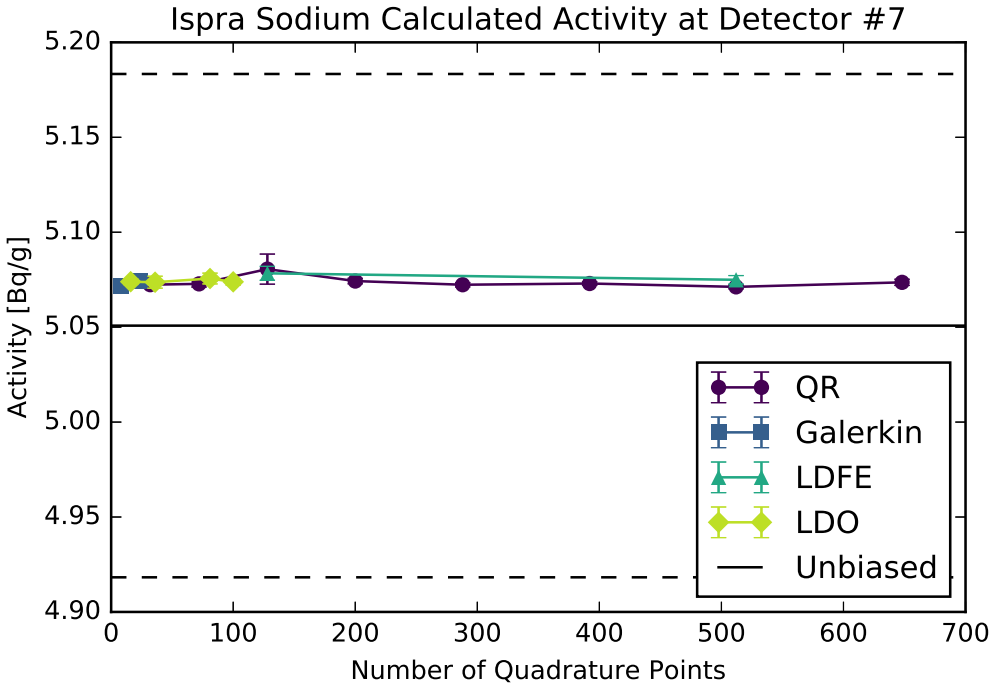

Figure 4.26: Ispra sodium calculated activity in the far detector with the CADIS method.

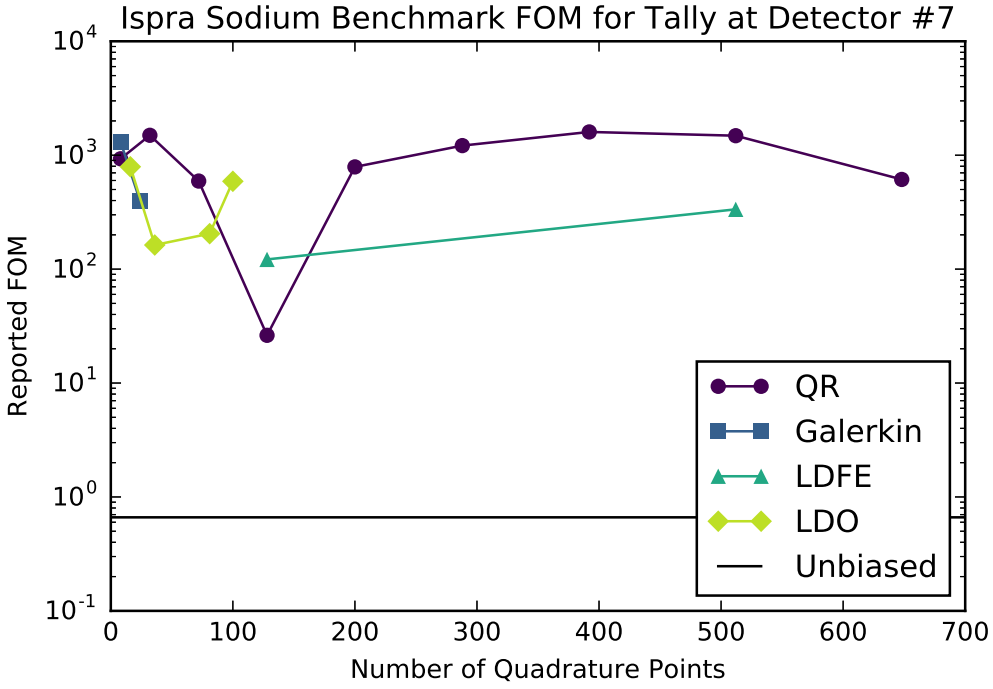

Figure 4.27: Ispra sodium far detector flux tally FOM values with the CADIS method.

4.3.4 Simplified Portal Monitor

To study calculations for the simplified portal monitor scenario in the context of the CADIS method, the adjoint source was set to be the top detector in the small array. The adjoint scalar flux solutions are plotted in Figure 4.28. Ray effects appear drastically in all of the adjoint scalar flux solutions. Figure 4.28b shows regions where the adjoint scalar flux solution is negative for the representative Galerkin quadrature set; these regions are plotted in white. Because of these negative flux regions, Table 4.14 shows the extremal values of the magnitudes of the relative flux differences, calculated as

$$\phi_{\text{diff}} = \frac{|\phi_{\text{LDO}} - \phi_{\text{ref}}|}{|\phi_{\text{ref}}|}. \tag{4.3}$$

All of the flux solutions show poor agreement, likely because of the localized source and streaming paths created by this scenario's materials and geometry. Still, the LDO adjoint scalar flux solution agrees with the QR adjoint scalar flux solution better than the Galerkin or LDFE solutions, on average.

Table 4.14: Portal monitor CADIS adjoint scalar flux extremal and average relative differences.

Comparison	**Min. Diff.**	**Max. Diff.**	**Avg. Diff.**
LDO/QR	2×10^{-4}	1.83×10^{2}	2.27×10^{0}
LDO/Galerkin	1×10^{-4}	6.20×10^{4}	4.29×10^{1}
LDO/LDFE	2×10^{-4}	2.54×10^{2}	3.46×10^{0}
Galerkin/QR	1×10^{-3}	2.59×10^{2}	3.81×10^{0}
LDFE/QR	6×10^{-5}	6.48×10^{1}	2.21×10^{0}

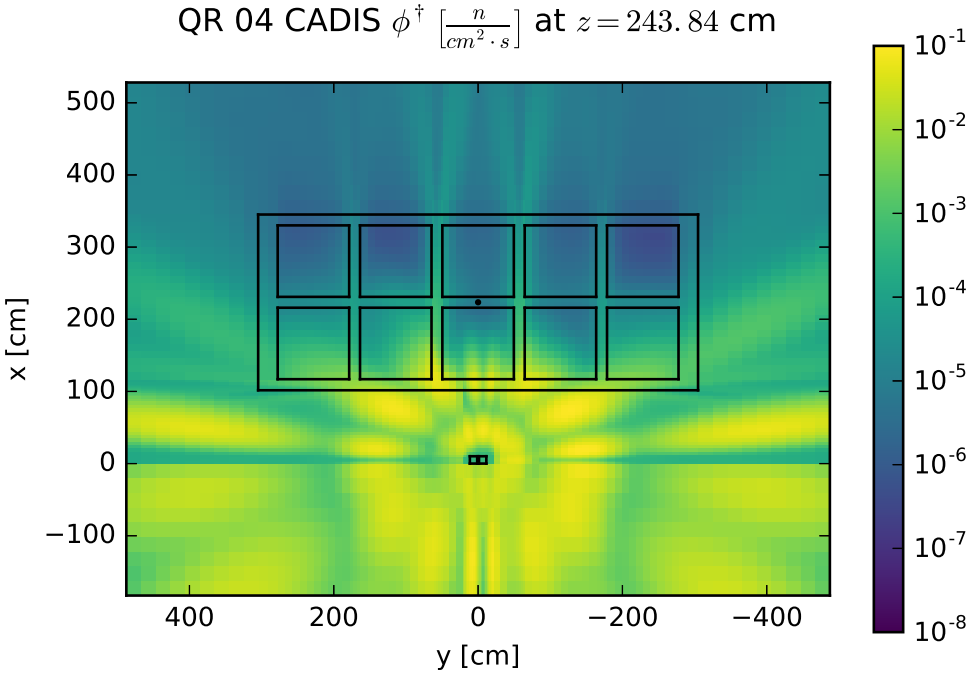

(a) QR adjoint flux slice.

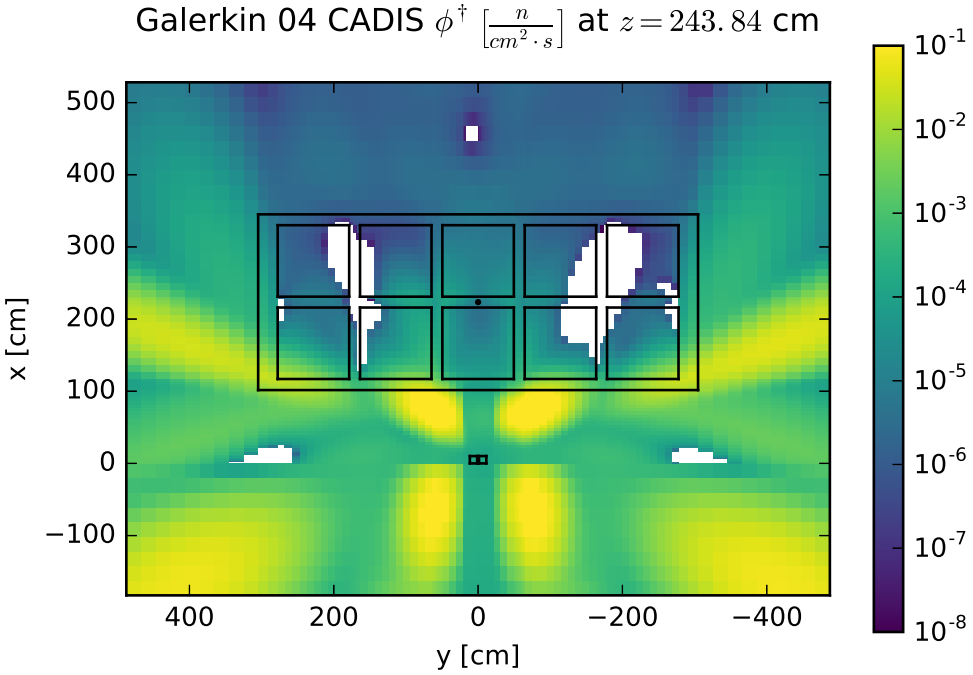

(b) Galerkin adjoint flux slice.

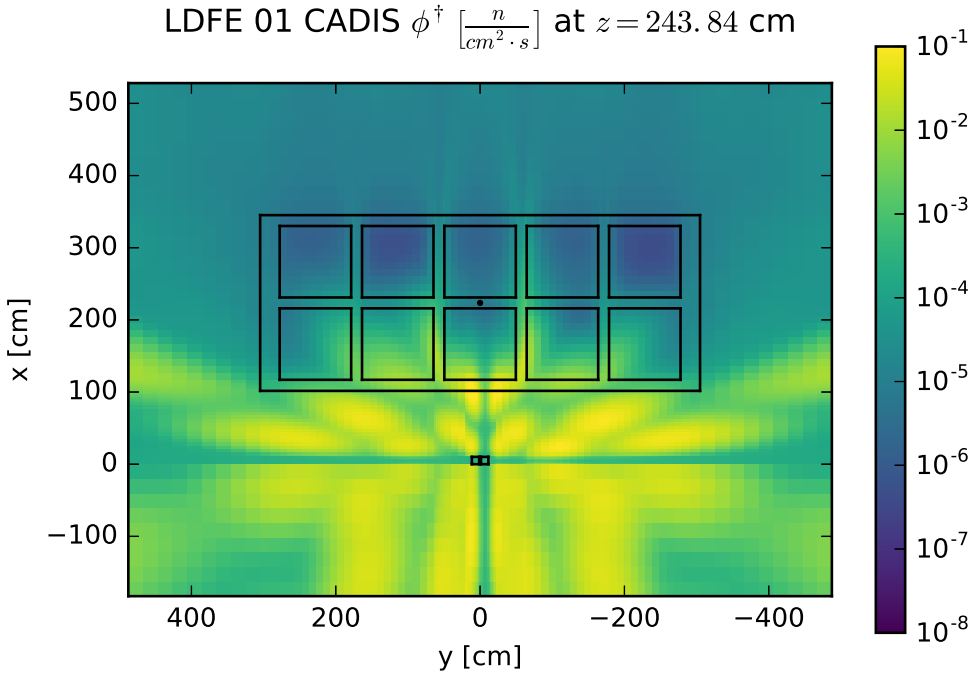

(c) LDFE adjoint flux slice.

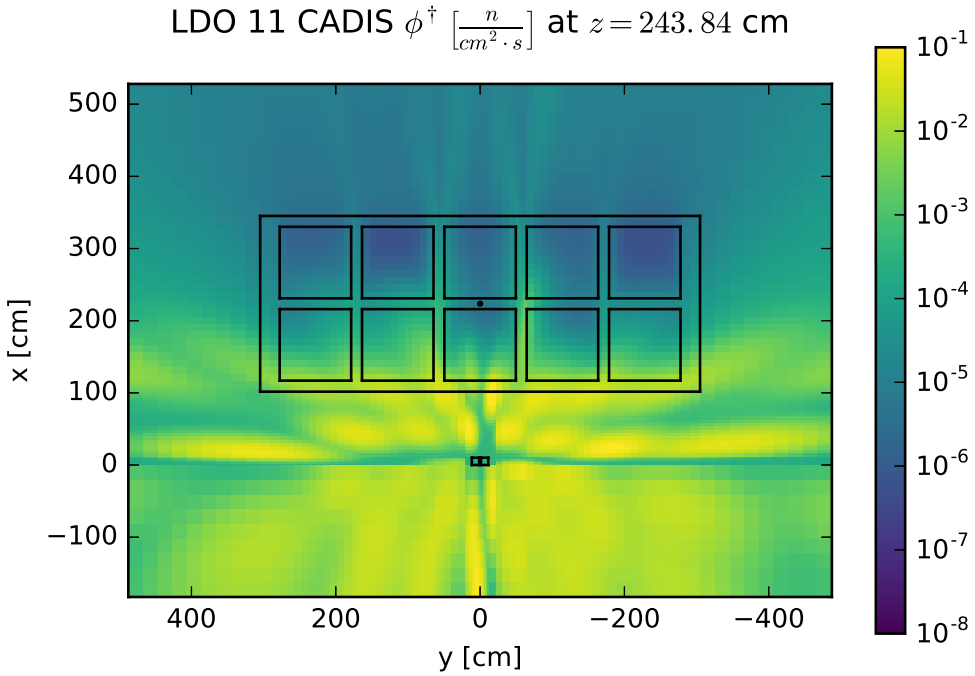

(d) LDO adjoint flux slice.

Figure 4.28: Simplified portal monitor adjoint scalar flux slices for the CADIS method.

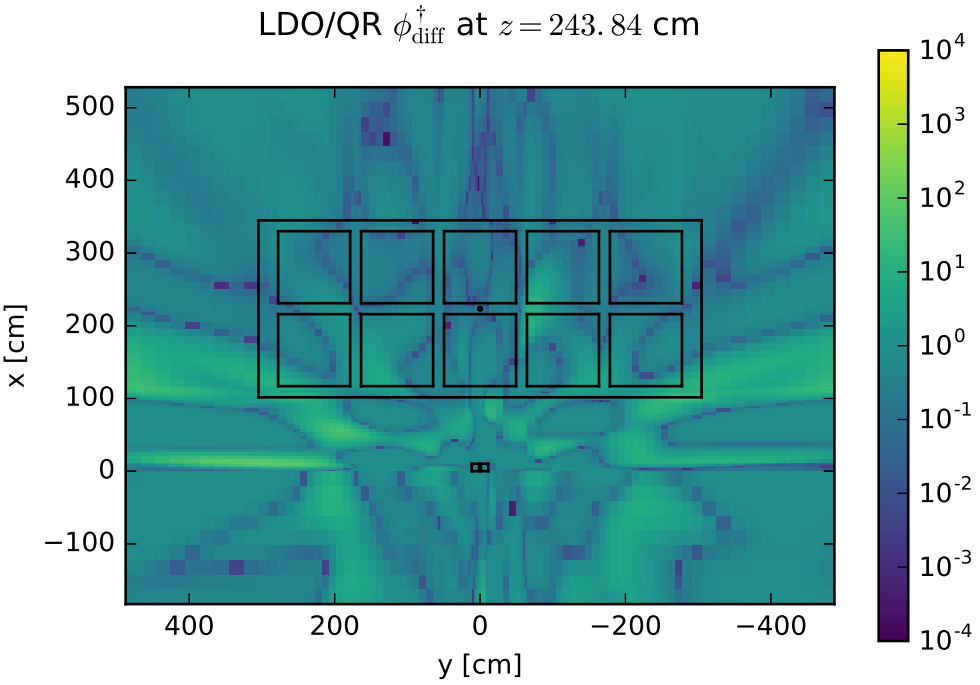

(a) LDO/QR flux relative difference.

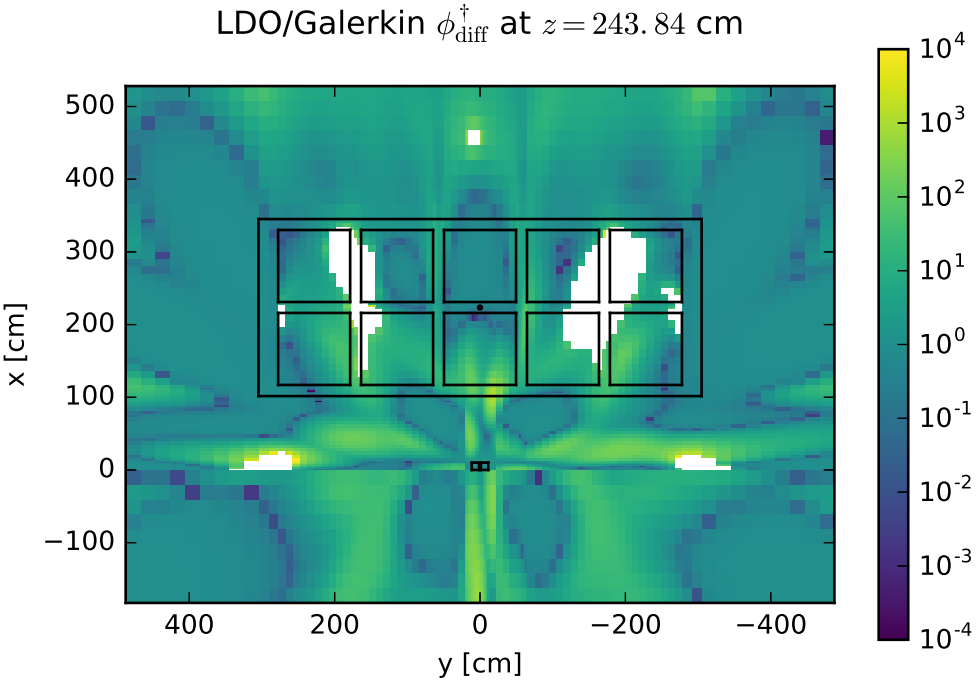

(b) LDO/Galerkin flux relative difference.

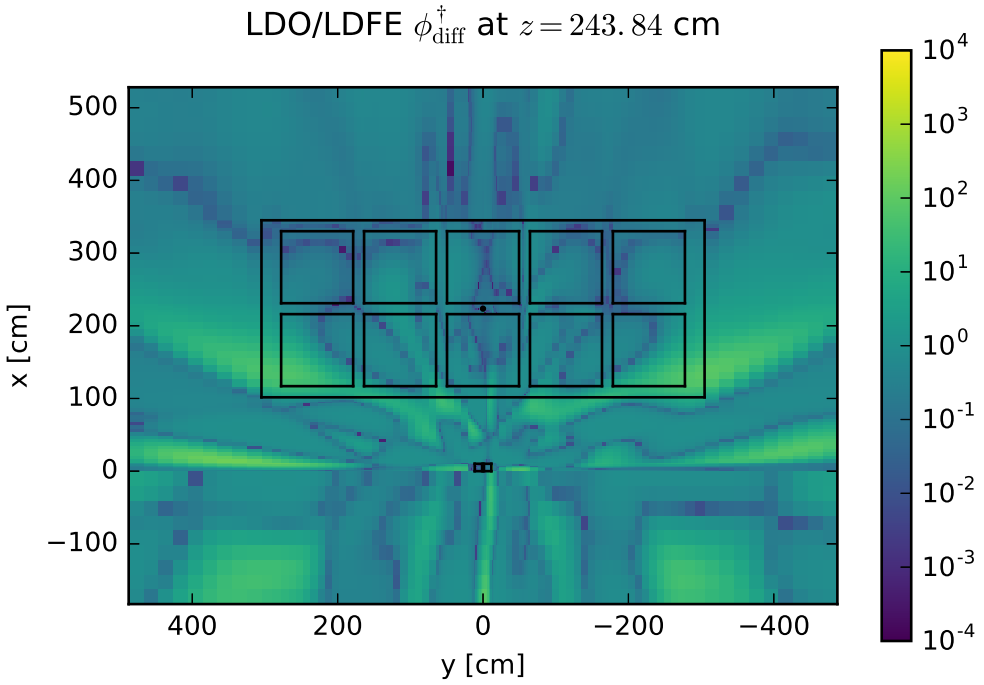

(c) LDO/LDFE flux relative difference.

Figure 4.29: Portal monitor adjoint scalar flux relative difference slices for the CADIS method.

Finally, we move on to the results and analysis of the Monte Carlo calculations, in which 1×10^{9} particle histories were simulated. Again, since the CADIS adjoint source was set to be the top detector location, we focus the discussion in this section on the results for that specific location. Figures 4.30 and 4.31 show the MCNP-reported forward scalar flux tally values and Figures of Merit, respectively. As with the other test cases, the values are plotted as a function of the number of quadrature points used to generate the biasing parameters in order to explore the impact of angular mesh refinement on flux tally and FOM.

Similar to other test cases, the flux tally values reported in Figure 4.30 show a trend of converging to a stable value after the first few coarsest angular meshes. The flux tally values from the biased calculations all fall within the statistical error of that of the unbiased calculation but appear to require a minimum value of approximately 100 discrete angular values in order to stabilize. Figure 4.31 shows a strong correlation between the number of quadrature points and the flux tally FOM, eventually approaching an upper limit around 100. The LDO Figures of Merit increase most rapidly with the number of quadrature points used, so one would want to use a higher-order LDO quadrature set to generate Monte Carlo biasing parameters.

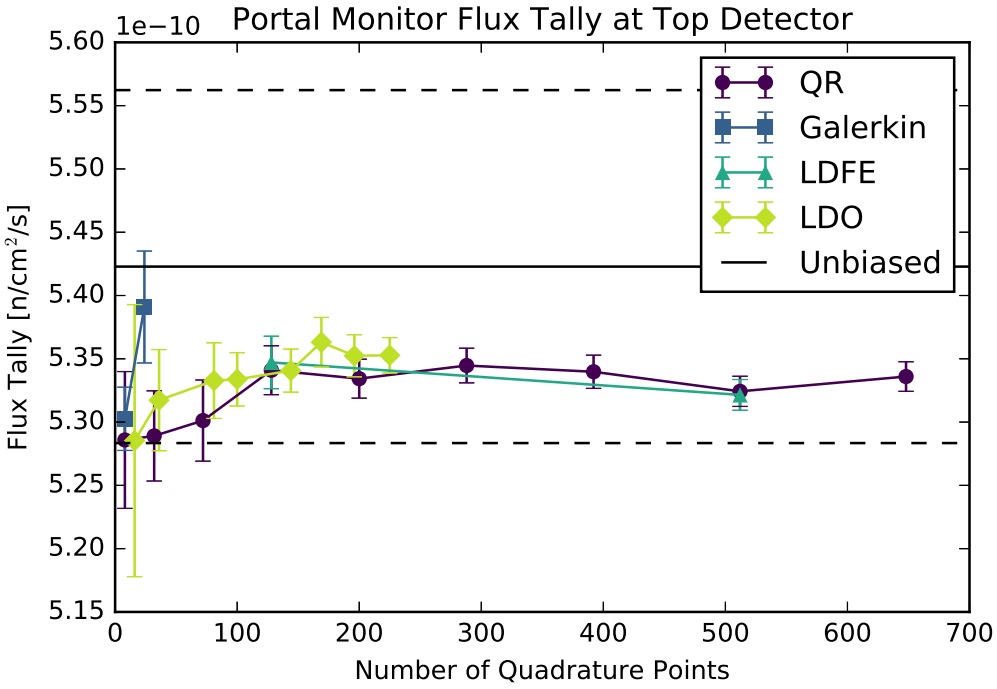

Figure 4.30: Flux tally in the portal monitor top detector using the CADIS method.

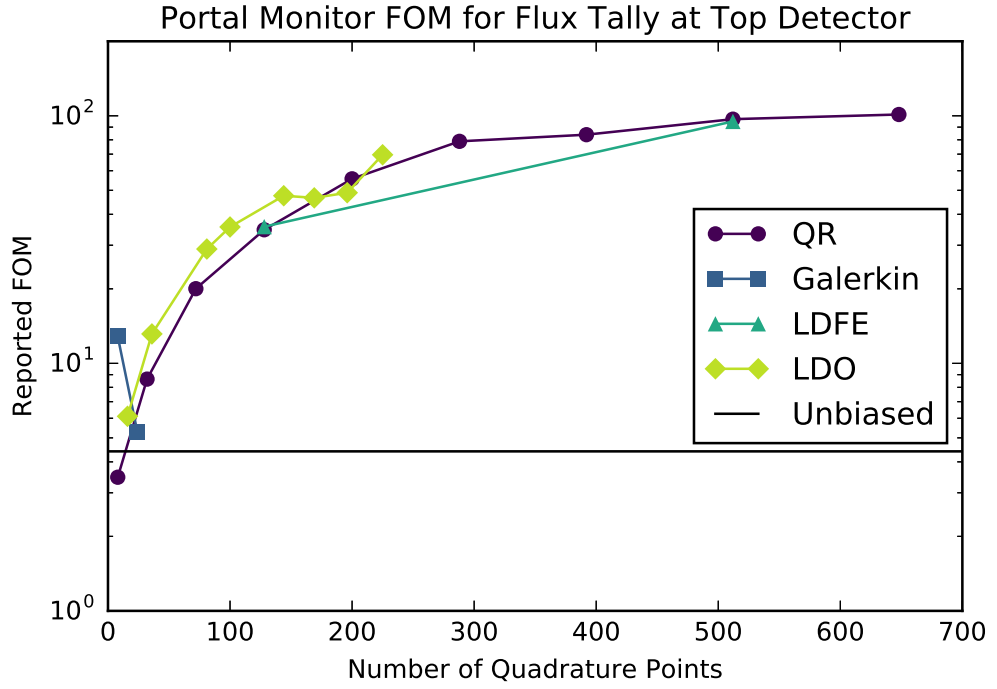

Figure 4.31: CADIS method FOM values for the portal monitor top detector flux tally.

4.3.5 Summary

In this section, we examined the deterministic and Monte Carlo results for the four test case scenarios in the context of the CADIS method. For all of the test cases, little correlation was noted between angular mesh refinement and MCNP-reported forward flux tally value beyond the suggestion to use at least 100 discrete angles for the simplified portal monitor scenario. The reported FOM values also exhibited minimal correlation with angular mesh refinement except in the case of the portal monitor scenario, where the flux tally FOM increased with angular mesh refinement while approaching an upper limit.

For the three test cases in which neutrons were transported, the LDO quadrature sets of lower orders (3 and 8) were the most effective of the LDO sets for both flux tally value and FOM achievement. That is, if one were interested in using an LDO quadrature set to generate Monte Carlo biasing parameters for a given neutron transport problem in the context of the CADIS method, we would suggest performing the deterministic calculation with an LDO quadrature set of order 8. For a photon transport problem considered in the CADIS context, we would suggest the finest available LDO quadrature set, based on the results seen here.

4.4 FW-CADIS Calculations

Finally, we examine the performance of the various quadrature types in the context of the FW-CADIS method. Similar to the analysis for the CADIS method, we will first look at the deterministic adjoint scalar flux solutions from the representative quadrature sets to compare the calculations using the LDO equations versus the standard quadrature types. Recalling Section 2.2.1.2, the FW-CADIS method incorporates both forward and adjoint scalar flux solutions. Because the adjoint source may be specified differently between the CADIS and FW-CADIS methods, it is instructive to look at the FW-CADIS deterministic adjoint scalar flux solutions. However, the deterministic forward flux solutions used in the FW-CADIS method are the same as those discussed in Section 4.2 and so we will not repeat the analysis here. Lastly, we again look at result metrics from the various Monte Carlo runs to compare the variance reduction parameter generation efficacy of the different quadrature types.

4.4.1 Steel Plate in Water

For the FW-CADIS calculations for the steel plate in water, the adjoint source was set to be a mesh tally over all of the air beyond the steel plate. The discretization for the adjoint source mesh tally is the same as that listed in Section 4.1.1. Specifically, the adjoint source mesh is identical to the overall problem mesh in the $x-$ and $y-$directions but starts at $z = 130$ cm and extends to the problem boundary at $z = 140$ cm.

Figure 4.32 shows the adjoint scalar flux solutions for the representative quadrature sets for the steel plate embedded in water. As expected, in each solution, the adjoint flux is highest in the chosen adjoint source region for the problem and decreases logarithmically

in the $z-$direction. Table 4.15 lists the minimum, maximum, and average relative adjoint scalar flux solution differences for the comparisons plotted in Figure 4.33. As with earlier cases, the Galerkin/QR and LDFE/QR comparisons are also tabulated for reference. Like other deterministic flux comparisons for the steel plate embedded in water, the LDO flux solution best matches the QR flux solution, with an average relative difference of 4.6% for the FW-CADIS adjoint scalar flux.

Table 4.15: Steel plate FW-CADIS adjoint scalar flux extremal and average relative differences.

Comparison	**Min. Diff.**	**Max. Diff.**	**Avg. Diff.**
LDO/QR	2×10^{-4}	1.66×10^{-1}	4.63×10^{-2}
LDO/Galerkin	2×10^{-5}	1.85×10^{0}	7.16×10^{-1}
LDO/LDFE	8×10^{-2}	2.41×10^{-1}	1.92×10^{-1}
Galerkin/QR	5×10^{-4}	5.98×10^{0}	2.85×10^{0}
LDFE/QR	3×10^{-2}	3.37×10^{-1}	2.09×10^{-1}

Comparing Figure 4.33 with Figure 4.14, we see that the relative differences among the FW-CADIS adjoint scalar flux solutions are more uniform than those of the CADIS adjoint flux solutions. This is to be expected, as the CADIS adjoint source is much more localized than the FW-CADIS for the steel plate scenario studies conducted here.

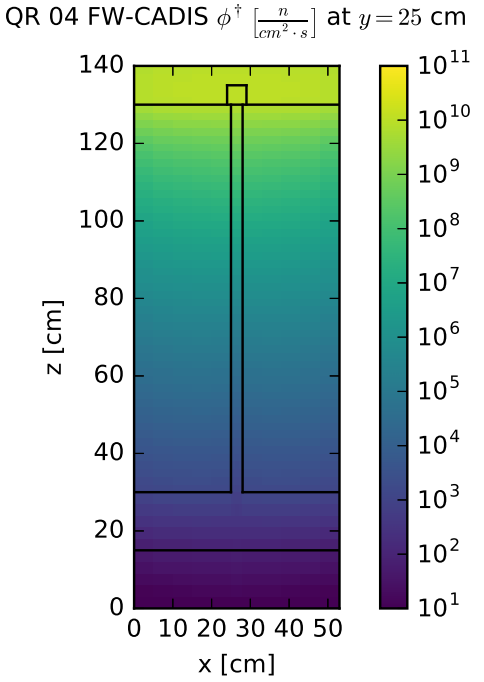

(a) QR adjoint flux slice.

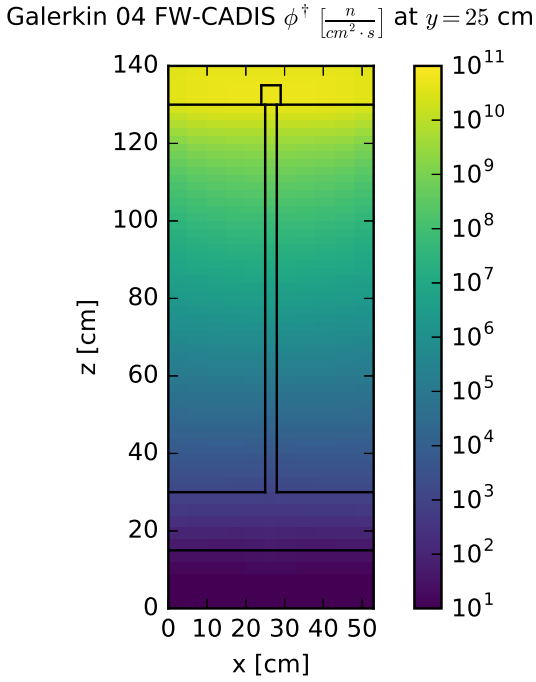

(b) Galerkin adjoint flux slice.

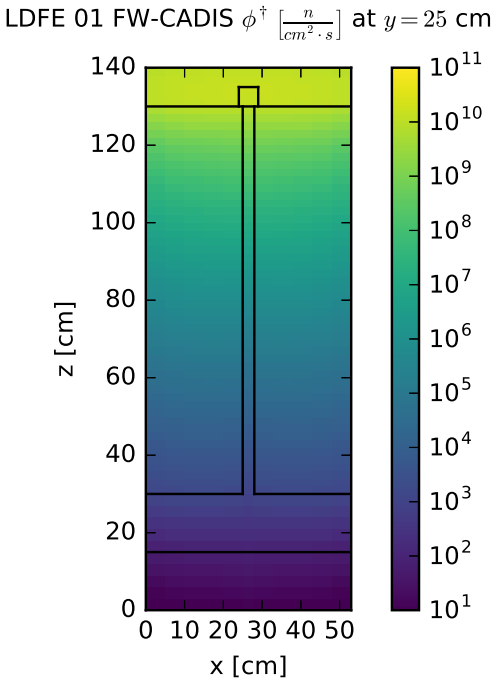

(c) LDFE adjoint flux slice.

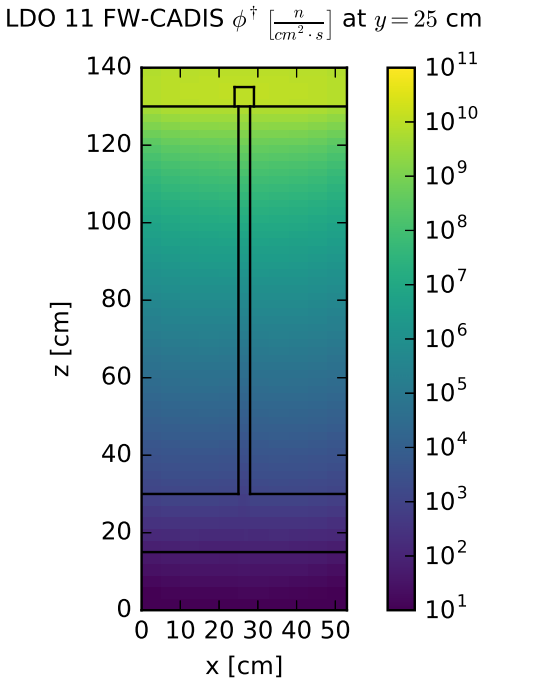

(d) LDO adjoint flux slice.

Figure 4.32: Steel plate adjoint scalar flux slices for the FW-CADIS method.

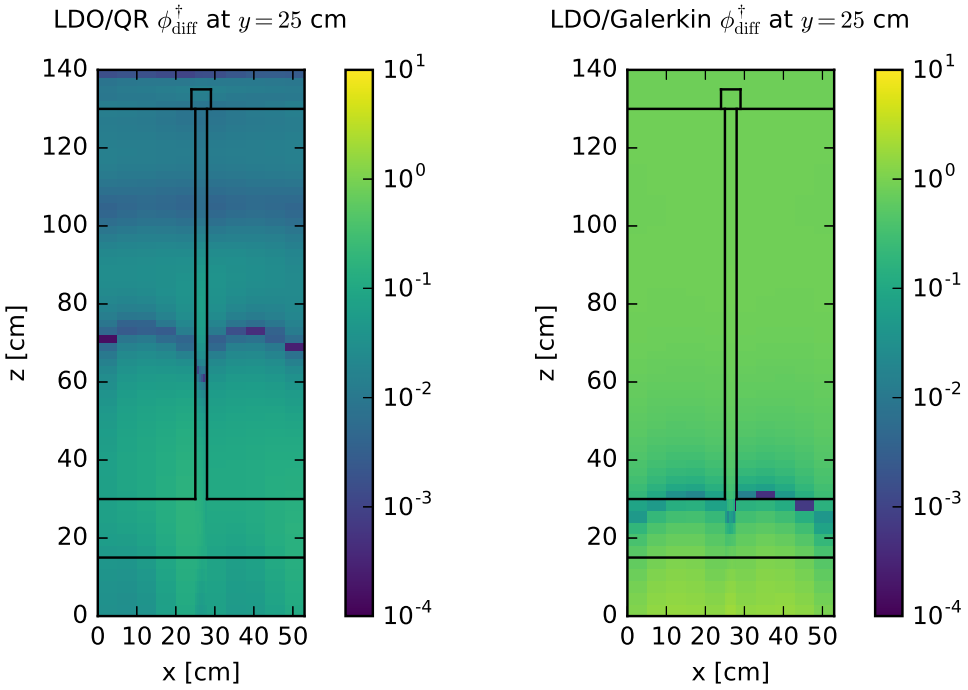

(a) LDO/QR flux rel. diff.

(b) LDO/Galerkin flux rel. diff.

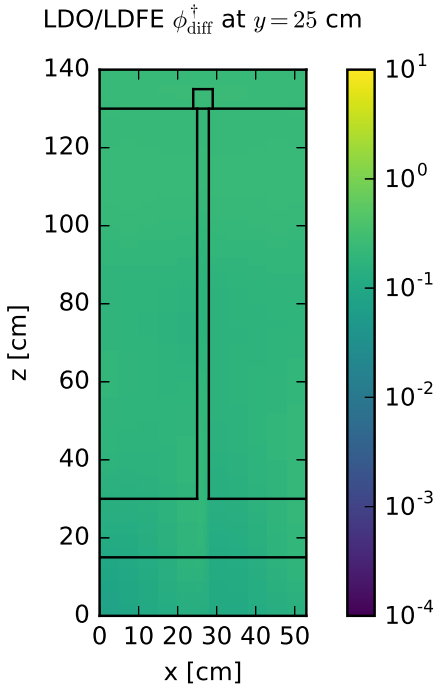

(c) LDO/LDFE flux rel. diff.

Figure 4.33: Steel plate adjoint flux relative difference slices for the FW-CADIS method.

Next, we will look at the results for the mesh tally in the air region of the scenario. The Monte Carlo run with biasing parameters from the Galerkin quadrature set of order 2 was not able to finish in a timely manner for the hardware configuration used in this work, so Monte Carlo results for this data point are not included here. The calculations for this test case scenario used 1×10^9 neutron histories.

Figure 4.34 shows the total tally summed over all air in the problem for the biased and unbiased calculations. The biased calculations are plotted as a function of angular mesh refinement and the unbiased calculation value is shown as a black horizontal line. Like the CADIS method, the FW-CADIS method generates biasing parameters such that the biased Monte Carlo flux tally results all fall far below that of the unbiased calculation. Similarly, in this case, the angular mesh refinement has little impact on the tally result. So, if using an LDO quadrature set to generate biasing parameters with the FW-CADIS method in a similar scenario, a low-order LDO angular mesh could be used to good effect.

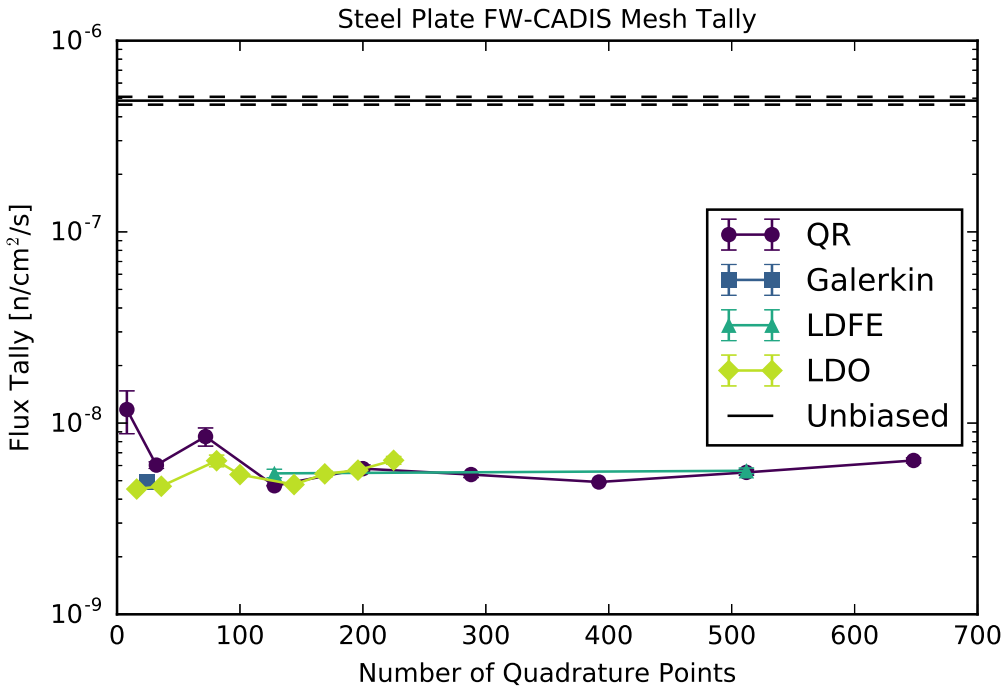

Figure 4.34: Flux tally over the air region in the steel plate test with the FW-CADIS method.

To analyze the performance of the representative quadrature sets' variance reduction parameters for the steel plate in water case using the FW-CADIS method, we will look at the average FOM values over the entire adjoint source mesh tally. The Figures of Merit were calculated by taking the average relative error over all spatial cells in the air block mesh tally and using that mean value in combination with the MCNP-reported computer time and Equation 2.10. Figure 4.35 shows these average Figures of Merit as a function of

the number of angles used in generating the biasing parameters. The average FOM for the unbiased calculation is shown as a horizontal black line.

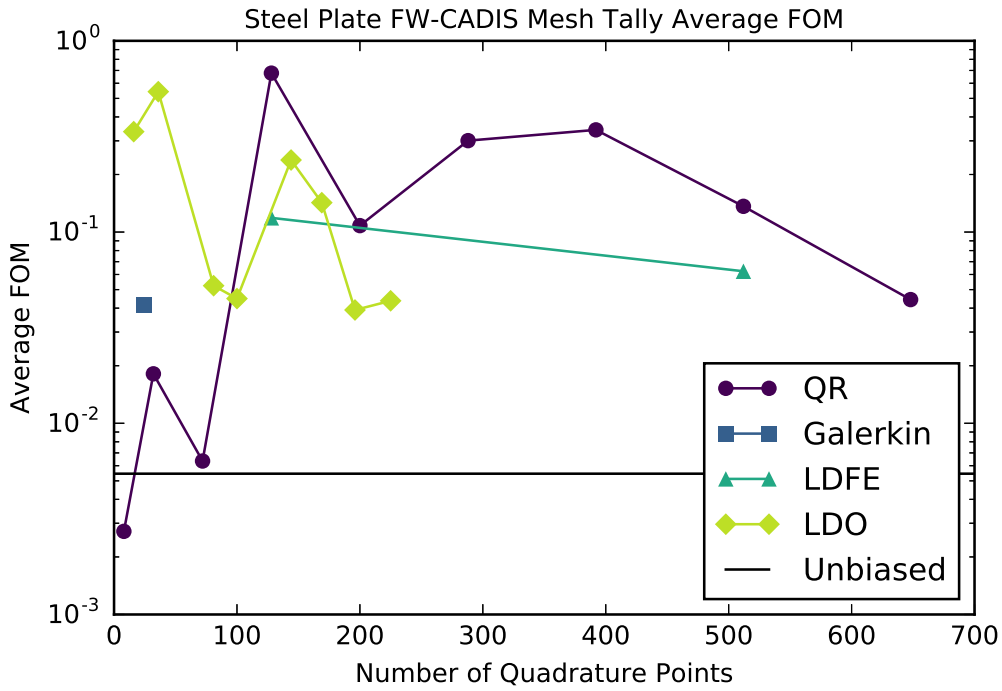

Figure 4.35: Average FOM values for the mesh tally in the FW-CADIS steel plate scenario.

We see a different trend here in that the highest average FOM values tend to come from quadrature sets with mid-range angular mesh refinement; the coarsest and finest angular meshes produce Monte Carlo biasing parameters that result in reduced Figures of Merit. Considering Figures 4.34 and 4.35, we note that one would wish to use a lower-order (e.g., order 5) LDO quadrature set to generate variance reduction parameters for a Monte Carlo mesh tally using the FW-CADIS method.

4.4.2 DLVN

Considering the DLVN case with the FW-CADIS method, the adjoint source was specified to be the combination of all of the detector locations in the problem. In accordance with this, the adjoint scalar flux solutions shown in Figure 4.36 demonstrate the highest source values in the region where four out of the six detector locations are concentrated. Figure 4.37 displays the relative differences between the LDO adjoint scalar flux solution and those of the three standard quadrature types with extremal and average relative difference values listed in Table 4.16. Of the standard quadrature types, the LDO adjoint flux solution differs the least from the QR adjoint flux solution, with an average relative difference of about 11% for this FW-CADIS adjoint source specification for the DLVN problem. Given the

more spatially generalized source specification, it is unsurprising to see uniform differences in Figures 4.37a and 4.37c. The nonuniform differences in Figure 4.37b may be attributed to the relative coarseness of the representative Galerkin quadrature set.

Table 4.16: DLVN FW-CADIS adjoint scalar flux extremal and average relative differences.

Comparison	**Min. Diff.**	**Max. Diff.**	**Avg. Diff.**
LDO/QR	1×10^{-3}	4.32×10^{-1}	1.12×10^{-1}
LDO/Galerkin	2×10^{-5}	1.90×10^{0}	1.79×10^{-1}
LDO/LDFE	1×10^{-2}	3.97×10^{-1}	1.73×10^{-1}
Galerkin/QR	2×10^{-4}	6.88×10^{-1}	2.68×10^{-1}
LDFE/QR	4×10^{-4}	2.58×10^{-1}	5.42×10^{-2}

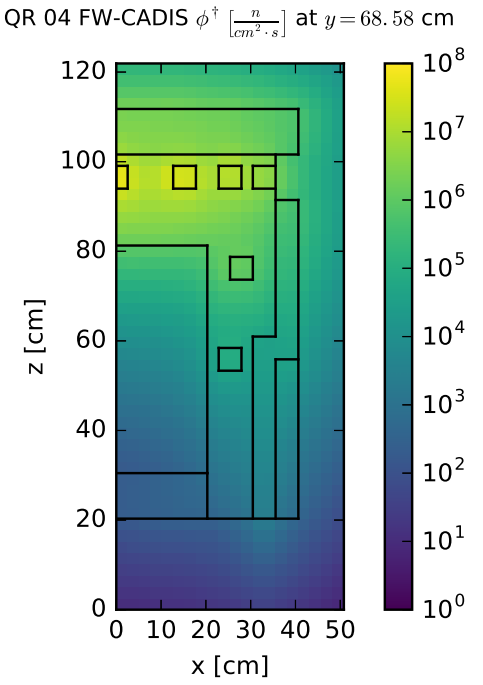

(a) QR adjoint flux slice.

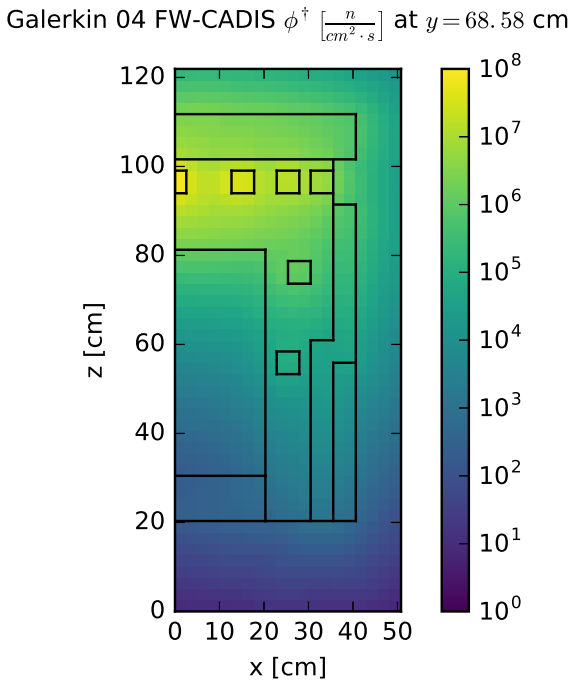

(b) Galerkin adjoint flux slice.

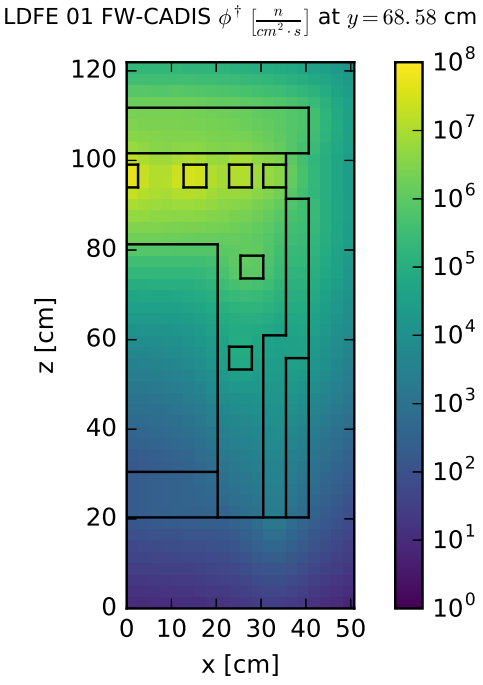

(c) LDFE adjoint flux slice.

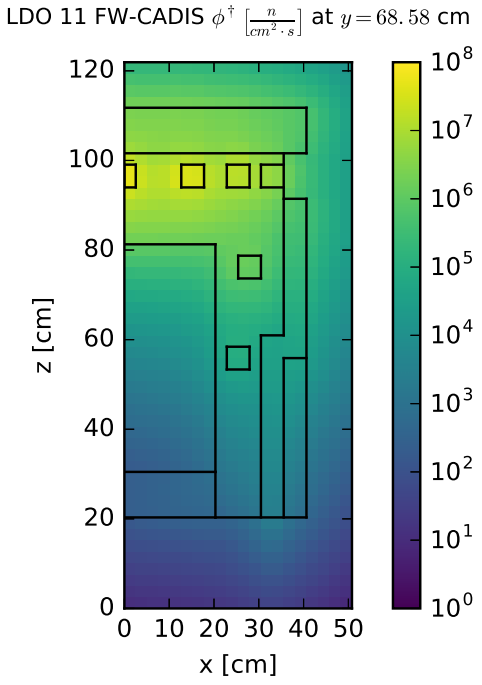

(d) LDO adjoint flux slice.

Figure 4.36: DLVN adjoint scalar flux slices for the FW-CADIS method.

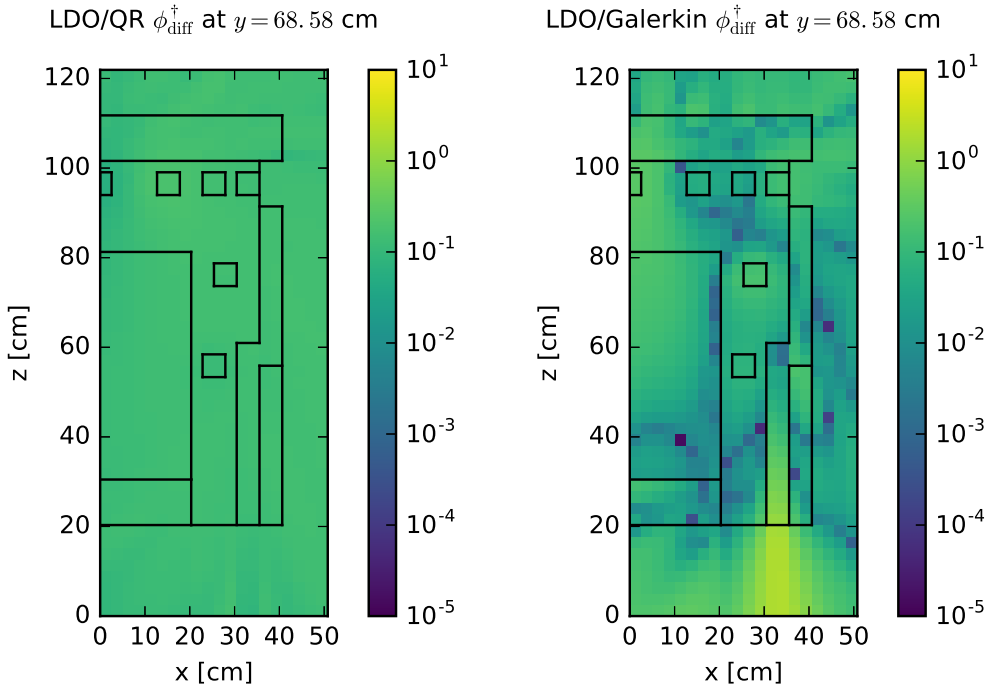

(a) LDO/QR flux rel. diff.

(b) LDO/Galerkin flux rel. diff.

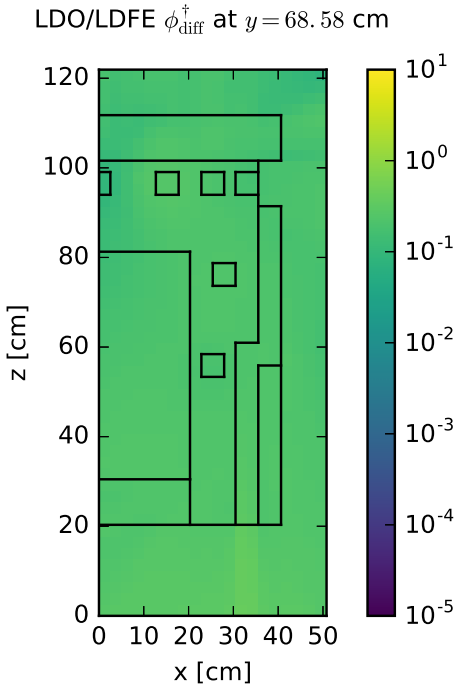

(c) LDO/LDFE flux rel. diff.

Figure 4.37: DLVN adjoint scalar flux relative difference slices for the FW-CADIS method.

Moving on to the Monte Carlo results and analysis, we look at the flux tallies and Figures of Merit for all of the detector locations in the DLVN experimental benchmark. Recall that 1×10^{10} particle histories were simulated. Figure 4.38 shows all of the detector locations' MCNP-reported forward scalar flux tallies plotted as a function of angular mesh refinement used to generate biasing parameters in addition to the Figures of Merit for the flux tallies. In each plot, the unbiased flux tally result is shown as a horizontal black line.

Figures 4.38a and 4.38b exhibit the same lack of trend in flux tally as a function of angular mesh refinement. That is, in general, for detector locations #5 and #9, using more discrete angles in the FW-CADIS deterministic calculations does not greatly impact the flux tally result from MCNP. Figures 4.38e and 4.38f show similar behavior with the exception of the most coarse angular meshes. For these detector locations, any angular mesh refinement other than the coarsest angular mesh will produce a consistent forward scalar flux tally result. Figures 4.38c and 4.38d show slightly more variation in flux tally result with angular mesh refinement. These two detector locations' tallies have also higher statistical error relative to those at the other detector locations. Overall, though, the flux tallies at detectors #11 and #12 are not heavily impacted by the refinement of the angular mesh used in generating the Monte Carlo biasing parameters, but a mid-range number of quadrature points should be used to avoid the large statistical errors seen at the extreme ends of the angular mesh refinement spectrum.

Like their corresponding flux tally graphs, Figures 4.38a, 4.38b, and 4.38e show almost no variation in FOM with angular mesh refinement for the tallies at detector locations #5, #9, and #13. This is to be expected, considering the uniform statistical error and stable flux tally results at these locations. Figure 4.38c shows variation in FOM with angular mesh refinement that is more varied, which corresponds to the larger statistical uncertainties in the flux tally values for detector #11. Figure 4.38d shows little variation in FOM with angular mesh refinement with the exception of the finest QR set. Lastly, 4.38f shows an upper FOM limit of approximately 200 across all quadrature types, with the Figure of Merit largely consistent across quadrature types with the exception of QR angular meshes.

In Table 4.17 we compare the Monte Carlo forward flux tally results for the representative quadrature sets listed in Section 4.1.5.1. Results from the unbiased Monte Carlo calculation are also included for comparison. All Monte Carlo flux tally values are reported with an uncertainty of one standard deviation. For all detector locations, the Monte Carlo flux tallies do not match the experimentally measured flux values for any of the representative quadrature sets or the unbiased calculation, so we only compare the Monte Carlo calculations in this table. We do note that the Monte Carlo calculations overestimate the flux tally at all detector locations with the exception of detector #13. The flux tallies at detectors 5, 9, 13, and 14 all match within statistical uncertainty for all of the Monte Carlo calculations. At detector #11, the biased Monte Carlo calculations match within standard error, but the calculations using the QR and LDO biasing parameter fall outside of the error bounds of the unbiased calculation. Somewhat similarly, at detector #14, all of the biased calculations match one another within statistical uncertainty, but they are all outside of the error bounds of the unbiased flux tally calculation.

Table 4.17: DLVN benchmark flux tallies [n/cm^2/s] calculated with FW-CADIS.

	QR	**Galerkin**	**LDFE**	**LDO**	**Unbiased**
Det. #5 ($\times 10^{-7}$)	1.3341 ± 0.0003	1.3344 ± 0.0003	1.3347 ± 0.0004	1.3344 ± 0.0003	1.3315 ± 0.0092
Det. #9 ($\times 10^{-7}$)	2.5225 ± 0.0005	2.5224 ± 0.0005	2.5229 ± 0.0004	2.2555 ± 0.0004	2.5104 ± 0.0127
Det. #11 ($\times 10^{-5}$)	1.4420 ± 0.0005	1.4451 ± 0.0027	1.4446 ± 0.0026	1.4463 ± 0.0015	1.4463 ± 0.0010
Det. #12 ($\times 10^{-6}$)	2.4749 ± 0.0004	2.4743 ± 0.0004	2.4751 ± 0.0004	2.4744 ± 0.0004	2.4684 ± 0.0042
Det. #13 ($\times 10^{-7}$)	4.3984 ± 0.0011	4.3997 ± 0.0011	4.3994 ± 0.0011	4.3983 ± 0.0011	4.4170 ± 0.0175
Det. #14 ($\times 10^{-7}$)	7.0070 ± 0.0025	7.0829 ± 0.0045	7.0813 ± 0.0026	7.0834 ± 0.0032	7.0694 ± 0.0216

To examine the FOM values in a more quantifiable way, Table 4.18 lists the FOM values for all detector locations for each of the representative quadrature sets as well as the unbiased calculation. The maximum FOM value at each detector location is emphasized. Of the six detector locations, the LDO quadrature set achieves the highest FOM for two of the locations. The QR quadrature set is the only other type to also deliver the highest FOM for two out of six detectors; the Galerkin and LDFE quadrature set biasing parameters each only achieve the highest FOM at one detector. So, the LDO quadrature set's biasing parameters perform comparably to those from the QR quadrature set with respect to obtaining high FOM values for multiple detector locations using the FW-CADIS method for the DLVN problem.

Table 4.18: FW-CADIS FOM values for representative quadratures for the DLVN problem.

Quad. Type	Det. #5	Det. #9	Det. #11	Det. #12	Det. #13	Det. #14
QR	483.01	709.51	**202.66**	747.91	380.84	**185.40**
Galerkin	**527.79**	649.88	5.9934	798.88	326.11	52.098
LDFE	310.28	710.43	6.6749	926.28	**391.62**	166.51
LDO	478.24	**721.22**	19.959	**943.96**	369.42	110.40
Unbiased	0.14912	0.27845	14.555	2.5256	0.45376	0.76362

In summary, for test case scenarios such as the DLVN problem in which the FW-CADIS method is used to generate Monte Carlo variance reduction parameters to optimize the response at multiple flux tally detector locations, a relatively coarse quadrature set of any of the types studied here can be used to sufficient effect. However, the coarsest available quadrature sets should be avoided; flux tally results and Figures of Merit for the various detector locations tend to level out as a function of angular mesh refinement beyond the quadrature sets with the fewest number of angles. In particular, if using an LDO quadrature set in another similar scenario, we would suggest using a point set of order 5 or 8.

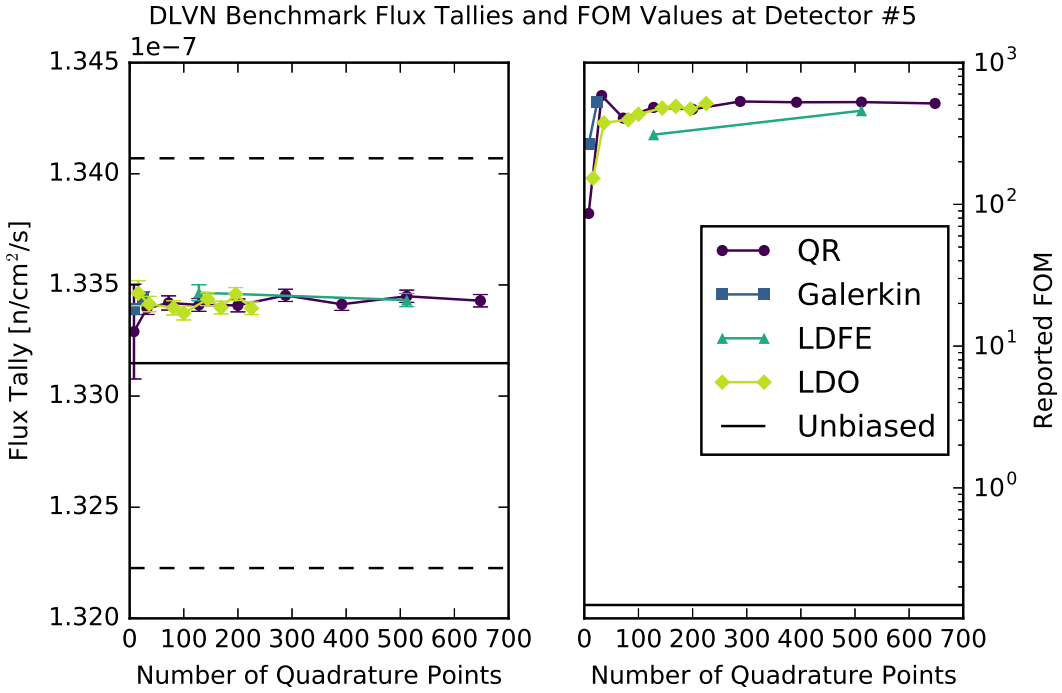

(a) MCNP-reported forward flux tally and FOM values at detector #5.

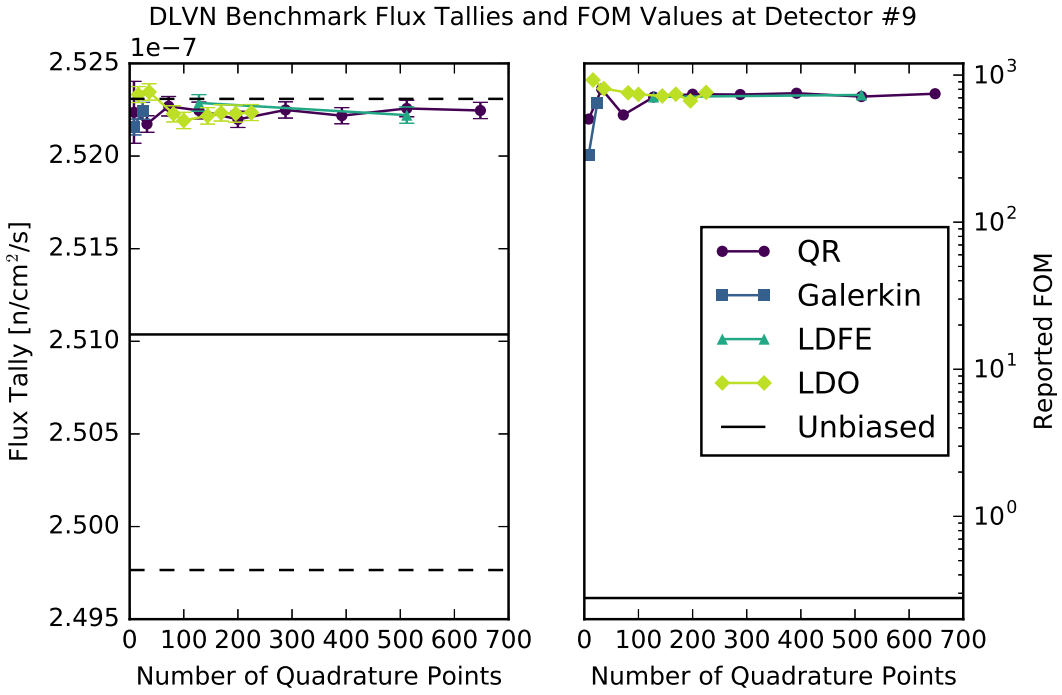

(b) MCNP-reported forward flux tally and FOM values at detector #9.

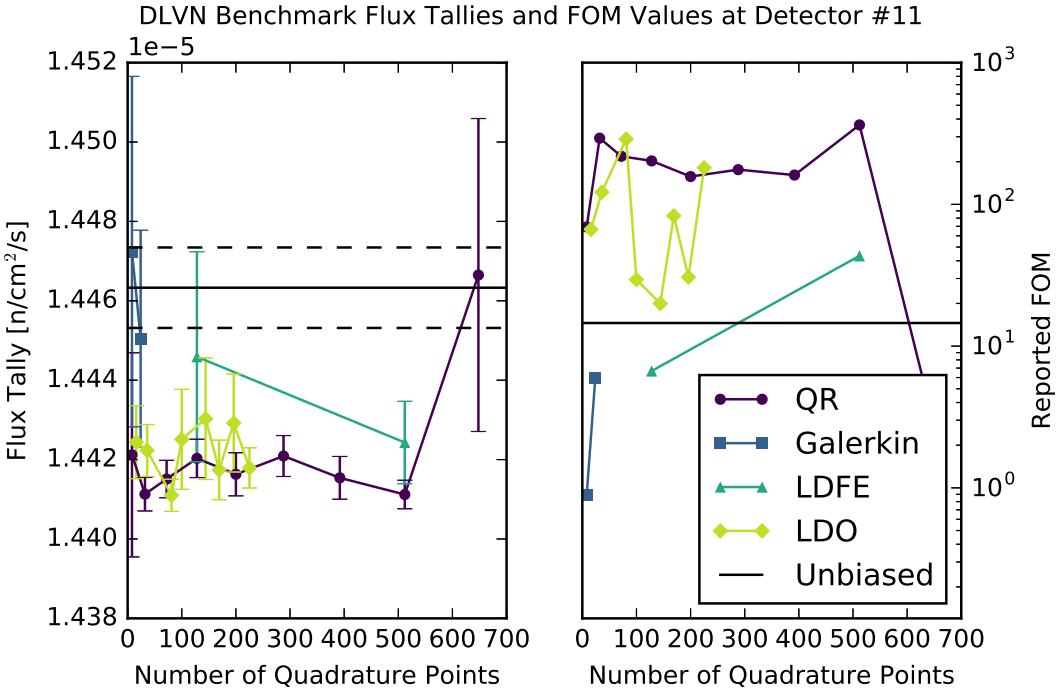

(c) MCNP-reported forward flux tally and FOM values at detector #11.

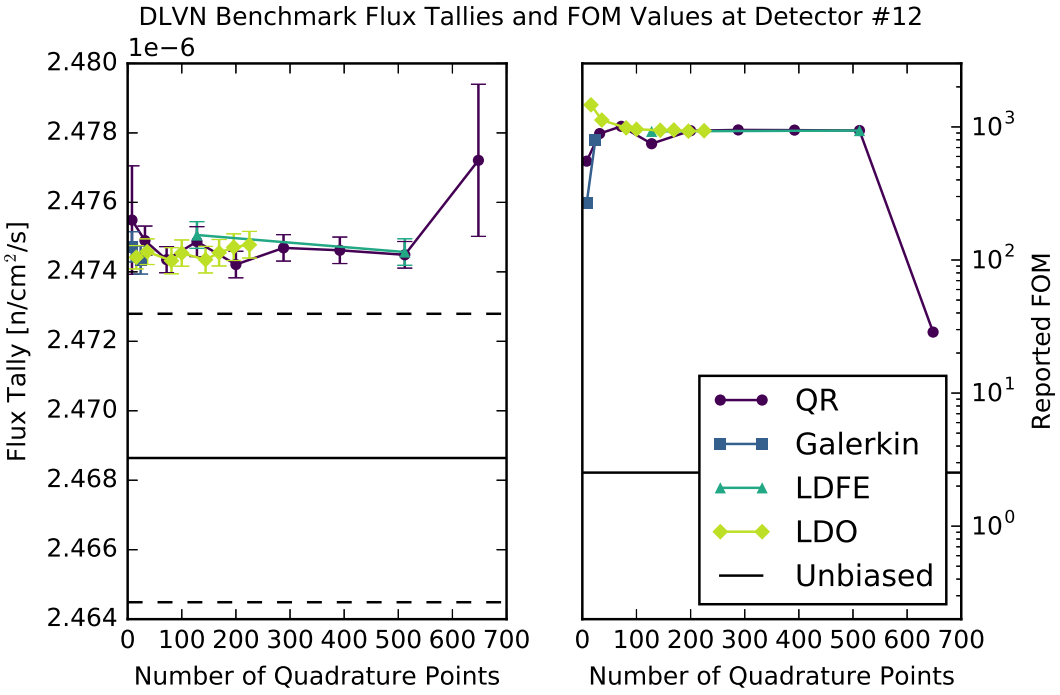

(d) MCNP-reported forward flux tally and FOM values at detector #12.

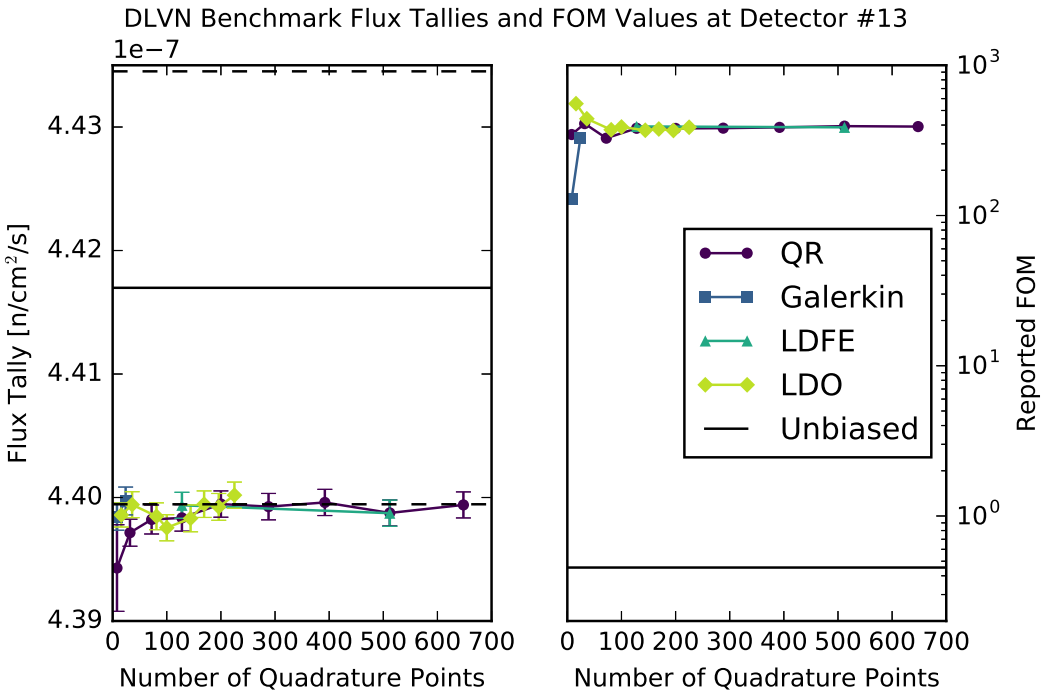

(e) MCNP-reported forward flux tally and FOM values at detector #13.

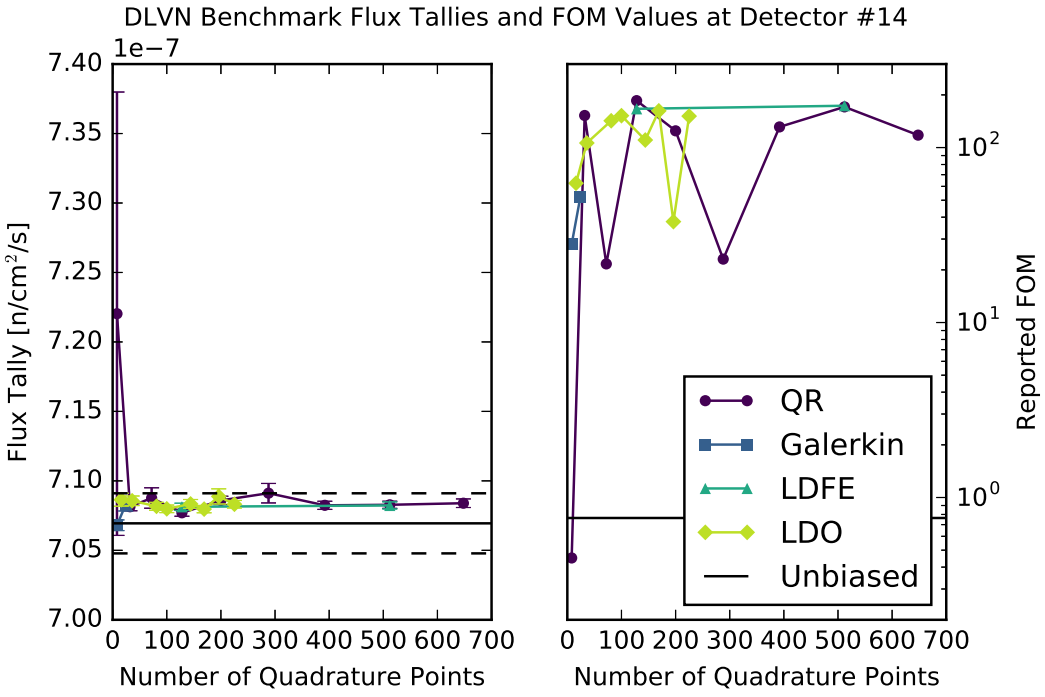

(f) MCNP-reported forward flux tally and FOM values at detector #14.

Figure 4.38: FW-CADIS flux tallies and FOM values for the DLVN problem.

4.4.3 Ispra Sodium Benchmark

As in the previous case, the adjoint source for the Ispra sodium benchmark problem in the context of the FW-CADIS method was specified to be the combination of all of the detector locations in the problem. Figure 4.39 shows the adjoint scalar flux solutions for the representative quadrature sets based on this specification. Relative differences between the representative LDO adjoint scalar flux and the standard quadratures' adjoint scalar fluxes are shown in Figure 4.40 with minimum, maximum, and average relative differences listed in Table 4.19. Again, comparisons of the QR flux solution against the Galerkin and LDFE flux solutions are tabulated for reference as well.

Table 4.19: Ispra sodium FW-CADIS adjoint flux extremal and average relative differences.

Comparison	**Min. Diff.**	**Max. Diff.**	**Avg. Diff.**
LDO/QR	2×10^{-6}	4.40×10^{1}	5.93×10^{-1}
LDO/Galerkin	6×10^{-7}	4.45×10^{4}	1.63×10^{2}
LDO/LDFE	1×10^{-6}	1.30×10^{2}	7.42×10^{-1}
Galerkin/QR	2×10^{-6}	1.00×10^{0}	4.42×10^{-1}
LDFE/QR	3×10^{-6}	5.05×10^{1}	8.00×10^{-1}

Comparing these differences to the values listed in Table 4.13, we see that the LDO adjoint flux matches those of the standard quadratures more closely on average in the FW-CADIS method than the CADIS method. This is to be expected, as the adjoint source in the FW-CADIS method is much less localized than in the CADIS method for this scenario. As with the forward and CADIS adjoint flux comparisons for the Ispra sodium benchmark, the differences between the representative LDO flux solution and the representative standard quadratures' flux solutions are exacerbated by the relatively coarse LDO angular mesh.

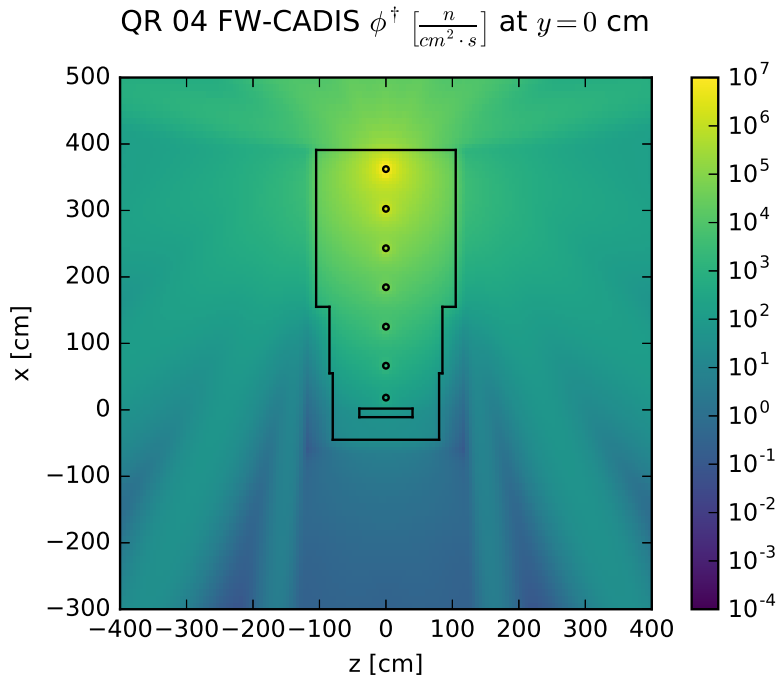

(a) QR adjoint flux slice.

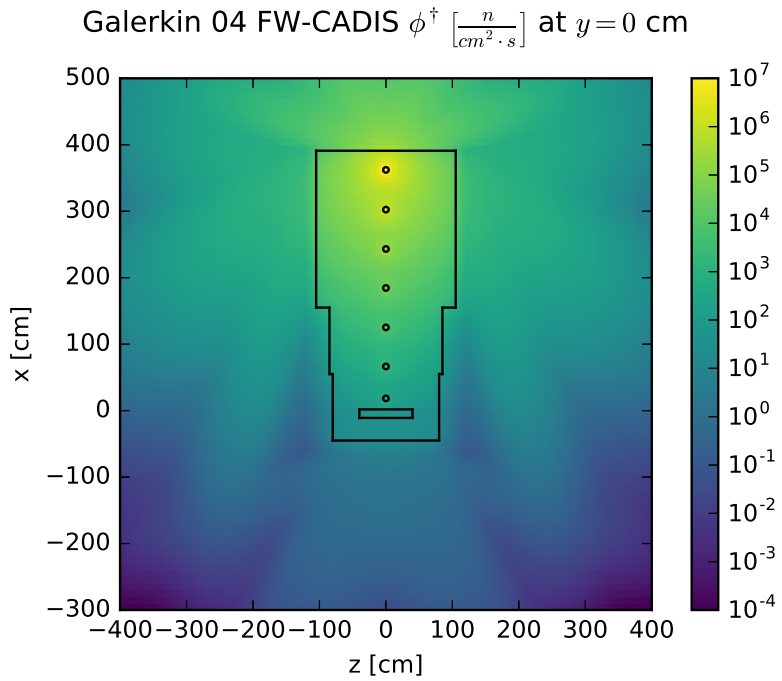

(b) Galerkin adjoint flux slice.

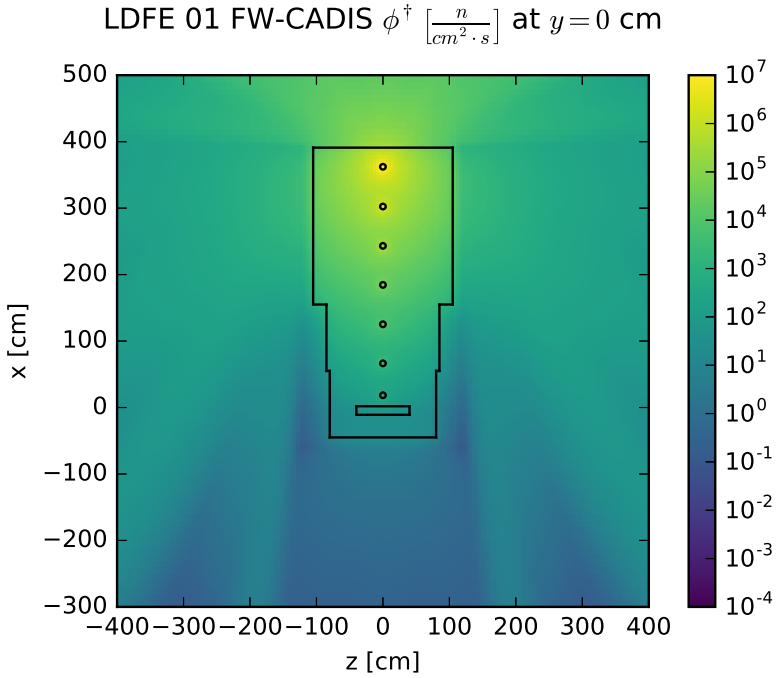

(c) LDFE adjoint flux slice.

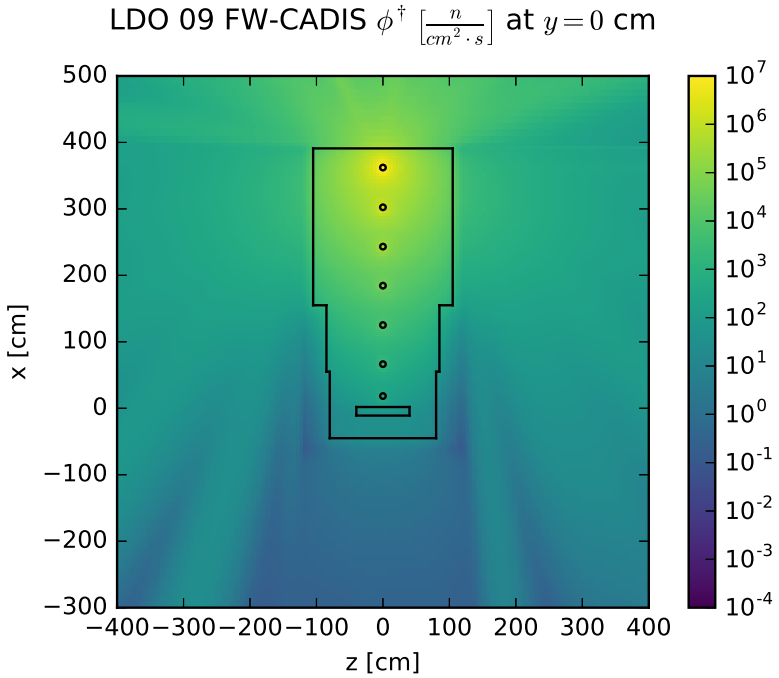

(d) LDO adjoint flux slice.

Figure 4.39: Ispra sodium benchmark adjoint scalar flux slices for the FW-CADIS method.

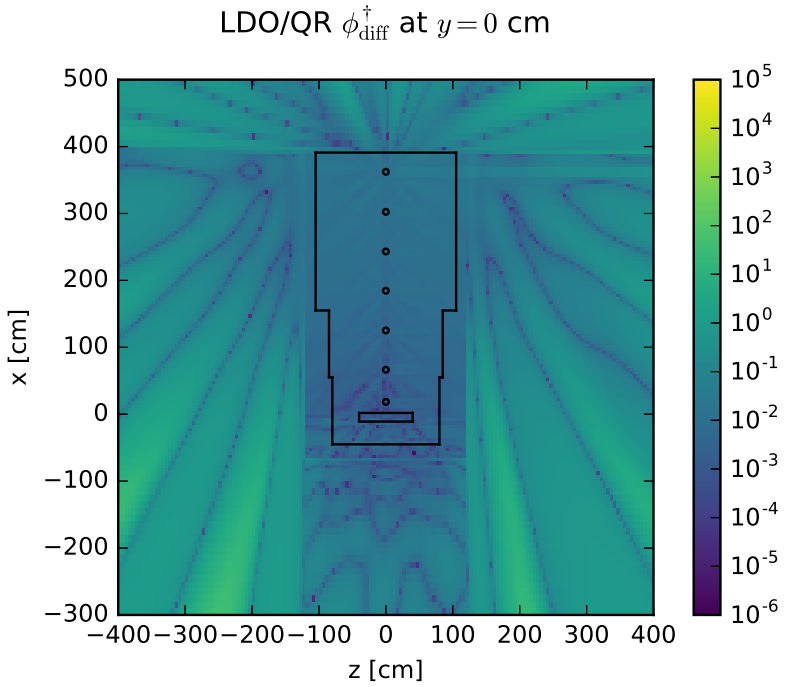

(a) LDO/QR flux relative difference.

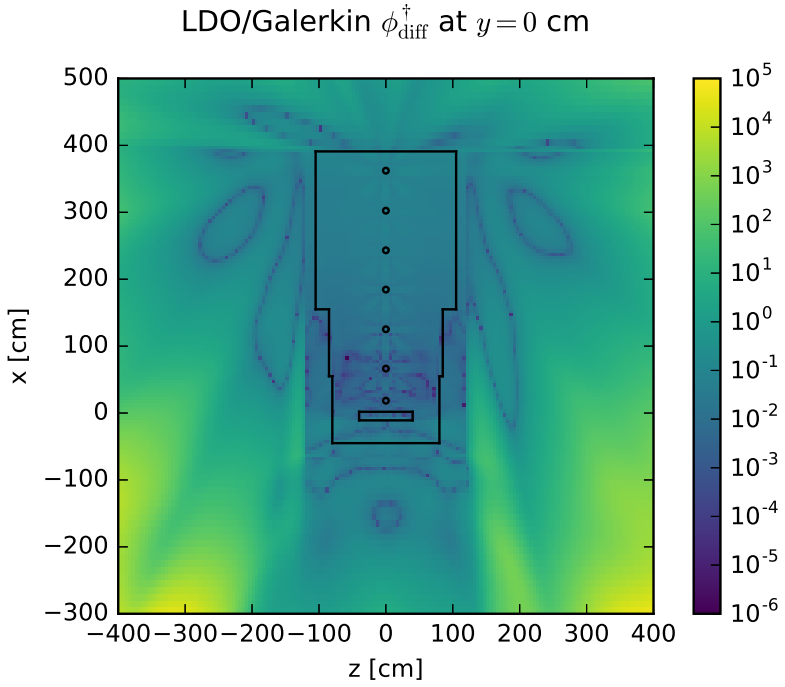

(b) LDO/Galerkin flux relative difference.

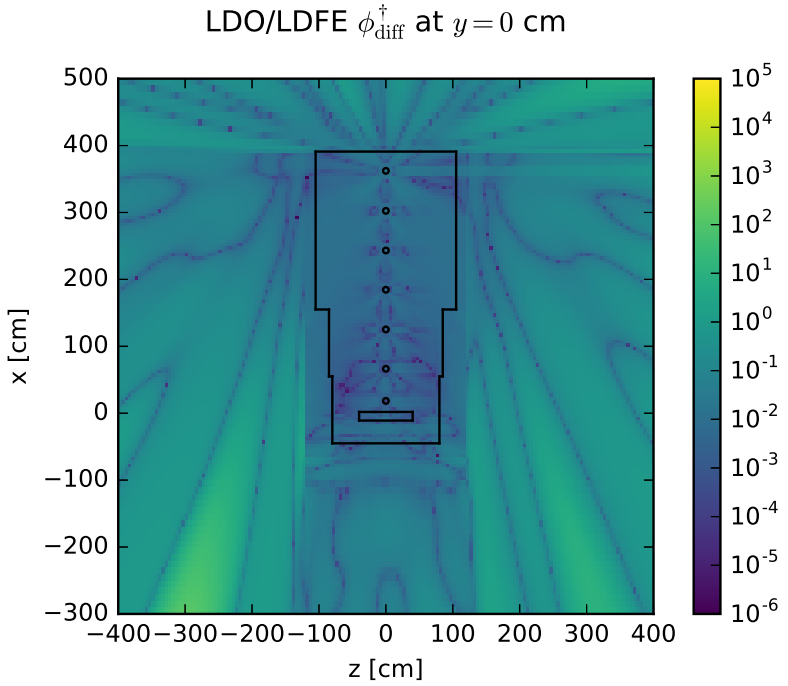

(c) LDO/LDFE flux relative difference.

Figure 4.40: Ispra sodium adjoint scalar flux relative difference slices for the FW-CADIS method.

Having looked at the deterministically calculated adjoint flux solutions for the FW-CADIS method, we move on to examine the results of the Monte Carlo calculations run using the corresponding biasing parameters. All calculations here used $1{\times}10^{9}$ neutron histories. Figure 4.41 shows the saturation activities calculated for the various detector locations using Equation 4.2 and the parameters listed in Section 4.2.4. Figures of Merit for the forward flux tallies are also shown. The detectors are numbered such that detector #1 is the closest to the experimental neutron source location with increasing detector number as the distance between the neutron source and the detector location increases.

Comparing Figures 4.39 and 4.41, it is clear to see that the statistical uncertainty associated with the calculated activity (propagated from that of the forward flux tally) is heavily correlated to the adjoint source strength at the detector location. That is, detector #7, which has the highest adjoint source strength, sees the lowest uncertainty in the activity values calculated there. Even with the variation in statistical uncertainty, the behaviors of the FOM values for all detectors are fairly consistent between the locations for the biased calculations. For all detector locations, the biasing parameters from the coarser angular meshes produce higher FOM values than the mid-range and fine angular meshes for the quadrature types studied here.

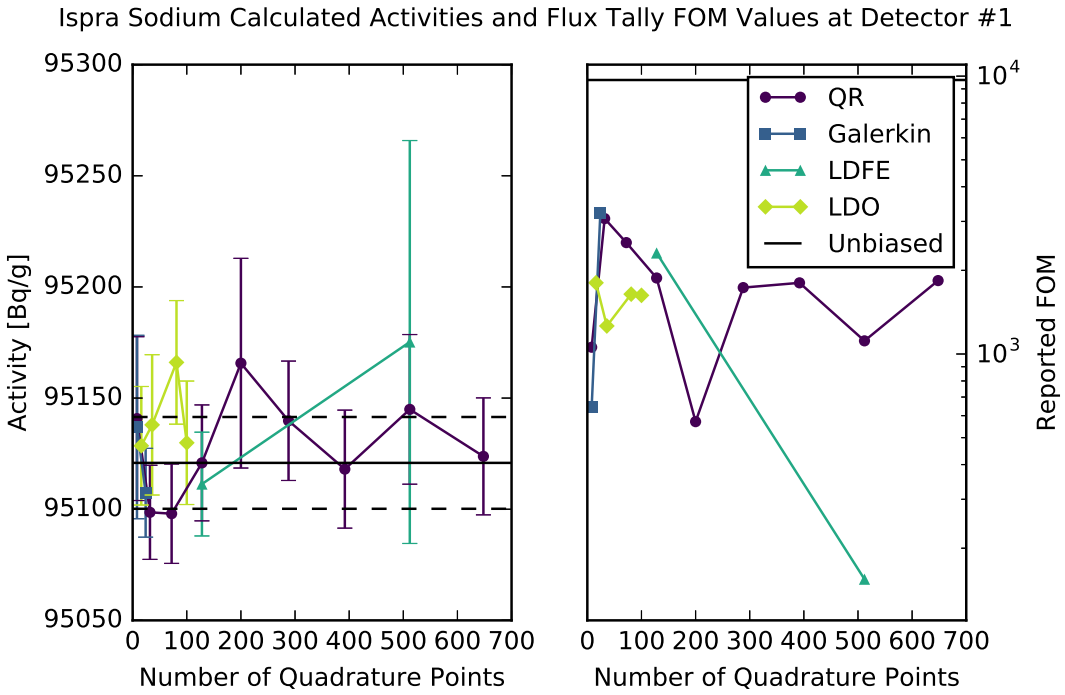

(a) Calculated activities and flux tally FOM values at detector #1.

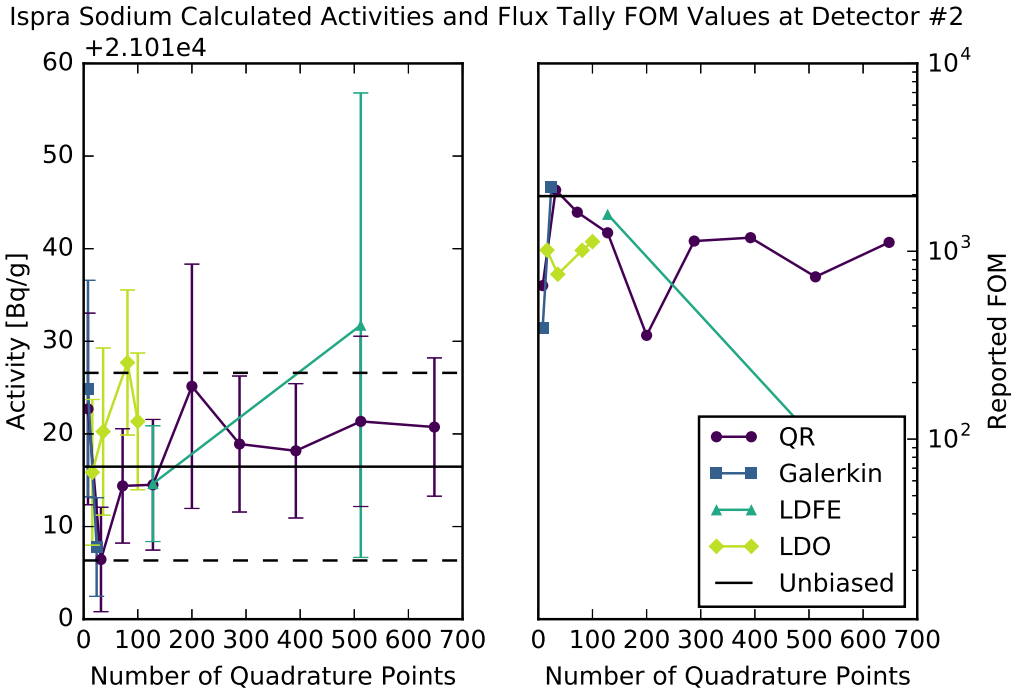

(b) Calculated activities and flux tally FOM values at detector #2.

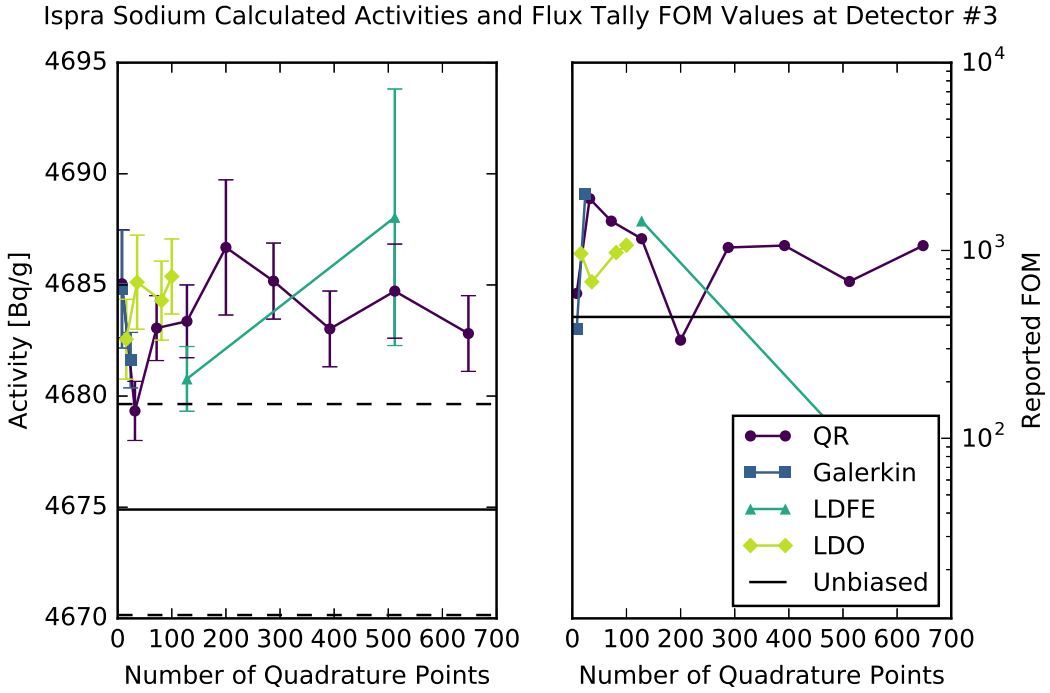

(c) Calculated activities and flux tally FOM values at detector #3.

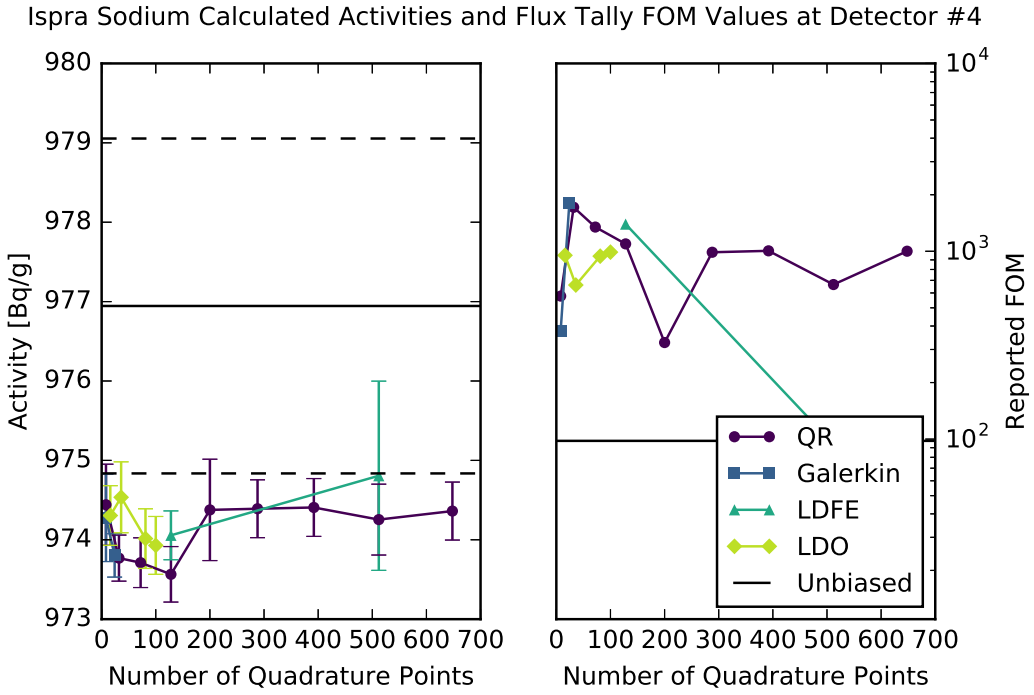

(d) Calculated activities and flux tally FOM values at detector #4.

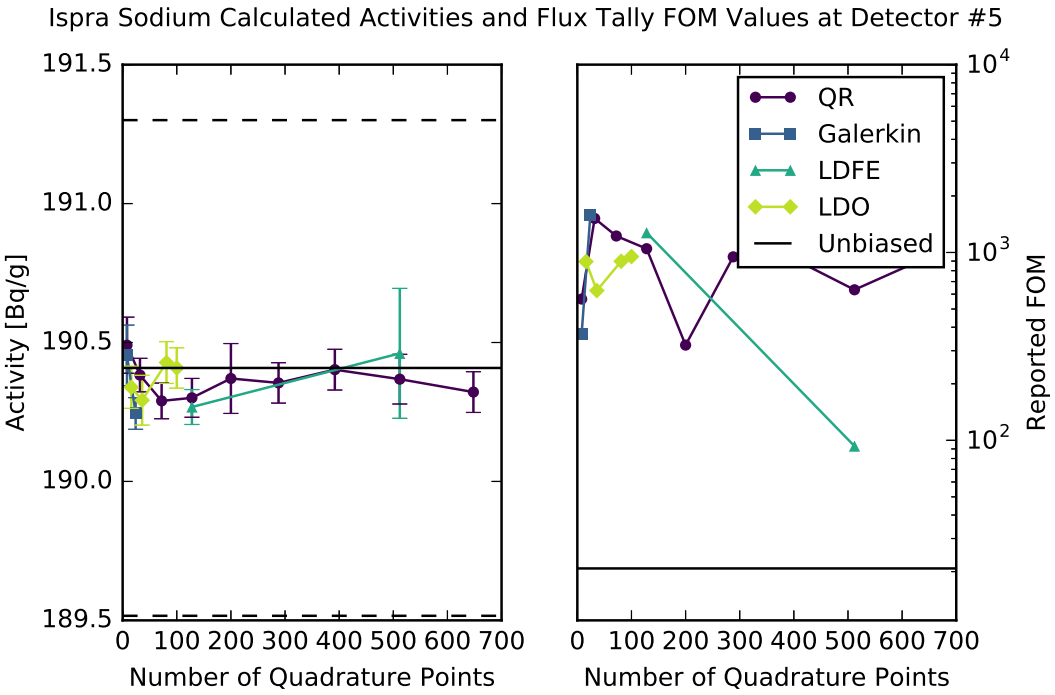

(e) Calculated activities and flux tally FOM values at detector #5.

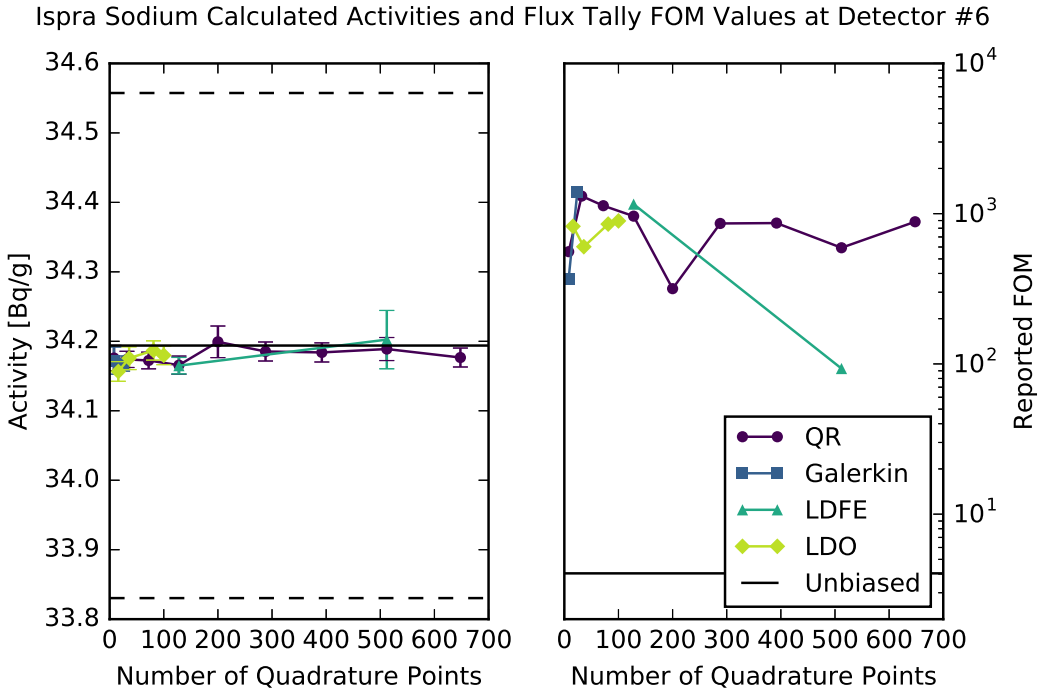

(f) Calculated activities and flux tally FOM values at detector #6.

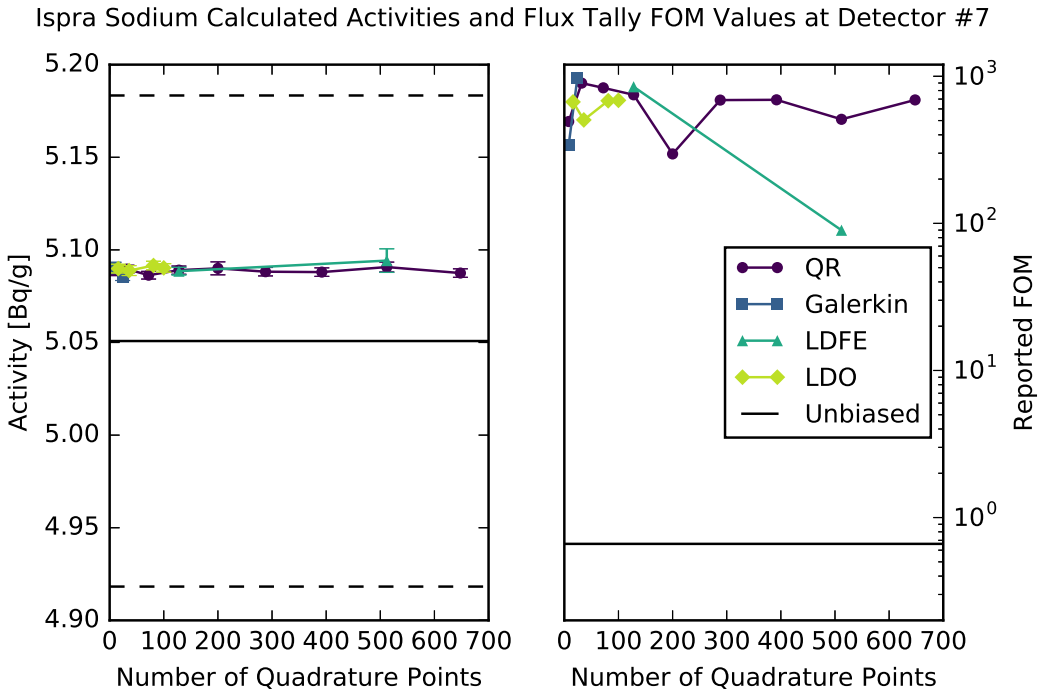

(g) Calculated activities and flux tally FOM values at detector #7.

Figure 4.41: Ispra sodium benchmark FW-CADIS calculated activity and FOM values.

Table 4.20 lists the Figures of Merit for all detector locations for the representative quadrature sets. The FOM values from the unbiased Monte Carlo calculation are also included for reference. For all detector locations except that closest to the experimental neutron source, the representative Galerkin quadrature set generates biasing parameters that produce the highest FOM. The unbiased calculation results in the highest overall FOM for the detector closest to the neutron source, which is unsurprising given the relative proximity of the neutron source and closest detector and the relatively low adjoint source strength for that detector location in the FW-CADIS adjoint scalar flux solutions.

Table 4.20: Representative quadratures' FW-CADIS FOM values for the Ispra sodium test.

Quad. Type	Det. #1	Det. #2	Det. #3	Det. #4	Det. #5	Det. #6	Det. #7
QR	1877.6	1254.2	1155.3	1094.7	1047.4	962.76	748.32
Galerkin	3211.0	**2205.2**	**1999.1**	**1797.5**	**1578.1**	**1398.1**	**969.99**
LDFE	2309.4	1573.0	1436.7	1394.9	1273.9	1157.4	848.77
LDO	1626.0	1125.3	1066.2	989.45	950.75	895.03	686.34
Unbiased	**9685.4**	1966.4	442.76	97.875	20.791	4.0357	0.66237

Lastly, in Table 4.21, we compare the activities calculated from the biased and unbiased Monte Carlo forward flux tallies. At all detector locations, the calculations from the biased

and unbiased Monte Carlo runs severely overestimate the experimentally measured saturation activity (see Section 4.3.3), so we examine the Monte Carlo results amongst themselves. All of the calculations match within statistical uncertainty at detector locations 1, 2, 5, 6, and 7. At detector #4, the biased calculations match within their respective statistical errors but are all outside of the error bounds of the unbiased calculation. Detector #3 sees calculated activities all on the same order of magnitude; not all of the biased calculations match within statistical uncertainty and only the calculated activity using the LDFE biasing parameters matches the unbiased calculation within error bounds.

Table 4.21: Ispra sodium benchmark activities [Bq/g] calculated with FW-CADIS.

	QR	**Galerkin**	**LDFE**	**LDO**	**Unbiased**
Det. #1 ($\times 10^4$)	9.5121 ± 0.0026	9.5107 ± 0.0020	9.5111 ± 0.0023	9.5130 ± 0.0028	9.5121 ± 0.0021
Det. #2 ($\times 10^4$)	2.1024 ±0.0007	2.1018 ± 0.0005	2.1024 ± 0.0006	2.1031 ±0.0007	2.1026 ± 0.0010
Det. #3 ($\times 10^3$)	4.6834 ± 0.0016	4.6816 ± 0.0012	4.6808 ± 0.0015	4.6854 ± 0.0017	4.6749 ± 0.0047
Det. #4 ($\times 10^2$)	9.7356 ± 0.0035	9.7380 ± 0.0027	9.7406 ± 0.0031	9.7393 ± 0.0036	9.7695 ± 0.0211
Det. #5 ($\times 10^2$)	1.9030 ± 0.0007	1.9024 ± 0.0006	1.9027 ± 0.0006	1.9041 ± 0.0007	1.0941 ± 0.0089
Det. #6 ($\times 10^1$)	3.4166 ± 0.0013	3.4168 ± 0.0011	3.4165 ± 0.0012	3.4180 ± 0.0013	3.4194 ± 0.0363
Det. #7 ($\times 10^0$)	5.0891 ± 0.0022	5.0854 ± 0.0019	5.0885 ± 0.0021	5.0903 ± 0.0023	5.0508 ± 0.1326

To summarize the results in this section, we note that the detector activity calculations from the LDO biasing parameters are comparable within statistical uncertainty to those from the standard quadrature types, but the LDO biasing parameters do not generate the highest Figure of Merit for any detector location for the representative quadrature set. So, we would not suggest using an LDO quadrature set in the FW-CADIS method for a situation such as this scenario with fast reactor materials and detectors (adjoint source locations) all along one line. Of the LDO quadrature sets tested in this scenario, the coarsest and finest angular meshes produce comparable FOM values for all of the detector locations.

4.4.4 Simplified Portal Monitor

To generate Monte Carlo variance reduction parameters for the simplified portal monitor using the FW-CADIS method, the adjoint source was set to be all four detector locations in the problem's detector array. Figure 4.42 shows the adjoint scalar flux solutions from the representative quadrature sets for this case. Ray effects are seen in the $x - y$ plane for all quadrature sets; this is unsurprising given the relatively localized adjoint source with respect

to this plane. Differences between the representative LDO adjoint flux solution and the other adjoint flux solutions are shown in Figure 4.43 and listed in Table 4.22.

Table 4.22: Portal monitor FW-CADIS adjoint flux extremal and average relative differences.

Comparison	**Min. Diff.**	**Max. Diff.**	**Avg. Diff.**
LDO/QR	8×10^{-5}	8.59×10^{1}	2.95×10^{0}
LDO/Galerkin	3×10^{-4}	2.53×10^{2}	1.02×10^{1}
LDO/LDFE	3×10^{-5}	3.46×10^{1}	8.54×10^{-1}
Galerkin/QR	4×10^{-4}	1.19×10^{2}	3.23×10^{0}
LDFE/QR	1×10^{-4}	8.67×10^{1}	2.88×10^{0}

As with all other test cases, the listed differences are relative and comparisons between the standard representative quadrature sets are included for reference. Unlike other scenarios, the LDO adjoint flux best matches the LDFE adjoint flux for the simplified portal monitor scenario and this FW-CADIS adjoint source specification. However, this best agreement is an average relative difference of 85%; none of the flux solutions agree particularly well here. The relative difference flux plots show ray effects similar to those seen for the forward and CADIS adjoint scalar fluxes for all quadrature types in the simplified portal monitor scenario.

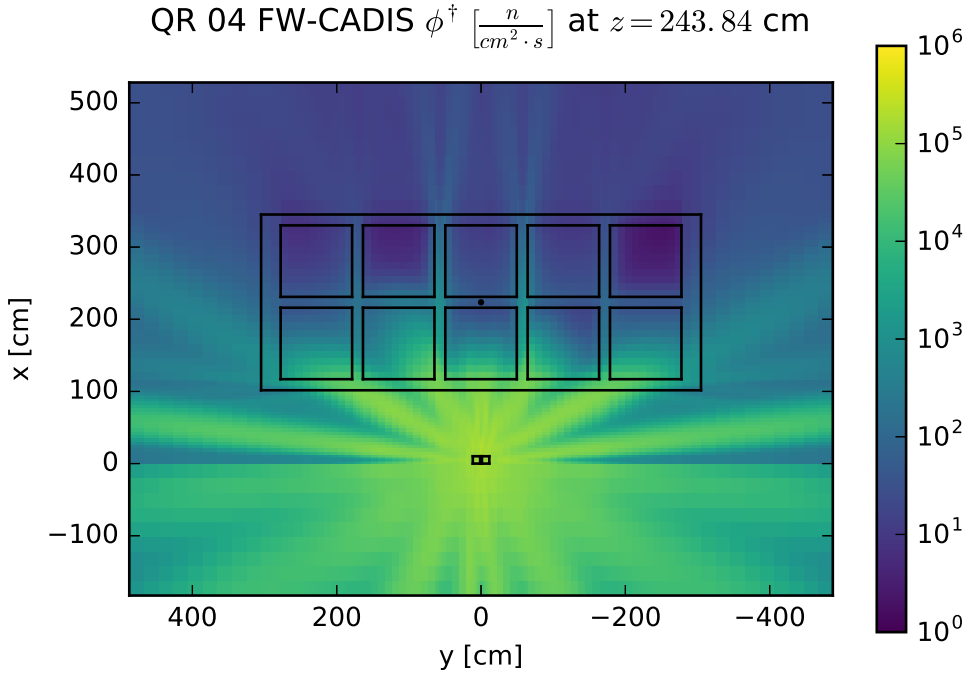

(a) QR adjoint flux slice.

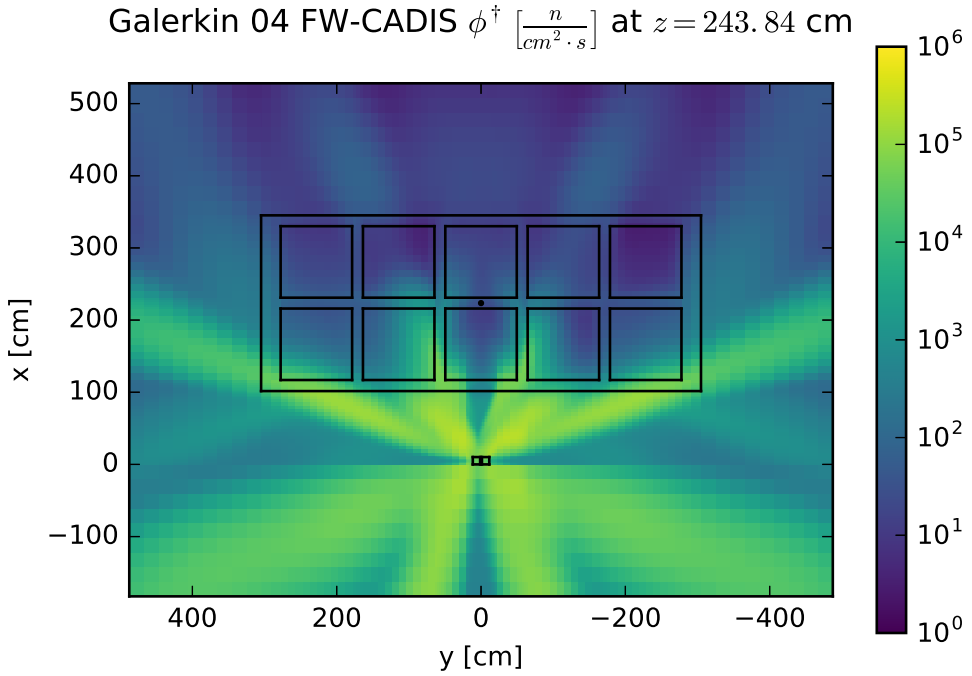

(b) Galerkin adjoint flux slice.

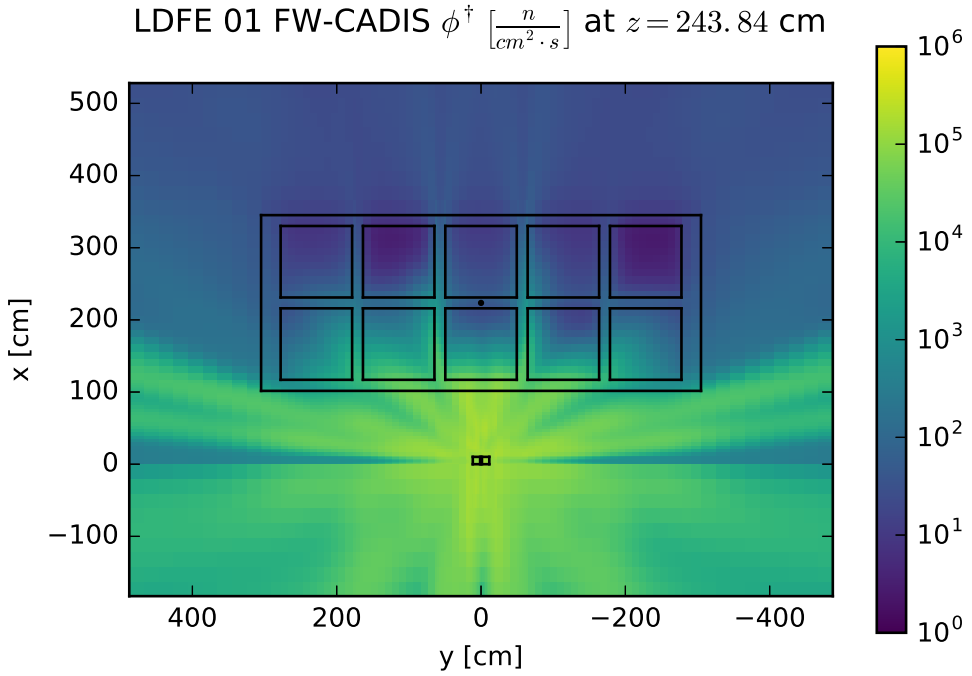

(c) LDFE adjoint flux slice.

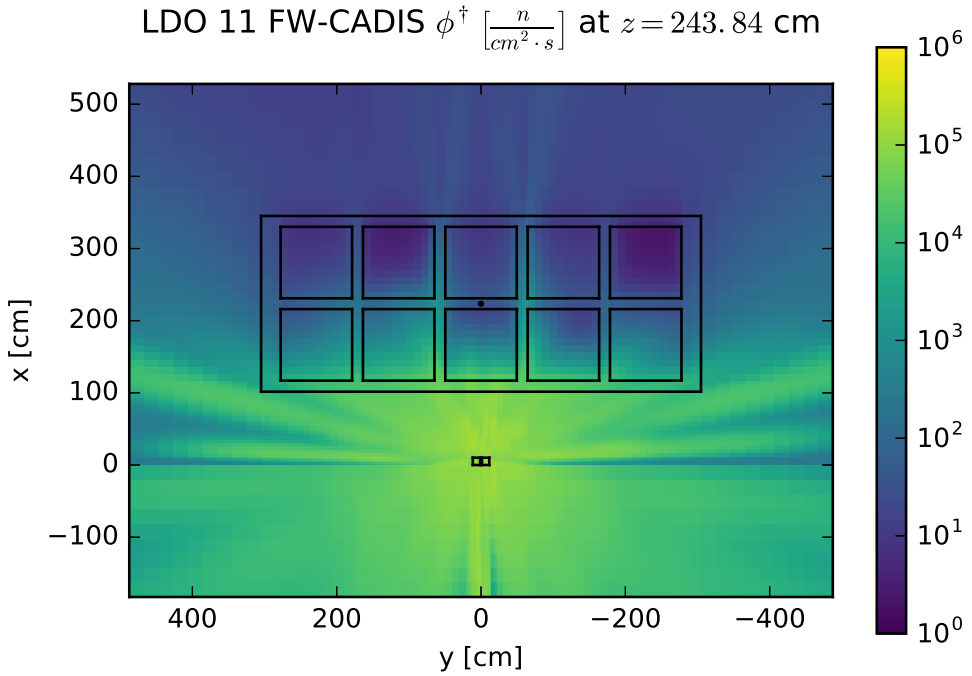

(d) LDO adjoint flux slice.

Figure 4.42: Simplified portal monitor adjoint flux slices for the FW-CADIS method.

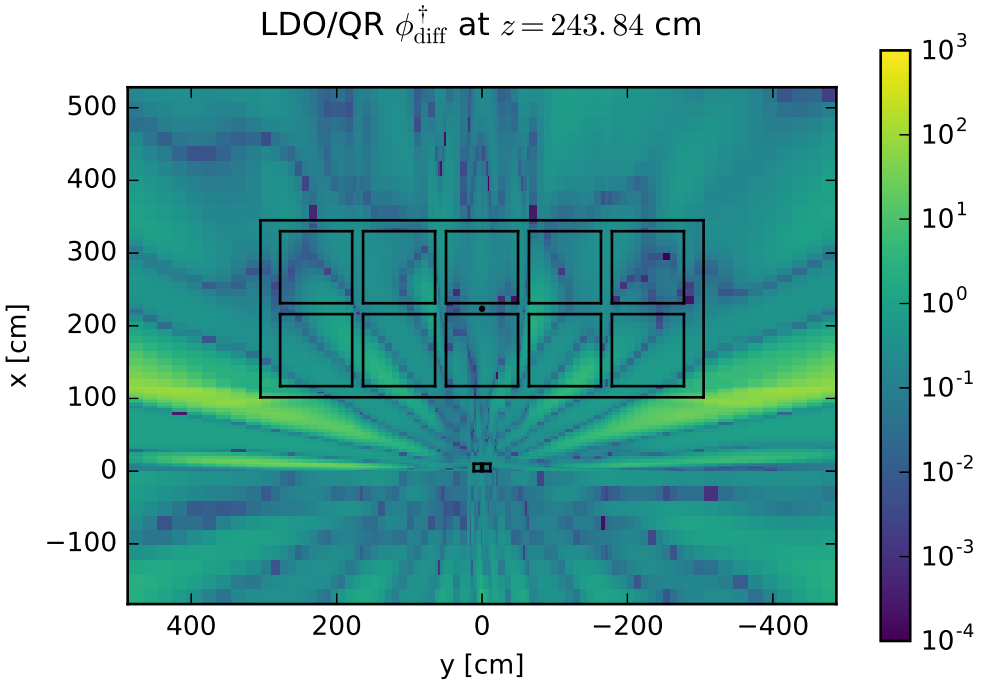

(a) LDO/QR flux relative difference.

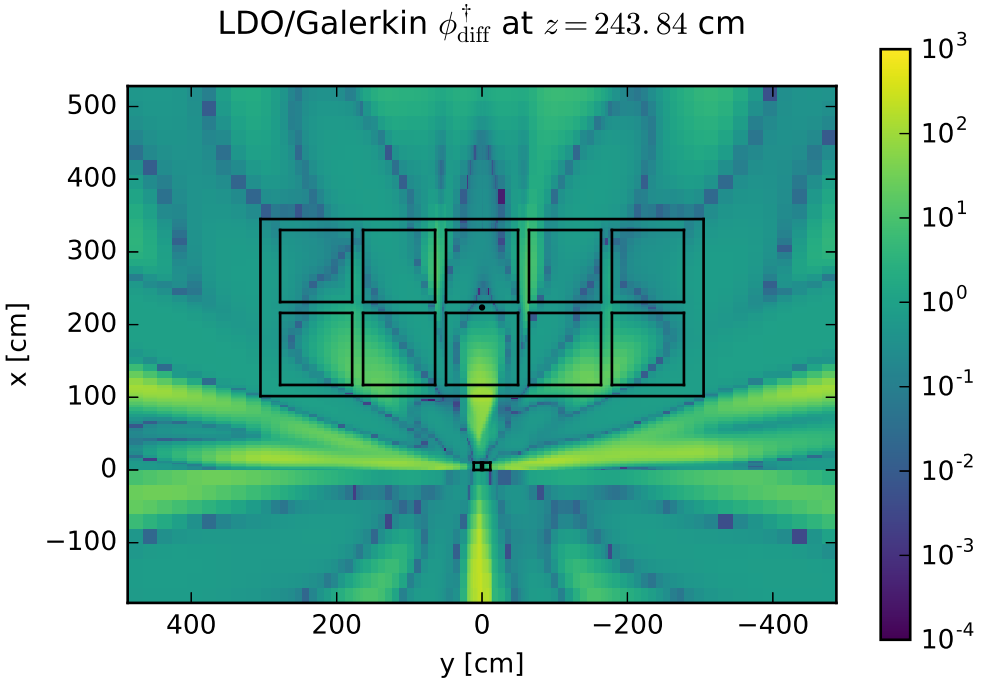

(b) LDO/Galerkin flux relative difference.

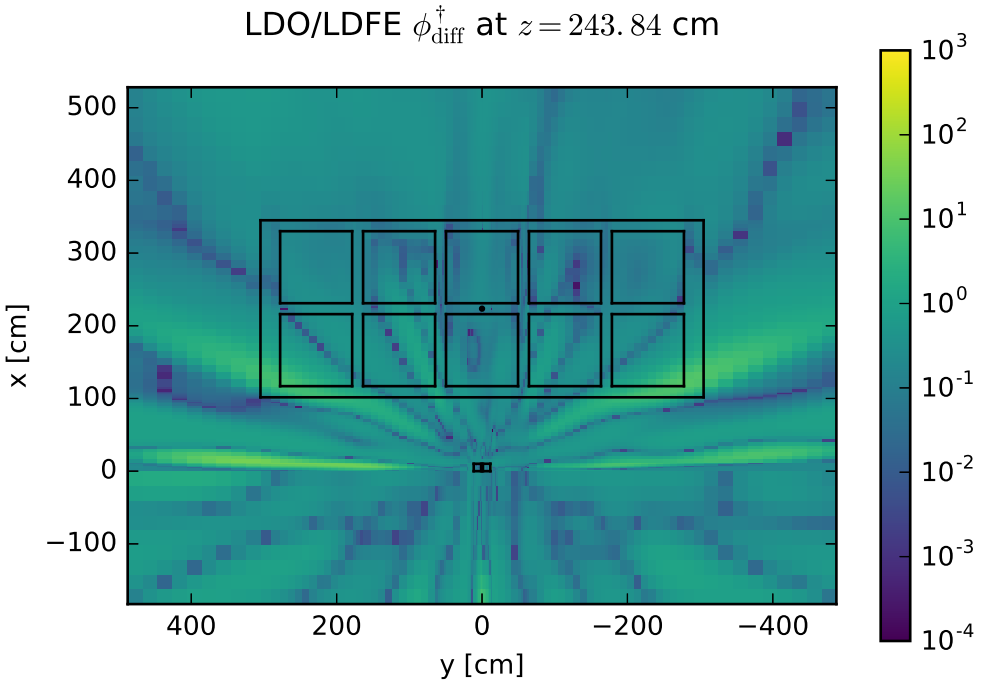

(c) LDO/LDFE flux relative difference.

Figure 4.43: Portal monitor adjoint flux relative difference slices for the FW-CADIS method.

Figure 4.44 shows MCNP-reported forward scalar flux tallies and Figures of Merit for all four detectors in the array. The flux tallies and FOM values are each plotted as a function of the number of discrete angles used in the quadrature sets that were used to generate biasing parameters. In all plots, the unbiased calculation result is shown as a horizontal black line. At all detector locations, the forward flux tallies and FOM values show the same trend of leveling off to a stable value once the angular mesh used for the FW-CADIS biasing parameters has been refined past the few coarsest numbers of discrete angles. At all detector locations except for the 2nd in the array, the unbiased calculation and the calculations with biasing parameters resultant from the representative quadrature sets all match within statistical uncertainty. The 2nd detector sees all representative biased flux tallies matching one another but outside the error bounds of the unbiased flux tally calculation.

Table 4.23 lists the Figures of Merit for the various detector locations for the representative quadrature sets. The unbiased calculation FOM values are also tabulated for reference. We see that the biasing parameters from the representative LDO quadrature set produce the highest Figures of Merit for three out of four detector locations, with the representative QR quadrature set's biasing parameters achieving the highest FOM for the bottom detector in the array.

Table 4.23: FW-CADIS FOM values for representative quadratures for the portal monitor.

Quad. Type	Top Detector	2nd Detector	3rd Detector	Bottom Detector
QR	76.115	121.24	128.9	**81.125**
Galerkin	30.249	38.139	34.01	29.016
LDFE	65.613	96.156	115.5	61.655
LDO	**85.707**	**132.96**	**140.3**	75.135
Unbiased	4.4096	3.1520	2.096	2.8313

To conclude, using LDO quadrature sets to generate Monte Carlo biasing parameters in the FW-CADIS method is particularly promising for cases such as the simplified portal monitor scenario. When selecting an LDO quadrature set to generate variance reduction parameters for similar photon transport problems, a relatively coarse angular mesh of order 5 or 8 may be used to good effect.

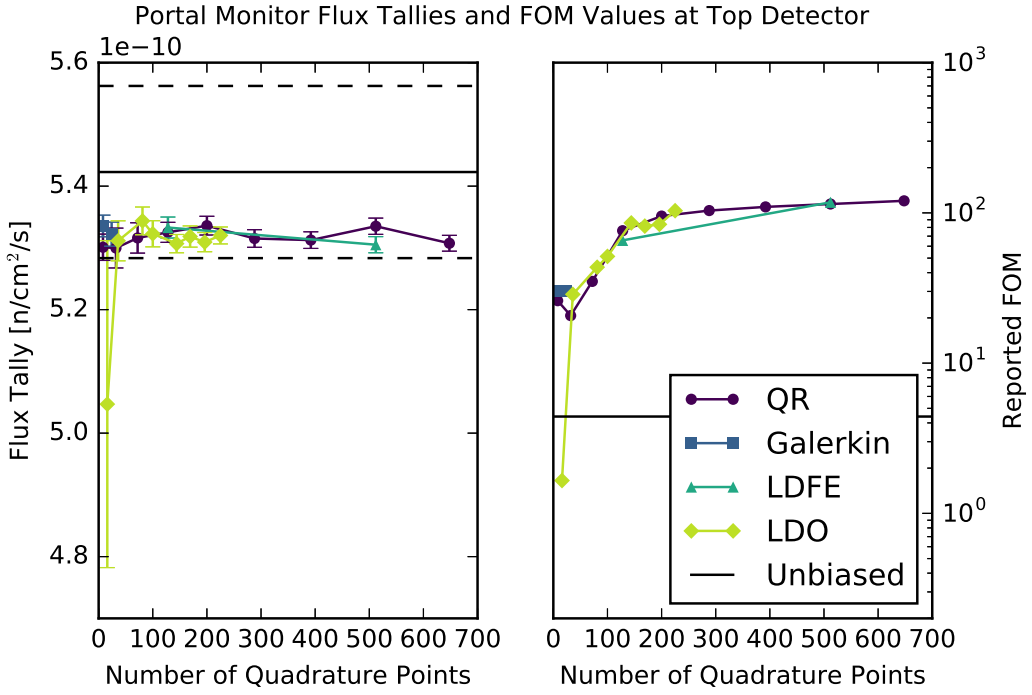

(a) MCNP-reported forward flux tally and FOM values at the top detector.

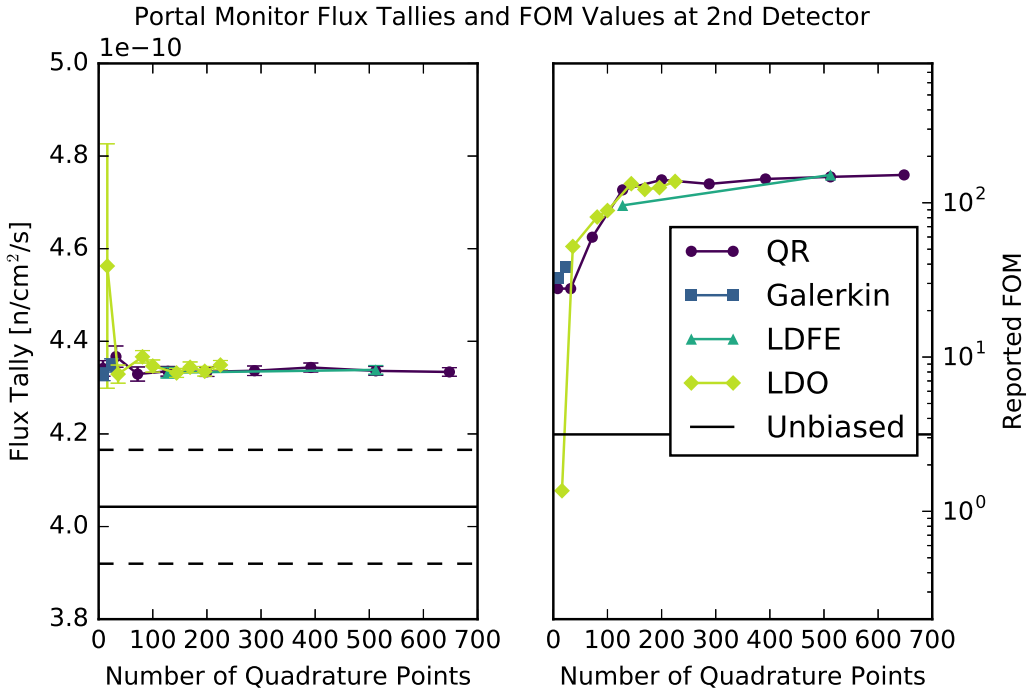

(b) MCNP-reported forward flux tally and FOM values at the second detector.

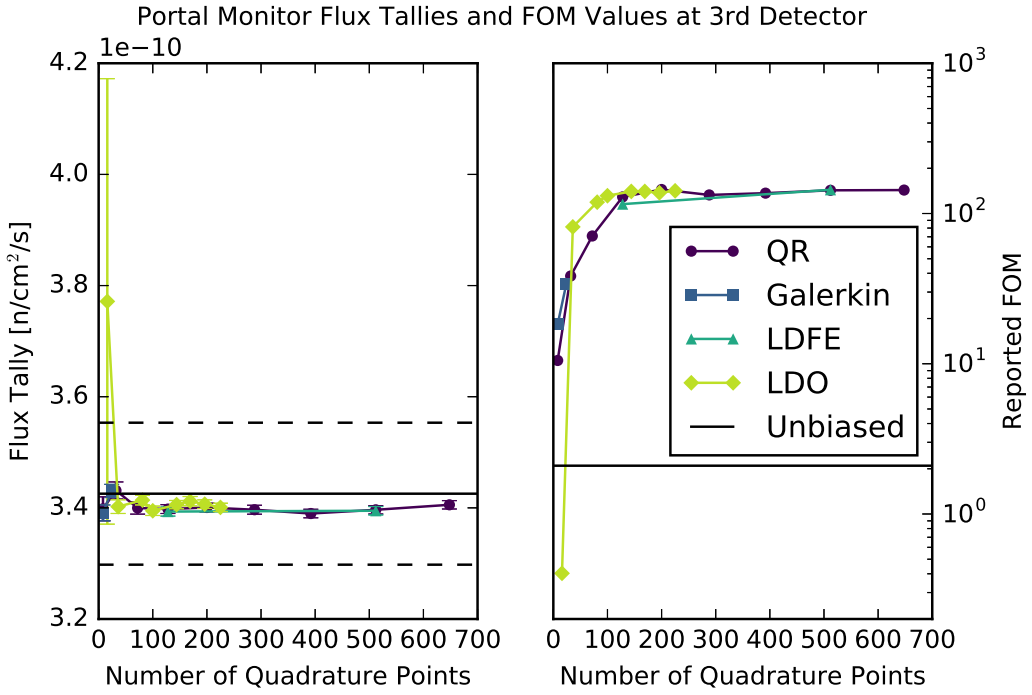

(c) MCNP-reported forward flux tally and FOM values at the third detector.

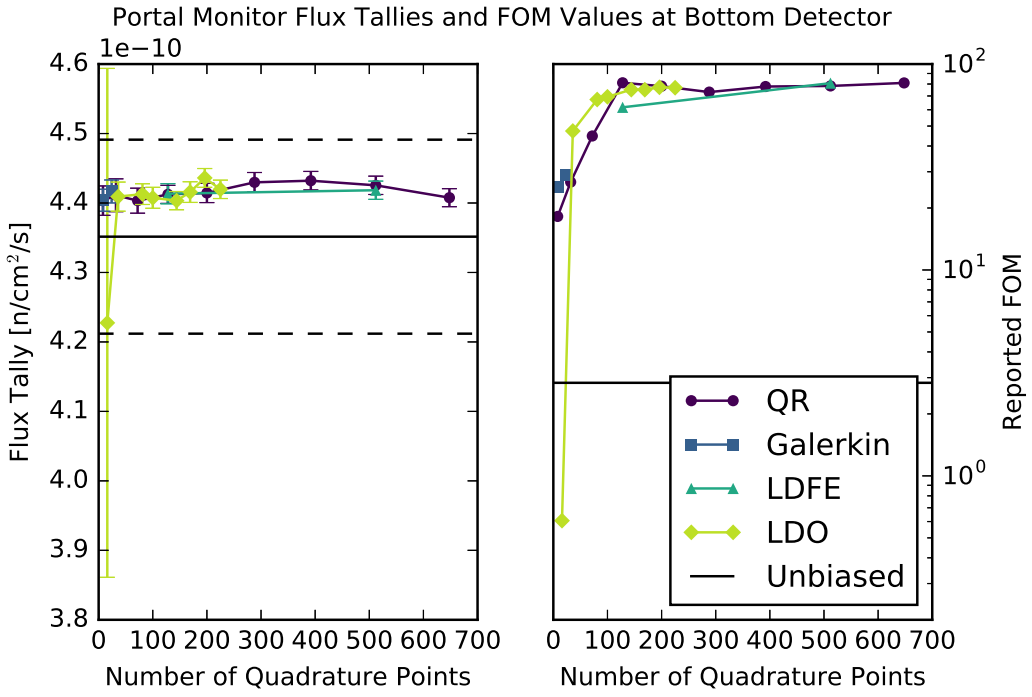

(d) MCNP-reported forward flux tally and FOM values at the bottom detector.

Figure 4.44: FW-CADIS flux tallies and FOM values for the portal monitor scenario.

4.4.5 Summary

We conclude the FW-CADIS method section by summarizing the results presented here. As in Section 4.3, the representative LDO adjoint scalar flux solutions were compared with those of representative standard quadrature types for each test case scenario. Compared to the CADIS calculations, the steel plate in water and DLVN experimental benchmark cases showed much more uniform relative differences for the adjoint scalar flux solutions in the context of the FW-CADIS method. Differences in the Ispra sodium benchmark and simplified portal monitor scenarios still appeared as ray effects due to the small scale of the FW-CADIS adjoint sources in the large problem geometries.

For the Monte Carlo results using the biasing parameters of the various quadrature sets from the FW-CADIS method, the forward flux tally results using the LDO biasing parameters were comparable to those of standard quadrature types across all of the test case scenarios. We generally recommend using a coarse LDO angular mesh of order 5 or 8 to generate biasing parameters for Monte Carlo neutral particle transport problems in the context of the FW-CADIS method. Highlights of the LDO quadratures' performance in this section include the representative LDO quadrature set producing the highest FOM values for two out of the six detector locations in the DLVN benchmark and three out of four detector locations in the simplified portal monitor scenario. To this end, further exploration of using LDO solutions for Monte Carlo variance reduction parameter generation for photon transport using the FW-CADIS method is an area of future work and interest.

4.5 Chapter Summary

Finally, we end the chapter with an overall summary of the results and discussion presented, with a specific focus on outcomes from LDO quadrature sets. Before exploring the LDO equations' solutions as input for Monte Carlo variance reduction parameter generation, we first performed comparative studies for the LDO equations' forward scalar flux solutions versus those of QR, Galerkin, and LDFE quadrature sets for four test case scenarios. Because QR quadrature sets are commonly used in Monte Carlo variance reduction parameter generation, particular attention was paid to the comparisons between the LDO and QR forward flux results. At best, the average relative difference between the representative LDO and QR forward flux solutions was 2.2% for the steel plate in water test case. The Ispra sodium benchmark case saw the greatest LDO/QR forward flux difference at an average of 50%. Based on this general agreement and all quadrature types capturing the same physical phenomena in each test case, we moved forward to explore the LDO equations' solutions in Monte Carlo variance reduction parameter generation.

Before looking at the results of the Monte Carlo calculations using biasing parameters from the CADIS method, the deterministic adjoint scalar flux solutions were explored for the different quadrature types. In this context, the LDO/QR adjoint flux solution comparison had the smallest relative difference (3.8%) for the DLVN experimental benchmark. The

responses of interest for the Monte Carlo calculations were studied as a function of angular mesh refinement used in the generation of biasing parameters. On the whole, little correlation was seen between angular mesh refinement and the MCNP-reported forward flux tally values in the CADIS context. If using an LDO quadrature set to generate biasing parameters in this context for any of the neutron transport scenarios, a low-order (3 - 8) quadrature set may be used to sufficient effect for flux tally value and FOM achievement. For generating biasing parameters in the CADIS context for a photon problem with an LDO quadrature set, the finest available angular mesh should be used. This is consistent with what is expected based on the difference between neutron and photon scattering in the materials in these test case scenarios.

Finally, studies of deterministic adjoint scalar flux solutions and their efficacy as input for Monte Carlo variance reduction parameter generation were performed in the context of the FW-CADIS method. Here the LDO adjoint flux solution best matched the QR adjoint flux solution in the steel plate scenario with an average relative difference of 4.6% between the representative quadrature sets' solutions. Again in this context we found that low-order (5 or 8) angular meshes are sufficient to produce forward flux tally and Figure of Merit values comparable to those of more refined angular meshes when using LDO quadrature sets. The superior FOM values resultant from the representative LDO quadrature set for three of four detectors in the simplified portal monitor scenario begets interest in further exploration of LDO equations' solutions as input for Monte Carlo biasing parameters for photon transport in the FW-CADIS context.

Chapter 5

Conclusions and Future Work

To conclude this dissertation, we present a summary of the results and analysis delivered in the previous chapter followed by an outlook for future work based on the preliminary endeavors undertaken here. The ultimate research goal achieved in this work as well as the complementary objectives met along the way serve to contribute to the body of knowledge regarding hybrid methods for neutral particle radiation transport in shielding and deep penetration applications.

5.1 Summary and Conclusions

In this work, the LDO equations were implemented in the Exnihilo parallel neutral particle radiation transport framework for the purpose of using the equations' solutions in Monte Carlo variance reduction parameter generation via the ADVANTG software to improve the results of simulations run with MCNP5. A small variety of test case scenarios were examined in the CADIS and FW-CADIS contexts with biasing parameters generated from flux solutions of different quadrature types to ascertain the LDO solutions' performance relative to unbiased Monte Carlo calculations as well as those with biasing parameters from standard quadrature types.

Deterministically-calculated forward and adjoint scalar flux solutions from the LDO equations were found to be comparable to those of standard quadrature types. The LDO equations saw their best-performing Monte Carlo biasing parameters in the FW-CADIS context. For the DLVN experimental benchmark, LDO variance reduction parameters generated the highest Figures of Merit for two of the six detector locations in the assembly. Of those studied here, the only other quadrature type to achieve this was the QR quadrature set. In the case of the simplified portal monitor scenario studied in the FW-CADIS context, the LDO biasing parameters attained the highest FOM values for three out of four detector locations. Considering results from the test case scenarios in which neutrons were transported using the CADIS and FW-CADIS methods, we suggest a coarse angular mesh for Monte Carlo variance reduction parameter generation based on flux solutions resultant from solving the

LDO equations. For photon transport problems, a more refined LDO angular mesh is recommended for generating Monte Carlo biasing parameters and achieving detector responses with high Figures of Merit.

In general, the LDO formulation is most useful in the specific context of Monte Carlo variance parameter generation using the FW-CADIS method for photon transport problems. It is also effective in the FW-CADIS method for neutron transport problems, though somewhat less so. However, the LDO representation is currently limited in applicability by its current implementation in the Exnihilo framework and the ADVANTG software. The problem space available to explore is limited to those with vacuum boundary conditions and isotropic fixed particle sources with non-zero volume. Adopting the LDO formulation in another radiation transport and Monte Carlo variance reduction parameter generation framework would be of interest if the framework is flexible in allowing for asymmetric quadrature sets to be used and if the framework allows for relative ease in implementing the unique features of the LDO representation such as interpolation in angle.

To conclude, we note that the novel work towards this dissertation includes the implementation of the LDO equations in a radiation transport framework as well as the study of the resultant scalar flux solutions' efficacy in Monte Carlo variance parameter generation in both the CADIS and FW-CADIS methods. The results and analysis presented here are of interest to the community at large in that the LDO representation treats particle scattering differently than the traditional discrete ordinates formulation and incorporates angular information into scalar flux solutions in a new way. This improves the performance of hybrid methods in shielding problems with highly anisotropic particle movement and particle streaming pathways when using the FW-CADIS method, especially for photon transport problems.

5.2 Future Work

Various avenues of future work have become apparent over the course of this work. Some facets of investigation are more rudimentary and concern details regarding the implementation of the LDO equations in a radiation transport software framework, while others are more research-oriented questions.

We will first discuss suggested future work that concerns implementation details and studies that may follow. As reflective boundary conditions are commonly used in both deterministic and Monte Carlo transport methods to reduce problem space and compute time, one of the first next steps to take would be to enable the use of reflective boundary conditions with the LDO equations in Denovo. This is less straightforward than for standard quadrature types because of the LDO equations' asymmetry in angle, but it should be possible using the interpolation property of the LDO representation. In a similar vein, enabling the use of analytic approximations of uncollided flux sources in combination with solving the LDO equations in Denovo would be a next logical development. This would enable the direct use of point sources when solving the LDO equations through the Exnihilo

framework and help to mitigate the ray effects from the point sources in the resultant flux solutions.

Modifying the ADVANTG software to support more variety in deterministic calculations and Monte Carlo variance parameter generation would open doors for more interesting studies with the LDO equations as well as standard quadrature types. Specifically, implementing the use of anisotropic particle sources would allow for studies involving commonly-used directional particle sources such as beams. Additionally, generalizing the FW/CADIS-Ω methods implemented in the ADVANTG software such that quadrature sets that are not rotationally symmetric could be directly used in concert with the methods would bring about an additional channel for capturing the LDO equations' unique scattering treatment in angle-informed scalar flux solutions used to generate Monte Carlo biasing parameters. Currently, the LDO equations' deterministic flux solutions could be used in combination with the FW/CADIS-Ω methods with the use of the interpolation property of the LDO equations. This interpolation functionality does not exist in either the Exnihilo framework or the ADVANTG software at the time of this writing.

Broader research questions involving solving the LDO equations are of interest as well. The test case scenarios in this work were limited to relatively small scales with respect to computational hardware usage; studies with finer LDO angular meshes across larger hardware configurations would be instructive to see at what subspace degree, if any, the LDO equations' flux solutions mitigate ray effects in relevant real-world scenarios. Additionally, we suggest testing rotated versions of the LDO quadrature sets to study the relationship between ordinate placement and problem geometry in detector response and FOM production. This would be a fairly straightforward next step; the point sets generated by Womersley used in this work are rotationally invariant and the Exnihilo framework imports the LDO quadrature sets from plain text files. So, rotation matrices or formulae could be applied to the already-existing LDO point sets with the new rotated quadratures directly input to Exnihilo (and ADVANTG) for study in deterministic calculations as well as in Monte Carlo variance reduction parameter generation. As an alternative to conducting studies with increased angular resolution, we suggest undertaking investigations that use the interpolatory nature of the LDO representation once this ability has been realized in the various software frameworks involved.

Bibliography

[1] James J. Duderstadt and Louis J. Hamilton. *Nuclear Reactor Analysis*. New York, NY: John Wiley & Sons, Inc., 1976.

[2] E.E. Lewis and W.F. Miller. *Computational Methods of Neutron Transport*. New York, NY: John Wiley & Sons, Inc., 1984.

[3] X-5 Monte Carlo Team. *MCNP – A General Monte Carlo N-Particle Transport Code, Version 5*. Volume I: Overview and Theory. LA-UR-03-1987. Revised 2/1/2008. Los Alamos National Laboratory, Los Alamos, NM, Apr. 2003. URL: `https://laws.lanl.gov/vhosts/mcnp.lanl.gov/pdf_files/la-ur-03-1987.pdf`.

[4] Richard H. Olsher. "A Practical Look at Monte Carlo Variance Reduction Methods in Radiation Shielding". In: *Nuclear Engineering and Technology* 38.3 (2006), pp. 225–230.

[5] Cory D. Ahrens. "Lagrange Discrete Ordinates: A New Angular Discretization for the Three-Dimensional Linear Boltzmann Equation". In: *Nuclear Science and Engineering* 180.3 (2015), pp. 273–285.

[6] Thomas Evans et al. *Exnihilo Transport Methods Manuals*. Tech. rep. CASL-U-2015-0080-000, Revision 0. Oak Ridge National Laboratory, Mar. 2015.

[7] Thomas M. Evans et al. "Denovo: A new three-dimensional parallel discrete ordinates code in SCALE". In: *Nuclear Technology* 171.2 (2010), pp. 171–200. URL: `https://doi.org/10.13182/NT171-171`.

[8] S.W. Mosher et al. *ADVANTG – An Automated Variance Reduction Parameter Generator*. Tech. rep. ORNL/TM-2013/416, Rev. 1. Oak Ridge National Laboratory, Aug. 2015.

[9] Kaye D. Lathrop. "Ray Effects in Discrete Ordinates Equations". In: *Nuclear Science and Engineering* 32.3 (1968), pp. 357–369.

[10] Ray E. Alcouffe et al. *PARTISN: A Time-Dependent, Parallel Neutral Particle Transport Code System*. Tech. rep. LA-UR-05-3925. Los Alamos National Laboratory, May 2005.

[11] John C. Wagner and Alireza Haghighat. "Automated Variance Veduction of Monte Carlo Shielding Calculations using the Discrete Ordinates Adjoint Function". In: *Nuclear Science and Engineering* 128.2 (1998), pp. 186–208.

[12] John C. Wagner, Edward D. Blakeman, and Douglas E. Peplow. "Forward-weighted CADIS Method for Variance Reduction of Monte Carlo Calculations of Distributions and Multiple Localized Quantities". In: *Proceedings of the 2009 Int. Conference on Advances in Mathematics, Computational Methods, and Reactor Physics, Saratoga Springs, NY*. 2009.

[13] Douglas E. Peplow, Scott W. Mosher, and Thomas M. Evans. *Consistent Adjoint Driven Importance Sampling using Space, Energy, and Angle*. Tech. rep. ORNL/TM-2012/7. Oak Ridge National Laboratory, 2012.

[14] M. Munk et al. "FW/CADIS-Ω: An angle-informed hybrid method for deep-penetration radiation transport". In: *Proceedings of the PHYSOR 2016 Meeting in Sun Valley, ID* (May 2016). URL: https://arxiv.org/pdf/1612.00793.pdf.

[15] Madicken Munk. "FW/CADIS-Ω: An Angle-Informed Hybrid Method for Neutron Transport". PhD thesis. University of California, Berkeley, 2017.

[16] Kenneth A. Van Riper et al. "AVATAR – Automatic variance reduction in Monte Carlo calculations". In: *Proceedings of the Joint International Conference on Mathematical Methods & Supercomputing for Nuclear Applications in Saratoga Springs, NY* (October 1997). URL: http://www.osti.gov/scitech/biblio/527548.

[17] Raymond E. Alcouffe. *THREEDANT: A Code To Perform Three-Dimensional, Neutral Particle Transport Calculations*. Tech. rep. LA-UR-94-3259. Los Alamos National Laboratory, 1994.

[18] Marc A. Cooper and Edward W. Larsen. "Automated weight windows for global Monte Carlo particle transport calculations". In: *Nuclear science and engineering* 137.1 (2001), pp. 1–13. URL: http://www.ans.org/pubs/journals/nse/a_2171.

[19] Scott A. Turner and Edward W. Larsen. "Automatic variance reduction for three-dimensional Monte Carlo simulations by the local importance function transform-I: Analysis". In: *Nuclear Science and Engineering* 127.1 (1997), pp. 22–35. URL: https://doi.org/10.13182/NSE127-22.

[20] Scott A. Turner and Edward W. Larsen. "Automatic variance reduction for three-dimensional Monte Carlo simulations by the local importance function transform-II: Numerical Results". In: *Nuclear Science and Engineering* 127.1 (1997), pp. 36–53. URL: https://doi.org/10.13182/NSE127-36.

[21] C.D. Ahrens. *Derivation of New 3D Discrete Ordinate Equations*. Tech. rep. American Nuclear Society, Inc., 555 N. Kensington Avenue, La Grange Park, Illinois 60526 (United States), 2012.

[22] Thomas Evans et al. *Exnihilo Documentation: Release 6.2.0 (Dev)*. Tech. rep. Oak Ridge National Laboratory, 2017.

[23] B. T. Rearden and M. A. Jessee, eds. *SCALE Code System*. ORNL/TM-2005/39, Version 6.2.1. Available from Radiation Safety Information Computational Center as CCC-834. Oak Ridge National Laboratory. 2016.

[24] Greg Davidson and Tom Evans. *Refactoring of Sweep Sources in Denovo (Rev. 3)*. Tech. rep. NMDS-10-004. Oak Ridge National Laboratory, November 28, 2016.

[25] Rob Womersley. *Extremal (Maximum Determinant) points on the sphere S^2*. `http://web.maths.unsw.edu.au/~rsw/Sphere/Extremal/New/index.html`.

[26] S.C. Wilson and R.N. Slaybaugh. "Improved Monte Carlo Variance Reduction for Space and Energy Self-Shielding". In: *Nuclear Science and Engineering* 179.1 (2015), pp. 22–41. URL: `https://doi.org/10.13182/NSE13-109`.

[27] Andrej Trkov. "Analysis of the Rowlands Uranium Oxide Pin-Cell Benchmark with an Updated WIMS-D Library". In: *Annals of Nuclear Energy* 25.10 (1998), pp. 747–752.

[28] Ronald J. McConn et al. *Compendium of Material Composition Data for Radiation Transport Modeling*. Tech. rep. PIET-43741-TM-963, PNNL-15870 Rev. 1. Pacific Northwest National Laboratory (PNNL), Richland, WA (US), 2011. URL: `https://doi.org/10.2172/1023125`.

[29] R. N. Slaybaugh and S. C. Wilson. "Deterministic Parameter Study for Fixed-Source Calculations Using FW-CADIS". In: *Trans. Am. Nucl. Soc* 108 (2013), p. 441.

[30] Joshua J. Jarrell, Marvin L. Adams, and Joel M. Risner. "Application of Quadruple Range Quadratures to Three-Dimensional Model Shielding Problems". In: *Nuclear Technology* 168.2 (2009), pp. 424–430.

[31] Douglas Allen Barnett Jr. "Benchmark measurements and Calculations of a Three-Dimensional Neutron Streaming Experiment". In: *International Topical Meeting on Advances in Mathematics, Computations, and Reactor Physics, Pittsburgh, PA, USA*. 1991.

[32] I. Kodeli, E. Sartori, and B. Kirk. "SINBAD Shielding Benchmark Experiments Status and Planned Activities". In: *The American Nuclear Society's 14th Biennial Topical Meeting of the Radiation Protection and Shielding Division, Carlsbad, New Mexico, USA*. Citeseer. 2006.

[33] Advanced Micro Devices Inc. *AMD Opteron™ 6300 Series Processors*. `http://www.amd.com/en-us/products/server/opteron/6000/6300`. 2017.

[34] Berkeley Research Computing. *System Overview*. `http://research-it.berkeley.edu/services/high-performance-computing/system-overview`. 2018.

[35] Joshua J. Jarrell and Marvin L. Adams. "Discrete-Ordinates Quadrature Sets Based on Linear Discontinuous Finite Elements". In: *International Conference on Mathematics and Computational Methods Applied to Nuclear Science and Engineering (M&C 2011), Rio de Janeiro, RJ, Brazil*. 2011.

[36] J. E. Morel. "A Hybrid Collocation-Galerkin-S_N Method for Solving the Boltzmann Transport Equation". In: *Nuclear Science and Engineering* 101.1 (1989), pp. 72–87.

[37] R. Nicks, G. Perlini, and H. Rief. "Fission Neutron Penetration in Iron and Sodium – I. Activation Measurements". In: *Annals of Nuclear Energy* 15.9 (1988), pp. 457–469.

[38] H. Depuydt and M. Neve de Mevergnies. "Average Cross Section of the $^{32}S(n,p)^{32}P$ and ^{27}Al (n, α)^{24}Na Reactions for Fission Neutrons". In: *Journal of Nuclear Energy. Parts A/B. Reactor Science and Technology* 16.9 (1962), pp. 447–453.

[39] International Atomic Energy Agency. *Evaluated Nuclear Data File (ENDF)*. `https://www-nds.iaea.org/exfor/endf.htm`. 2018.